D 2022

U.PORTO
FEUP FACULDADE DE ENGENHARIA
UNIVERSIDADE DO PORTO

EFFECTS OF PROCESSING PARAMETERS ON DIRECT LASER DEPOSITED MATERIALS FOR INDUSTRIAL COMPONENTS REPAIR

ANDRÉ ALVES FERREIRA

Doctoral Thesis in Metallurgical and Materials Engineering, in the field of Engineering Sciences and Technologies - Materials Engineering, supervised by Professor Doctor Manuel Fernando Gonçalves Vieira and Professor Doctor Ana Rosanete Lourenço Reis, submitted to the Faculty of Engineering of the University of Porto.

January 2022

Faculty of Engineering of the University of Porto

EFFECTS OF PROCESSING PARAMETERS ON DIRECT LASER DEPOSITED MATERIALS FOR INDUSTRIAL COMPONENTS REPAIR

ANDRÉ ALVES FERREIRA

Doctoral Thesis in Metallurgical and Materials Engineering, in the field of Engineering Sciences and Technologies - Materials Engineering, supervised by Professor Doctor Manuel Fernando Gonçalves Vieira and Professor Doctor Ana Rosanete Lourenço Reis, submitted to the Faculty of Engineering of the University of Porto.

January 2022

"You are my God, and I will give you praise; my God, and I will give honour to your name. O give praise to the Lord, for he is good: for his mercy is unchanging for ever." Psalms 118 : 28-29

Acknowledgements

First of all, I would like to thank God for allowing us to reach the end of this long journey. Thank you, Lord, for Your mercy is infinite.

I´m very grateful to my wife, Lidiane Ferreira and my sons Caetano Ferreira and Pedro Ferreira, whose constant support and prayers helped me complete it successfully. I would also like to thank my dear parents, Laci Ferreira and Vania Ferreira, for believing in and helping me to achieve what I have dreamed of in my life so far. I thank all my relatives and friends for their support over the years.

I want to express my deepest gratitude to my advisor Prof. Dr Manuel Fernando Gonçalves Vieira, for his support during all these years. He was a caring and dedicated supervisor who always helped me with his time, advice, insights; he encouraged me to publish my research and inspired my growing passion for science. He provided all the necessary resources for my investigation. I am particularly grateful for the opportunity and confidence he placed with me when he agreed to supervise me even before we met in person when the first contact was made in Brazil.

I also sincerely appreciate the support of my co-advisor, Prof. Dr Ana Rosanete Reis. Her support and discussions have been fundamental throughout all these years. Thank you for providing the resources to complete this PhD thesis.

I thank Prof. Dr Luis Filipe Malheiros and Prof. Dr Laura Ribeiro, for all the opportunities and advice given to me during this journey. It was, is, and will greatly contribute to my professional and academic life.

It is essential to thank Prof. Dr Filomena Viana for the advice and all the scientific discussions that enriched this doctoral thesis.

I also express my thanks to all Professors and Technicians in the Department of Metallurgical and Materials Engineering who made the work environment very positive every day in addition to their excellent work at the university.

I am extremely grateful to the SERMEC Group that, through Eng. João Cruz and Dr. Mário Duarte, it was possible to develop all the experimental activities and technical discussions that enriched this doctoral thesis. I am also grateful for the opportunity to be part of this group that has helped me in my technical-scientific growth throughout these years.

I express my deep gratitude to the GEAR3D project (POCI-01-0247-FEDER-039848) and to the Associate Laboratory in Energy, Transport and Aeronautics (LAETA), for their assistance on many fronts, such as finance (experiences, conferences, raw materials, and so on), for the equipment and resources that were indispensable for the PhD completion.

I thank the ADDing (reference POCI-01-0145-FEDER-030490) and the Add.Additive (reference POCI-01-0247-FEDER-024533) projects for all the support given throughout my PhD.

I am grateful to Dr Omid Emadinia, Dr Rubem Santos and Dr Rui Rocha for countless discussions, conversations and help along the way. All of our discussions helped me in the course of this investigation.

It is also essential to thank my colleagues MSc. Aida Beatriz, MSc. Iris Carneiro, MSc. Marcionilo Neri and MSc. Tânia Peixoto at the Department of Metallurgical and Materials Engineering for their friendship and companionship.

I thank my colleagues at INEGI, MSc. Diogo Fula, MSc. João Sousa, MSc. Ricardo Cardoso, MSc. Roya Darabi, Dr Rui Amaral and MSc. Rui Soares for his friendship, conversations, assistance, and exchange of experiences were fundamental throughout this journey.

Finally, I thank the professors at PUC-Rio: Prof. Dr Fernando Rizzo, Prof. Dr Ivani Bott, Prof. Dr José Roberto D'almeida, Prof. Dr Maurício de Jesus, Prof. Dr Roberto de Avillez, Prof. Dr Sydney Parcionik and Prof. Dr Valter Rocha; EQ/UFRJ: Prof. Dr Eliana Flávia (EQ/ UFRJ) and INT: Prof. Dr Márcia Lutterbach, for inspiring me throughout my academic life.

Cofinanciado por:

COMPETE 2020 PORTUGAL 2020 UNIÃO EUROPEIA Fundo Europeu de Desenvolvimento Regional

Abstract

The world's ambitious renewable energy goals push wind energy to become a mainstream energy source. Wind turbines are subject to harsh/hostile environments, which shorten the life cycle considerably. In many cases, gears are replaced with only one or two pinion teeth with total or partial breakage, or even worse, with only excessive wear on one or two teeth. In these cases, the repair would avoid complete pinion replacement, substantially reducing costs and downtime.

Motivated by this emerging need, this PhD project aimed to explore an additive direct laser deposition (DLD) technology, derived from the laser cladding technique (i.e. laser cladding), for the repair/rebuild process of large industrial components, such as the teeth of gears used in machine organs of wind generator gearboxes. The introduction of additive manufacturing technologies for repair/rebuild procedures, as opposed to replacement, will result in a radical and disruptive innovation in the area of industrial maintenance. A repair procedure with additive manufacturing will potentially be faster, thus reducing downtime due to breakdown.

The material deposition procedures must allow the deposition of small successive layers compatible with the dimensions of the pinion teeth. The additive materials (powders) must be completely compatible with the materials present in the original teeth to ensure a good metallurgical bond. The bonding properties between the additive material and the substrate must transfer loads.

The research promoted the process's optimisation and evaluation of preheating conditions by deposition of single lines of Inconel 625 and AISI 431 powders on 42CrMo4 structural steel substrate. Functionally Graded Materials (FGM) production aimed to seek the best chemical composition promoted by the powder mixture, varying the mass composition of powder gradually and initiating the deposition with pure Inconel 625. Through the characterisations of the FGM, it was possible to

determine the ideal composition of powder mixture (Inconel 625 + 50% AISI 431). The production of this innovative material can meet different demands of the wind power sector and the most diverse industrial sectors.

In order to evaluate the 3D construction by additive manufacturing, bulks were produced using powders of AISI 431 or Inconel 625, and with the composition Inconel 625 + 50% AISI 431, allowing the comparison of mechanical and microstructural properties.

However, matching the carburised layer hardness of the gear teeth with the teeth produced by additive manufacturing is a challenge to be answered in the GEAR3D project. A new innovative FGM was produced to respond to this task mixing Inconel 625 with a nickel-superalloy, type NiCrWMo. The metallurgical, chemical and mechanical characterisations, and the correlation with processing parameters, are established and discussed throughout this investigation.

Keywords: Additive Manufacturing; Direct Laser Deposition; Functionally Graded Materials; Mechanical Properties; Microstructure; Nickel Superalloys; Repair; Steel.

Resumo

As ambiciosas metas mundiais da energia renovável estão pressionando a energia eólica a se tornar uma fonte de energia convencional. As turbinas eólicas estão sujeitas a ambientes severos/hostis que podem encurtar consideravelmente o ciclo de vida de um componente. Frequentemente, engrenagens são substituídas com apenas um ou dois dentes do pinhão com rotura total ou parcial, ou ainda pior, com apenas desgaste excessivo em um ou dois dentes. Nestes casos, a reparação evitaria a substituição completa do pinhão, reduzindo substancialmente os custos e tempo de paragem.

Motivada por esta necessidade emergente, este projeto de doutoramento visou a exploração de uma tecnologia aditiva de deposição direta por laser (DLD), derivada da técnica de revestimento por laser (i.e., laser cladding), para o processo de reparação/ reconstrução de componentes industriais de grandes dimensões, como os dentes de engrenagens utilizadas em órgãos de máquina de redutores de geradores eólicos. A introdução de tecnologias de manufatura aditiva para os procedimentos de reparação/reconstrução em detrimento da substituição resultará numa inovação radical e disruptiva na área da manutenção industrial. Um procedimento de reparação com manufatura aditiva, potencialmente será mais rápido, reduzindo assim o tempo inoperacional devido a avaria.

Os procedimentos de deposição de material devem permitir a deposição de camadas sucessivas de pequena dimensão, de forma a serem compatíveis com as dos dentes dos pinhões, e os materiais de adição (pós) devem ser compatíveis com os materiais presentes nos dentados originais, de forma a garantir uma boa ligação metalúrgica. As propriedades de ligação entre o material aditivo e o substrato devem ser tais que permitam a transmissão de carregamentos.

A investigação realizada promoveu a otimização do processo e a avaliação das condições de pré-aquecimento através da deposição de monocamadas de pós de

Inconel 625 e AISI 431 em substrato de aço estrutural 42CrMo4. A produção de Materiais em Gradiente Funcional (FGM), teve como objetivo selecionar a melhor composição química promovida pela mistura do pós, variando gradualmente a composição mássica de pó e iniciando a deposição com 100% Inconel 625. Através da caracterização do FGM, foi possível determinar a composição ideal de mistura de pó (Inconel 625 + 50% AISI 431), sendo produzido um material inovador que pode atender diferentes demandas do setor eólico, como também dos mais diversos setores industriais.

Com o objetivo de avaliar a construção 3D por fabricação aditiva, foram produzidos maciços com os pós de AISI 431, Inconel 625 e Inconel 625 + 50% AISI 431, permitindo a comparação das propriedades mecânicas e microestruturais.

Entretanto, tentar igualar a dureza da capa cementada do dentado, com o dentado produzido por fabricação aditiva é um desafio a ser respondido no projeto GEAR3D. Para isto, um inovador FGM foi produzido através da mistura de Inconel 625 com uma superliga de níquel do tipo NiCrWMo. As caracterizações metalúrgicas, químicas e mecânicas e a correlação com os parâmetros do processo foram determinadas e discutidas nesta investigação.

Palavras-chave: Aço; Fabricação Aditiva; Deposição Direta por Laser; Materiais Funcionalmente Graduados; Reparação; Microestrutura; Propriedades Mecânicas; Superligas de Níquel.

Summary

Acronyms and Symbols

φ	Laser spot size
γ	Surface tension gradient
ϱ_c	Molten powder density [kg/m^3]
ϱ_s	Substrate material density [kg/m^3]
θ	wetting angle
AM	Additive manufacturing
AC	Clad Area
b	Crater diameter
CL	Cladding layer
CTE	Coefficient of thermal expansion
D	Dendrites
d	depth
D4006	Diamalloy 4006 - NiCrWMo
DED	Directed Energy Deposition
DLD	Direct Laser Deposition
DM	Digital microscope
EBSD	Electron Backscatter Diffraction
EDX	Energy-dispersive X-ray spectroscopy
EG	Equiaxed grains
$E_{specific}$	Specific energy
e_t	Total elongation
e_u	Uniform elongation
FEM	Finite Element Method
FGAM	Functionally Graded Additive Manufacturing
FL	Fusion line

FR	Feed Rate
G	Thermal gradient at the solid-liquid interface
G_p	Powder density
h	height
HAZ	Heat-affected zone
HRC	Rockwell C Hardness
HV	Vickers Hardness
HVOF	High-Velocity Oxygen Fuel
K	Abrasive Wear Rate
LBAM	Laser-based additive manufacturing
M42C	Martensitic stainless steel – AISI 431
M625	Inconel 625
MA	Melting Area
MSWR	Mean Specific Wear Rates
OM	Optical microscope
P or LP	Laser Power
PDD	Powder Deposition Density
PHT	Preheating
R	Ball radius
R	Cooling rate
R_m	Ultimate tensile strength
RMSE	Root Mean Squared Error
$R_{p0.2}$	Yield stress
RSM	Response Surface Model
S	Sliding distance
SEM	Scanning Electron Microscopy
SS	Scanning Speed

TCP	Topologically close-packed
V	Worn volume
w	width
X_c	Percentage by weight of element X in the powder [%]
X_s	Percentage by weight of element X in the substrate [%]

Chapter 1

BACKGROUND

Background

Direct Laser Deposition (DLD) is an additive manufacturing (AM) technology capable of creating net-shaped parts from powders or wires, depositing them in the desired geometry, ensuring excellent bonding and metallurgical properties [1]–[4]. Due to its geometric freedom, scalability and adaptability to different scenarios, which other metals AM technologies cannot offer, this technique is often used to repair industrial components and confer improved mechanical properties throughout. However, the most significant advantage of this technology is the expandability of the material feeders, allowing the processing of various materials in the same operation. Therefore, this technology can be assumed as a method of deposition of multimaterial and gradient materials, since it can deposit different materials in sequential layers or combine them in the same layer.

Previous studies on FGM type processes focus on all additive manufacturing technologies that can produce them [5]. In this PhD research, an in-depth analysis was performed on the production of gradient materials and process optimisation to obtain the best mechanical and microstructural properties for the realisation of the remanufacturing of industrial components, mainly large gears. This work aims to describe the approaches adopted by other authors, categorising the advances made in the process and comparing them with others.

Direct Laser Deposition

Direct laser deposition (DLD) is a kind of advanced rapid manufacturing technology, which can produce near net shape parts by depositing metal powders layer by layer [6]. DLD technology is an emerging laser aided manufacturing technology based on a new additive manufacturing principle, which combines laser cladding with rapid prototyping into a solid freeform fabrication process that can be used to manufacture near net shape components from their CAD files [7]. Recent studies have indicated that DLD can repair deep or internal cracks and defects in metallic industrial components. Metal deposition by DLD is also referenced with an additive manufacturing process because, compared to other processes, the formation rates and processing time are high. The mixture of powders creating their alloys increases resistance (fatigue, corrosion, wear, mechanical) following the component's specificity and current standards.

DLD is an additive manufacturing process featuring in the industrial context, which uses metal alloys in powder and is melted by a source of energy, the laser beam. It is a technique that can be used in cladding production for repair and components reconstruction. Compared to conventional processes, it has many advantages, such as arc welding, due to better coatings with controlled heat input producing better surface quality and resistance to wear and corrosion [8]–[10].

Many components are operated under extreme conditions involving impact, abrasion, high temperature and pressure, making them prone to fracture. The main failure modes, such as wear, local corrosion, crack formation and fracture, are directly related to loading during service. Equipment failures cause significant economic losses to businesses. Repair of industrial components is an effective way to favourably reduce a large part of primary resource use and energy consumption, and emissions of pollutants into the environment. If a successful repair cannot be achieved, the damaged components will have to be disposed of, and a significant loss will be caused.

The conventional repair methods currently include mechanical machining, arc welding, and thermal spraying processes such as High-Velocity Oxygen Fuel (HVOF). Although these methods have different advantages, there are still many disadvantages in this repair, such as being time-consuming and laborious, having a limited thickness of deposition layers, low metallurgical bonding, formation of a large number of porosities and cracks, and distortion of substrates (caused by excessive components heating). Therefore, it is of great industrial interest to develop high efficiency and precision repair technologies aiming at increasing the lifetime of the components.

DLD deposition is one of the appropriate techniques for developing these processes when producing high-quality repairs. With proper addition material, structures with mechanical properties similar or superior to those of the substrate can be obtained. These structures present an excellent metallurgical bond, the formation of a small heat-affected zone (HAZ) by the control of heat transfer and minimum dilution. The localised repair of components in necessary positions with high precision, associated with low distortion that minimises machining time after the repair, are major attractions for different industrial sectors for the use of laser processing [11]–[14]. Moreover, innovative material systems can be produced by gradually changing the chemistry of the individual layers, thus adjusting the composition of the materials to the desired properties of the component [15]. DLD is advantageous with high precision, allowing high economic gain, and due to its unique characteristics, the laser enables material processing with high efficiency and ease of automation.

Due to these factors, DLD is one of the most attractive and competitive component repair processes. This technique consists of an effective way to minimise monetary losses and environmental impacts resulting from the transformation of resources (raw materials, water and energy) by repairing or rebuilding components that have suffered breakdowns, putting them back into service.

The growing demands for quality and reliability/reproducibility of results have contributed to the increasing use of automated special welding processes. DDL has occupied a space in the most diverse industrial sectors. Numerous industrial applications demonstrate the technological and economic feasibility of repairing components by laser in sectors as diverse as aeronautics, petrochemicals (offshore), energy, rail, maritime transport, steelmaking, among others. Examples of products that DLD can repair are gearboxes, gears, blowers, combustion engine parts, couplings, extruders, pumps, shafts, turbine parts, rollers, winches, among other components [16].

The process can produce high energy densities, forming a melt pool that will allow the powder deposition. High cooling rates are characteristic of this process, where the laser beam promotes a localised thermal delivery, and the dimensions of the structures are an industrial problem. Preheating (PHT) of the substrate is one of the processes that allow the reduction of the cooling rate. PHT decreases the hardness in HAZ [17], reduces accentuated thermal gradients and increases the laser absorption rate in a substrate, improving the stress distribution and avoiding the formation of hard structures that are harmful to the cladding mechanical properties [18].

The efficiency of the process depends mainly on the formation of the melt pool, which allows the capture of the injected powder particles. In particular, the material efficiency is strongly dependent on the melt size relative to the size of the impact area of the powder flow [19], [20]. Many operational parameters and physical phenomena determine the cladding quality produced by laser processing, such as geometry, microstructure, dilution, defects, residual stresses, distortion, surface roughness, and metallurgical changes in the substrate the efficiency of the process. The functional properties and quality of the claddings produced with laser are strongly dependent on the final microstructure. The first prerequisite for a successful laser cladding process is the homogenisation of the melt, which is guaranteed by convection.

The relationships between processing conditions and material responses are not well established or understood. There is a need for further research in this area to optimise the process allowing for generalisation.

Process Parameters

Many operational parameters and physical phenomena determine the quality of the cladding produced by DLD, such as the geometry, microstructure, dilution, defects, residual stresses, distortion, surface roughness, metallurgical changes in the substrate and the efficiency of the process.

The DLD process is determined by beam characteristics, materials and operating parameters. Beam and feed rate parameters are generally fixed and dictated by equipment, laser, and optics. Materials parameters relate to the choice of additive material and substrate and include the properties of the powder particles (particle size and morphology, chemical composition, thermophysical and optical properties) and the properties of the substrate (geometry and mass, chemical composition, surface condition, thermophysical and optical properties) [19][21].

Operating parameters can be changed, and their variation affects the process results. Among these, laser power (P), scanning speed (V) and feed rate (F) are considered the main parameters as they have the greatest effect on the cladding characteristics. The cladding height increases proportionally with increasing feed rate. In DLD, the correlations between height and feed rate (F) and height and powder feed rate per unit length (F/V) are generally linear. In addition to height, the coating cross-sectional area (A) increases with increasing F and F/V. Above a feed rate threshold value, the increment of A can accelerate due to the multiple scattering of the laser beam caused by the dense powder cloud [21][22].

While other parameters are held constant, an increase in laser power increases the bead height. The cladding width is mainly dictated by the focal point of the laser beam. However, a width greater than the spot size can be obtained at very low processing speeds and high laser powers. In general, the cladding width increases with decreasing scanning speed and increasing laser power. These correlations are linear in the laser cladding process using a coaxial nozzle [23]–[25].

Characteristics of a Cladding Produced by Direct Laser Deposition

According to the information previously mentioned, the properties of claddings produced by DLD can be determined by a wide variety of factors. In this point, the main characteristics of cladding will be discussed.

Dilution

The laser cladding process requires achieving a strong metallurgical bond between the cladding material and the substrate, which in turn requires the formation of a melt pool on the substrate. However, the depth of this melt (additive material + substrate) should be as small as possible to obtain a pure surface layer that is not fully diluted by the base material [26].

Dilution is considered an important factor in controlling the contamination of the cladding by the substrate material and can be used to characterise the deposition quality. Indeed, although a minimum level of mixing is required to ensure a good metallurgical bond to the substrate, as noted above, excessive dilution can negatively influence cladding properties [27], [28]. Dilution can be measured in two ways. The first method is based on the cladding geometry layer (Figure 1).

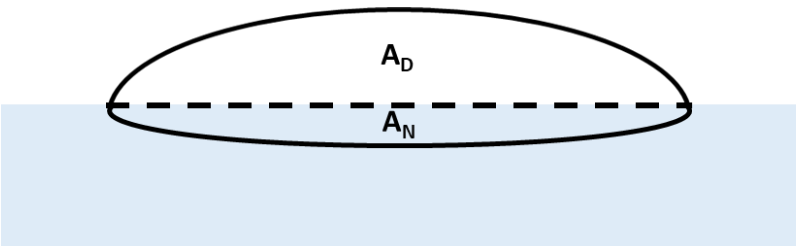

Figure 1. Schematic representation of the cross-sectional area emerging from the original surface of the plate (AN) and submerged part of the cross-sectional area (AD). Adapted from [29].

This geometric approach assumes a homogeneous distribution of elements in the cross-section. The dilution is given by Equation 1, being the ratio of the depth of the coating on the substrate (A1) to the total height (A1 + A2) [29]. It is important to highlight that dilution increases with increasing laser power but decreases with increasing scanning speed.

$$\boldsymbol{D}\ (\%) = \frac{\boldsymbol{A_N}}{(\boldsymbol{A_D} + \boldsymbol{A_N})} \boldsymbol{x100} \qquad \text{Equation 1}$$

In alternative to Equation 1, dilution can be calculated by the percentage of the total volume of the surface layer that results from substrate fusion, as indicated by Equation 2 [30].

$$\boldsymbol{D} = \frac{\boldsymbol{\rho_c}(\boldsymbol{X_{c+s}} - \boldsymbol{X_c})}{\boldsymbol{\rho_s}(\boldsymbol{X_s} - \boldsymbol{X_{c+s}}) + \boldsymbol{\rho_c}(\boldsymbol{X_{c+s}} - \boldsymbol{X_c})} \qquad \text{Equation 2}$$

Where ρ_c is the density of the molten powder [kg/m^3], ρ_s is the density of the substrate material [kg/m^3], X_{c+s} is the percentage by weight of element X in the total surface area of the coating region [%], X_c is the percentage by weight of element X in the powder [%], and X_s is the percentage by weight of element X in the substrate [%].

Microstructure features

The functional properties and quality of the claddings produced with laser cladding technology are strongly dependent on the final microstructure. The first prerequisite for a successful laser cladding process is the homogenisation of the melt, which is ensured by convection.

The melting pool material flow in processes such as laser cladding directly affects the bead penetration and width, the solidification structure and the probability of porosity and lack of melting. Surface tension and buoyancy force are two of the most important driving forces for flow in the melting pool. The surface tension force produces thermocapillary flow due to temperature changes [31], [32]. The material flow driven by surface tension is also known as Marangoni convection or the Marangoni effect, where large thermal gradients within the melt generate intense convection. The buoyancy force is also considered a gravitational force and manifests itself due to differences in density originating temperature gradients within the melting pool [33]–[35]. The Marangoni effect is illustrated in Figure 2.

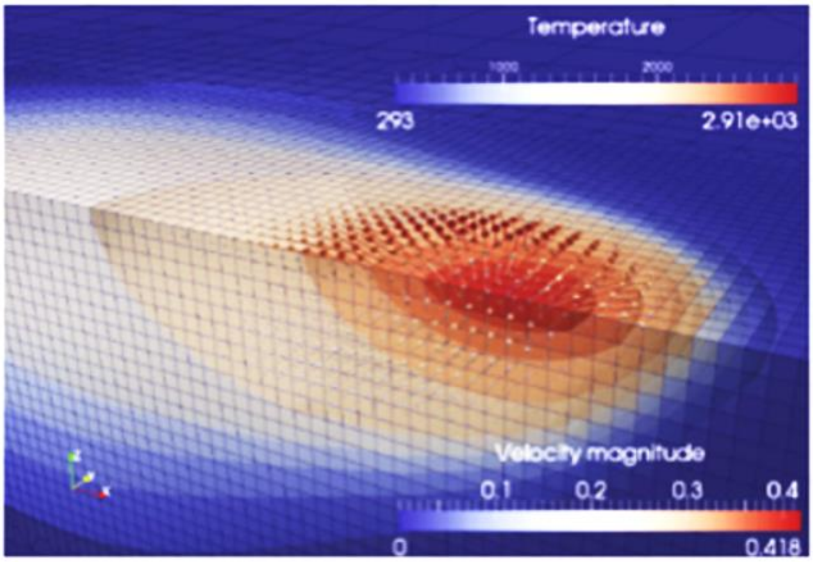

Figure 2. Marangoni flow in weld pool during single weld bead pass [36].

Surface tension gradients are present on the surface of the melting pool due to temperature differences. In these situations, a material flow is induced where the material moves from locations with lower surface tension to locations with higher surface tension [37]. Surface tension gradients are generally dependent on the presence of temperature gradients, as noted above, and the surface tension gradient can be negative (i.e. decrease with increasing temperature); in this case, there is a radial flow out of the molten metal, promoting the formation of a wider and shallower melting pool [33]. Conversely, the gradient leads to radial inward flow for a positive tension surface, producing a deeper and narrower melt pool [38]. Marangoni convection creates a whirlpool at the laser beam periphery, but as the velocity increases, the maximum velocity of the liquid moves from the sides of the melting pool to the back of the pool [39], [40].

The solidification microstructure for a given alloy depends on the local solidification conditions determined by the cooling rate (R) and the thermal gradient at the solid-liquid interface (G). Specifically, the growth morphology of rapidly solidified layers is controlled by the parameter G/R. If G/R is higher than a critical value (G/R)* a planar solidification front occurs. Otherwise, if G/R is lower than this critical value, the planar solid-liquid interface is destabilised, and cellular or dendritic solidification occurs [41]–[44]. The G/R effect on the microstructure can be schematically represented in Figure 3.

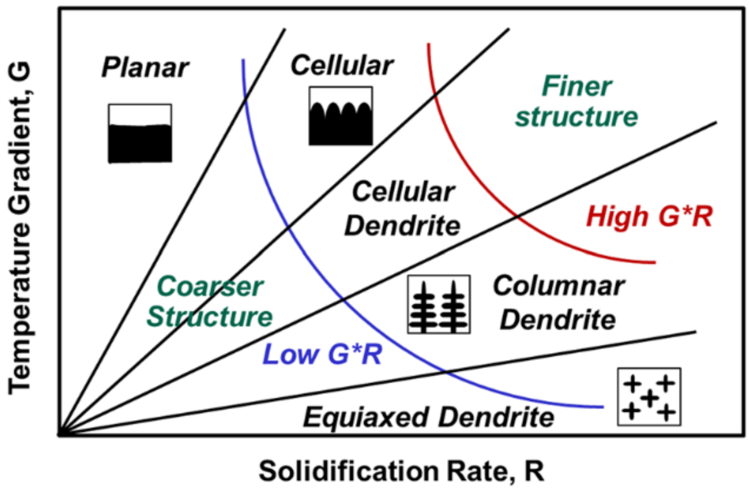

Figure 3. Influence of temperature gradient and solidification rate on the solidification process [45].

These solidification conditions (G and R) are a function of the size and geometry of the melting zone, which in turn is influenced by the laser processing conditions, such as laser power, scanning speed, feed rate, beam diameter or substrate temperature. In contrast to R, the thermal gradient G is at a maximum at the bottom of the melt pool and progressively decreases towards the surface [46].

In cases where solidification occurs without nucleation, solidification is epitaxial, starts by growth from the substrate and proceeds unidirectionally towards the top. At the beginning of solidification, at the bottom of the melt pool, a flat solidification zone appears as the liquid metal maintains contact with the solid substrate (the solidification rate is 0, and the value of G/R is infinite) [47], [48]. As the solid-liquid interface propagates, R increases rapidly, and G decreases, leading to a lower value of G/R: the planar front evolves to a cellular interface and eventually to a dendritic when G/R decreases further. Due to the rapid variation of G/R, the planar interface is very narrow [45].

G/R decreases with the evolution of the solidification process until it reaches a value that remains practically constant during the final solidification phase: in this region, which follows the cellular interface zone, dendritic solidification appears [47]. The cellular and dendritic solidifications are generally columnar and grow perpendicular to the substrate-cladding interface (or perpendicular to isothermal lines) since the substrate mainly dissipates the heat and, in this direction, the thermal gradient is greater. Near the surface of the cladding layer, the heat is mainly dissipated through the surrounding atmosphere, which significantly decreases the G value, and the dendrites become very thin and disoriented [48], [49]. G/R determines the solidification morphology, and GxR impacts the scale of solidification microstructure.

The cladding production requires an understanding of thermal and thermophysical properties: coefficient of thermal expansion (CTE), melting temperature and thermal conductivity. The inequality in heat flow is due to the faster dissipation at the material interface that presents higher thermal conductivity, resulting in distortion and the possibility of lack of fusion formed in material with lower thermal conductivity, promoted by insufficient heat [50]. Multiple layers reduce the CTE difference and the mesh misalignment between the consecutive layers. As the number of layers increases, an analytical solution for thermal stresses makes the system more complex and promotes residual stresses formation [51].

In order to relieve the residual stresses, preheating treatment is a solution, reducing the cooling rate of both the substrate and the cladding and thus preventing the formation of fragile phases in the bonding area and gradient minimizing the likelihood of crack formation. In steels, increasing preheating temperature (PHT) decreases the cooling rate, thus promoting the decomposition of granular bainite and increasing the percentage of ferrite [52]. Preheated substrates present a lower susceptibility cracks formation, decreasing the cooling rate and formation of residual stresses [53]–[55]. Preheating promotes control of the thermal gradients between the substrate and the deposited layers as in the case of FGM's, decreasing cooling rate and residual stresses, promoting better mechanical properties [56].

Repair of Industrial Components by Direct Laser Deposition

In addition to part repair, laser deposition by a powder injection technique has been widely used in other industrial applications such as rapid manufacturing, surface coating and innovative alloy development. The ability to mix two or more powders and control each powder feed rate makes laser cladding a flexible process for manufacturing heterogeneous and gradient components at the microstructure level.

Materials can be tailored for flexible, functional performance in particular applications. The inherently rapid heating and cooling rates associated with this process allow the production of materials with extended solid solubility and out-of-equilibrium (metastable) phases, offering the possibility of creating new materials with advanced properties [22].

However, to achieve a successful laser cladding process, a precise and controllable method of applying filler material at the edge of the melt zone created by the laser beam is required. Additionally, using an uncontrolled method or inadequate filler materials results in poor deposition of this often costly material. DLD process for detail repair on components, such as turbine blades and gears, requires high control in powder deposition, leading to innovation in the development of highly controlled methods [57].

The component repair by DLD follows a series of steps to obtain a structure similar to the original. Figure 4 describes the sequences of activities involved in the repair process.

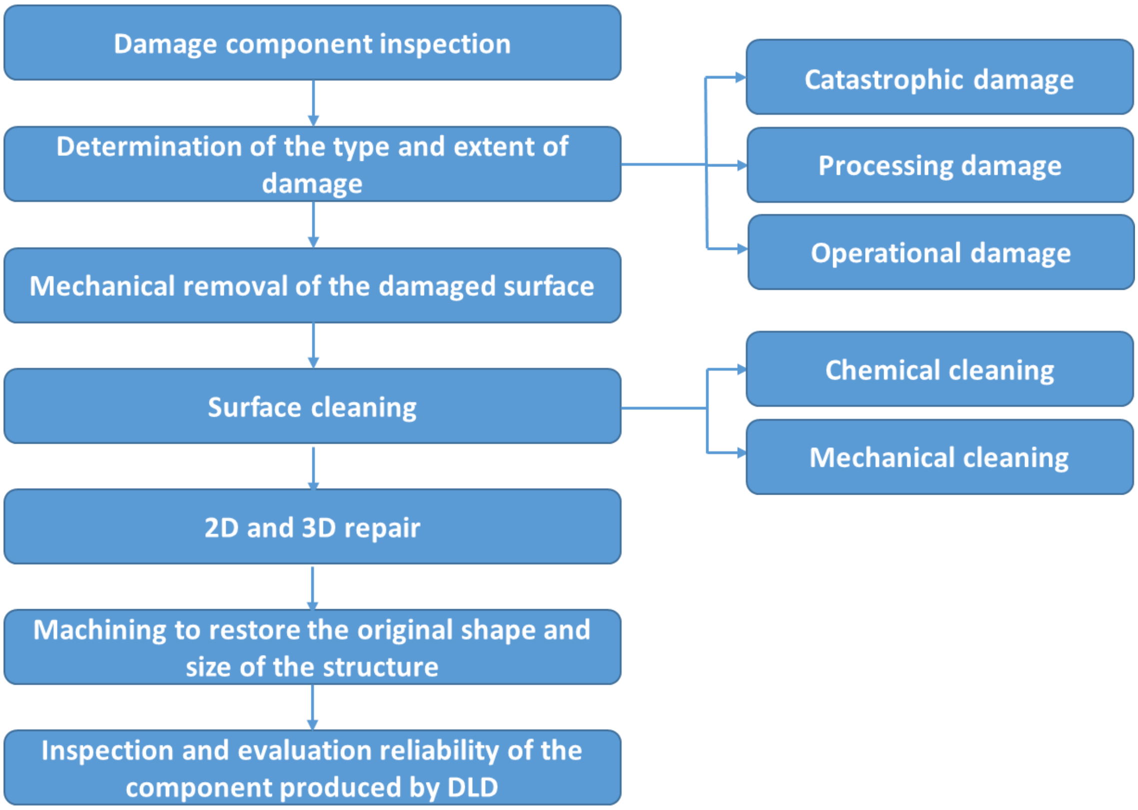

Figure 4. The industrial component repair process sequence via Direct Laser Deposition (DLD).

The major challenges of the component repair operation are:

(i) removing the damaged layer due to the high surface hardness of these transmission elements;

ii) ensure the metallurgical bond between the additive material and the substrate;

(iii) produce a new surface coating with high surface hardness and ensure a high contact fatigue resistance of the repaired element; and

(iv) machining the repaired regions without compromising the area that was not laser-processed.

Currently, the DLD process is one of the main means of remanufacturing components. It is an effective way to minimise monetary losses and environmental impacts resulting from transforming inputs (raw materials, water and energy) by repairing or rebuilding components that have suffered breakdowns and putting them back into service [8]. The adoption of new technologies, such as laser, allows remanufactured components to equal or exceed the performance of new traditionally manufactured products [58].

Several authors have developed studies to physically model the DLD process [59]–[62]. However, it is very complex to provide a comprehensive description of the process due to the interactions in the laser/ powder/ substrate system and the various physical, chemical and metallurgical phenomena involved in the process [63]–[65]. The remanufacturing of components is also considered a technique of additive manufacturing to generate complete parts of components and the combination of different manufacturing processes [16], [66]–[68]. The creation of own and specific alloys is one of the innovations sought throughout this study.

Proposed Solution Concept

The maintenance of wind turbine gearboxes follows a standardised procedure consisting of 6 main steps:

i. On-site inspection and disassembly (lead time ≈ two days): Determination of gearbox condition, bearing settings, gear backlash and size and crack check. The exact condition of the gearbox is identified, with backlash, contact patterns and bearing settings all being carefully recorded before the gearbox is disassembled. This stage may include tasks such as visual inspection, vibration measurement and analysis; alignments; replacement of bearings in the wind turbine generator; replacement of bearings in the gearboxes' high-speed shaft; oil replacement, among others.

ii. Transport to the workshop (lead time ≈ two days): The damaged parts of the gearbox are transported to the company's premises.

iii. Gearbox disassembly, inspection report and failure analysis (lead time ≈ three days): The gearbox is disassembled, and an inspection report and damage analysis will be carried out.

iv. Rapid gearbox reconditioning and accessory parts manufacturing (lead time ≈ three weeks): The gearbox will be overhauled, and spare parts can be manufactured or purchased. This step involves several technologies and tools: machining centres, milling machines, internal grinding machines, gear grinding machines, reverse engineering systems, butchers and surface treatment (surface tempering, thermal spraying, HVOF, laser cladding).

v. Gearbox assembly and advanced test on test bench (lead time ≈ four days): The gearbox with new parts will be assembled. Bearing and gear backlash are adjusted, and contact patterns are recorded and checked against specifications. Once correctly assembled, the gearbox will be bench tested.

vi. Transportation and on-site assembly of the gearbox and accessory parts (lead time ≈ six days).

The actual service life of wind turbine gearboxes is generally shorter than the projected 20 years, and the warranty for these components is only seven years (on average). Failures can be found in several bearing locations, i.e. in the planetary ones, those of the intermediate shafts and those of the high-speed shafts.

The most common gearboxes in wind turbines consist of three stages: one planetary stage and two cylindrical shafts or two planetary stages and one cylindrical shaft. The high-speed output shaft and its bearings are the most susceptible to failure in both architectures. These failures often start in one of the bearings, are followed by misalignment between the shafts and off-centre loading (overloading) at the contact between teeth, resulting in gear contact fatigue or gear tooth failure (total or partial). These failures result in costly maintenance interventions due to high repair costs and equipment downtime. Given the position of the gearbox on the wind generator, its dismantling and transport to the repair shop represent a considerable effort and cost as well.

Wind turbines are subject to widely varying temperatures, speeds and loads. Combined with contamination, moisture, and the chemical effects of lubricants highly doped with anti-wear agents lead to harsh/hostile environments that can sometimes considerably shorten a component's life cycle. Much premature damage in wind gearbox bearings results from failure modes caused by classical rotating contact fatigue (RCF) mechanisms. Generally, the first cracks occurred in the first and three-year operating time or 5 to 10% of the calculated nominal service life.

The repair of wind generator gearboxes typically consists of replacing all bearings (invariant of their damage condition) with new ones, re-fabricating the bearing housings to meet the imposed geometric tolerance requirements, replacing damaged gears with new ones and possibly re-finishing gear teeth to correct minor defects and remove wear marks. Replacement of damaged gears is costly due to their high dimensions (modules ranging from 6 mm to 20 mm and pitch diameters greater than 500 mm), high-cost alloyed steel alloys and complex and time-consuming manufacturing processes. In many cases, gears are replaced with only one or two pinion teeth with total or partial breakage, or even worse, with only excessive wear on one or two teeth. In these cases, the repair would avoid complete pinion replacement, substantially reducing costs and downtime.

The operation and maintenance (O&M) cost for a wind turbine can easily represent 20-25% of the total cost per kWh produced over the turbine's lifetime. If the turbine is relatively new, the share may only be 10-15%, but this can increase to at least 20-35% towards the end of the turbine's life. Thus, manufacturers and maintenance service providers are willing to adopt any costly technology that reduces maintenance costs and downtime.

Motivated by this emerging need, the present PhD project explores an additive direct laser deposition (DLD) technology derived from the laser cladding technique for the 3D reconstruction of gear teeth used in machine organs of wind generator gearboxes.

The introduction of additive manufacturing technologies for the repair/rebuild procedures concerned and repair/rebuild instead of replacement will result in a radical and disruptive innovation in the field of industrial maintenance, more specifically in the repair of wind power generators. In the case of an unscheduled repair due to failure of the gearbox's mechanical parts, the generator downtime can be quite significant due to the need to manufacture the crowns and the replacement of the shaft bearings and repair the remaining mechanical elements. Since, unlike the bearings, the worm gears are not off-the-shelf components, and given their size, geometric and tolerance complexity, manufacturing them from scratch can be time-consuming. A repair procedure with additive manufacturing will potentially be faster, thus reducing downtime due to failure. However, the repair of individual gear teeth is a complex operation, and several aspects must be considered:

i. The methodology to be adopted to remove the damaged cemented layer due to its high surface hardness;

ii. The material deposition procedures must allow the deposition of small successive layers to be compatible with the gear teeth dimensions (modules between 6 mm and 20 mm).

The powders must be completely compatible with the materials present in the original teeth to ensure a good metallurgical bond. The adhesion properties between the materials must be such that load transmission is possible. Transition zones between original and repaired materials and between added materials and surface coatings are the potential weak points of repaired teeth from a mechanical point of view. The surface hardness has to be similar to that existing in the original teeth (≥60 HRC), which are normally hardened via carburising (or other similar treatments). This requirement may require the deposition of different surface materials for the repaired tooth. The machinability of the added material and its hardened coating must be guaranteed, as machining and finishing are required to ensure geometric tolerances.

The load-carrying capacity of the additive material and its hardened coating must withstand the contact pressures between tooth flanks and the stresses at the tooth sockets to ensure a long fatigue life. The wear of the additive material and its hardened coating shall be similar to the original material. They should minimise tangential loads and the coefficient of friction between tooth flanks.

The mechanical requirements and complex loads to which large gears are subjected were considered in this study, in which innovative and potentially disruptive procedures were developed. The ability of the repaired machine organs to meet the imposed requirements was also sought. However, considering the reliability requirements of this equipment and the general conservatism of the wind power industry (without the approval of this procedure), there is a need to, in addition to developing the repair/rebuild methodologies, create a high level of confidence in the solutions developed.

Thesis Outline

The thesis is composed of papers produced throughout the development of this PhD thesis in an industrial environment. Chapter 2 comprises two review articles, one published as a book chapter and the other as a mini-review. This chapter focuses on Functionally graded materials (FGMs) and the main characteristics promoted by the interaction of the laser beam on the substrate. Besides the fundamental characteristics for the production of FGMs, such as the essential process parameters, the solidification process, the microstructures formed during the laser processing of materials, and the main associated defects are described. It is highlighted throughout the text the influence of the essential parameters (laser power, scanning speed and feed rate), as well as the effect of substrate preheating that has been intensively investigated.

Chapter 3 presents three studies concerning the processing conditions for AISI 431 martensitic stainless steel (M42C) and Inconel 625 nickel superalloy powders on 42CrMo4 steel substrate. The production of single lines was carried out with the variation of parameters, allowing the optimisation of the process. In this chapter, the PHT influence in the different conditions used during the processing of the single lines and the effect on the microstructural, mechanical properties of the produced claddings are investigated. Samples were produced with and without preheating to evaluate this effect. Chapter 3 also presents the simulation of a thermal deposition evolution of M625 powder to DED process using the commercial FEM software ABAQUS. The transient heat transfer model associated with the phase-field concept is implemented through user coding in FORTRAN language, taking into account the latent heat of fusion and vaporisation.

The production of the FGM, produced with the mixture of M42C and M625 powders, is described in Chapter 4. In this chapter, the microstructural and mechanical analyses performed to define the best powder mixture composition are described.

In Chapter 5, the properties and microstructures of bulks produced with the composition of 100% M42C, 100% M625 and one with the mixture of 50% M625 + 50% M42C were described, allowing a competitive analysis. The composition of the mixture was selected based on the studies presented on the previous chapter.

Chapter 6 introduces future and ongoing work focused on producing a new FGM by mixing Inconel 625 (M625) and NiCrWMo (D4006) powders, leading to an FGM with an enhanced mechanical response.

General Conclusions are presented in Chapter 7.

Scientific disseminations are shown in the appendices.

References

[1] A. Saboori, G. Piscopo, M. Lai, A. Salmi, and S. Biamino, "An investigation on the effect of deposition pattern on the microstructure, mechanical properties and residual stress of 316L produced by Directed Energy Deposition," *Mater. Sci. Eng. A*, vol. 780, no. March, p. 139179, 2020, doi: 10.1016/j.msea.2020.139179.

[2] W. Paatsch, "Energy turnaround – a challenge for surface technology," *Trans. Inst. Met. Finish.*, vol. 94, no. 5, pp. 228–230, 2016, doi: 10.1080/00202967.2016.1209295.

[3] Y. Gao, D. Xiong, C. Wang, and Y. Chen, "Influences of laser powers on microstructure and properties of the coatings on the AZ91HP magnesium alloy," *Acta Metall. Sin. (English Lett.*, vol. 22, no. 3, pp. 167–173, 2009, doi: https://doi.org/10.1016/S1006-7191(08)60085-X.

[4] J. Chen, S.-H. Wang, and L. Xue, "On the development of microstructures and residual stresses during laser cladding and post-heat treatments," *J. Mater. Sci.*, vol. 47, no. 2, pp. 779–792, 2012, doi: 10.1007/s10853-011-5854-4.

[5] G. H. Loh, E. Pei, D. Harrison, and M. D. Monzón, "An overview of functionally graded additive manufacturing," *Addit. Manuf.*, vol. 23, no. May, pp. 34–44, 2018, doi: 10.1016/j.addma.2018.06.023.

[6] Q. Wang *et al.*, "Functionally graded stainless steel fabricated by direct laser deposition: Anisotropy of mechanical properties and hardness," *Acta Metall. Sin. (English Lett.*, vol. 31, no. 1, pp. 19–26, 2018, doi: 10.1007/s40195-017-0668-2.

[7] G. P. Dinda, A. K. Dasgupta, and J. Mazumder, "Laser aided direct metal deposition of Inconel 625 superalloy: Microstructural evolution and thermal stability," *Mater. Sci. Eng. A*, vol. 509, no. 1–2, pp. 98–104, 2009, doi: 10.1016/j.msea.2009.01.009.

[8] M. Alimardani, V. Fallah, A. Khajepour, and E. Toyserkani, "The effect of localised dynamic surface preheating in laser cladding of Stellite 1," *Surf.*

Coatings Technol., vol. 204, no. 23, pp. 3911–3919, 2010, doi: 10.1016/j.surfcoat.2010.05.009.

[9] J. Leunda, V. García Navas, C. Soriano, and C. Sanz, "Effect of laser tempering of high alloy powder metallurgical tool steels after laser cladding," *Surf. Coatings Technol.*, vol. 259, no. PC, pp. 570–576, 2014, doi: 10.1016/j.surfcoat.2014.10.028.

[10] A. Dass and A. Moridi, "State of the Art in Directed Energy Deposition: From Additive Manufacturing to Materials Design," *Coatings*, vol. 9, no. 7, p. 418, Jun. 2019, doi: 10.3390/coatings9070418.

[11] R. Vilar, E. C. Santos, P. N. Ferreira, N. Franco, and R. C. da Silva, "Structure of NiCrAlY coatings deposited on single-crystal alloy turbine blade material by laser cladding," *Acta Mater.*, vol. 57, no. 18, pp. 5292–5302, 2009, doi: 10.1016/j.actamat.2009.06.049.

[12] F. Fu, Y. Zhang, G. Chang, and J. Dai, "Analysis on the physical mechanism of laser cladding crack and its influence factors," *Optik (Stuttg).*, vol. 127, no. 1, pp. 200–202, 2016, doi: 10.1016/j.ijleo.2015.10.043.

[13] N. Hutasoit, V. Luzin, A. Blicblau, W. Yan, M. Brandt, and R. Cottam, "Fatigue life of laser clad hardfacing alloys on AISI 4130 steel under rotary bending fatigue test," *Int. J. Fatigue*, vol. 72, pp. 42–52, 2015, doi: 10.1016/j.ijfatigue.2014.11.001.

[14] J. Y. Chen, K. Conlon, L. Xue, and R. Rogge, "Experimental study of residual stresses in laser clad AISI P20 tool steel on pre-hardened wrought P20 substrate," *Mater. Sci. Eng. A*, vol. 527, no. 27–28, pp. 7265–7273, 2010, doi: 10.1016/j.msea.2010.07.098.

[15] E. Brandl, V. Michailov, B. Viehweger, and C. Leyens, "Deposition of Ti-6Al-4V using laser and wire, part II: Hardness and dimensions of single beads," *Surf. Coatings Technol.*, vol. 206, no. 6, pp. 1130–1141, 2011, doi: 10.1016/j.surfcoat.2011.07.094.

[16] P. Zhang and Z. Liu, "On sustainable manufacturing of Cr-Ni alloy coatings by laser cladding and high-efficiency turning process chain and consequent corrosion resistance," *J. Clean. Prod.*, vol. 161, pp. 676–687, 2017, doi: 10.1016/j.jclepro.2017.05.169.

[17] J. Jiang, G. Lian, M. Xu, C. Li, B. Chen, and B. Li, "Influence of Preheating Temperature on Mechanical Properties of Laser Cladding Layer," no. June, 2016, doi: 10.1115/msec2016-8718.

[18] J. Su, X. Qiu, F. Xing, and Y. Ruan, "Effect of preheating temperature on microstructure and properties of 42CrMo4/38mnvs6 heterogeneous laser welded joint," *Metals (Basel).*, vol. 9, no. 8, 2019, doi: 10.3390/met9080870.

[19] E. Toyserkani, A. Khajepour, and S. Corbin, "Laser Cladding," *New York*, vol. 11, no. 2, p. 221, 2017, doi: 10.2351/1.521888.

[20] H. L. Wei, J. Mazumder, and T. DebRoy, "Evolution of solidification texture during additive manufacturing," *Sci. Rep.*, vol. 5, pp. 1–7, 2015, doi: 10.1038/srep16446.

[21] W. Steen and Jyotirmoy Mazumder, *Laser Material Processing*. 2008.

[22] R. M. Mahamood, *Laser Metal Deposition of Metals and Alloys*. 2018.

[23] S. M. Yusuf and N. Gao, "Influence of energy density on metallurgy and properties in metal additive manufacturing," *Mater. Sci. Technol. (United Kingdom)*, vol. 33, no. 11, pp. 1269–1289, 2017, doi: 10.1080/02670836.2017.1289444.

[24] U. de Oliveira, V. Ocelík, and J. T. M. De Hosson, "Analysis of coaxial laser cladding processing conditions," *Surf. Coatings Technol.*, vol. 197, no. 2–3, pp. 127–136, 2005, doi: 10.1016/j.surfcoat.2004.06.029.

[25] S. M. Kelly and S. L. Kampe, "Microstructural evolution in laser-deposited multilayer Ti-6Al-4V builds: Part II. Thermal Modeling," *Metall. Mater. Trans. A Phys. Metall. Mater. Sci.*, vol. 35 A, no. 6, pp. 1869–1879, 2004, doi: 10.1007/s11661-004-0095-7.

[26] S. Kou, *Welding Metallurgy*, 2nd ed. John Wiley & Sons, 2003.

[27] T. E. Abioye, J. Folkes, and A. T. Clare, "A parametric study of Inconel 625 wire laser deposition," *J. Mater. Process. Technol.*, vol. 213, no. 12, pp. 2145–2151, 2013, doi: 10.1016/j.jmatprotec.2013.06.007.

[28] T. E. Abioye, P. K. Farayibi, and A. T. Clare, "A comparative study of Inconel 625 laser cladding by wire and powder feedstock," *Mater. Manuf. Process.*, vol. 32, no. 14, pp. 1653–1659, 2017, doi: 10.1080/10426914.2017.1317787.

[29] S. Zanzarin, S. Bengtsson, and A. Molinari, "Study of dilution in laser cladding of a carbon steel substrate with Co alloy powders," *Powder Metall.*, vol. 59, no. 1, pp. 85–94, 2016, doi: 10.1080/00325899.2015.1118842.

[30] E. Toyserkani, A. Khajepour, and S. Corbin, *Laser Cladding Laser Cladding*, no. 2. 2005.

[31] A. Joshi, A. Patnaik, B. Gangil, and S. Kumar, "Laser assisted rapid manufacturing technique for the manufacturing of functionally graded materials," *2012 Students Conf. Eng. Syst. SCES 2012*, pp. 12–14, 2012, doi: 10.1109/SCES.2012.6199074.

[32] A. Kumar and S. Roy, "Effect of three-dimensional melt pool convection on process characteristics during laser cladding," *Comput. Mater. Sci.*, vol. 46, no. 2,

pp. 495–506, 2009, doi: 10.1016/j.commatsci.2009.04.002.

[33] J. M. Drezet and S. Mokadem, "Marangoni Convection and Fragmentation in LASER Treatment," *Mater. Sci. Forum*, vol. 508, no. January 2006, pp. 257–262, 2006, doi: 10.4028/www.scientific.net/msf.508.257.

[34] J. C. Heigel, P. Michaleris, and T. A. Palmer, "In situ monitoring and characterisation of distortion during laser cladding of Inconel® 625," *J. Mater. Process. Technol.*, vol. 220, pp. 135–145, 2015, doi: 10.1016/j.jmatprotec.2014.12.029.

[35] Y. P. Lei, H. Murakawa, Y. W. Shi, and X. Y. Li, "Numerical analysis of the competitive influence of Marangoni flow and evaporation on heat surface temperature and molten pool shape in laser surface remelting," *Comput. Mater. Sci.*, vol. 21, no. 3, pp. 276–290, 2001, doi: 10.1016/S0927-0256(01)00143-4.

[36] M. M. Francois *et al.*, "Modeling of additive manufacturing processes for metals: Challenges and opportunities," *Curr. Opin. Solid State Mater. Sci.*, vol. 21, no. 4, pp. 198–206, 2017, doi: 10.1016/j.cossms.2016.12.001.

[37] C. L. Chan, J. Mazumder, and M. M. Chen, "Effect of surface tension gradient driven convection in a laser melt pool: Three-dimensional perturbation model," *J. Appl. Phys.*, vol. 64, no. 11, pp. 6166–6174, 1988, doi: 10.1063/1.342121.

[38] C. Limmaneevichitr and S. Kou, "Experiments to simulate effect of Marangoni convection on weld pool shape," *Weld. J. (Miami, Fla)*, vol. 79, no. 8, 2000.

[39] Q. Chen, G. Guillemot, C. A. Gandin, and M. Bellet, "Numerical modelling of the impact of energy distribution and Marangoni surface tension on track shape in selective laser melting of ceramic material," *Addit. Manuf.*, vol. 21, pp. 713–723, 2018, doi: 10.1016/j.addma.2018.03.003.

[40] Y. Jiang, Y. Cheng, X. Zhang, J. Yang, X. Yang, and Z. Cheng, "Simulation and experimental investigations on the effect of Marangoni convection on thermal field during laser cladding process," *Optik (Stuttg).*, vol. 203, no. December 2019, p. 164044, 2020, doi: 10.1016/j.ijleo.2019.164044.

[41] A. Frenk and W. Kurz, "High speed laser cladding: solidification conditions and microstructure of a cobalt-based alloy," *Mater. Sci. Eng. A*, vol. 173, no. 1–2, pp. 339–342, 1993, doi: 10.1016/0921-5093(93)90240-F.

[42] E. Kannatey, *Materials Processing Principles of Laser*. 2009.

[43] Z. Gan, H. Liu, S. Li, X. He, and G. Yu, "Modeling of thermal behavior and mass transport in multi-layer laser additive manufacturing of Ni-based alloy on cast iron," *Int. J. Heat Mass Transf.*, vol. 111, pp. 709–722, 2017, doi: 10.1016/j.ijheatmasstransfer.2017.04.055.

[44] T. N. Le and Y. L. Lo, "Effects of sulfur concentration and Marangoni convection

on melt-pool formation in transition mode of selective laser melting process," *Mater. Des.*, vol. 179, p. 107866, 2019, doi: 10.1016/j.matdes.2019.107866.

[45] Y. Lee, M. Nordin, S. S. Babu, and D. F. Farson, "Effect of Fluid Convection on Dendrite Arm Spacing in Laser Deposition," 2014, doi: 10.1007/s11663-014-0054-7.

[46] L. Song, G. Zeng, H. Xiao, X. Xiao, and S. Li, "Repair of 304 stainless steel by laser cladding with 316L stainless steel powders followed by laser surface alloying with WC powders," *J. Manuf. Process.*, vol. 24, pp. 116–124, 2016, doi: 10.1016/j.jmapro.2016.08.004.

[47] Y. S. Lee, M. Nordin, S. S. Babu, and D. F. Farson, "Influence of fluid convection on weld pool formation in laser cladding," *Weld. J.*, vol. 93, no. 8, 2014.

[48] Z. Zhang, P. Farahmand, and R. Kovacevic, "Laser cladding of 420 stainless steel with molybdenum on mild steel A36 by a high power direct diode laser," *JMADE*, vol. 109, pp. 686–699, 2016, doi: 10.1016/j.matdes.2016.07.114.

[49] S. Bontha, N. W. Klingbeil, P. A. Kobryn, and H. L. Fraser, "Thermal process maps for predicting solidification microstructure in laser fabrication of thin-wall structures," *J. Mater. Process. Technol.*, vol. 178, no. 1–3, pp. 135–142, 2006, doi: 10.1016/j.jmatprotec.2006.03.155.

[50] A. Reichardt *et al.*, "Advances in additive manufacturing of metal-based functionally graded materials," *Int. Mater. Rev.*, vol. 0, no. 0, pp. 1–29, 2020, doi: 10.1080/09506608.2019.1709354.

[51] A. Bhattacharyya and D. Maurice, "Residual stresses in functionally graded thermal barrier coatings," *Mech. Mater.*, vol. 129, no. November 2018, pp. 50–56, 2019, doi: 10.1016/j.mechmat.2018.11.002.

[52] C. Ding, X. Cui, J. Jiao, and P. Zhu, "Effects of substrate preheating temperatures on the microstructure, properties, and residual stress of 12CrNi2 prepared by laser cladding deposition technique," *Materials (Basel).*, vol. 11, no. 12, 2018, doi: 10.3390/ma11122401.

[53] K. Dai, X. X. Li, and L. L. Shaw, "Comparisons between thermal modeling and experiments: Effects of substrate preheating," *Rapid Prototyp. J.*, vol. 10, no. 1, pp. 24–34, 2004, doi: 10.1108/13552540410512507.

[54] B. Zheng, Y. Zhou, J. E. Smugeresky, J. M. Schoenung, and E. J. Lavernia, "Thermal behavior and microstructural evolution during laser deposition with laser-engineered net shaping: Part I. Numerical calculations," *Metall. Mater. Trans. A Phys. Metall. Mater. Sci.*, vol. 39, no. 9, pp. 2228–2236, 2008, doi: 10.1007/s11661-008-9557-7.

[55] A. Sadhu *et al.*, "A study on the influence of substrate preheating on mitigation

of cracks in direct metal laser deposition of NiCrSiBC-60%WC ceramic coating on Inconel 718," *Surf. Coatings Technol.*, vol. 389, no. January, p. 125646, 2020, doi: 10.1016/j.surfcoat.2020.125646.

[56] G. Bidron, A. Doghri, T. Malot, F. Fournier-dit-Chabert, M. Thomas, and P. Peyre, "Reduction of the hot cracking sensitivity of CM-247LC superalloy processed by laser cladding using induction preheating," *J. Mater. Process. Technol.*, vol. 277, no. January 2019, p. 116461, 2020, doi: 10.1016/j.jmatprotec.2019.116461.

[57] K. F. Walker, J. M. Lourenço, S. Sun, M. Brandt, and C. H. Wang, "Quantitative fractography and modelling of fatigue crack propagation in high strength AerMet®100 steel repaired with a laser cladding process," *Int. J. Fatigue*, vol. 94, pp. 288–301, 2017, doi: 10.1016/j.ijfatigue.2016.06.031.

[58] V. Kumar, P. S. Shirodkar, J. A. Camelio, and J. W. Sutherland, "Value flow characterisation during product lifecycle to assist in recovery decisions," *Int. J. Prod. Res.*, vol. 45, no. 18–19, pp. 4555–4572, 2007, doi: 10.1080/00207540701474633.

[59] H. Zhang, S. Liu, H. Lu, H. Zhang, and Y. Hu, *HandBook of Manufacturing Engineering and Technology*. 2015.

[60] P. Nie, O. A. Ojo, and Z. Li, "Modeling analysis of laser cladding of a nickel-based superalloy," *Surf. Coatings Technol.*, vol. 258, pp. 1048–1059, 2014, doi: 10.1016/j.surfcoat.2014.07.030.

[61] M. F. Gouge, J. C. Heigel, P. Michaleris, and T. A. Palmer, "Modeling forced convection in the thermal simulation of laser cladding processes," *Int. J. Adv. Manuf. Technol.*, vol. 79, no. 1–4, pp. 307–320, 2015, doi: 10.1007/s00170-015-6831-x.

[62] I. Tabernero, A. Lamikiz, E. Ukar, S. Martínez, and A. Celaya, "Modeling of the geometry built-up by coaxial laser material deposition process," *Int. J. Adv. Manuf. Technol.*, vol. 70, no. 5–8, pp. 843–851, 2014, doi: 10.1007/s00170-013-5284-3.

[63] S. Y. Wen, Y. C. Shin, J. Y. Murthy, and P. E. Sojka, "Modeling of coaxial powder flow for the laser direct deposition process," *Int. J. Heat Mass Transf.*, vol. 52, no. 25–26, pp. 5867–5877, 2009, doi: 10.1016/j.ijheatmasstransfer.2009.07.018.

[64] I. Tabernero, A. Lamikiz, E. Ukar, L. N. López De Lacalle, C. Angulo, and G. Urbikain, "Numerical simulation and experimental validation of powder flux distribution in coaxial laser cladding," *J. Mater. Process. Technol.*, vol. 210, no. 15, pp. 2125–2134, 2010, doi: 10.1016/j.jmatprotec.2010.07.036.

[65] C. Y. Liu and J. Lin, "Thermal processes of a powder particle in coaxial laser cladding," *Opt. Laser Technol.*, vol. 35, no. 2, pp. 81–86, 2003, doi: 10.1016/S0030-

3992(02)00145-7.

[66] E. Toyserkani, A. Khajepour, and S. Corbin, “3-D finite element modeling of laser cladding by powder injection: Effects of laser pulse shaping on the process,” *Opt. Lasers Eng.*, vol. 41, no. 6, pp. 849–867, 2004, doi: 10.1016/S0143-8166(03)00063-0.

[67] K. Salonitis, L. D’Alvise, B. Schoinochoritis, and D. Chantzis, “Additive manufacturing and post-processing simulation: laser cladding followed by high speed machining,” *Int. J. Adv. Manuf. Technol.*, vol. 85, no. 9–12, pp. 2401–2411, 2016, doi: 10.1007/s00170-015-7989-y.

[68] V. Infante, L. Reis, and M. de Freitas, “Failure analysis of landing gears trunnions due to service,” *Eng. Fail. Anal.*, vol. 41, pp. 118–123, 2014, doi: 10.1016/j.engfailanal.2014.02.011.

Chapter 2

INTRODUCTION

Book Chapter - Functionally Graded Materials (FGM) Fabricated by Direct Laser Deposition: A Review

Prime Archives in Material Science: 3rd Edition

ISBN: 978-81-953047-9-0

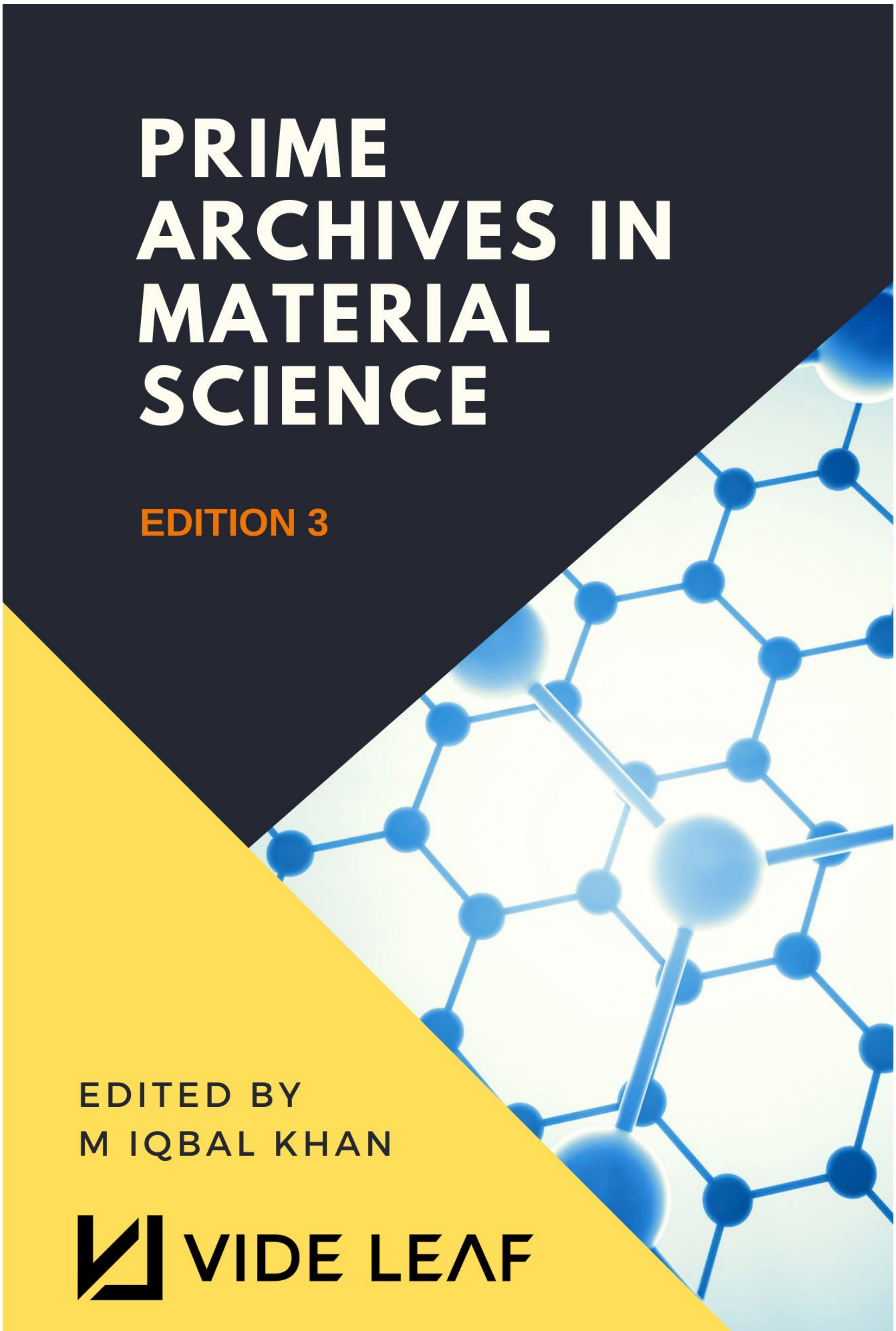

Article 1 - Functionally graded materials (FGM) fabricated by Direct Laser Deposition: A Review.

Ferreira, A. A.[1,2*]; Romio, P.C.[1]; Sousa, J. P.[2]; Omid, E.[2]; Cruz, J.[3]; Reis, A. R. [1,2]; Vieira, M.F.[1,2*]

[1]Faculty of Engineering of the University of Porto, 4200-465 Porto, Portugal

[2]LAETA/INEGI—Institute of Science and Innovation in Mechanical and Industrial Engineering, 4200-465 Porto, Portugal

[3]SERMEC-Group, 4425-348 Folgosa-Maia, Portugal

***Corresponding Authors:** André Alves Ferreira and Manuel Fernando Gonçalves Vieira, Faculty of Engineering of the University of Porto, 4200-465, Porto, Portugal.

Funding: This research was funded by FEDER through the program P2020|COMPETE, Projetos em Copromoção (project POCI-01-0247-FEDER-039848).

Acknowledgements: The authors are grateful to CEMUP (Centro de Materiais da Universidade do Porto) for expert assistance with SEM analysis.

Abstract

This review article analyses recent advances in developing functionally graded materials (FGM) produced by Direct Laser Deposition (DLD). Industrial development has supported the production of new materials that are more efficient and effective, including this new class of composite materials. Initially conceived for the aerospace and nuclear sectors, their application has been extended to several other industrial sectors, such as automotive, biomedical, energy, and military. In addition, FGM manufacturing technologies have evolved from manufacturing conceptual prototypes to creating full-scale end-use components. This article discusses the principal mechanical and metallurgical characteristics of an FGM, the manufacturing processes, with an emphasis on Direct Laser Deposition, material selection, and associated defects. The main challenges in the production of gradient materials are also addressed.

Keywords: Additive Manufacturing; Functionally Graded Materials; Direct Laser Deposition; Microstructure; Mechanical Characterisation.

Introduction

Functionally graded materials (FGMs) are characterised by presenting a gradual change in, density, composition, or microstructure from one side to another. This combination is associated with a gradient of properties, either mechanical, thermal, magnetic, chemical, or electrical. FGMs are considered advanced materials that can have excellent properties, not attainable by the materials used alone. With FGMs it is possible to tailor the microstructures/properties leading to the desired performance [1], [2]. This non-uniform set of properties across the whole part makes it attractive for a wide range of applications. Aerospace industry use FGMs for rocket components capable of withstanding high loads, presenting a high thermal dissipation capability [3]–[5]. The automotive industry resources these materials to promote surface wear resistance in engine cylinders [6], [7]. Biomedical applications are also a point of interest for FGM materials through the porosity grading of parts, allowing bone or tissue generation [8]. Overall, properties such as corrosion, wear, and oxidation resistance can be added to materials in which properties such as mechanical strength and toughness would prevail [9].

FGM was initially developed for thermal barrier applications by the Japanese space project [10]. It was intended that the material would be able to withstand a gradient of 2000K to 1000K through a 10 mm thickness section. The development of a gradient material was propelled by the constant crack failure of traditional laminate composite materials due to improper interfacial adhesion between materials. The solution for this problem was reducing sharp interfaces by decreasing the particle size and gradually adding the second material, minimizing high-stress concentration points and consequently the failure of the material [7].

FGM can be divided into distinct categories. The joining of different materials, from now on named multi-material FGM, consists in one hand on the fabrication of a part with a mixture of two or more materials, benefiting from their performance result. Also, graded parts can be created in the multi-material category by adding distinct materials in separate layers. The other category is referred to the single material graded parts. Post-processing is applied, getting its microstructural behaviour modified locally (usually at surface level) to promote distinct surface properties [11].

The development of additive manufacturing has expanded the possibilities in the production of these materials, namely allowing FGMs with density gradient [12]. FGMs processing methods are traditionally divided into two groups that depend on the cross-section of material to be produced: thin films and bulk graded materials. Thin films or coatings are produced by methods such as physical vapor deposition (PVD) and chemical vapor deposition (CVD), which are the most common to introduce a gradient of properties without significantly altering the part geometry. These methods are often used to improve mechanical properties at the surface level, distinguishing them from the interior ones. Powder metallurgy and casting fabrication methods such as centrifugal casting, slip casting, and tape casting, unlike coatings, allow the part to be created with a full gradient of properties throughout its entire thickness. Additive manufacturing, specifically Direct Laser Deposition (DLD) technology, brings the opportunity of an alternative and flexible process, enabling the production and repair of components with this type of functionality, either in bulk, through the deposition of several layers, or on the surface, depositing few layers [2][6].

DLD is an additive manufacturing (AM) technique capable of creating near net shape parts from powder or wire, melting them into the desired geometry, ensuring excellent bonding and metallurgical properties [13]–[16]. Due to its geometric freedom, scalability, and adaptability to distinct scenarios, that other metal AM technologies cannot offer, DLD is often used for the production of complex and custom parts, and coating/repairing of metal components [17]–[19]. Yet, the greatest advantage of this technology is the possibility of processing several materials in the same operation, granted with the use of several powder feeders. Therefore, this technology can be assumed to be a multi-material/graded deposition method, as it can simultaneously take advantage of using different powders enabling the deposition of distinct materials in consequent layers or the combination of different amounts of each material in each layer. The DLD equipment, an example of which is shown in Figure 1, is versatile and modular, allowing the manufacture of components with different geometries, including structures with functional gradients, as already mentioned, by a single process, without the use of additional equipment [20].

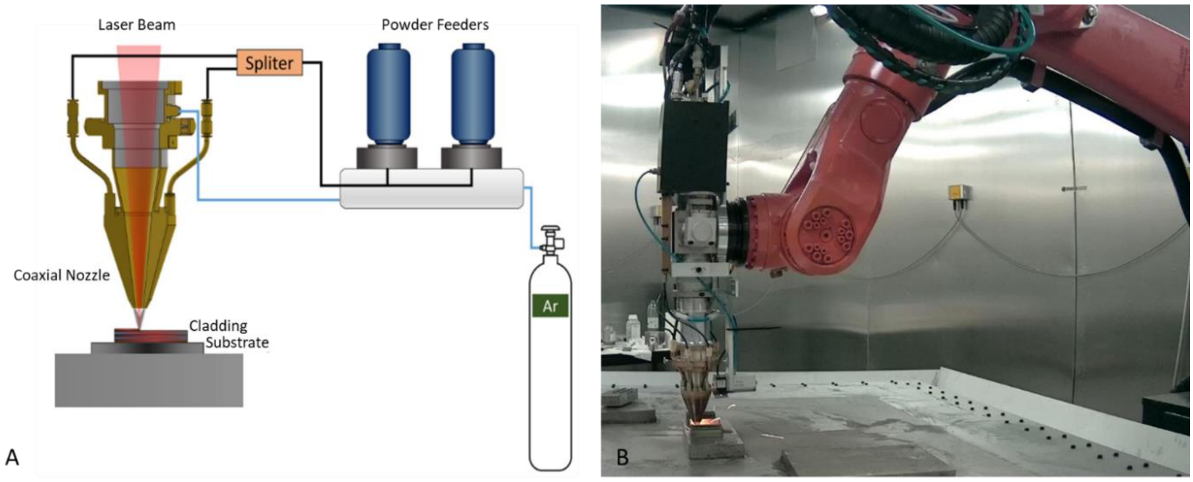

Figure 1. Direct laser deposition (DLD) equipment. (a) Schematic representation of a coaxial configuration with two powder feeders and (b) equipment during processing.

Recently, several works have reviewed the knowledge about the production of FGMs by different AM technologies [7], [12], [17], [21]. In this study, an in-depth analysis is made only on the FGMs produced by DLD, the metallurgical and mechanical properties obtained, and the phenomena involved. This review intends to describe the different approaches adopted, categorizing, and comparing the various advances achieved in the process.

This review is organized into five sections. After the introductory section, there is a section that addresses the state of the art and classification of FGM studies produced with DLD. The description of phenomena involved in the solidification process and the microstructures formed are summarized in the following section. The most common defects in FGMs are described in session four. Finally, the mechanical properties of the FGMs fabricated by DLD are given in the last section.

Production and Characteristics of FGMs

The production of FGM by AM has been the object of study by several research groups [22]–[24]. From these studies it is evident that production is generally limited to small samples. Extending the construction to larger components with functional gradient properties depends on optimizing the process parameters. These are fundamental for controlling microstructure and improving properties. High-performance and versatile FGMs can meet performance requirements and be used successfully in a variety of industries [3], [25].

The ability to mix two or more types of powders and control the feed rate of each flow makes DLD a flexible process for manufacturing complex components, for the innovative development of alloys, and to produce materials with a gradient of functionality [7], [22], [26]. DLD uses a deposition system equipped with two or more powder feeders that make it possible to create gradients that are traditionally difficult to achieve. This technology makes it possible to produce materials with a gradient at the microstructure level; this gradient is achieved due to localized melting and strong mixing movement in the melt. Thus, materials can be tailored for functional performance in particular applications.

Using DLD, it is possible to gradually change the composition of a component by controlling the powder feed rate, as shown in Figure 2. The production of these multi-materials improves the interfacial bond between dissimilar materials, minimising chemical and metallurgical incompatibility through the formation of smooth gradients, avoiding the formation of common defects such as porosities and cracks [27], [28]. In addition, FGM promotes a better homogenization of the thermal expansion coefficients of two or more different metallic alloys and even other types of material, such as ceramics, where the direct union could lead to the failure of the deposit.

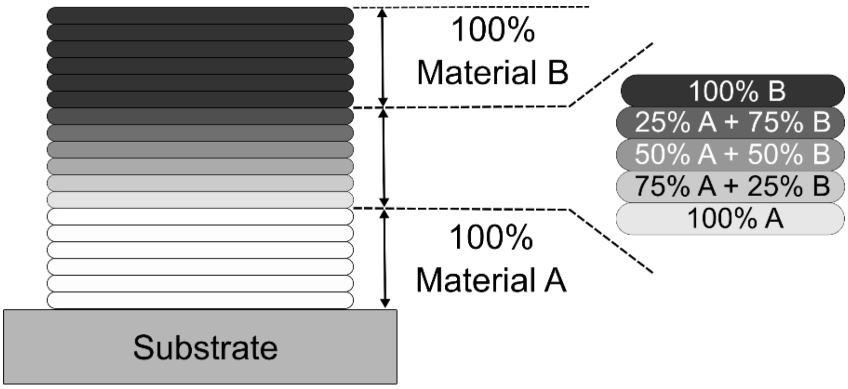

Figure 2. A layered deposition scheme with chemical composition gradient for fabricating an FGM. Adapted from [23].

One of the main factors for producing FGMs by DLD is the proper selection of the mixing of powders that must be in accordance with the metallurgical, mechanical, chemical, and tribological requirements of the components, which is an aspect that promotes innovation [29]. Powders present different densities, and the lighter and smaller particles are carried by the gas flow more easily than the heavy and larger ones, promoting an uneven distribution in particle gradient, thus reducing the performance of the component. The control of the particle size, finding the optimum mixing condition, promotes the manufacture of gradient materials with great control of the chemical composition and microstructure [30], [31].

As the composition of the material varies throughout the FGM, several phases with different chemical compositions will form. These phases help to achieve the intended performance of the FGM for the selected application. The different phases formed depend on the composition of the materials (powders and substrate) and the manufacturing conditions, such as laser power, feed rate, scanning speed, cooling rate, and treatments conducted on the material, emphasizing preheating.

Traditionally, the manufacturing process of an FGM can be divided into two stages: gradation, which consists of building a spatially non-homogeneous structure, and consolidation, which is the transformation of this structure into a bulk material [2]. In turn, the gradation processes can be classified as constitutive, homogenizing, or segregating, depending on the manufacturing process. FGMs produced by DLD have a constitutive gradation process. The graded structure is gradually built up by the precursor materials (usually the powders), and the consolidation process occurs almost simultaneously. DLD is the technology that makes it possible to manufacture a greater variety of FGMs in a single step and is the result of advances in additive manufacturing technology that made it technologically and economically viable.

Table 1 presents an overview of the materials used in the production of FGMs in different studies, as well as the main results and expected applications for these innovative materials.

From the analysis of Table 1, the importance of steels as a substrate material is highlighted. This is related to the industrial implementation of steels and the ability of FGMs to improve the behavior of gears. As for the material of the FGMs, the highlight goes to nickel superalloys, steels and, in general, materials that can provide high hardness and resistance to wear or other surface degradation processes.

The selection of austenitic stainless steel (316L or 304L) as the material of choice for the substrate is due to the fact that this material does not undergo martensitic transformation unless under very special conditions, such as cryogenic treatments. Thus, this steel withstands the melting of a superficial layer of the substrate, the rapid expansion and contraction that substrate suffers, and the high cooling rates from high temperatures usually imposed on the substrates, without significant microstructural changes. This allows it to minimize one of the main problems in using DLD, which is the appearance of high residual stresses in both the clad and the substrate.

In fact, producing FGMs requires an understanding of thermal and thermophysical properties: coefficient of thermal expansion (CTE), melting temperature, and thermal conductivity. The inequality in the heat flow is due to its faster dissipation at the material interface that presents higher thermal conductivity, resulting in distortion and the possibility of lack of fusion in the material with lower thermal conductivity, promoted by insufficient heat [32].

High residual stresses in FGMs can be due to the thermal expansion differences and to lattice misfit. In DLD, the extremely high thermal gradient enhances thermal stresses; these are related with the expansion associated with the melting pool and the contraction during rapid cooling [33]. These mismatches can arise between the first layers of the FGM and the substrate and through the FGM and be the cause of cracking or interfacial delamination between the clad and the substrate or between the FGM layers. The distribution of these stresses is highly dependent on the substrate and on the FGM materials and can be tensile on the substrate and compressive on the FGM or vice versa. However, experimental and numerical results have proven that increasing the number of layers, with a composition gradient to reduce the CTEs difference and lattice misalignment, can minimize this effect [34][35]. The thickness and composition of each layer are also critical factors in the residual stress profile [36]. Processing conditions are also determinant in the magnitude of residual stresses, this being particularly important in processes such as DLD in which thermal energy is transferred to the cold substrate quickly. For example, in the deposition of an Fe-V-Cr powder (CPM 9V) on tool steel (H13), it was observed that the normal residual stresses increase with an increase in laser power and decrease with an increase in scanning speed [37].

Preheat treatment is a solution to relieve the residual stresses in FGMs. Preheating reduces the thermal mismatch between the melt pool and the solid material (substrate or newly solidified clad), thus decreasing the cooling rate of both the substrate and the cladding and the formation of residual thermal stresses [38]–[40]. The slower cooling rate also prevents the formation of brittle phases in the FGM and in the substrate, minimizing the likelihood of cracking. In steels, increasing preheat temperature prevents the formation of brittle martensite and can promote bainite decomposition and increase the percentage of ferrite, leading to a reduction of hardness and residual stresses [41].

Table 1 - General description of FGM fabricated by DLD

Substrate	FGM Materials	Functionality (Applications)	Main Results	Ref.
Carbon steel	SS316L Inconel 718	FGM for wear-resistance applications.	Production of linear FGMs, presenting a microstructure with a transition from columnar to equiaxial. Increased resistance to wear.	[42]
Carbon steel	Inconel 690 TiC	Test pieces.	The addition of TiC changes the microstructure of the Inconel 690 matrix, presenting a refinement of grains, and promoting a significant increase in hardness and wear resistance.	[21]
Carbon steel	SS 316L CrCo alloy (Stellite 6)	Aeronautical and biomedical industries.	Development of a process modelling and a system control to manufacture FGM parts. Comparison with experimental results.	[1]
Carbon steel	Fe-16Ni-4Cr Fe-21Cr-8Ni	Fabrication of gear parts.	Three different powders were used to build a gear with a hardness gradient between the inner region (lower hardness) and the outer region (greater hardness), which is in contact with other structures. The FGM was easily produced using the DLD technique.	[43]
Carbon steel	SS 316 Fe	Test Pieces	The FGM deposited on the mild steel showed a reduction in the number of defects (pores and cracks) compared to the direct deposition of SS316.	[24]
Carbon steel (A516) Inconel 718	YSZ (ZrO2, 8 YSZ) NiCrAlY Inconel 625	Thermal barrier claddings	The residual stresses distribution through the layers of a functionally graded cermet were modelled. The model was validated using two FGMs.	[34]
Carbon steel (SAE387 Gr22)	Fe-2.25Cr Pure iron Pure chromium	Applications in superheater tubes and vessels of nuclear energy generation facilities.	FGM transition joints promoted the control of carbon diffusion across dissimilar alloys for nuclear energy applications	[44]

Table 1 - General description of FGM fabricated by DLD *(continuation)*

SS 316L	SS 316L Inconel 625 Ti6Al4V	Components that require both high corrosion resistance and a high strength-to-weight ratio.	Synchronous preheating proved to be fundamental for the production of crack-free FGMs by altering the formed phases.	[52]
SS 304L	SS 304L Inconel 625	Extreme-environment applications such as in aerospace or nuclear power generation.	Cracks were observed in the gradient zone and are associated with small amounts of transition metal carbides particles.	[7]
SS 304L	SS 316L Inconel 625	Engineering fields: aerospace, biological, nuclear and photoelectric.	FGMs with continuous composition gradient show strong metallurgical bond between each deposition. Wear resistance increased with increasing Inconel 625 amount. Higher hardness was obtained for 50% Inconel 625 + 50% 316L..	[3]
SS 304L	SS 316L Inconel 625 (50%/50%)	Test Pieces	The FGM has been successfully produced with no defects. Yield strength and tensile strength of FGMs are close to that of pure Inconel 625 and pure SS 316L, respectively.	[53]
AISI 304L	SS 316L Inconel 728	Components to harsh situations, such as nuclear power plants and oil refineries.	The brittle Laves phase was detected when the content of Inconel 718 exceeded 40 %. The fracture mechanism of the FGMs was the microporous aggregation fracture, induced by the Laves phase.	[54]
Nodular cast iron	Inconel 625 SS 420	Repair of components for different industries.	Repair of nodular cast iron structures using FGM's is appropriate. The FGM has good wear resistance.	[55]
Inconel 718	NiCrSiBC WC	Protective ceramic-metal composite coatings.	Controlling process parameters did not prevent cracking. Crack-free coatings could only be obtained by pre-heating the substrate (300 °C and 500 °C).	[40]

Table 1 - General description of FGM fabricated by DLD *(continuation)*

Ti6Al4V	Ti6Al4V Mo Inconel 718	Test Pieces	The importance of using a buffer material (transition layer) and controlling the different cooling speeds of the FGM materials to obtain a sound FGM is emphasized.	[56]
TI6Al4V	TI6Al4V Ti48Al2Cr2Nb	Materials for blisks of turbine blades (Ti48Al2Cr2Nb) and turbine disks (TI6Al4V) on aero engines.	FGM without cracks or metallurgical defects has been successfully manufactured. FGM reduces the sensitivity to cracking, particularly in titanium aluminide.	[57], [58]

Solidification and Microstructure Formation

The functional properties and quality of claddings produced by DLD are strongly dependent on the final microstructure. Rapid solidification in additive manufacturing can lead to solute segregation and the formation of unwanted, and unexpected, brittle phases. In fact, the DLD process promotes very high cooling rates, in the range of $5x10^3$ - 10^6 K/s, and diffusive transformations in the solid-state are usually suppressed. For this reason, homogenisation and control of the solidification process are fundamental to obtain the desired microstructure. Thus, one of the prerequisites for a successful process is homogenizing the melt in each layer. Several physical phenomena act in the melt pool; however, the fluid flow is dominated by Marangoni convection [59]–[61]. The melt pool is well-mixed due to this intense Marangoni convection that directly affects the shape and penetration of the pool, the chemical composition, the microstructure, and therefore the final properties of the FGM [62]–[64]. This convection, in which the surface tension gradient drives the material flow, also determines the formation of defects, such as porosities and cracks [61], [65]–[68].

Process parameters and material properties influence the Marangoni convection [61], [66]. An example is shown in Figure 3, which presents computed results evidencing the influence of laser scanning speed on liquid velocity; as the speed increases, the maximum liquid velocity moves from the sides to the rear of the pool, affecting the extension and the shape of the liquid pool [66]. This directly influences the microstructure, as illustrated in Figure 4, which shows EBSD images of a Ni superalloy processed with three different scanning speeds.

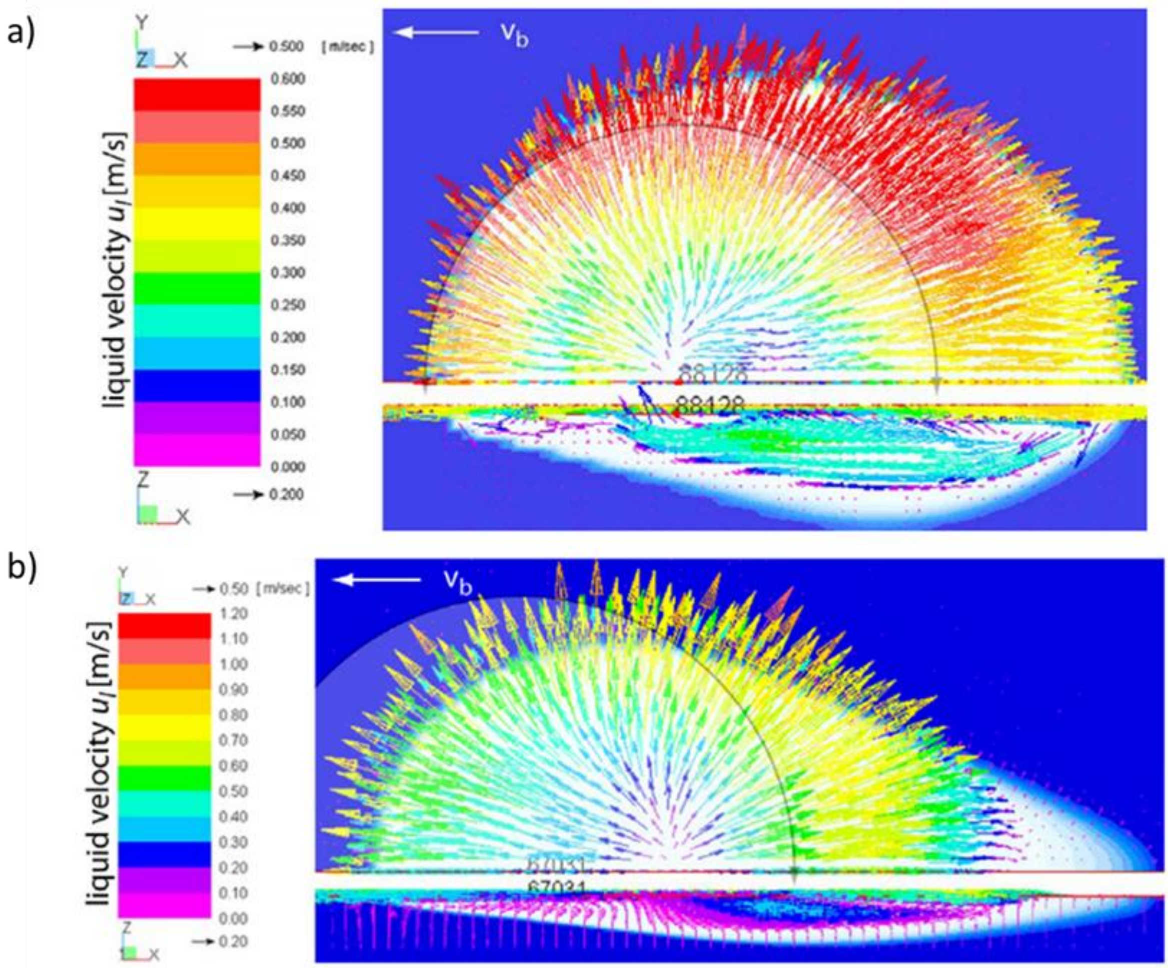

Figure 3. Simulation of Marangoni convection. The figures represent computed liquid pool and flow fields for two scanning speeds: (a) 3.5 and (b) 100 mm/sec [66].

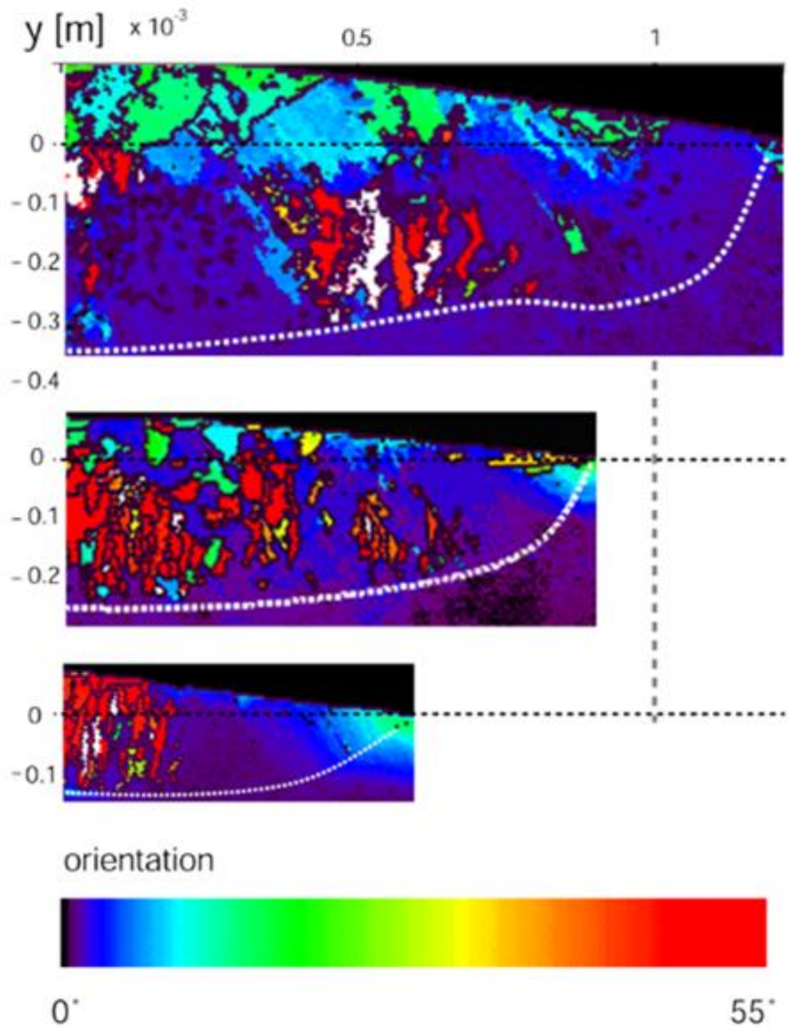

Figure 4. EBSD maps (right) for three scanning speeds [66].

Another example of the influence of processing parameters is shown in Figure 5. The cross-section analysis shows the influence of laser power on the shape and dimensions of the melt pool, modification of grain orientations, layer thickness, and surface finishing. All these modifications are direct effects of the influence of laser power on Marangoni flow [69].

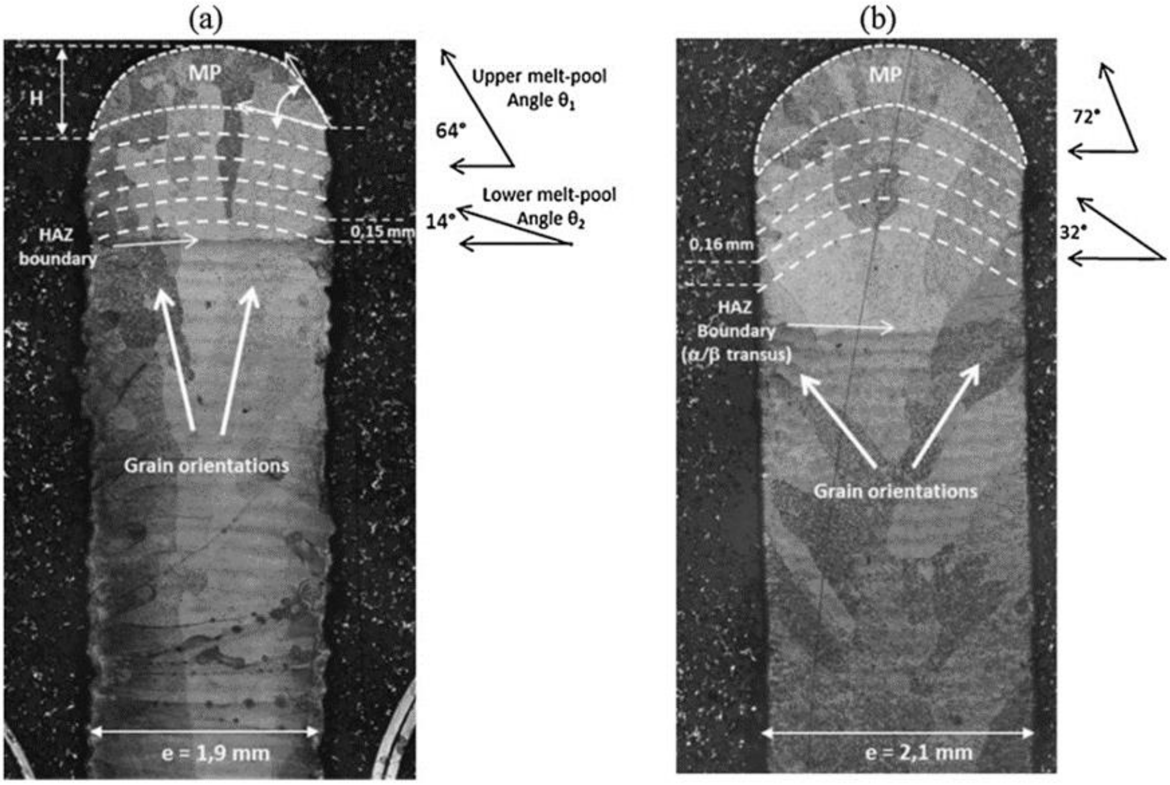

Figure 5. Influence of laser power on the microstructure of Ti6Al4V clads. Cross sections of clads produced with laser powers of (a) 320 W and (b) 500 W [69].

Figure 5 is a typical microstructure of a clad produced by DLD. In this process, the solidification modes evolve rapidly due to changes in solidification rate (R) and temperature gradient at the solid-liquid interface (G). These changes lead to the development of different microstructures that can be observed in laser additive manufacturing [68], [70], [71]. For a given alloy, the microstructure depends on the local solidification conditions. Specifically, the morphology of rapidly solidified layers is controlled by the G/R parameter. If G/R is greater than a critical value, a planar solidification front occurs, while if G/R is smaller than this critical value, the planar solid-liquid interface is destabilised, and cellular or dendritic solidification occurs [60], [68], [72].

At the beginning of the solidification, the planar solidification zone appears at the bottom of the melt pool, where the liquid metal maintains contact with the solid substrate (solidification rate is 0, and the G/R is infinite). With the propagation of the solid-liquid interface, R rapidly increases, and G decreases, leading to a lower G/R value: the planar front evolves into a cellular interface and eventually to a dendritic one when G/R decreases even more. In the DLD process, due to the fast variation of G/R, the planar zone is very narrow [61], [73], [74], as seen in Figure 6.

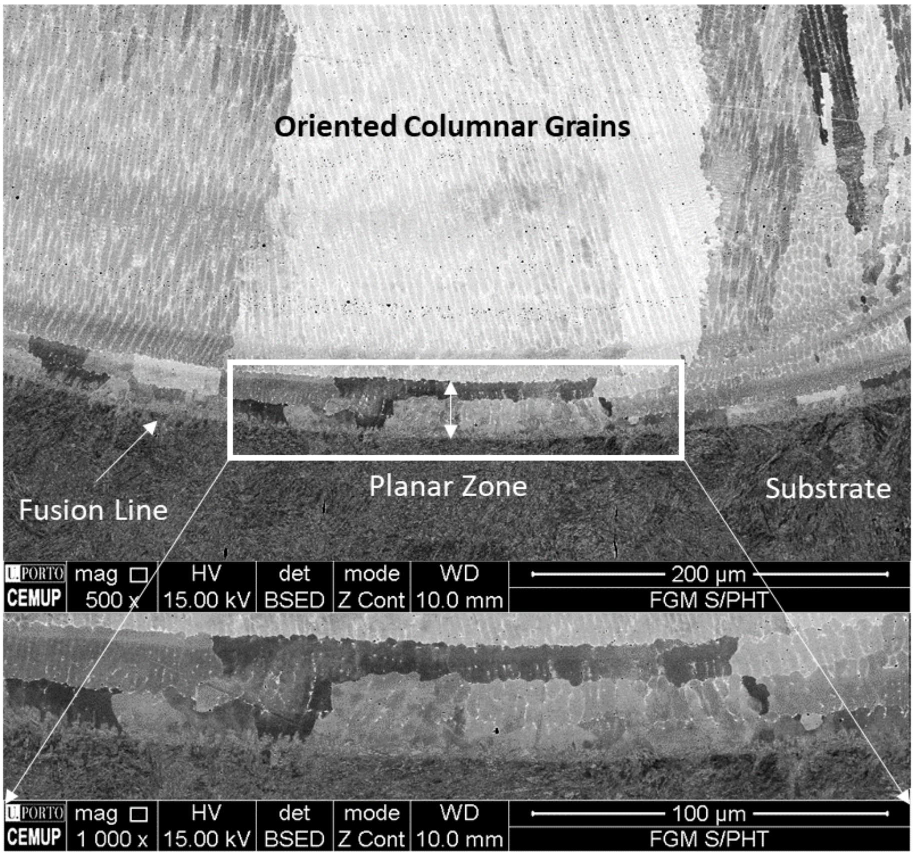

Figure 6. SEM micrograph of the cross section of a layer of Inconel 625 deposited on 42CrMo4 steel in which the planar zone and columnar grains can be observed.

With the evolution of the solidification process, the decrease in G/R slows down until reaching a value that remains practically constant. In this region, which follows the cellular interface zone, dendritic solidification appears. Cellular and dendritic solidifications are generally columnar and grow perpendicular to the substrate/solidified layers. This is due to the rapid heat dissipation by the substrate and solidified layers, the thermal gradient being higher in this direction. Near the surface of the cladding layer, heat is also dissipated through the surrounding atmosphere, which significantly decreases the G value. In this region, dendrites become very thin and disoriented [61], [73], [75]. For a detailed description of G and

R influence in solidification modes and microstructure development, see, for instance [76], [77].

The laser processing conditions and the clad building direction are factors that influence the microstructure and, therefore, the functional properties of claddings [78], [79].

In FGMs with composition gradients, the microstructure is also influenced by different materials characteristics, making solidification control more complex. An example of the microstructure formed in FGMs materials with a gradual change in composition is present in Figure 7. This figure shows the microstructure of an Inconel 625/ NiCrWMo superalloy (D4006) FGM. The first layers deposited are 100% Inconel 625, which gradually changes up to 100% D4006. Three intermediate zones have been sequentially deposited (75% Inconel 625 + 25% D4006, 50% Inconel 625 + 50% D4006, 25% Inconel 625 + 75% D4006).

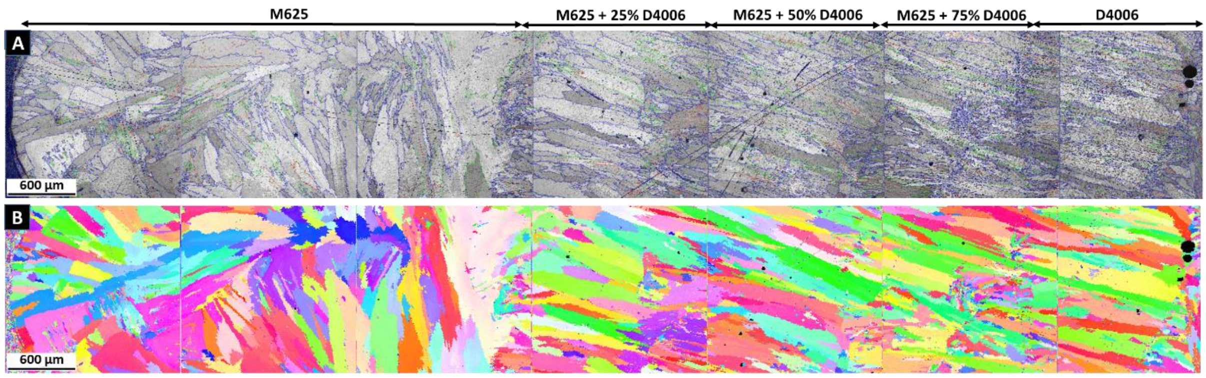

Figure 7. SEM images of the microstructure of an Inconel 625 (M625)/ NiCrWMo superalloy (D4006) FGM. (a) Microstructure evolution along the FGM, and (b) EBSD inverse pole figures (IPF).

From the analysis of the figure, some columnar grains that cross several layers stand out. These grains do not seem to be influenced by compositional changes, indicating the possibility of epitaxial growth. This type of microstructure occurs because the deposition of a new layer implies the remelting of part of the previous one, allowing the grains to function as nucleation sites for subsequent solidification. Despite this epitaxial growth, the IPF images do not show the formation of a strong preferential orientation (texture).

Defects

The most frequently detected defects in claddings produced using the DLD technique are cracks [80], porosity [81], chemical segregation [82], formation of intermetallics [83], and unmelted powder particles [84], all of which promote the deterioration of the mechanical properties of the components. Some of these defects, even if of a submicrometric dimension, can have serious consequences. In fact, micro segregation, and the formation of brittle phases, like intermetallics, enhance the nucleation of microcracks, leading to component collapse. Defect reduction is therefore essential so that the FGMs do not fail in service.

The main causes of the development of defects are associated with processing parameters, as in most manufacturing processes. Laser power, powder feed rate, scanning speed, and powder particle size are factors that can promote cracking and pore formation. The optimization of processing conditions will allow a good metallurgical bond between the deposit and the substrate, and an adequate dilution. Dilution is an essential aspect of DLD clads and assesses the contribution of the substrate area that is melted by the laser to the total area of the clad, controlling clad contamination by the substrate and affecting the deposition yield. This optimization minimizes defects such as cracks and porosities, which can act as stress concentrators and nucleate fatigue cracks [29], [85]. For some materials, it has been shown that increasing laser power intensifies residual stresses, cracks formation, and the deterioration of mechanical properties [33], [86].

The formation of cracks can also be associate with phases that locally introduce high discontinuity in the hardness, brittleness, and thermal stability of the FGMs (see Figure 8). Attention has been paid to the formation of intermetallic compounds [58], eutectics (low melting point) and borides [87], and Laves phase [82], [88]–[93].

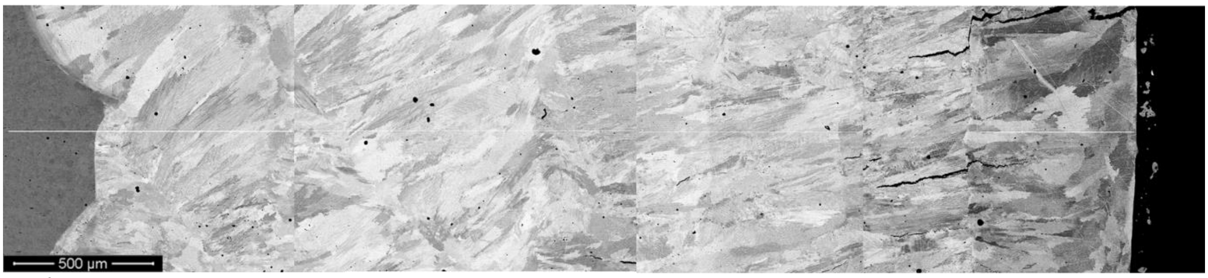

Figure 8. SEM images of the microstructure of an Inconel 625 (M625)/martensitic stainless-steel (M42C) FGM showing cracking formation in the 25% Inconel 625 + 75% M625 layer.

The formation of the Laves phase in nickel-based superalloys has been widely studied since this material is one of the most manufactured using DLD, including in the production of FGMs. The brittle intermetallic Laves phase is formed due to the interdendritic segregation of chemical elements of the matrix. This phase is a product of the eutectic reaction, L→(γ + Laves), is dependent on local elements concentration during non-equilibrium solidification [84], [90], and leads to the reduction of useful alloying elements (Ni, Fe, Cr, Nb, Mo, Ti) in the matrix, as shown in Figure 9 for niobium. The formation of Laves phase is highly undesirable, as it deteriorates the mechanical properties of the cladding, such as ductility, tensile strength, and fatigue life [88], [92]. Furthermore, it increases the susceptibility to hot cracking [89]. The amount of this phase is higher in FGM regions processed with higher energy density [91]. A high cooling rate promotes less redistribution of elements, forming larger Laves phase particles, with a detrimental effect in mechanical response [82], [92]. The addition of vanadium inhibits niobium segregation, thus reducing Laves phase formation, positively influencing the microstructure. In addition, vanadium changes the morphology of the Laves phase from a rod-like to particle-like shape [93].

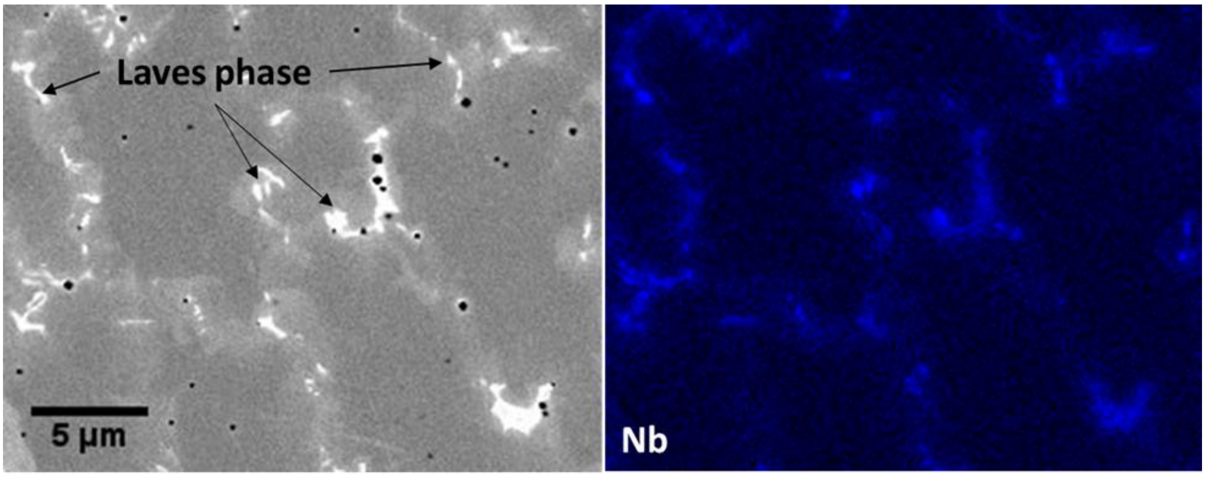

Figure 9. SEM images showing the morphologies of Laves phase particles and Nb element distributions in the interdendritic regions.

Porosity is another extremely harmful defect to the performance of the FGMs. It is mainly the result of gases encapsulated in the powder feed system or powder particles and by an inadequate selection of process parameters [22], [81], [85]. Porosity may also be associated with high melt pool cooling rates [94].

Unmelted powder particles are another defect that induces the degradation of FGMs performance. This defect is formed due to insufficient energy density, causing low absorption of laser energy and promoting the non-fusion of the powder, favouring the formation of cracks due to low metallurgical bond [95], [96]. In the production of FGMs, this problem increases since the different powders have different thermophysical properties [56].

One procedure that promotes the reduction of residual stresses and defects, such as cracks, is the preheating of the substrate and the maintenance of this preheating during the deposition process [56]. Preheating also inhibits the formation of harmful phases such as eutectics and borides [87], thus reducing defects in FGMs. Preheating is also essential in controlling thermal gradients between the substrate and the deposited layers, by decreasing the cooling rate and residual stresses [40], [97] and attenuating the difference in thermal expansion coefficients between the several powders [58], thus inhibiting the formation of cracks and promoting better mechanical properties.

In summary, to overcome the current challenges to FGMs production by DLD on different substrates, it is necessary to develop integrated methodologies that consider and integrate all processing phases, such as parameter definition, process optimization, and thermomechanical simulations.

Mechanical Characterisation

Undoubtedly, one of the main objectives of the production of FGMs is to obtain different mechanical properties from the combination of materials. Another objective is to ensure gradual and crack-free transition between substrate and last cladding layers, which also translates into the variation of mechanical properties. This section highlights some of the most important mechanical properties of several FGMs, such as microhardness, tensile properties, and wear resistance. As already mentioned, one of the main groups of FGMs produced results from combinations of steels with nickel superalloys. This review of the mechanical properties of FGMs begins with the analysis of this combination.

An FGM with a composition gradient between pure stainless-steel 316L (SS316L) and pure Inconel 718 (IN718), with three intermediate layers (25%, 50%, and 75 of IN718) deposited on SS 316L was manufactured [47]. The influence of laser power (LP) and powder feed rate (FR) on the mechanical performance of the material was studied. Crack-free FGMs were produced for the four laser powers and two feed rates tested. Tensile tests on the specimens revealed reduced ductility with the fracture starting in the steel. The tensile strength decreases with the increase in laser power and the decrease in the feed rate, being 596 MPa for LP = 450 W and FR = 0.834 g/s and 527 MPa for and LP = 750 W and FR = 0.632 g/s.

The Vickers microhardness analysis along the FGM shows an approximately parabolic hardness distribution with an initial decrease as the amount of steel decreases, a minimum for the layer with an equal amount of both powders and increasing to a maximum corresponding to the last layer of pure Inconel, the only non-reheated layer [47]. As with tensile strength, an increase in laser power leads to a decrease in hardness.

The Mean Specific Wear Rates (MSWR) of constant composition layers, produced with the four laser powers and the two powder feed rates, were also determined [47]. MSWR is lower in pure steel for all conditions, goes through a maximum for the 75% SS 316L + 25% Inconel 718 composition, and decreases with the increasing amount of Inconel. The highest MSWR values were obtained for the highest laser power and lower feed rate.

This evolution of the mechanical properties, related to the spacing of the secondary dendritic arms and carbide formation, shows that tailored mechanical properties can be obtained by optimizing the processing parameters and composition, allowing the adequate selection to fulfil the FGMs requirements.

The SS316 L/Inconel718 FGM with different composition gradients were also fabricated by DLD [54]. The composition changed from pure SS316L to pure IN718, increasing by 5%, 10%, or 20% the IN718 amount every ten layers. This composition gradient affects the mechanical response of the FGMs. The fracture of the tensile sample occurred at layers corresponding to 20–40%, 50–60%, and 25%–30% IN718, for the composition gradients of 20%, 10%, and 5%, respectively. The best tensile properties, with the highest tensile strength (527 MPa) and the highest elongation (26%), were obtained by the FGM with a composition gradient of 10 %. These results evidenced that the gradient variation is essential for FGMs fabricated by additive manufacturing.

316L stainless steel (SS316L) and Inconel 625 (IN625) powders have also been mixed to make FGMs [98]. In this study, FGMs produced with an abrupt transition between SS316L and IN625, and with a transition zone, where the relative amount of IN625 gradually increases by 12.5% every two layers, were analysed. Mechanical properties were compared with those of pure materials produced under the same conditions.

The mechanical response of the FGMs was determined by the softest material (SS316L) and, assuming that the toughest IN625 has negligible plastic deformation, the tensile properties of both FGMs are almost identical to those of SS316, with no noticeable differences in mechanical strength and ductility [98]. This means that, in this case, a good interfacial resistance between the two materials has been achieved and the transition zone, which makes the manufacture of the FGM much more complex, is not necessary. Recently, another SS316L/IN625 FGM, deposited on the same substrate (SS304), was produced with other processing conditions, and the mechanical properties were investigated [3]. The FGM produced had a transition zone in which the relative amount of IN625 increased by 10% in each region. In this FGM the tensile specimens also showed a noticeable plastic deformation and ductile fracture. An analysis of the fracture surfaces indicated that the fracture occurred in layers with 60% SS316L + 40% IN625. In this analysis, particles rich in Nb were detected at the bottom of the dimples, indicating that fragile particles resulting from the segregation of this element, eventually phase Laves, maybe at the origin of the fracture.

The average yield strength obtained for five samples were 823 MPa and the average tensile strenght 1030 MPa [3]. These values are much higher than the average values reported in [98] (310 and 540 MPa for yield strength and tensile strenght, respectively) and even higher than typical of 316L stainless steel.

The microhardness along the transition zone showed a gradual upward trend, with a maximum of 347 HV for the deposited layer with 50% SS316L + 50% IN625. The wear of samples with various compositions was also analyzed. It was determined that the wear resistance first decreases slightly with an increasing percentage of IN625 but then increases significantly, approaching that of the superalloy for 20% SS316L + 80% IN625 (as can be seen in the Table 2) [3].

Table 2. Wear rate for FGM samples and pure materials [3].

Sample composition	Wear rate (x10^{-3}cm^{-3}.N.m^{-1})
100% SS316l	1.58
80% SS316L + 20% IN625	1.60
60% SS316L + 40% IN625	1.32
40% SS316L + 60% IN625	1.15
20% SS316L + 80% IN625	0.79
100% IN625	0.74

The microhardness evolution of an FGM fabricated using two nickel superalloys powders, Inconel 625 (IN625) and NiCrWMo (D4006), is shown in Figure 10. This FGM has five different regions; the first layers of the FGM were 100% IN625, and the amount of the NiCrWMo superalloy increase by 25% in each of the three intermediate regions, ending the deposition with 100% NiCrWMo. The microhardness increase as the amount of NiCrWMo powder is increasing. This factor is related to the strengthening effect of alloying elements (Cr, W, Mo).

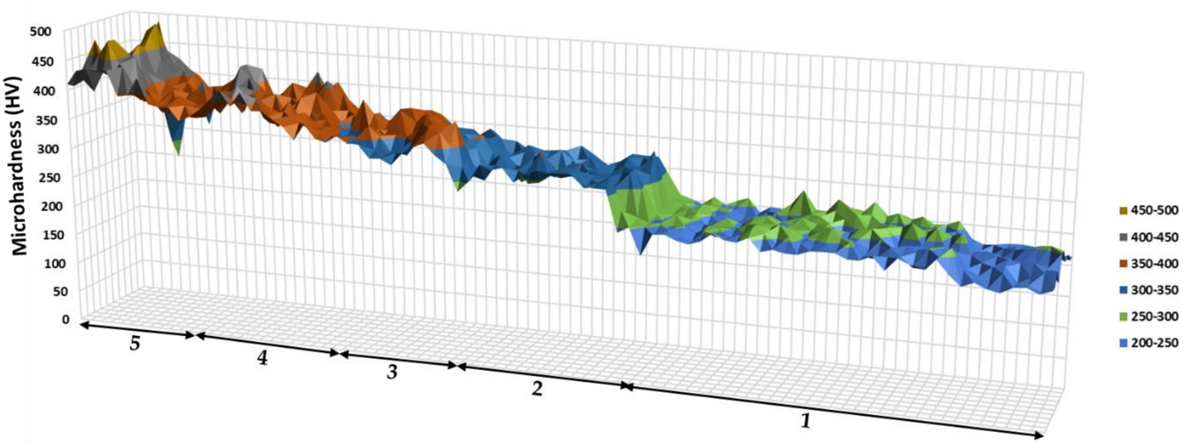

Figure 10. Vickers microhardness mapping of an FGM along the sample. The composition of the regions is: 1 - 100% IN625; 2 - 75% IN625 + 25% NiCrWMo; 3 - 50% IN625 + 50% NiCrWMo; 4 - 75% IN625 + 75% NiCrWMo; 5 - 100% NiCrWMo.

Another group of FGMs that has been studied a lot is the one that uses Ti6Al4V powders and powders of a much harder material. An example is a FGM deposited by DLD on a Ti6Al4V substrate, with composition changing from 100% Ti6Al4V to 50% Ti6Al4V + 50% TiC, and with a gradual increase in composition of 5% TiC in each zone

[99]. One FGM was produced with constant processing parameters (FGM A) and the other with parameters optimized for each condition (FGM B). The results presented in Table 3 showed that the optimized FGM has the best wear-resistance behaviour, with a reduction of 82.5% in the wear volume compared with the substrate. The last layers of this FGM (with a composition of 50% Ti6Al4V + 50% TiC) has a microhardness value (1200 VHN) which is four times that of the Ti6Al4V.

Table 3. Wear volume for FGMs and substrate [99].

Sample designation	Wear volume (mm^3)
FGM A	0.033
FGM B	0.021
Substrate	0.120

These results show how the proper selection of the processing conditions for each zone (each composition) can be decisive in obtaining an optimized FGM behaviour.

Ti6Al4V/TiC FGM production with a 1% TiC increase in each of the 50 layers of up 50% TiC has also been tested [100]. The FGM microhardness gradually increases from 380 HV in the Ti6Al4V layer to 737 HV in the top layer (with 50% TiC), which means it almost doubles. This hardness variation is less important than reported in [99], emphasizing the effect of processing parameters and powders characteristics.

To analyse the tensile properties of this Ti6Al4V/TiC FGM, samples with fixed composition were deposited (each sample was the result of the deposition of ten layers). Six compositions were produced, with 0, 10, 20, 30, 40, and 50% TiC. The last two compositions were not tested as cracks appeared during the FGMs production. The ultimate tensile strength of the FGM with a TiC amount of 5% is improved by 12% compared to Ti6Al4V. Contrary to what was expected considering the hardness evolution, further increase of the TiC amount decreases the tensile strength, and the elongation drops to less than 1%. This unexpected behaviour was explained by increasing unmelted TiC particles and dendritic TiC phases, which promote premature damage of FGMs [100].

The brittleness of the Ti6Al4V/TiC FGM is a problem that should be carefully considered during its manufacture by DLD technology. The effect of laser power and scan speed on hardness of Ti6Al4V/TiC FGM deposited in a Ti6Al4V substrate was analyzed [101]. FGMs were deposited with increase of TiC through three zones, with 10, 20, and 30% TiC, and laser power ranging from 400 to 700 W and scan speeds of 200, 300, and 400 mm/min. The Vickers hardness gradually increases from 300 HV to 600 HV with the increase of TiC amount. No significant differences were observed for the set of processing parameters tested. Samples with constant composition (0, 10, 20, and 30% TiC) were produced for tensile tests [101]. Ultimate tensile strength and elongation decreases with increasing TiC amount, being this more noticeable for 20 and 30% TiC, which confirms the results reported in [100].

Ti6Al4V and Invar 36 (64 wt% Fe, 36 wt% Ni) powers were used to produce an FGM [102]. The FGM started with the deposition of 21 layers of Ti6Al4V powder onto a Ti6Al4V substrate, followed by a 32 layers gradient region with a 3% decrease in Ti6Al4V per layer (replaced by 3% Invar powder), and, finally, 22 layers of pure Invar. Hardness shows a noticeable increase for layers with 40-60% Invar. In these layers, values close to 900 HV were measured, being much higher than the average values of Ti6Al4V and Invar, which are 380 and 141 HV, respectively. These significantly higher hardness values were associated with the formation of iron and nickel titanides in the FGM. These intermetallic phases are very hard but also very brittle, which may explain the macroscopic cracking of the FGM. Although hardness values measured in the FGM central region are excellent, the defects preclude Ti6Al4V/Invar from being used in industrial applications.

Ti/SiC was another metal/ceramic FGM produced by DLD with a combination of powders similar to the one described above, a ductile titanium alloy gradually reinforced with a carbide. In this FGM, a layer of 100% Ti was first deposited on a Ti6Al4V substrate, then eight more layers were deposited with a constant decrease of 10% Ti (an increase of 10% SiC), with the final layer having the composition of 20% Ti + 80 % SiC [103].

One of the main challenges of these FGMs is to successfully achieve a high volume content of the ceramic constituent at the exterior layer, surmounting the problems caused by the great brittleness and the poor melting fluidity of most ceramics. To achieve this goal, the composition and thickness of the Ti/SiC FGMs layers were optimized, first eliminating the layers with a greater tendency to cracking (namely the layer with 70% Ti + 30% SiC), and then halving the thickness of the layers. After this optimization, it was possible to avoid forming the more cracking and microcracking inducing phases and producing an FGM without evident defects. In this optimized FGM, the hardness continuously increases from 339 HV in the Ti layer to 1608 HV in the outer layer (10% Ti+90% SiC), and average three-point bending strength of 286 MPa was measured at room temperature [103].

These mechanical properties show that it is possible to produce metal/ceramic FGMs with the proper selection of the layer construction strategy. In summary, some aspects related to mechanical properties can be highlighted:

• Final mechanical properties are not necessarily a combination of the mechanical properties of the materials used in the FGM and may vary significantly across the deposited zone.

• The variation of mechanical properties along the FGM is not necessarily gradual or linear and is strongly related to the microstructure.

• In some cases, defects induced by the FGM process, such as cracks and porosities, can negatively affect the mechanical properties, making its industrial application unfeasible.

• The production of FGMs has often proven to be able to improve mechanical properties such as wear-resistance and hardness.

• The deposition parameters, including the composition and thickness of the various layers, play a significant role in the final properties and must be optimized to achieve the intended requirements.

Conclusions

Functional Gradient Materials (FGM) combine materials with different compositions, leveraging the best properties of each and exploring reactions that can give rise to unexpected properties. FGMs respond to the growing demand from various industrial sectors for materials with better performance, allowing them to produce components with unique characteristics and a gradient of properties along a specific direction. The production of FGMs by Direct Laser Deposition (DLD) is an attractive solution for many engineering applications, thus opening new perspectives for several industrial sectors, such as aerospace, automotive, nuclear, and biomedical. In this review, the current status of research on using the DLD process for manufacturing FGMs has been summarized. The main characteristics of this manufacturing process, the microstructures and mechanical properties of FGMs, and their main defects, were described. DLD is the technology that makes it possible to manufacture the widest range of FGMs and results from additive manufacturing progress that makes it technologically and economically viable. This process provides freedom to design more complex components, built layer by layer, with strategically controlled compositional variations that enable the directionality of properties. The production of FGM by DLD has been widely used as it opens up the possibility of blending different types of materials, such as metals (steel, superalloys, and titanium alloys) and ceramics. This review also highlights the need for more studies in producing these materials, expanding the analyzed systems, optimizing processing conditions, and properly establishing the correlation of microstructures, phase changes, and defects with the properties of the FGM, thus enhancing its performance in service.

References

[1] P. Muller, P. Mognol, and J. Y. Hascoet, “Modeling and control of a direct laser powder deposition process for Functionally Graded Materials (FGM) parts manufacturing”, *J. Mater. Process. Technol.*, vol. 213, no. 5, pp. 685–692, 2013, doi: 10.1016/j.jmatprotec.2012.11.020.

[2] B. Kieback, A. Neubrand, and H. Riedel, “Processing techniques for functionally graded materials”, *Mater. Sci. Eng. A*, vol. 362, no. 1–2, pp. 81–106, 2003, doi: 10.1016/S0921-5093(03)00578-1.

[3] B. Chen, Y. Su, Z. Xie, C. Tan, and J. Feng, “Development and characterization of 316L/Inconel625 functionally graded material fabricated by laser direct metal deposition”, *Opt. Laser Technol.*, vol. 123, no. May 2019, 2020, doi: 10.1016/j.optlastec.2019.105916.

[4] H. P. Qu, P. Li, S. Q. Zhang, A. Li, and H. M. Wang, “Microstructure and mechanical property of laser melting deposition (LMD) Ti/TiAl structural gradient material”, *Mater. Des.*, vol. 31, no. 1, pp. 574–582, 2010, doi: 10.1016/j.matdes.2009.07.004.

[5] X. Lin, T. M. Yue, H. O. Yang, and W. D. Huang, “Microstructure and phase evolution in laser rapid forming of a functionally graded Ti-Rene88DT alloy”, *Acta Mater.*, vol. 54, no. 7, pp. 1901–1915, 2006, doi: 10.1016/j.actamat.2005.12.019.

[6] R. M. Mahamood and E. T. Akinlabi, *Laser Additive Manufacturing*. 2016

[7] B. E. Carroll, R. A. Otis, J. P. Borgonia, J. Suh, R. P. Dilon, A. A. Shapiro, D. C. Hofmann, Z. Liu and A. M. Beese, “Functionally graded material of 304L stainless steel and inconel 625 fabricated by directed energy deposition: Characterization and thermodynamic modeling”, *Acta Mater.*, vol. 108, pp. 46–54, 2016, doi: 10.1016/j.actamat.2016.02.019.

[8] C. Petit, L. Montanaro, and P. Palmero, “Functionally graded ceramics for biomedical application: Concept, manufacturing, and properties”, *Int. J. Appl. Ceram. Technol.*, vol. 15, no. 4, pp. 820–840, 2018, doi: 10.1111/ijac.12878.

[9] N. Radhika, K. Teja, K. Rahul, and A. Shivashankar, “Fabrication of Cu-Sn-Ni /SiC FGM for Automotive Applications: Investigation of its Mechanical and Tribological Properties”, *Silicon*, vol. 10, no. 4, pp. 1705–1716, 2018, doi: 10.1007/s12633-017-9657-3.

[10] M. Koizumi, “FGM activities in Japan”, *Compos. Part B Eng.*, vol. 28, no. 1–2, pp. 1–4, 1997, doi: 10.1016/s1359-8368(96)00016-9.

[11] M. Soodi, S. H. Masood, and M. Brandt, "Thermal expansion of functionally graded and wafer-layered structures produced by laser direct metal deposition", *Int. J. Adv. Manuf. Technol.*, vol. 69, no. 9–12, pp. 2011–2018, 2013, doi: 10.1007/s00170-013-5157-9.

[12] Y. Li, Z. Feng, L. Hao, L. Huang, C. Xin, Y. Wang, E. Bilotti, K. Essa, H. Zhang, Z. Li, F. Yan and T. Peijs, "A Review on Functionally Graded Materials and Structures via Additive Manufacturing: From Multi-Scale Design to Versatile Functional Properties", *Adv. Mater. Technol.*, vol. 1900981, 2020, doi: 10.1002/admt.201900981.

[13] A. Saboori, G. Piscopo, M. Lai, A. Salmi, and S. Biamino, "An investigation on the effect of deposition pattern on the microstructure, mechanical properties and residual stress of 316L produced by Directed Energy Deposition", *Mater. Sci. Eng. A*, vol. 780, no. March, p. 139179, 2020, doi: 10.1016/j.msea.2020.139179.

[14] W. Paatsch, "Energy turnaround - a challenge for surface technology", *Trans. {IMF}*, vol. 94, no. 5, pp. 228–230, 2016, doi: 10.1080/00202967.2016.1209295.

[15] Y. Gao, D. Xiong, C. Wang, and Y. Chen, "Influences of laser powers on microstructure and properties of the coatings on the AZ91HP magnesium alloy", *Acta Metall. Sin. (English Lett.*, vol. 22, no. 3, pp. 167–173, 2009, doi: https://doi.org/10.1016/S1006-7191(08)60085-X.

[16] J. Chen, S.-H. Wang, and L. Xue, "On the development of microstructures and residual stresses during laser cladding and post-heat treatments", *J. Mater. Sci.*, vol. 47, no. 2, pp. 779–792, 2012, doi: 10.1007/s10853-011-5854-4.

[17] S. M. Thompson, L. Bian, N. Shamsaei, and A. Yadollahi, "An overview of Direct Laser Deposition for additive manufacturing; Part I: Transport phenomena, modeling and diagnostics", *Addit. Manuf.*, vol. 8, pp. 36–62, 2015, doi: 10.1016/j.addma.2015.07.001.

[18] E. P. Cardozo, G. R. Pardal, S. Ríos, S. Ganguly, and A. S. C. M. D'oliveira, "Additive techniques to refurbish Ni based components", *Soldag. e Insp.*, vol. 24, pp. 1–11, 2019, doi: 10.1590/0104-9224/SI24.03.

[19] Q. Guo, S. Chen, M. Wei, J. Liang, C. Liu, and M. Wang, "Formation and Elimination Mechanism of Lack of Fusion and Cracks in Direct Laser Deposition 24CrNiMoY Alloy Steel", *J. Mater. Eng. Perform.*, vol. 29, no. 10, pp. 6439–6454, 2020, doi: 10.1007/s11665-020-05163-4.

[20] V. Promakhov, A. Zhukov, M. Ziatdinov, I. Zhukov, N. Schulz, S. Kovalchuk, Y. Dubkova, D. Korsmik, O. Klimova-Korsmik, G. Turichin and A. Perminov, "Inconel 625/TiB 2 metal matrix composites by direct laser deposition", *Metals (Basel).*, vol. 9, no. 2, pp. 1–15, 2019, doi: 10.3390/met9020141.

[21] J. M. Wilson and Y. C. Shin, "Microstructure and wear properties of laser-

deposited functionally graded Inconel 690 reinforced with TiC", *Surf. Coatings Technol.*, vol. 207, pp. 517–522, 2012, doi: 10.1016/j.surfcoat.2012.07.058.

[22] A. Dass and A. Moridi, "State of the art in directed energy deposition: From additive manufacturing to materials design", *Coatings*, vol. 9, no. 7, 2019, doi: 10.3390/COATINGS9070418.

[23] L. Yan, Y. Chen, and F. Liou, "Additive manufacturing of functionally graded metallic materials using laser metal deposition", *Addit. Manuf.*, vol. 31, no. November 2019, p. 100901, 2020, doi: 10.1016/j.addma.2019.100901.

[24] S. Nam, H. Cho, C. Kim, and Y. M. Kim, "Effect of process parameters on deposition properties of functionally graded STS 316/Fe manufactured by laser direct metal deposition", *Metals (Basel).*, vol. 8, no. 8, 2018, doi: 10.3390/met8080607.

[25] R. M. Mahamood, *Laser Metal Deposition of Metals and Alloys*. 2018.

[26] G. H. Loh, E. Pei, D. Harrison, and M. D. Monzón, "An overview of functionally graded additive manufacturing", *Addit. Manuf.*, vol. 23, no. May, pp. 34–44, 2018, doi: 10.1016/j.addma.2018.06.023.

[27] G. H. Loh, E. Pei, D. Harrison, and M. D. Monzón, "An overview of functionally graded additive manufacturing", *Addit. Manuf.*, vol. 23, no. c, pp. 34–44, 2018, doi: 10.1016/j.addma.2018.06.023.

[28] D. T. Sarathchandra, S. Kanmani Subbu, and N. Venkaiah, "Functionally graded materials and processing techniques: An art of review", *Mater. Today Proc.*, vol. 5, no. 10, pp. 21328–21334, 2018, doi: 10.1016/j.matpr.2018.06.536.

[29] K. F. Walker, J. M. Lourenço, S. Sun, M. Brandt, and C. H. Wang, "Quantitative fractography and modelling of fatigue crack propagation in high strength AerMet®100 steel repaired with a laser cladding process", *Int. J. Fatigue*, vol. 94, pp. 288–301, 2017, doi: 10.1016/j.ijfatigue.2016.06.031.

[30] W. Li, J. Zhang, X. Zhang, and F. Liou, "Effect of optimizing particle size on directed energy deposition of Functionally Graded Material with blown Pre-Mixed Multi-Powder", *Manuf. Lett.*, vol. 13, pp. 39–43, 2017, doi: 10.1016/j.mfglet.2017.07.001.

[31] M. Naebe and K. Shirvanimoghaddam, "Functionally graded materials: A review of fabrication and properties", *Appl. Mater. Today*, vol. 5, pp. 223–245, 2016, doi: 10.1016/j.apmt.2016.10.001.

[32] A. Reichardt, "Additive Manufacturing of Metal-based Functionally Graded Materials. UC Berkeley. ProQuest ID: Reichardt_berkeley_0028E_17635. Merritt ID: ark:/13030/m5zh1phm. Retrieved from https://escholarship.org/uc/item/32h5c2vp", 2017, [Online]. Available:

https://escholarship.org/uc/item/32h5c2vp.

[33] S. Zhou, X. Zeng, Q. Hu, and Y. Huang, “Analysis of crack behavior for Ni-based WC composite coatings by laser cladding and crack-free realization”, *Appl. Surf. Sci.*, vol. 255, no. 5 PART 1, pp. 1646–1653, 2008, doi: 10.1016/j.apsusc.2008.04.003.

[34] A. Bhattacharyya and D. Maurice, “Residual stresses in functionally graded thermal barrier coatings”, *Mech. Mater.*, vol. 129, no. November 2018, pp. 50–56, 2019, doi: 10.1016/j.mechmat.2018.11.002.

[35] X. C. Zhang, B. S. Xu, H. D. Wang, Y. Jiang, and Y. X. Wu, “Modeling of thermal residual stresses in multilayer coatings with graded properties and compositions”, *Thin Solid Films*, vol. 497, no. 1–2, pp. 223–231, 2006, doi: 10.1016/j.tsf.2005.09.184.

[36] K. Z. Uddin and B. Koohbor, “Gradient optimization of transversely graded Ti-TiB structures for enhanced fracture resistance”, *Int. J. Mech. Sci.*, vol. 187, no. June, p. 105917, 2020, doi: 10.1016/j.ijmecsci.2020.105917.

[37] P. Kattire, S. Paul, R. Singh, and W. Yan, “Experimental characterization of laser cladding of CPM 9V on H13 tool steel for die repair applications”, *J. Manuf. Process.*, vol. 20, pp. 492–499, 2015, doi: 10.1016/j.jmapro.2015.06.018.

[38] K. Dai, X. X. Li, and L. L. Shaw, “Comparisons between thermal modeling and experiments: Effects of substrate preheating”, *Rapid Prototyp. J.*, vol. 10, no. 1, pp. 24–34, 2004, doi: 10.1108/13552540410512507.

[39] B. Zheng, Y. Zhou, J. E. Smugeresky, J. M. Schoenung, and E. J. Lavernia, “Thermal behavior and microstructural evolution during laser deposition with laser-engineered net shaping: Part I. Numerical calculations”, *Metall. Mater. Trans. A Phys. Metall. Mater. Sci.*, vol. 39, no. 9, pp. 2228–2236, 2008, doi: 10.1007/s11661-008-9557-7.

[40] A. Sadhu, A. Choudhary, S. Sarkar, A. M. Nair, P. Nayak, S. D. Pawar, G. Muvvala, S. K. Pal, andr A. K. Nath, “A study on the influence of substrate pre-heating on mitigation of cracks in direct metal laser deposition of NiCrSiBC-60%WC ceramic coating on Inconel 718”, *Surf. Coatings Technol.*, vol. 389, no. March, p. 125646, 2020, doi: 10.1016/j.surfcoat.2020.125646.

[41] C. Ding, X. Cui, J. Jiao, and P. Zhu, “Effects of substrate preheating temperatures on the microstructure, properties, and residual stress of 12CrNi2 prepared by laser cladding deposition technique”, *Materials (Basel).*, vol. 11, no. 12, 2018, doi: 10.3390/ma11122401.

[42] X. Liang, D. Wu, Q. Li, and L. Jiang, “Laser rapid manufacturing of stainless steel 316L/Inconel718 functionally graded materials: Microstructure evolution and mechanical properties”, *Int. J. Opt.*, vol. 2010, pp. 1–6, 2010, doi:

10.1155/2010/802385.

[43] W. J. Ji and Y. H. Moon, "Fabrication of functionally graded properties by direct laser melting of compositionally selective metallic powder", *ICCAS 2015 - 2015 15th Int. Conf. Control. Autom. Syst. Proc.*, pp. 1955–1957, 2015, doi: 10.1109/ICCAS.2015.7364686.

[44] J. S. Zuback, T. A. Palmer, and T. DebRoy, "Additive manufacturing of functionally graded transition joints between ferritic and austenitic alloys", *J. Alloys Compd.*, vol. 770, pp. 995–1003, 2019, doi: 10.1016/j.jallcom.2018.08.197.

[45] D. K. Kim, W. Woo, E. Y. Kim, and S. H. Choi, "Microstructure and mechanical characteristics of multi-layered materials composed of 316L stainless steel and ferritic steel produced by direct energy deposition", *J. Alloys Compd.*, vol. 774, pp. 896–907, 2019, doi: 10.1016/j.jallcom.2018.09.390.

[46] L. D. Bobbio, B. Bocklund, A. Reichardt, R. Otis, J. P. Borgonia, R. P. Dillon, A. A. Shapiro, B. W. McEnerney, P. Hosemann, Z. Liu and A. M. Beese, "Analysis of formation and growth of the σ phase in additively manufactured functionally graded materials", *J. Alloys Compd.*, vol. 814, p. 151729, 2020, doi: 10.1016/j.jallcom.2019.151729.

[47] K. Shah, I. ul Haq, A. Khan, S. A. Shah, M. Khan, and A. J. Pinkerton, "Parametric study of development of Inconel-steel functionally graded materials by laser direct metal deposition", *Mater. Des.*, vol. 54, pp. 531–538, 2014, doi: 10.1016/j.matdes.2013.08.079.

[48] R. Koike, I. Unotoro, Y. Kakinuma, T. Aoyama, Y. Oda, T. Kuriya and M. Fujishima, "Evaluation for mechanical characteristics of Inconel625-SUS316L joint produced with direct energy deposition", *Procedia Manuf.*, vol. 14, pp. 105–110, 2017, doi: 10.1016/j.promfg.2017.11.012.

[49] J. del Val, A. Arias-González, O. Barro, A. Riveiro, R. Comesaña, J. Penide, L. Lusquiños, M. Bountinguiza, F. Quintero and J. Pou, "Functionally graded 3D structures produced by laser cladding", *Procedia Manuf.*, vol. 13, pp. 169–176, 2017, doi: 10.1016/j.promfg.2017.09.029.

[50] A. Bayode, S. Pityana, and E. Titilayo Akinlabi, "4. Fabrication of stainless steel-based FGM by laser metal deposition", *Hierarchical Compos. Mater.*, pp. 55–72, 2019, doi: 10.1515/9783110545104-004.

[51] S. M. Banait, C. P. Paul, A. N. Jinoop, H. Kumar, R. S. Pawade, and K. S. Bindra, "Experimental investigation on laser directed energy deposition of functionally graded layers of Ni-Cr-B-Si and SS316L", *Opt. Laser Technol.*, vol. 121, no. May 2019, p. 105787, 2020, doi: 10.1016/j.optlastec.2019.105787.

[52] W. Meng, W. Zhang, W. Zhang, X. Yin, L. Guo, and B. Cui, "Additive fabrication of 316L/Inconel625/Ti6Al4V functionally graded materials by laser synchronous

preheating", *Int. J. Adv. Manuf. Technol.*, vol. 104, no. 5–8, pp. 2525–2538, 2019, doi: 10.1007/s00170-019-04061-x.

[53] X. Zhang, Y. Chen, and F. Liou, "Fabrication of SS316L-IN625 functionally graded materials by powder-fed directed energy deposition", *Sci. Technol. Weld. Join.*, vol. 24, no. 5, pp. 504–516, 2019, doi: 10.1080/13621718.2019.1589086.

[54] Y. Su, B. Chen, C. Tan, X. Song, and J. Feng, "Influence of composition gradient variation on the microstructure and mechanical properties of 316 L/Inconel718 functionally graded material fabricated by laser additive manufacturing", *J. Mater. Process. Technol.*, vol. 283, no. January, 2020, doi: 10.1016/j.jmatprotec.2020.116702.

[55] Y. Liu, F. Weng, G. Bi, Y. Chew, S. Liu, G. Ma and S. K. Moon, "Characterization of wear properties of the functionally graded material deposited on cast iron by laser-aided additive manufacturing", *Int. J. Adv. Manuf. Technol.*, vol. 105, no. 10, pp. 4097–4105, 2019, doi: 10.1007/s00170-019-03414-w.

[56] A. Thiriet, C. Schneider-Maunoury, P. Laheurte, D. Boisselier, and L. Weiss, "Multiscale study of different types of interface of a buffer material in powder-based directed energy deposition: Example of Ti6Al4V/Ti6Al4V - Mo/Mo - Inconel 718", *Addit. Manuf.*, vol. 27, no. February, pp. 118–130, 2019, doi: 10.1016/j.addma.2019.02.007.

[57] R. Ma, Z. Liu, W. Wang, G. Xu, and W. Wang, "Laser deposition melting of TC4/TiAl functionally graded material", *Vacuum*, vol. 177, no. April, p. 109349, 2020, doi: 10.1016/j.vacuum.2020.109349.

[58] R. Ma, Z. Liu, W. Wang, G. Xu, and W. Wang, "Microstructures and mechanical properties of Ti6Al4V-Ti48Al2Cr2Nb alloys fabricated by laser melting deposition of powder mixtures", *Mater. Charact.*, vol. 164, no. April, p. 110321, 2020, doi: 10.1016/j.matchar.2020.110321.

[59] D. Dai and D. Gu, "Thermal behavior and densification mechanism during selective laser melting of copper matrix composites: Simulation and experiments", *Mater. Des.*, vol. 55, pp. 482–491, 2014, doi: 10.1016/j.matdes.2013.10.006.

[60] T. N. Le and Y. L. Lo, "Effects of sulfur concentration and Marangoni convection on melt-pool formation in transition mode of selective laser melting process", *Mater. Des.*, vol. 179, p. 107866, 2019, doi: 10.1016/j.matdes.2019.107866.

[61] Y. S. Lee, M. Nordin, S. S. Babu, and D. F. Farson, "Influence of fluid convection on weld pool formation in laser cladding", *Weld. J.*, vol. 93, no. 8, 2014.

[62] Y. P. Lei, H. Murakawa, Y. W. Shi, and X. Y. Li, "Numerical analysis of the competitive influence of Marangoni flow and evaporation on heat surface temperature and molten pool shape in laser surface remelting", *Comput. Mater.*

Sci., vol. 21, no. 3, pp. 276–290, 2001, doi: 10.1016/S0927-0256(01)00143-4.

[63] B. Bocklund, L. D. Bobbio, R. A. Otis, A. M. Beese, and Z. K. Liu, "Experimental validation of Scheil–Gulliver simulations for gradient path planning in additively manufactured functionally graded materials", *Materialia*, vol. 11, no. April, 2020, doi: 10.1016/j.mtla.2020.100689.

[64] T. DebRoy, H. L. Wei, J. S. Zuback, T. Mukherjee, J. W. Elmer, J. O. Milewski, A. M. Beese, A. Wilson-Heid, A. De, W. Zhang, "Additive manufacturing of metallic components – Process, structure and properties", *Prog. Mater. Sci.*, vol. 92, pp. 112–224, 2018, doi: 10.1016/j.pmatsci.2017.10.001.

[65] A. Reichardt, A. A. Shapiro, R. Otis, R. P. Dillon, J. P. Borgonia, B. W. McEnerney, P. Hosemann and A. M. Beese, "Advances in additive manufacturing of metal-based functionally graded materials", *Int. Mater. Rev.*, vol. 0, no. 0, pp. 1–29, 2020, doi: 10.1080/09506608.2019.1709354.

[66] J. M. Drezet and S. Mokadem, "Marangoni Convection and Fragmentation in LASER Treatment", *Mater. Sci. Forum*, vol. 508, no. January 2006, pp. 257–262, 2006, doi: 10.4028/www.scientific.net/msf.508.257.

[67] L. Aucott, H. Dong, W. Mirihanage, R. Atwood, A. Kidess, S. Gao, S. Wen, J. Marsden, S. Feng, M. Tong, T. Connolley, M. Drakopoulos, C. R. Kleijn, I. M. Richardson, D. J. Browne, R. H. Mathiesen and H. V. Atkinson, "Revealing internal flow behaviour in arc welding and additive manufacturing of metals", *Nat. Commun.*, vol. 9, no. 1, pp. 1–7, 2018, doi: 10.1038/s41467-018-07900-9.

[68] E. Kannatey, *Materials Processing Principles of Laser*. 2009.

[69] M. Gharbi, P.Peyre, C. Gorny, M. Carin, S. Morville, P. Le Masson, D. Carron and R. Fabbro, "Influence of various process conditions on surface finishes induced by the direct metal deposition laser technique on a Ti-6Al-4V alloy", *J. Mater. Process. Technol.*, vol. 213, no. 5, pp. 791–800, 2013, doi: 10.1016/j.jmatprotec.2012.11.015.

[70] L. Song, G. Zeng, H. Xiao, X. Xiao, and S. Li, "Repair of 304 stainless steel by laser cladding with 316L stainless steel powders followed by laser surface alloying with WC powders", *J. Manuf. Process.*, vol. 24, pp. 116–124, 2016, doi: 10.1016/j.jmapro.2016.08.004.

[71] R. Acharya, J. A. Sharon, and A. Staroselsky, "Prediction of microstructure in laser powder bed fusion process", *Acta Mater.*, vol. 124, pp. 360–371, 2017, doi: 10.1016/j.actamat.2016.11.018.

[72] Z. Gan, H. Liu, S. Li, X. He, and G. Yu, "Modeling of thermal behavior and mass transport in multi-layer laser additive manufacturing of Ni-based alloy on cast iron", *Int. J. Heat Mass Transf.*, vol. 111, pp. 709–722, 2017, doi: 10.1016/j.ijheatmasstransfer.2017.04.055.

[73] Z. Zhang, P. Farahmand, and R. Kovacevic, "Laser cladding of 420 stainless steel with molybdenum on mild steel A36 by a high power direct diode laser", *JMADE*, vol. 109, pp. 686–699, 2016, doi: 10.1016/j.matdes.2016.07.114.

[74] Y. Lee, M. Nordin, S. S. Babu, and D. F. Farson, "Effect of Fluid Convection on Dendrite Arm Spacing in Laser Deposition", 2014, doi: 10.1007/s11663-014-0054-7.

[75] S. Bontha, N. W. Klingbeil, P. A. Kobryn, and H. L. Fraser, "Thermal process maps for predicting solidification microstructure in laser fabrication of thin-wall structures", *J. Mater. Process. Technol.*, vol. 178, no. 1–3, pp. 135–142, 2006, doi: 10.1016/j.jmatprotec.2006.03.155.

[76] J. C. Lippold, *Welding metallurgy and weldability*. 2014.

[77] E. Toyserkani, A. Khajepour, and S. Corbin, *Laser Cladding Laser Cladding*, vol. 11, no. 2. 2017.

[78] I. Hemmati, V. Ocelík, and J. T. M. De Hosson, "Microstructural characterization of AISI 431 martensitic stainless steel laser-deposited coatings", *J. Mater. Sci.*, vol. 46, no. 10, pp. 3405–3414, 2011, doi: 10.1007/s10853-010-5229-2.

[79] P. Guo, B. Zou, C. Huang, and H. Gao, "Study on microstructure, mechanical properties and machinability of efficiently additive manufactured AISI 316L stainless steel by high-power direct laser deposition", *J. Mater. Process. Technol.*, vol. 240, pp. 12–22, 2017, doi: 10.1016/j.jmatprotec.2016.09.005.

[80] X. Luo, J. Li, and G. J. Li, "Effect of NiCrBSi content on microstructural evolution, cracking susceptibility and wear behaviors of laser cladding WC/Ni-NiCrBSi composite coatings", *J. Alloys Compd.*, vol. 626, pp. 102–111, 2015, doi: 10.1016/j.jallcom.2014.11.161.

[81] C. Zeng, W. Tian, W. H. Liao, and L. Hua, "Microstructure and porosity evaluation in laser-cladding deposited Ni-based coatings", *Surf. Coatings Technol.*, vol. 294, pp. 122–130, 2016, doi: 10.1016/j.surfcoat.2016.03.083.

[82] Y. Chen, Q. Zhang, Z. Chen, L. Wang, J. Yao, and V. Kovalenko, "Study on the element segregation and Laves phase formation in the carbon nanotubes reinforced IN718 superalloy by laser cladding", *Powder Technol.*, vol. 355, pp. 163–171, 2019, doi: 10.1016/j.powtec.2019.07.063.

[83] J. J. Candel, V. Amigó, J. A. Ramos, and D. Busquets, "Sliding wear resistance of TiCp reinforced titanium composite coating produced by laser cladding", *Surf. Coatings Technol.*, vol. 204, no. 20, pp. 3161–3166, 2010, doi: 10.1016/j.surfcoat.2010.02.070.

[84] H. Kim, W. Cong, H. C. Zhang, and Z. Liu, "Laser engineered net shaping of nickel-based superalloy inconel 718 powders onto aisi 4140 alloy steel

substrates: Interface bond and fracture failure mechanism", *Materials (Basel).*, vol. 10, no. 4, 2017, doi: 10.3390/ma10040341.

[85] C. Huang, X. Lin, F. Liu, H. Yang, and W. Huang, "High strength and ductility of 34CrNiMo6 steel produced by laser solid forming", *J. Mater. Sci. Technol.*, vol. 35, no. 2, pp. 377–387, 2019, doi: 10.1016/j.jmst.2018.09.062.

[86] Y. Kakinuma, M. Mori, Y. Oda, T. Mori, M. Kashihara, A. Hansel and M. Fujishima, "Influence of metal powder characteristics on product quality with directed energy deposition of Inconel 625", *CIRP Ann. - Manuf. Technol.*, vol. 65, no. 1, pp. 209–212, 2016, doi: 10.1016/j.cirp.2016.04.058.

[87] A. Ramakrishnan and G. P. Dinda, "Direct laser metal deposition of Inconel 738", *Mater. Sci. Eng. A*, vol. 740–741, no. October 2018, pp. 1–13, 2019, doi: 10.1016/j.msea.2018.10.020.

[88] H. Xiao, S. Li, X. Han, J. Mazumder, and L. Song, "Laves phase control of Inconel 718 alloy using quasi-continuous-wave laser additive manufacturing", *Mater. Des.*, vol. 122, pp. 330–339, 2017, doi: 10.1016/j.matdes.2017.03.004.

[89] H. Xiao, S. M. Lia, W. J. Xiao, Y. Q. Lia, L. M. Cha, J. Mazumder and L. J. Song, "Effects of laser modes on Nb segregation and Laves phase formation during laser additive manufacturing of nickel-based superalloy", *Mater. Lett.*, vol. 188, no. November 2016, pp. 260–262, 2017, doi: 10.1016/j.matlet.2016.10.118.

[90] G. Singh, H. Vasudev, A. Bansal, S. Vardhan, and S. Sharma, "Microwave cladding of Inconel-625 on mild steel substrate for corrosion protection", *Mater. Res. Express*, vol. 7, no. 2, 2020, doi: 10.1088/2053-1591/ab6fa3.

[91] V. A. Popovich, E. V. Borisov, A. A. Popovich, V. S. Sufiiarov, D. V. Masaylo, and L. Alzina, "Functionally graded Inconel 718 processed by additive manufacturing: Crystallographic texture, anisotropy of microstructure and mechanical properties", *Mater. Des.*, vol. 114, pp. 441–449, 2017, doi: 10.1016/j.matdes.2016.10.075.

[92] H. Xie, K. Yang, F. Li, C. Sun, and Z. Yu, "Investigation on the Laves phase formation during laser cladding of IN718 alloy by CA-FE", *J. Manuf. Process.*, vol. 52, no. December 2019, pp. 132–144, 2020, doi: 10.1016/j.jmapro.2020.01.050.

[93] K. Yang, H. Xie, C. Sun, X. Zhao, and F. Li, "Influence of vanadium on the microstructure of IN718 alloy by laser cladding", *Materials (Basel).*, vol. 12, no. 23, pp. 1–12, 2019, doi: 10.3390/ma122333839.

[94] A. Yadollahi, N. Shamsaei, S. M. Thompson, and D. W. Seely, "Effects of process time interval and heat treatment on the mechanical and microstructural properties of direct laser deposited 316L stainless steel", *Mater. Sci. Eng. A*, vol. 644, pp. 171–183, 2015, doi: 10.1016/j.msea.2015.07.056.

[95] C. Tan, K. Zhou, and T. Kuang, "Selective laser melting of tungsten-copper functionally graded material", *Mater. Lett.*, vol. 237, pp. 328–331, 2019, doi: 10.1016/j.matlet.2018.11.127.

[96] E. O. Olakanmi, M. Sepako, J. Morake, S. E. Hoosain, and S. L. Pityana, "Microstructural Characteristics, Crack Frequency and Diffusion Kinetics of Functionally Graded Ti-Al Composite Coatings: Effects of Laser Energy Density (LED)", *Jom*, vol. 71, no. 3, pp. 900–911, 2019, doi: 10.1007/s11837-018-3272-7.

[97] G. Bidron, A. Doghri, T. Malot, F. Fournier-dit-Chabert, M. Thomas, and P. Peyre, "Reduction of the hot cracking sensitivity of CM-247LC superalloy processed by laser cladding using induction preheating", *J. Mater. Process. Technol.*, vol. 277, no. January 2019, p. 116461, 2020, doi: 10.1016/j.jmatprotec.2019.116461.

[98] U. Savitha, G. Jagan Reddy, A. Venkataramana, A. Sambasiva Rao, A. A. Gokhale, and M. Sundararaman, "Chemical analysis, structure and mechanical properties of discrete and compositionally graded SS316-IN625 dual materials", *Mater. Sci. Eng. A*, vol. 647, pp. 344–352, 2015, doi: 10.1016/j.msea.2015.09.001.

[99] R. M. Mahamood and E. T. Akinlabi, "Laser metal deposition of functionally graded Ti6Al4V/TiC", *Mater. Des.*, vol. 84, pp. 402–410, 2015, doi: 10.1016/j.matdes.2015.06.135.

[100] L. Li, J. Wang, P. Lin, and H. Liu, "Microstructure and mechanical properties of functionally graded TiCp/Ti6Al4V composite fabricated by laser melting deposition", *Ceram. Int.*, vol. 43, no. 18, pp. 16638–16651, 2017, doi: 10.1016/j.ceramint.2017.09.054.

[101] J. Zhang, Y. Zhang, W. Li, S. Karnati, F. Liou, and J. Newkirk, "Microstructure and properties of functionally graded materials Ti6Al4V/TiC fabricated by direct laser deposition", *Rapid Prototyp. J.*, vol. 10, no. 1, pp. 5–6, 2004.

[102] L. D. Bobbio, R. A. Otis, J. P. Borgonia, R. P. Dillon, A. A. Shapiro, Z. Liu and A. M. Beese, "Additive manufacturing of a functionally graded material from Ti-6Al-4V to Invar: Experimental characterization and thermodynamic calculations", *Acta Mater.*, vol. 127, pp. 133–142, 2017, doi: 10.1016/j.actamat.2016.12.070.

[103] S. N. Li, H. P. Xiong, N. Li, B. Q. Chen, C. Gao, W. J. Zou and H. S. Ren, "Mechanical properties and formation mechanism of Ti/SiC system gradient materials fabricated by in-situ reaction laser cladding", *Ceram. Int.*, vol. 43, no. 1, pp. 961–967, 2017, doi: 10.1016/j.ceramint.2016.10.026.

Article 2 - Effects of Processing Parameters on Functionally Graded Materials for Industrial Components Repair

Modern Concepts in Material Science

DOI: 10.33552/MCMS.2021.04.000583

ISSN: 2692-5397

Modern Concepts in Material Science

DOI: 10.33552/MCMS.2021.04.000583

Iris Publishers

Mini Review

Effects of Processing Parameters on Functionally Graded Materials for Industrial Components Repair

André Alves Ferreira[1,2]*, Ana Rosanete Reis[1,2], João Manuel Cruz[3] and Manuel Fernando Vieira[1,2]*

[1]*Faculty of Engineering of the University of Porto, R. Dr. Roberto Frias, Portugal*

[2]*LAETA/INEGI - Institute of Science and Innovation in Mechanical and Industrial Engineering, R. Dr. Roberto Frias, Portugal*

[3]*SERMEC-Group, R. de Montezelo 540, Portugal*

Article 2 - Effects of Processing Parameters on Functionally Graded Materials for Industrial Components Repair

André Alves Ferreira[1,2*], Ana Rosanete Reis[1,2], João Manuel Cruz[3], Manuel Fernando Vieira[1,2*]

[1]Faculty of Engineering of the University of Porto

[2]LAETA/INEGI—Institute of Science and Innovation in Mechanical and Industrial Engineering

[3]SERMEC-Group

*Correspondence: André Alves Ferreira; Manuel Fernando Vieira

Abstract

The production of functional gradient materials (FGM) is an option for the various industrial sectors and a solution for many engineering applications, including components repair. FGM's are a class of materials that can also be characterized as metal composites that gradually change composition and structure, where the properties are not uniform throughout the material, depending on the spatial position in the bulk structure of the material. This article is a brief approach presenting FGM as new material and emphasizing the processing parameters and optimization.

Keywords: additive manufacturing; functionally graded material; direct laser deposition; optimization.

Abbreviations: FGM: Functionally Graded Materials; FGAM: Functionally Graded Additive Manufacturing; AM: Additive Manufacturing; SEM: Scanning Electron Microscopy; BSE: Backscattered Electrons; DLD: Direct Laser Deposition; CTE: Coefficient of Thermal Expansion

Mini-Review

Functionally Graded Materials (FGMs) are a particular class of metal composites with a spatial variation of properties along a specific direction. By choosing the FGMs, one can meet material requirements impossible to be achieved other than in this way. Among the FGMs advantages, one can cite: (1) connection of two complex and incompatible materials, thereby improving the bond strength; (2) diminishing of the internal residual stresses; and (3) reduction of the crack driving force developed within the materials [1].

In recent years, Additive Manufacturing (AM) technologies evolved from making conceptual prototypes to creating full-scale end-use components. The technological advancement of AM systems associated with the FGM approach led some authors to coin the term Functionally Graded Additive Manufacturing (FGAM). This layer-by-layer fabrication technique involves gradationally varying the material organization within a component to meet an intended function [2]. Figure 1 illustrates a higher magnification of FGM and the compositional transition regions. In the same plane of the image, a continuous chemical composition gradient is observed throughout the FGM.

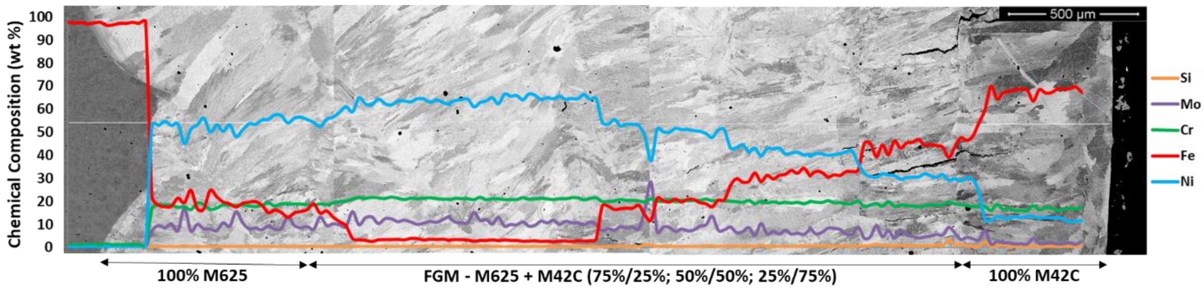

Figure 1. SEM/BSE obtained microstructural evolution along the longitudinal section of the FGM sample and in the same plane the linear chemical analysis (EDX). M625 – Nickel-based superalloy (Inconel 625); M42C – Martensitic Stainless Steel (SS 431).

According to the manufacturing processes, FGM's can be divided into constructing the non-homogeneous structure, also called "gradation" and transforming this structure into a bulk material, called "consolidation". The gradation is subdivided into constitutive, homogenizing and segregating processes. Constitutive use powders as precursors for gradual construction of FGM's structure. Homogenization is related to the transport and mixing of two or more materials. Segregation is when the material starts homogeneous and is later converted into a gradient due to a change in the feeding rate. The homogenization and segregation processes produce continuous gradients but limit the types of gradients produced [3].

The main limitations in FGMs are related to thermal and mechanical stresses where analyses are performed using the laminate composites theory. The properties of materials are, however, continuous position functions, and therefore, there are some objections to the analogy of materials functionally classified as composites [4], [5].

Additive Manufacturing (AM) becomes an important approach to build Metallic FGMs [6]. Metallic FGMs consists of two (or more) different metals, or their alloys, combined into a melt pool generated by a heat source. In FGMs produced by Direct Laser Deposition (DLD), an AM process widely used in metallic materials, a laser is used as the energy input. DLD has the advantage of local synthesizing of alloys by mixing different powders with the desired composition. By gradually varying the mixing at various locations, parts with graded material properties can be generated using DLD [7].

The newest DLD machines may have up to four nozzles (or more) with inert gas protection, allowing different combinations of alloys and minimizing the oxidization resulting from the elevated temperature on metal processing. The laser plays an essential role in DLD, and its development in terms of power and efficiency has impacted the growth of metal AM technologies. However, besides the laser choice, one must consider several other parameters during DLD, named: substrate, laser power, speed scanning; laser scanning pattern; laser beam diameter; hatch spacing; powder feed rate; powders composition, powder gradient variation, and preheating conditions [7], [8]. The selection of processing conditions that ensures a clad without defects, bonded to the substrate and with good material yield, is an essential and challenging task because the various variables interact. Their simultaneous optimization is difficult because they often act in opposite directions.

Hereupon, even though DLD appears as a real practical option for Metallic FGMs manufacturing, the inherent processes complexity must be adequately addressed. It is known that laser deposited materials experience complicated thermal history, presenting rapid solidification, high cooling rates, steep thermal gradients, and cyclic reheating and cooling. These phenomenons produce non-equilibrium microstructures and significant variations in structure from layer to layer and within individual layers. Furthermore, the final microstructure and properties are intimately connected to the cited process parameters that must be optimized on a material-specific basis [9], [10].

In fact, producing FGMs requires understanding thermal and thermophysical properties: coefficient of thermal expansion (CTE), melting temperature, and thermal conductivity. The inequality in the heat flow is due to its faster dissipation at the material interface that presents higher thermal conductivity, resulting in distortion and the possibility of lack of fusion in the material with lower thermal conductivity, promoted by insufficient heat [11].

High residual stresses in FGMs can be due to the thermal expansion differences and to lattice misfit. In DLD, the extremely high thermal gradient enhances thermal stresses; these are related to the expansion of the melting pool and the contraction during rapid cooling [12]. These mismatches can arise between the FGM first layers and the substrate and through the FGM, causing cracks or interfacial delamination between the clad and the substrate or between the FGM layers. The distribution of these stresses is highly dependent on the substrate and the FGM materials and can be tensile on the substrate and compressive on the FGM or vice versa.

However, experimental and numerical results have proven that increasing the number of layers with a composition gradient reduces the CTEs difference, and lattice misalignment can minimize this effect [13], [14]. The thickness and composition of each layer are also critical factors in the residual stress profile [15]. Processing conditions are also determinant in the magnitude of residual stresses, particularly important in processes such as DLD in which thermal energy is quickly transferred to the cold substrate.

However, to relieve the residual stresses in FGM's, the preheat treatment is a solution that reduces the cooling rate of both the substrate and the cladding, preventing the formation of fragile phases in the bonding area and gradient, minimizing the likelihood of crack formation. Preheating is also essential in controlling thermal gradients between the substrate and the deposited layers by decreasing the cooling rate and residual stresses [16], [17] and attenuating the difference in thermal expansion coefficients between the several powders [18], thus inhibiting the formation of cracks and promoting better mechanical properties. Preheated substrates present a lower susceptibility cracks formation, decreasing the cooling rate and formation of residual stresses, promoting the hardness reduction and residual stress [19]–[22].

One procedure that promotes reducing residual stresses and defects, such as cracks, is preheating the substrate and the maintenance of this preheating during the deposition process [23]. Preheating also inhibits the formation of harmful phases such as eutectics and borides [24], thus reducing defects in FGMs. Preheating is also essential in controlling thermal gradients between the substrate and the deposited layers by decreasing the cooling rate and residual stresses [16], [17] and attenuating the difference in thermal expansion coefficients between the several powders [18], thus inhibiting the formation of cracks and promoting better mechanical properties.

Additive manufacturing, specifically DLD technology, brings the opportunity of an alternative and flexible process, enabling the production and repair of components with this type of functionality, either in bulk, through the deposition of several layers, or on the surface, depositing few layers [3], [25].

Meanwhile, this technique can create near net shape parts from powder or wire, melting them into the desired geometry, ensuring excellent bonding and metallurgical properties [26]–[29]. Due to its geometric freedom, scalability, and adaptability to distinct scenarios, which other metals AM technologies cannot offer, DLD is often used to produce complex and custom parts and coating/repairing of metal components [8], [30], [31]. Yet, the greatest advantage of this technology is the possibility of processing several materials in the same operation, granted with several powder feeders. Therefore, this technology can be assumed to be a multi-material/graded deposition method. It can simultaneously use different powders, enabling the deposition of distinct materials in consequent layers or combining different amounts of material in each layer.

Funding

This research was funded by FEDER through the Operational Programme for Competitiveness and Internationalization (COMPETE 2020), Projetos em Copromoção (project POCI-01-0247-FEDER-039848).

Acknowledgements

The authors are grateful to CEMUP (Centro de Materiais da Universidade do Porto) for expert assistance with SEM.

Conflicts of Interest

The authors declare no conflict of interest.

References

[1] D. T. Sarathchandra, S. Kanmani Subbu, and N. Venkaiah, "Functionally graded materials and processing techniques: An art of review," *Mater. Today Proc.*, vol. 5, no. 10, pp. 21328–21334, 2018, doi: 10.1016/j.matpr.2018.06.536.

[2] G. H. Loh, E. Pei, D. Harrison, and M. D. Monzón, "An overview of functionally graded additive manufacturing," *Addit. Manuf.*, vol. 23, no. May, pp. 34–44, 2018, doi: 10.1016/j.addma.2018.06.023.

[3] B. Kieback, A. Neubrand, and H. Riedel, "Processing techniques for functionally graded materials," *Mater. Sci. Eng. A*, vol. 362, no. 1–2, pp. 81–106, 2003, doi: 10.1016/S0921-5093(03)00578-1.

[4] M. Jabbari, S. Sohrabpour, and M. R. Eslami, "General solution for mechanical and thermal stresses in a functionally graded hollow cylinder due to

nonaxisymmetric steady-state loads," *J. Appl. Mech. Trans. ASME*, vol. 70, no. 1, pp. 111–118, 2003, doi: 10.1115/1.1509484.

[5] D. Dai and D. Gu, "Thermal behavior and densification mechanism during selective laser melting of copper matrix composites: Simulation and experiments," *Mater. Des.*, vol. 55, pp. 482–491, 2014, doi: 10.1016/j.matdes.2013.10.006.

[6] L. Yan, Y. Chen, and F. Liou, "Additive manufacturing of functionally graded metallic materials using laser metal deposition," *Addit. Manuf.*, vol. 31, no. November 2019, p. 100901, 2020, doi: 10.1016/j.addma.2019.100901.

[7] R. M. Mahamood, *Laser Metal Deposition of Metals and Alloys*. 2018.

[8] S. M. Thompson, L. Bian, N. Shamsaei, and A. Yadollahi, "An overview of Direct Laser Deposition for additive manufacturing; Part I: Transport phenomena, modeling and diagnostics," *Addit. Manuf.*, vol. 8, pp. 36–62, 2015, doi: 10.1016/j.addma.2015.07.001.

[9] L. Costa, "Laser powder deposition," vol. 4, no. January, pp. 264–279, 2009, doi: 10.1108/13552540910979785.

[10] A. Reichardt, "Additive Manufacturing of Metal-based Functionally Graded Materials by Ashley Reichardt A dissertation submitted in partial satisfaction of the requirements for the degree of Doctor of Philosophy in Engineering – Nuclear Engineering in the Graduate Divisi," 2017.

[11] A. Reichardt, "Additive Manufacturing of Metal-based Functionally Graded Materials. UC Berkeley. ProQuest ID: Reichardt_berkeley_0028E_17635. Merritt ID: ark:/13030/m5zh1phm. Retrieved from https://escholarship.org/uc/item/32h5c2vp," 2017, [Online]. Available: https://escholarship.org/uc/item/32h5c2vp.

[12] S. Zhou, X. Zeng, Q. Hu, and Y. Huang, "Analysis of crack behavior for Ni-based WC composite coatings by laser cladding and crack-free realization," *Appl. Surf. Sci.*, vol. 255, no. 5 PART 1, pp. 1646–1653, 2008, doi: 10.1016/j.apsusc.2008.04.003.

[13] A. Bhattacharyya and D. Maurice, "Residual stresses in functionally graded thermal barrier coatings," *Mech. Mater.*, vol. 129, no. November 2018, pp. 50–56, 2019, doi: 10.1016/j.mechmat.2018.11.002.

[14] X. C. Zhang, B. S. Xu, H. D. Wang, Y. Jiang, and Y. X. Wu, "Modeling of thermal residual stresses in multilayer coatings with graded properties and compositions," *Thin Solid Films*, vol. 497, no. 1–2, pp. 223–231, 2006, doi: 10.1016/j.tsf.2005.09.184.

[15] K. Z. Uddin and B. Koohbor, "Gradient optimization of transversely graded Ti-

TiB structures for enhanced fracture resistance," *Int. J. Mech. Sci.*, vol. 187, no. June, p. 105917, 2020, doi: 10.1016/j.ijmecsci.2020.105917.

[16] G. Bidron, A. Doghri, T. Malot, F. Fournier-dit-Chabert, M. Thomas, and P. Peyre, "Reduction of the hot cracking sensitivity of CM-247LC superalloy processed by laser cladding using induction preheating," *J. Mater. Process. Technol.*, vol. 277, no. January 2019, p. 116461, 2020, doi: 10.1016/j.jmatprotec.2019.116461.

[17] A. Sadhu *et al.*, "A study on the influence of substrate preheating on mitigation of cracks in direct metal laser deposition of NiCrSiBC-60%WC ceramic coating on Inconel 718," *Surf. Coatings Technol.*, vol. 389, no. March, p. 125646, 2020, doi: 10.1016/j.surfcoat.2020.125646.

[18] R. Ma, Z. Liu, W. Wang, G. Xu, and W. Wang, "Microstructures and mechanical properties of Ti6Al4V-Ti48Al2Cr2Nb alloys fabricated by laser melting deposition of powder mixtures," *Mater. Charact.*, vol. 164, no. April, p. 110321, 2020, doi: 10.1016/j.matchar.2020.110321.

[19] C. Ding, X. Cui, J. Jiao, and P. Zhu, "Effects of substrate preheating temperatures on the microstructure, properties, and residual stress of 12CrNi2 prepared by laser cladding deposition technique," *Materials (Basel).*, vol. 11, no. 12, 2018, doi: 10.3390/ma11122401.

[20] K. Dai, X. X. Li, and L. L. Shaw, "Comparisons between thermal modeling and experiments: Effects of substrate preheating," *Rapid Prototyp. J.*, vol. 10, no. 1, pp. 24–34, 2004, doi: 10.1108/13552540410512507.

[21] B. Zheng, Y. Zhou, J. E. Smugeresky, J. M. Schoenung, and E. J. Lavernia, "Thermal behavior and microstructural evolution during laser deposition with laser-engineered net shaping: Part I. Numerical calculations," *Metall. Mater. Trans. A Phys. Metall. Mater. Sci.*, vol. 39, no. 9, pp. 2228–2236, 2008, doi: 10.1007/s11661-008-9557-7.

[22] A. A. Ferreira, R. Darabi, J. P. Sousa, J. M. Cruz, A. R. Reis, and M. F. Vieira, "Optimization of direct laser deposition of a martensitic steel powder (Metco 42c) on 42crmo4 steel," *Metals (Basel).*, vol. 11, no. 4, pp. 1–18, 2021, doi: 10.3390/met11040672.

[23] A. Thiriet, C. Schneider-Maunoury, P. Laheurte, D. Boisselier, and L. Weiss, "Multiscale study of different types of interface of a buffer material in powder-based directed energy deposition: Example of Ti6Al4V/Ti6Al4V - Mo/Mo - Inconel 718," *Addit. Manuf.*, vol. 27, no. February, pp. 118–130, 2019, doi: 10.1016/j.addma.2019.02.007.

[24] A. Ramakrishnan and G. P. Dinda, "Direct laser metal deposition of Inconel 738," *Mater. Sci. Eng. A*, vol. 740–741, no. October 2018, pp. 1–13, 2019, doi:

10.1016/j.msea.2018.10.020.

[25] R. M. Mahamood and E. T. Akinlabi, *Laser Additive Manufacturing*. .

[26] A. Saboori, G. Piscopo, M. Lai, A. Salmi, and S. Biamino, "An investigation on the effect of deposition pattern on the microstructure, mechanical properties and residual stress of 316L produced by Directed Energy Deposition," *Mater. Sci. Eng. A*, vol. 780, no. March, p. 139179, 2020, doi: 10.1016/j.msea.2020.139179.

[27] W. Paatsch, "Energy turnaround - a challenge for surface technology," *Trans. {IMF}*, vol. 94, no. 5, pp. 228–230, 2016, doi: 10.1080/00202967.2016.1209295.

[28] Y. Gao, D. Xiong, C. Wang, and Y. Chen, "Influences of laser powers on microstructure and properties of the coatings on the AZ91HP magnesium alloy," *Acta Metall. Sin. (English Lett.*, vol. 22, no. 3, pp. 167–173, 2009, doi: https://doi.org/10.1016/S1006-7191(08)60085-X.

[29] J. Chen, S.-H. Wang, and L. Xue, "On the development of microstructures and residual stresses during laser cladding and post-heat treatments," *J. Mater. Sci.*, vol. 47, no. 2, pp. 779–792, 2012, doi: 10.1007/s10853-011-5854-4.

[30] E. P. Cardozo, G. R. Pardal, S. Ríos, S. Ganguly, and A. S. C. M. D'oliveira, "Additive techniques to refurbish Ni based components," *Soldag. e Insp.*, vol. 24, pp. 1–11, 2019, doi: 10.1590/0104-9224/SI24.03.

[31] Q. Guo, S. Chen, M. Wei, J. Liang, C. Liu, and M. Wang, "Formation and Elimination Mechanism of Lack of Fusion and Cracks in Direct Laser Deposition 24CrNiMoY Alloy Steel," *J. Mater. Eng. Perform.*, vol. 29, no. 10, pp. 6439–6454, 2020, doi: 10.1007/s11665-020-05163-4.

Chapter 3

PROCESSING CONDITIONS FOR MARTENSITIC STEEL POWDER (METCO 42C) AND NICKEL-BASED SUPERALLOY (METCOCLAD 625) DEPOSITION ON LOW ALLOY STRUCTURAL STEEL

Article 3 - Optimization of Direct Laser Deposition of a Martensitic Steel Powder (Metco 42C) on 42CrMo4 Steel

METALS

https://doi.org/10.3390/met11040672

metals

Article

Optimization of Direct Laser Deposition of a Martensitic Steel Powder (Metco 42C) on 42CrMo4 Steel

André A. Ferreira [1,2,*], Roya Darabi [1,2], João P. Sousa [2], João M. Cruz [3], Ana R. Reis [1,2] and Manuel F. Vieira [1,2,*]

Article 3 - Optimization of Direct Laser Deposition of a Martensitic Steel Powder (Metco 42C) on 42CrMo4 Steel

André A. Ferreira [1,2,*], Roya Darabi [1,2], João P. Sousa [2], João M. Cruz [3], Ana R. Reis [1,2] and Manuel F. Vieira [1,2,*]

[1]Faculty of Engineering of the University of Porto, 4200-465 Porto, Portugal; darabi@inegi.up.pt (R.D.); areis@inegi.up.pt (A.R.R.)

[2]LAETA/INEGI—Institute of Science and Innovation in Mechanical and Industrial Engineering, 4200-465 Porto, Portugal; jpsousa@inegi.up.pt

[3]SERMEC-Group, 4425-348 Folgosa-Maia, Portugal; joaocruz@sermecgroup.pt

*Correspondence: andreferreira@fe.up.pt (A.A.F.); mvieira@fe.up.pt (M.F.V.); Tel.: +3519-1046-1480 (A.A.F.)

Abstract

In this study, the deposition of martensitic stainless-steel (Metco 42C) powder on 42CrMo4 structural steel by direct laser deposition (DLD) was investigated. Clads were produced by varying the laser power, scanning speed, feed rate, and preheating. The effect of these processing variables on the microstructure and microhardness of the clads was analyzed, as well as their soundness, yield (measured by dilution), and geometric characteristics (height, width, and depth). The complex interaction of the evaluated processing variables forced the application of complex parameters to systematize their effect on the clads. A genetic optimization algorithm was performed to determine the processing conditions warranting high-quality clads, that is, sound clads, metallurgically bonded to the substrate with required deposition yield.

Keywords: direct laser deposition; microstructure; EBSD; martensitic stainless steel; preheating; optimization

Introduction

Direct Laser Deposition (DLD) is one of the laser-based additive manufacturing (LBAM) processes investigated for additive metal part manufacture, repair, and reconstruction. DLD uses a laser beam as an energy source to melt metallic powders, manufacture parts layer by layer, and repair or cladding components by depositing one or a few layers. This technique has many advantages compared to conventional processes, such as arc welding, due to the production of better bead/layers with the controlled thermal distribution, promoting a lower heat-affected zone (HAZ), less dilution, minimum distortion, and better surface quality, which ensures a superior resistance to wear and corrosion [1–4].

The repair/remanufacturing of metallic components is one of the main applications of DLD. The use of suitable addition materials and process parameters allows the production of precise, durable, and high-quality repairs with properties similar or superior to those of the substrate, contributing to sustainable industrial development. The deposited layers have excellent metallurgical bonding, the heat-affected zone (HAZ) is small with adequate heat transfer control, dilution is minimal (evaluated through the extension of the remelted region with mixing between cladding and substrate materials) and allows localized repair of parts in difficult-to-reach places [5–8]. Moreover, innovative material systems can be used to produce complex components in which the chemical composition of the individual layers is gradually changed, adjusting them to the desired properties of the component [9].

Due to its characteristics, DLD is one of the most attractive and competitive component repair processes, being applied in industrial sectors as diverse as aeronautics, petrochemical (offshore), energy, transport, and defense, among others. Examples of products that can be repaired by DLD include gearboxes, gears, blowers, combustion engine parts, couplings, pumps, shafts, turbine parts, and rollers [10].

The geometry of the cladding (height, depth, and length) is directly related to physical phenomena, such as the Marangoni effect in the melt pool, which results from the interaction of the laser beam with the powder and the substrate [10,11]. Several studies correlated the thermal effects, in the melt pool and in the heat-affected zone (HAZ), with the structure and the mechanical and tribological properties of the laser cladding [12–14]. Although theoretical and experimental studies have developed relevant information about DLD, there are still many challenges, such as process optimization, 3D reconstruction of highly complex structures, and substrate preheating, which need to be clarified.

The laser processing parameters, laser power, scanning speed, and feed rate, directly correlate with melt pool geometry, strongly influencing claddings properties. Of the most important processing parameters in DLD processes, the laser power has the largest influence on melt pool size, with its size increasing almost linearly with laser power [15]. There is no formation of the melt pool for low laser power and high feed rate due to the absorption of the laser beam energy by the powder particles. However, for low feed rate and high laser power, significant melting of the substrate occurs, which compromises the cladding properties [16–18]. The laser power also significantly affects the HAZ [19]. The scanning speed and the powder feed rate have an interactive effect on the melt pool geometry and the HAZ, weakening the primary impact of laser power [15,19,20]. However, the interaction among the processing parameters is highly affected by the characteristics of the powder/substrate system.

DLD still has a way to go for broader industrial sectors. The application of wear-resistant steel beads on substrates of low and medium carbon steels is an aspect that may be extensively used, either in component repair or in its cladding with a more resistant layer. The use of steel entails a careful analysis of the processing conditions. The high cooling rates that are characteristic of this process, due to the localized heat inputs by the laser beam, are responsible for metallurgical defects associated with metastable phases both in the deposited material and in the HAZ. Preheating (PHT) of the substrate is one of the processes able to reduce the cooling rate. PHT decreases hardness in HAZ [9], reduces the sharp thermal gradients [3], and increases the laser absorption rate by the substrate, improving the stress distribution and preventing the formation of hard structures that are harmful to the mechanical properties of the cladding [11]. As the best knowledge of authors, few studies in the literature on these steel/steel systems correlate the process parameters with the dilution, structure, and hardness of the cladding and base materials [21–27]. In these studies, the influence of processing conditions on wear resistance and corrosion of the clads produced was also analyzed.

In this study, martensitic stainless-steel powder, type AISI 431, was deposited on 42CrMo4 steel, varying the process parameters, with and without performing preheating. 42CrMo4 steel is often used to produce components, such as gears and main-shafts, and martensitic steel powder 431 is used in the repair/remanufacturing of these components by the SERMEC-Group. Single clad tracks were formed to evaluate the metallurgical and mechanical characteristics of the deposits. The influence of several process parameters, such as laser power, scanning speed, powder feed rate, and preheating, was analyzed to achieve the desired clad quality without cracking and structural imperfections. A genetic algorithm was used to optimize the height, depth, and dilution values and overcome the complex nature of the effects of the involved parameters on each other. Strategies were developed to guarantee the compatibility and the metallurgical bond between cladding and substrate, taking into account avoiding the structural defects like cracks, and exploring synergies between the properties of the utilized materials.

Materials and Methods

Water atomized martensitic stainless-steel powder (Metco 42C), similar to AISI 431, was used for deposition. Scanning electron microscopy (SEM) images show powder particles have an irregular (non-spheroidal) morphology with particles size range between 45 to 106 μm (Figure 1).

42CrMo4 steel was utilized as the substrate for depositions. 42CrMo4 is medium carbon steel with excellent fatigue and impact resistance, high mechanical strength and toughness, and good machinability. This material is classified as a low-alloy structural steel type and has a widespread application in manufacturing critical industrial components, such as gears, automotive parts, drilling joints for deep wells, and wind generators [28,29]. Its mechanical and chemical properties are described in standard EN 10269 [30]. Chemical analysis of the Metco 42C powder and 42CrMo4 steel are shown in Table 1.

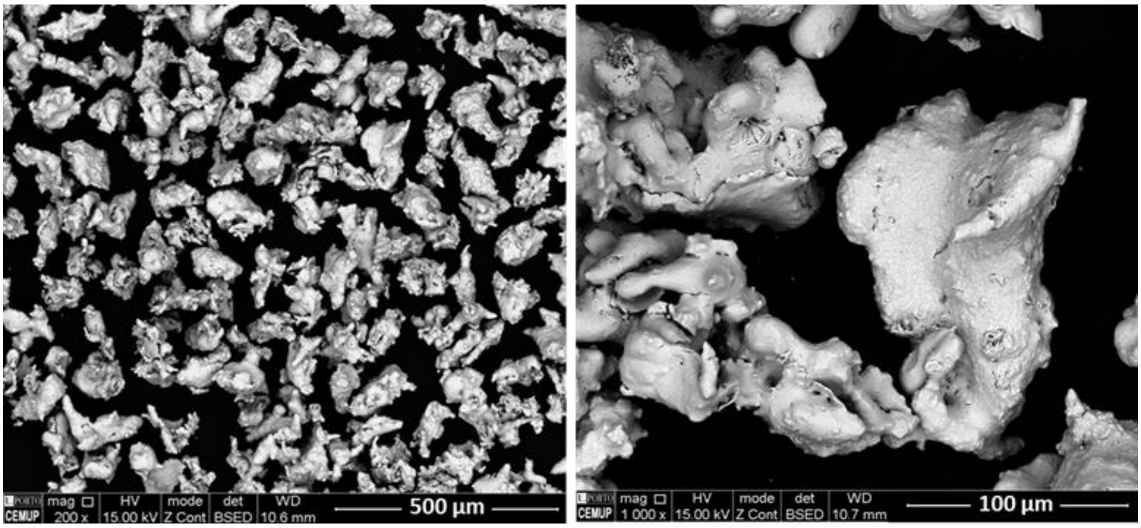

Figure 1. Scanning electron microscopy (SEM) images of martensitic stainless-steel powder (Metco 42C).

Table 1. Chemical composition of Metco 42C and 42CrMo4 steel (wt. %).

Materials	C	Cr	Ni	Mn	Mo	Si	P	S	Fe
Metco 42C	0.18	17.3	1.9	-	-	2.1	-	-	Bal.
42CrMo4	0.42	1.11	-	0.67	0.19	0.28	0.025	0.015	Bal.

Before deposition, the substrates were cleaned with pure acetone and preheated to approximately 300 °C by oxy torch, to decrease the cooling rate in melt pool and HAZ regions and eliminate moisture. The temperature was selected following welding practices for 42CrMo4 steel and controlled with a digital pyrometer gauge. The effect of preheating treatment (PHT) on microstructures, grain size, and formation of metastable phases (martensite) was evaluated.

The DLD machine consists of a modular coaxial processing head (Figure 2) and equipped with a fibre-coupled laser diode, model Laserline LDF 3000–100, with a nominal beam power of 6000 W. The powder nozzle is mounted on a KUKA KR 90 R3100 industrial robot, with six axes connected to the robot control unit.

The data of experiments was aquired through changes in the following parameters: laser power, scanning speed, powder feed rate, and preheating (PHT) as can be seen in Table 2. The terminology M_P_SS_FR was used to identify the samples, being: M—powder Metco 42C; P—laser power (kW); SS—scanning speed (mm/s); FR—feed rate (g/min). Then, the feed-driven results from experiments were employed on the implementation of the Genetic algorithm in order to the optimization of the process.

In all the tests, a spot size of 2.5 mm, and an offset in the *Z*-axis of 0.2 mm were applied. High purity argon (99.99%), with a 5.5 L/min flow rate, was used as the shielding gas to prevent contamination and oxidation of the melt pool during the DLD process. Samples with and without PHT were cooled in air.

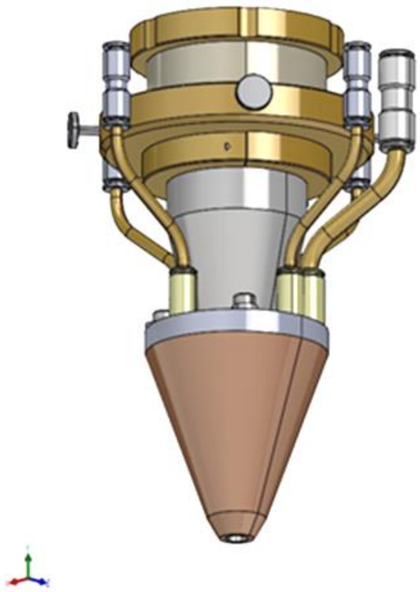

Figure 2. Coaxial configuration for powder feed.

Table 2. Samples and parameters used to optimize the DLD process.

Sample	P (kW)	SS (mm/s)	FR (g/min)
M_1_2_15	1	2	15
M_1_6_15	1	6	15
M_1.5_10_10	1.5	10	10
M_1.5_10_15	1.5	10	15
M_2_2_15	2	2	15
M_2_4_15	2	4	15
M_2_6_10	2	6	10
M_2_6_15	2	6	15
M_2_6_20	2	6	20
M_2_10_10	2	10	10
M_2_10_15	2	10	15
M_2.5_10_10	2.5	10	10
M_2.5_10_15	2.5	10	15
M_3_2_15	3	2	15
M_3_4_15	3	4	15
M_3_6_10	3	6	10
M_3_6_15	3	6	15
M_3_6_20	3	6	20

Samples from each deposition were cut for microstructural and mechanical characterization using a metallographic cut-off machine with refrigeration, to avoid substrate and cladding overheating. Samples were mounted in resin and polished down to 1 μm diamond suspension, and Kalling's No. 2 chemical etching ($CuCl_2$—5 g, Hydrochloric acid —100 mL, Ethanol—100 mL) was used to reveal the microstructures. The measurements of height, depth and width of the claddings produced by the DLD technique were performed using a Leica DVM6 A 2019 digital microscope (DM) (Wetzlar, Germany). Leica DM 4000M optical microscope (OM) (Wetzlar, Germany) was used for the microstructural characterization of samples. OM analysis at low magnifications allows a global characterization of clads to evaluate, for example, the size of the heat-affected zone.

A scanning electron microscope (FEI Quanta 400 FEG ESEM, Hillsboro, OR, USA) equipped with Energy Dispersive X-Ray Spectroscopy (EDX) (EDAX Genesis X4M, Oxford Instrument, Oxfordshire, UK) and Electron backscatter diffraction (EBSD)

(EDAX-TSL OIM EBSD, Mahwah, NJ, USA) units, was used for higher magnification observation and phase identification.

For EBSD evaluation, samples went through an additional polishing step, using a 0.06 μm silica colloidal suspension, for a superior surface finish and removal of polishing induced plastic deformation. This additional polishing is essential for obtaining Kikuchi patterns [31]. The EBSD allows obtaining information on microstructural characteristics with a small volume of interaction and high resolution. For all raw data, a dilatation clean-up routine was performed, with a grain tolerance angle of 15° and minimum grain size of 10 points, to avoid any spurious results from the incorrectly indexed patterns.

Vickers microhardness tests made the mechanical characterization. The tests were performed using a test force of 300 g for 15 s in a Struers Duramin 5 Vickers hardness tester. Each hardness value corresponds to the average of three indentations.

Results

Microstructural and Mechanical Characterization

The deposited clads characterization started with a macrographic observation to evaluate the effect of the processing conditions on the substrate and, mainly, on the geometry of the clad, its dilution, and eventual cracking (Figure 3). Different regions of this layer can be observed in Figure 3, such as the cladding layer (CL), the fusion line (FL), and the heat-affected zone (HAZ). The claddings produced must be strongly bonded to the substrate and free of discontinuities and cracks and must not induce them in the HAZ of the substrate.

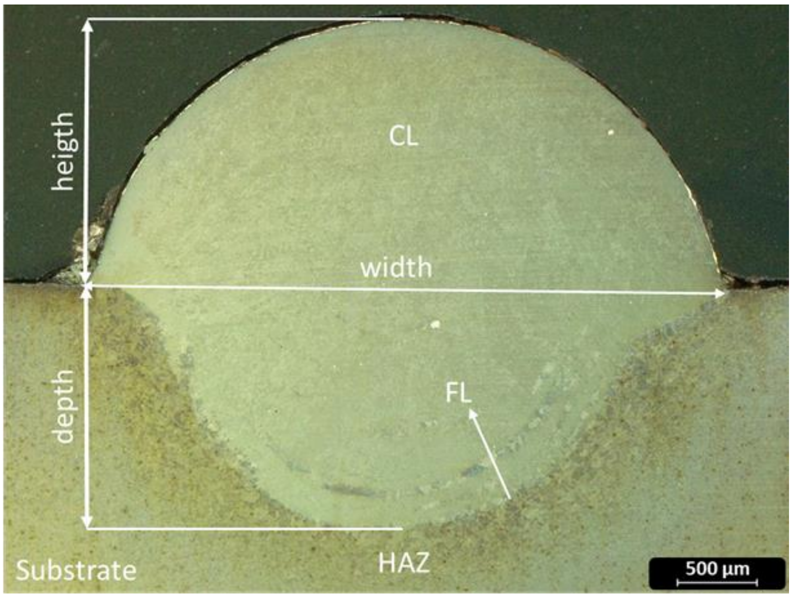

Figure 3. Optical microscopy image showing the morphology of a single-track clad produced by the DLD technique depositing Metco 42C powder on a 42CrMo4 steel substrate. CL—Cladding Layer; FL—Fusion Line; HAZ—Heat-affected Zone.

DM images allow the measurement of the clad (AC) and melting (AM) areas using ImageJ software. Tables 3 and 4 show the measurements made by DM of the length, height, and depth of the clad layers, for conditions with and without PHT, respectively.

The microstructure of a clad deposited by the DLD process (Figure 4) is typical of this laser process, showing a thin zone of planar growth composed of equiaxed grains (EG) close to the fusion line that are replaced by dendrites (D) in the central region of the clad area. This microstructure is directly related to the process and thermal convection phenomena: the planar zone forms due to the high-temperature gradient, which reduced with deposition, increasing the solidification rate (super-cooling), and the microstructure evolves to a dendritic/columnar type, as reported in other studies [22,31]. The PHT affects the size of dendrites, and samples with PHT showed dendrites of greater thickness.

Table 3. Dimensional analysis and dilution of clads produced by DLD without PHT. AC—Clad Area; AM—Melting Area.

Sample	Width (mm)	Height (mm)	Depth (mm)	AC (mm^2)	AM (mm^2)	Dilution (%)	Cracks
M1_2_15	3.420	2.360	0.000	6.76	0.00	0.0	No
M1_6_15	3.410	0.930	0.000	2.48	0.00	0.0	No
M1.5_10_10	3.200	0.520	0.120	1.16	0.22	16.0	No
M1.5_10_15	3.190	0.760	0.044	1.75	0.16	8.4	No
M2_2_15	3.510	2.860	1.330	9.47	3.00	24.1	No
M2_4_15	3.560	1.790	1.140	5.34	2.60	32.8	No
M2_6_10	3.370	0.880	1.170	2.20	2.29	51.1	No
M2_6_15	3.820	0.926	0.956	2.79	2.20	44.1	No
M2_6_20	3.580	1.083	0.970	3.07	1.74	36.2	No
M2_10_10	3.300	0.530	0.940	2.06	1.25	37.8	Yes
M2_10_15	3.350	0.790	0.680	1.19	1.64	58.0	Yes
M2.5_10_10	3.400	0.560	1.190	1.40	2.60	65.0	Yes
M2.5_10_15	3.340	0.770	1.050	1.91	2.11	52.4	No
M3_2_15	5.000	2.436	2.590	9.16	8.55	48.3	No
M3_4_15	4.950	1.282	1.673	3.64	4.14	53.2	No
M3_6_10	4.130	0.646	1.927	3.59	4.21	54.0	Yes
M3_6_15	3.870	1.061	1.910	2.17	6.15	74.0	Yes
M3_6_20	4.810	1.191	1.574	2.95	4.66	61.3	Yes

The localized cooling rate in the DLD process promotes significant microstructural alteration in the HAZ region with the formation of Martensite (M). PHT at 300 °C reduced the temperature gradient (and the resulting cooling rate) and induces microstructural changes at HAZ, allowing the martensite laths to have larger dimensions and the formation of a higher amount of ferrite.

To evaluate the PHT effect, mechanical and microstructural analyses were concentrated in the interface region between CL and HAZ. The microstructure in these regions was characterized by SEM observations. The clad is mainly composed of martensite, with a random crystallographic orientation, and vermicular δ-ferrite surrounding the martensite laths (Figure 5). A low percentage of retained austenite was detected by the EBSD analysis.

The effect of δ-ferrite is already known and widely studied by researchers linked to the welding process, but not much researched in laser material processing. According to Niessen et al. [32], the presence of the δ-ferrite phase promotes a severe reduction of toughness and ductility. This phase increases ductile-to-brittle transition temperature (DBTT), deteriorating impact properties, and the formation of brittle cracks in the martensitic matrix [33]. This can be a determining factor in clad cracking (Figure 6), which is dependent on the processing conditions, mainly on the laser power, being more frequent and more extensive in samples with PHT (Figure 7).

Table 4. Dimensional analysis and dilution of clads produced by DLD with PHT (300 °C). AC—Clad Area; AM—Melting Area.

Sample	Width (mm)	Height (mm)	Depth (mm)	AC (mm^2)	AM (mm^2)	Dilution (%)	Cracks
M1_2_15	3.720	2.224	0.000	7.43	0.00	0.0	No
M1_6_15	3.910	0.936	0.000	2.41	0.00	0.0	No
M1.5_10_10	3.430	0.490	0.074	1.21	1.36	53.0	No
M1.5_10_15	3.590	0.700	0.130	1.81	0.27	13.2	Yes
M2_2_15	4.180	2.830	1.890	10.38	4.84	31.8	No
M2_4_15	3.910	1.610	1.520	5.06	3.79	42.8	No
M2_6_10	3.600	0.890	1.550	2.33	3.31	58.7	No
M2_6_15	4.050	0.968	1.369	2.86	2.91	50.5	Yes
M2_6_20	3.780	1.241	1.312	3.52	2.83	44.5	Yes
M2_10_10	3.490	0.550	1.210	1.90	1.53	44.6	No
M2_10_15	3.460	0.760	0.880	1.39	2.38	63.2	Yes
M2.5_10_10	3.460	0.590	1.510	1.49	3.29	68.8	Yes
M2.5_10_15	3.460	0.790	1.320	1.92	2.58	57.4	Yes
M3_2_15	4.960	2.540	3.263	9.15	10.25	52.8	Yes
M3_4_15	5.190	1.342	2.289	4.66	8.18	63.7	Yes
M3_6_10	3.810	0.815	2.287	3.72	5.92	61.4	Yes
M3_6_15	3.860	1.105	2.018	2.29	6.24	73.1	Yes
M3_6_20	4.890	1.123	1.929	3.13	5.17	62.3	Yes

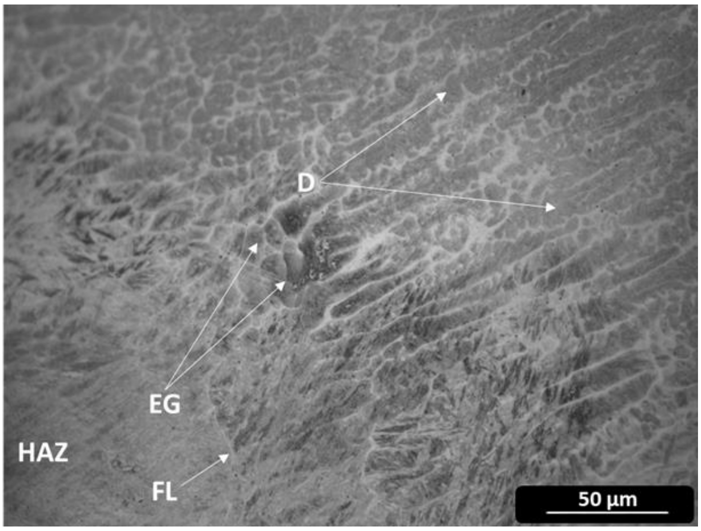

Figure 4. Optical microscopy image showing the solidification structure in the M2_6_15 sample. D—Dendrites; EG—Equiaxed Gains; FL—Fusion Line; HAZ—Heat-affected Zone.

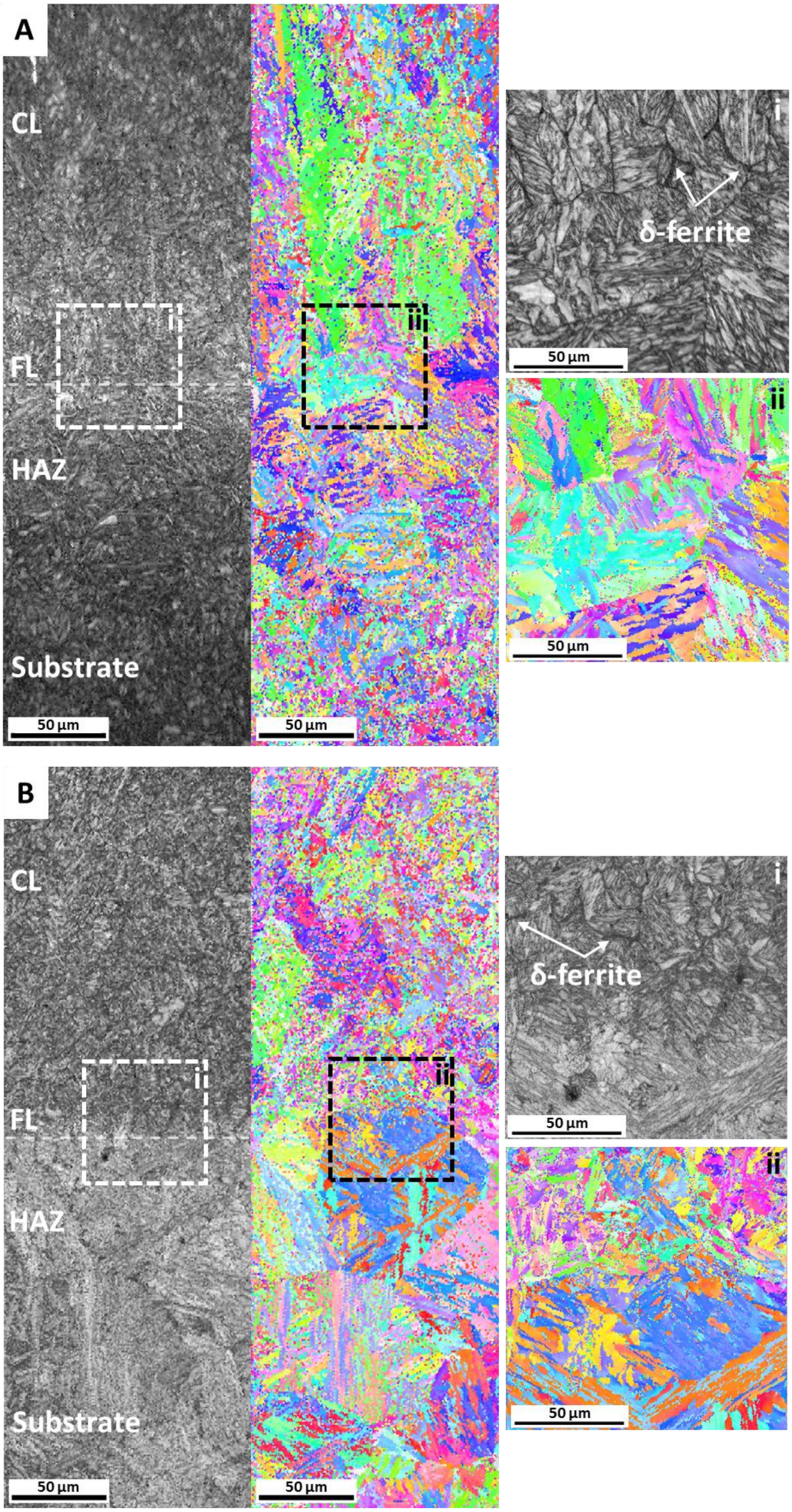
A
CL
FL
HAZ
Substrate
50 µm
i
ii
δ-ferrite
B
CL
FL
HAZ
Substrate
50 µm
i
ii
δ-ferrite

Figure 5. Electron backscatter diffraction (EBSD) images showing the microstructure of M2_6_15 samples (**A**) with and (**B**) without PHT.

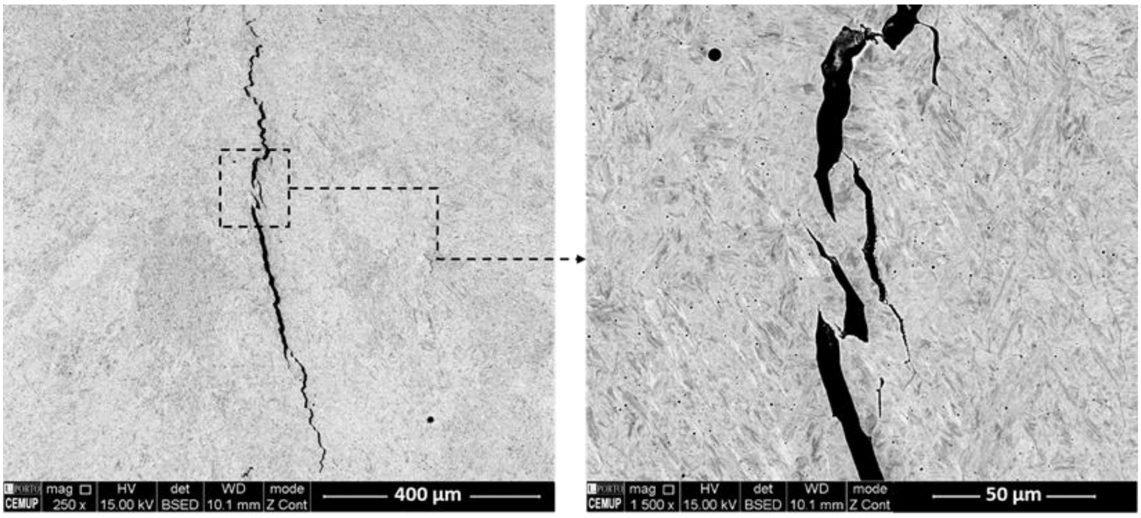

Figure 6. SEM images of cracks formed in the M2_6_15 sample with PHT.

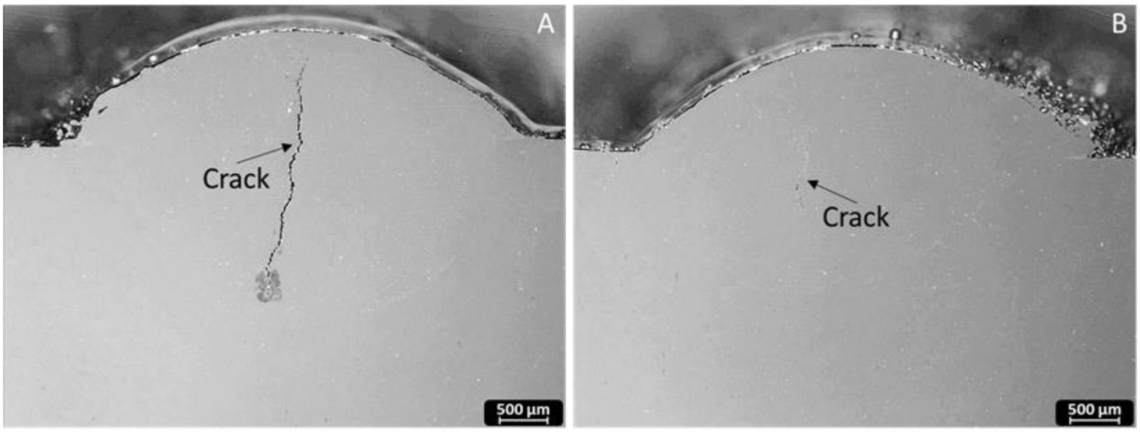

Figure 7. OM images of cracks formed in the centre of the cladding in M3_6_10 samples (**A**) with and (**B**) without PHT.

The influence of the PHT in microstructure has a direct consequence on mechanical behaviour. Microhardness profiles were determined to evaluate this influence on the mechanical response. Figure 8 shows microhardness evolution across the clad and substrate, including HAZ.

PHT reduces the hardness of both the clad areas near the substrate and HAZ. In fact, in HAZ a maximum hardness of 652HV0.3 and 524HV0.3 were measured in the samples without and with PHT, respectively, showing a significant decrease in hardness due to substrate preheating. This hardness variation can be explained by the lower cooling rate of PHT samples and its effect on microstructure, mainly increasing the quantity of ferrite formed and allowing martensite tempering. A smooth hardness gradient in HAZ is crucial to increase the substrate crack propagation resistance.

The presented microstructures in Figures 4 and 5 are representative of all produced clads and it was difficult to select the best processing conditions based on microstructural or mechanical analysis.

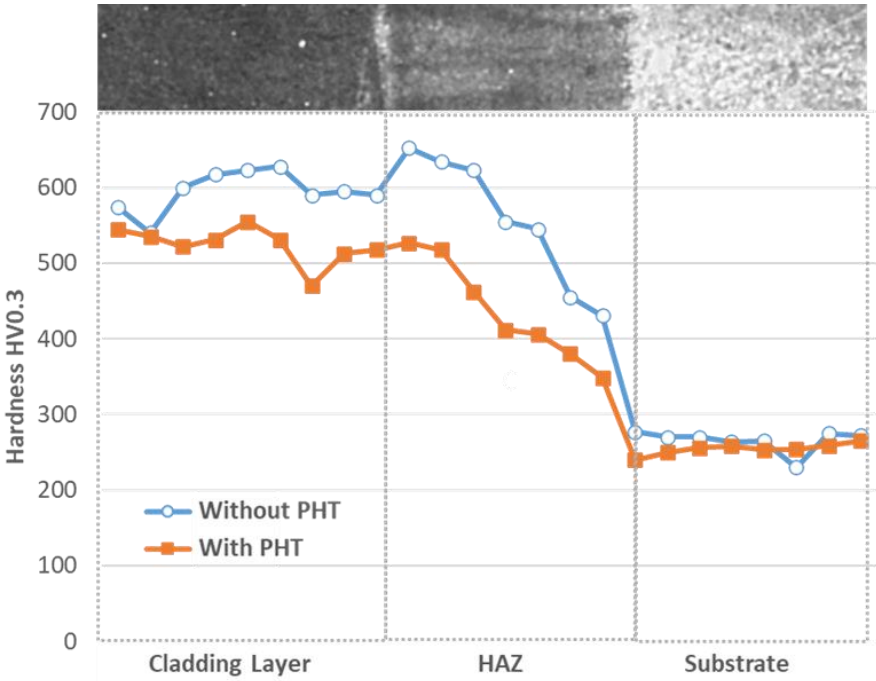

Figure 8. Microhardness profile of M2_6_15 samples with and without PHT.

Influence of Processing Conditions

According to the information described in Tables 2–4, all the processing parameters, such as laser power, scanning speed, powder feed rate, and preheating strongly influence the production, bonding, and quality of the cladding. The selection of processing conditions that ensures a clad without defects, bonded to the substrate and with good material yield, is an essential and challenging task because the various variables interaction. Their simultaneous optimization is difficult because they often act in opposite directions.

Dilution, which assesses the contribution of the substrate (area of the substrate that is melted by the laser) to the total area of the clad, is an important aspect of DLD clads. It allows the control of contamination of the clad by the substrate and affects the deposition yield. High dilutions can compromise the quality of the clad and increase distortion [34], but some dilution is necessary to ensure the metallurgical bond of the cladding to the substrate. With the measured clad and melting areas (Tables 3 and 4), dilution was determined using Equation (1). The dilution values are also shown in Tables 3 and 4.

$$\text{Dilution (\%)} = AM/(AC+AM) \times 100 \tag{1}$$

These results show that a laser power of 1 kW is enough to melt the powder and produce a clad. However, it is not sufficient to guarantee the metallurgical bonding of the clad to the substrate (dilution equal to 0%). The results in Tables 3 and 4 evidence that dilution increases with laser power.

However, the increase in laser power must be carefully performed because of its negative effect on clad soundness. Overheating, caused by an excessive energy input per unit area of the substrate, which is preheated, leads to an increase in residual stresses favouring the appearance of cracks in the cladding [34]. This also facilitates the formation of eutectic compounds resulting from the segregation of elements, such as silicon, for grain boundaries, and interdendritic regions [35]. In short, the thermal stresses generated by the PHT at 300 °C, high laser power and the presence of δ-ferrite most often cause cracks in samples with PHT, as evidenced in Tables 3 and 4.

Analysis of these data shows that keeping all other parameters equal, an increase in the feed rate causes an increase in the cladding height and usually a decrease in its depth. A higher feed rate implies a more significant amount of powder ejected from the coaxial nozzle in the same period; the powder particles will form a denser cloud, absorbing more of the beam energy of the laser resulting in a higher deposition rate (higher clads).

For the same feed rate, PHT produces clads with greater height and depth in most cases. This effect can be explained by the forced thermal convection phenomenon, with the samples with PHT having a higher internal heat and, consequently, allowing greater powder melting. Another contribution of PHT is the increase in the laser absorption rate by the substrate [36], making the melt pool more fluid, which allows a more significant deposition of the powder and increases the penetration depth, thus increasing the dilution.

Scanning speed affects the morphology of claddings produced by DLD, depending on the specific energy of the laser and the interaction with powder cloud. When the scanning speed is small, the mass of deposited powder per unit of length, and consequently the volume of the formed clad, is quite large due to the interaction for a more extended period between the laser beam and the powder. However, if the speed is higher, the interaction between the laser beam and the powder cloud will be less, decreasing the amount of deposited material. Increasing the scanning speed decreases the powder, and the energy deposited per unit length and melt pool volume [18].

Tables 3 and 4 show that lower scanning speed typically produces coatings with greater heights and depths. The greater depth is due to the more extended interaction of the laser beam with the substrate. PHT also increases the depth due to the Marangoni convection effect. This effect is caused by the surface tension gradient, which becomes more evident with increasing substrate temperature [11].

Although this detailed analysis of the individual effect of these three variables (scanning speed, laser power, and feed rate) is essential to clarify their role in the deposition of Metco42C on a 42CrMo4 steel substrate, the effect of each is difficult to isolate. It is necessary to apply combined parameters to obtain a more accurate relationship between processing and clad characteristics.

Powder Deposition Density (PDD) is a widely used parameter that can express the combined influence of feed rate, scanning speed, and laser spot size (φ) [37,38]. The powder deposition density is defined by Equation (2). Figure 9 shows that the cladding area increases linearly with the increase in the PDD parameter and that PHT has a negligible influence on this relationship.

$$PDD\ (g/mm^2) = FR/(SS * \varphi) \qquad (2)$$

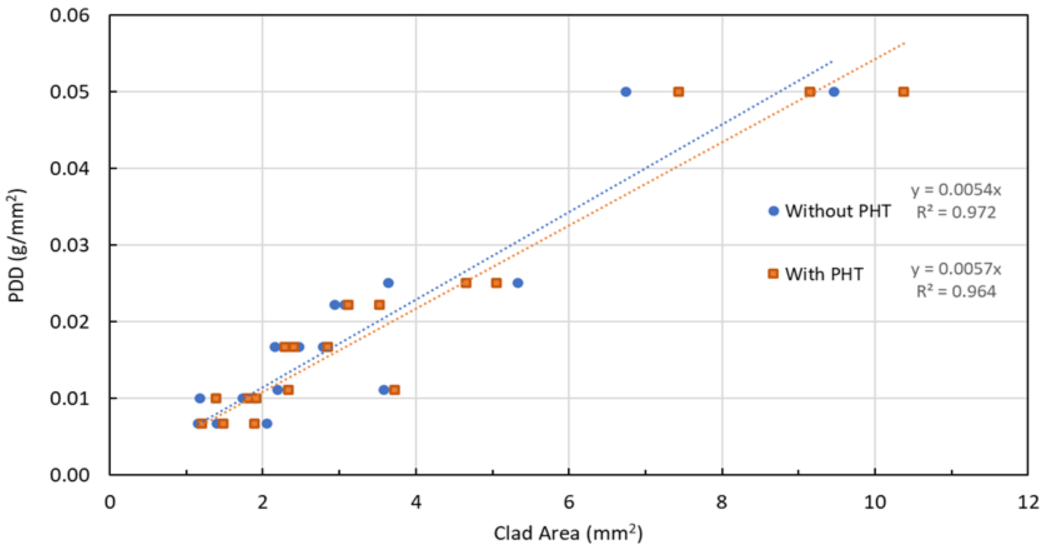

Figure 9. Relationship between the cladding area and the value of the PDD parameter.

A similar analysis was performed in which the three analyzed processing parameters (Laser power—P, Scanning speed—SS, and Feed rate—FR) were merged in an empirical combined parameter P*SS/FR [16] and correlated with the dilution (Figure 10).

As shown in Figure 10, PHT promoted a greater dilution compared to samples without PHT. As discussed above, this influence is mainly controlled by the Marangoni convection effect caused by the surface tension gradient.

It was more challenging to find a complex parameter that would allow the processing conditions to be associated with the appearance of cracks. This relationship was achieved when using $P^4.SS^2/FR$ as a complex parameter (Figure 11). The limit values of 2000 and 5000 $(kW)^4.(mm/s)^2/(g/s)$ allow the production of sound clads in samples with and without PHT, respectively.

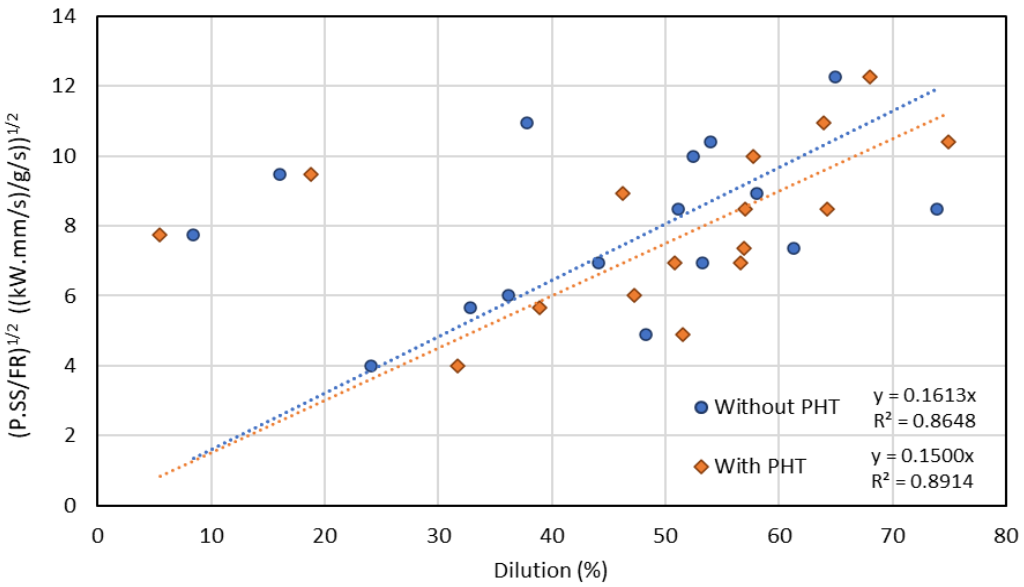

Figure 10. Dependence of dilution on the value of complex parameter P*SS/FR.

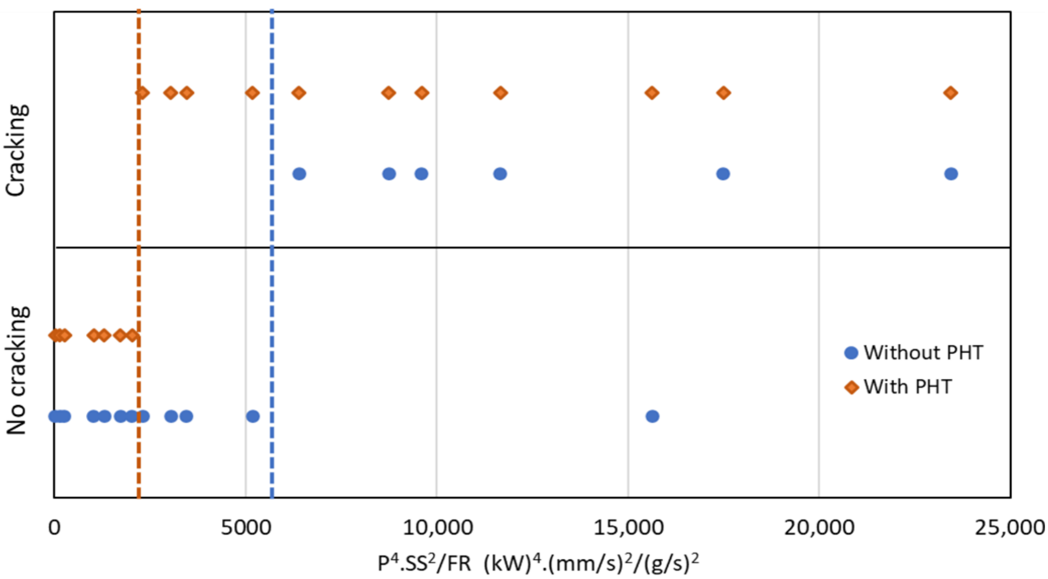

Figure 11. Relationship between the processing parameters expressed by the $P^4.SS^2/FR$ complex parameter in the formation of cracks.

Optimization of Processing Conditions

The complex interaction between the processing parameters, which implied the need to use complex parameters that must be adjusted to each process, makes it essential to apply an optimization algorithm. Optimization is an approach towards the best state among possible solutions that involves selection among many responses. Since there are constraints in real problems, generally just a better response is selected instead of the best one.

The interaction and interdependence of the different process variables led to applying a Genetic Optimization Algorithm to select a response in which the objective functions obtain the best-desired response. This multi-objective optimization problem is dynamic and is supported and validated with the experimental results [39,40].

In this study, the Response Surface Model (RSM) was used to calculate the ideal combination of laser power and scanning speed that minimizes the values of the height and depth of the clad and ensures a 10% dilution while guaranteeing sound clads with bonding to the substrate. These conditions make it possible to produce strands with a good wettability (minimizing height) and maximizing the yield of the deposition process (minimizing depth and dilution). The presented results are for a constant feed rate of 15 g/min. This feed rate was selected as the best after the first series of experimental results.

In the Response Surface Model (RSM), objective functions are derived considering different laser powers (x) and scanning speeds (y) as inputs, and using genetic algorithms, optimum values for these functions are specified, considering the constraints. Two polynomial models were defined, without and with preheating condition, the objective functions are shown in Equations (3)–(5) and Equations (6)–(8), respectively.

Without preheating:

$$obj_{height}(x,y) = 2560 + 1770 * x - 723.6 * y - 434.2 * x^2 - 190.7 * x * y + 70.4 * y^2 + 41.1 * x^2 * y + 2.976 * x * y^2 - 1.851 * y^3 \quad (3)$$

$$obj_{depth}(x,y) = -1774 + 2597 * x - 145.2 * y - 258.7 * x^2 - 368.8 * x * y + 92.09 * y^2 + 43.44 * x^2 * y + 12.62 * x * y^2 - 6.433 * y^3 \quad (4)$$

$$obj_{dilution}(x,y) = 791.3 - 1806 * x - 4.99 * y + 1424 * x^2 + 7.405 * x * y - 463.8 * x^3 - 2.844 * x^2 * y + 54.08 * x^4 + 0.3654 * x^3 * y \quad (5)$$

With preheating:

$$obj_{height}(x,y) = 2117 + 2917 * x - 1046 * y - 670.3 * x^2 - 470.2 * x * y + 184.8 * y^2 + 104.7 * x^2 * y + 3.83 * x * y^2 - 8.149 * y^3 \quad (6)$$

$$obj_{depth}(x,y) = -2352 + 3157 * x - 199.2 * y - 226 * x^2 - 248.2 * x * y + 82.54 * y^2 - 29.85 * x^2 * y + 26.23 * x * y^2 - 7.545 * y^3 \quad (7)$$

$$obj_{dilution}(x,y) = -35.85 + 34.75 * x - 10.71 * y - 1.294 * x^2 + 15.89 * x * y + 0.1334 * y^2 - 4.257 * x^2 * y + 0.2834 * x * y^2 - 0.08753 * y^3 \quad (8)$$

The fitted curves for Equations (3)–(5) are shown in Figures 12–14, respectively. Data validation is verified using the Matlab software and curve-fitting toolbox. When variables are selected, the mentioned toolbox can calculate validation statistics such as Root Mean Squared Error (RMSE), and the best fitting has the least amount of RMSE. The same approach was used to fit the curves for the condition of without preheating.

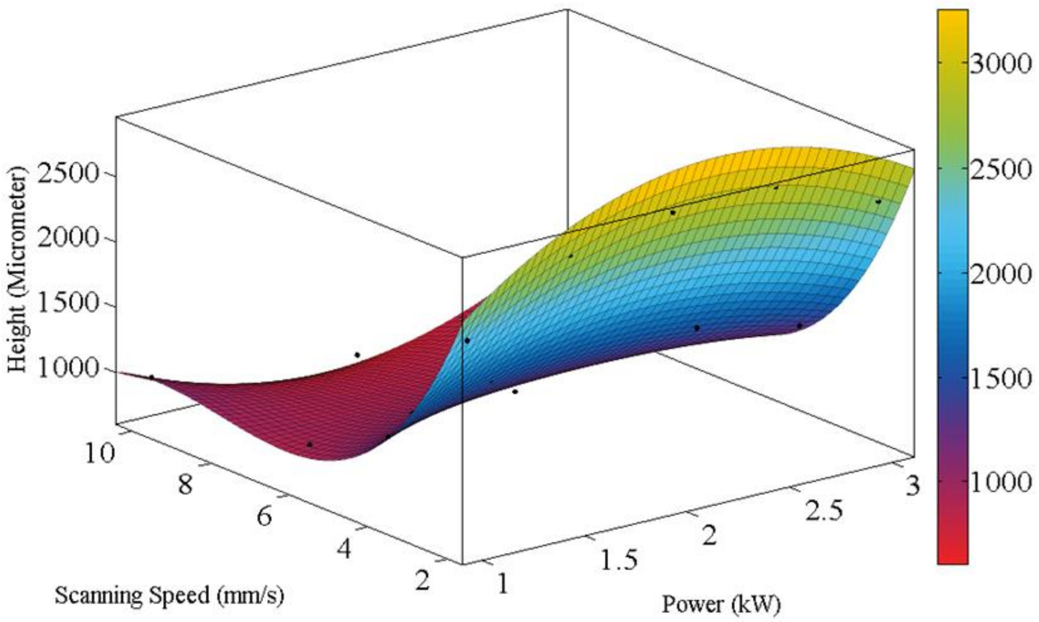

(**A**)

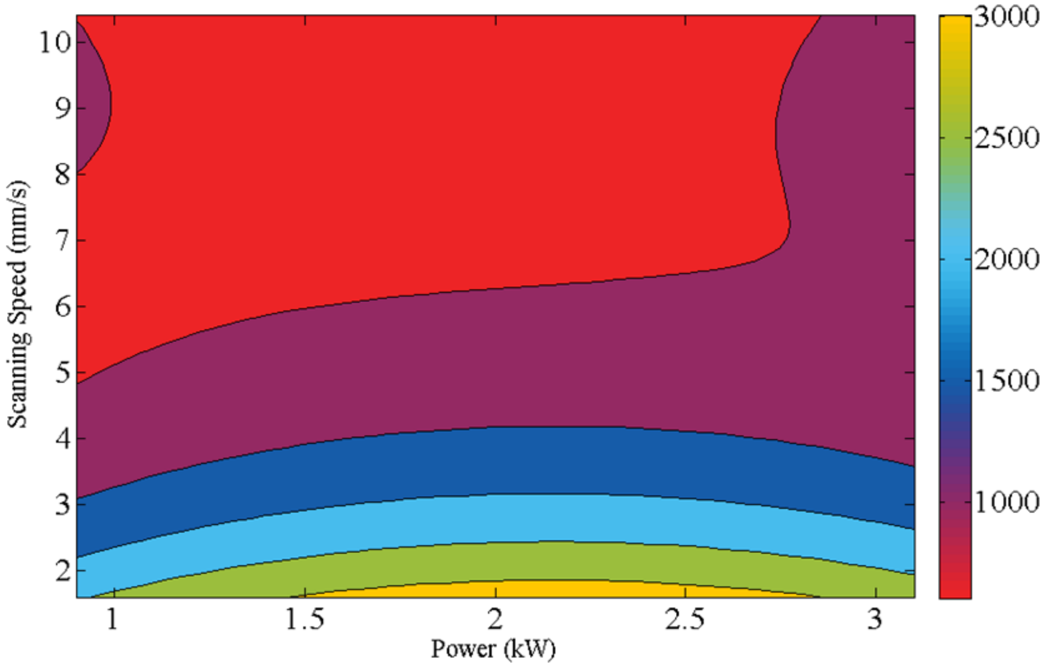

(**B**)

Figure 12. (**A**) The best curved surface (R-square: 0.9908; Adjusted R-square: 0.9539; RMSE: 0.1347) and (**B**) contour plot for the height (in micrometers) of deposited clad regarding the combination of the laser power and scanning speed.

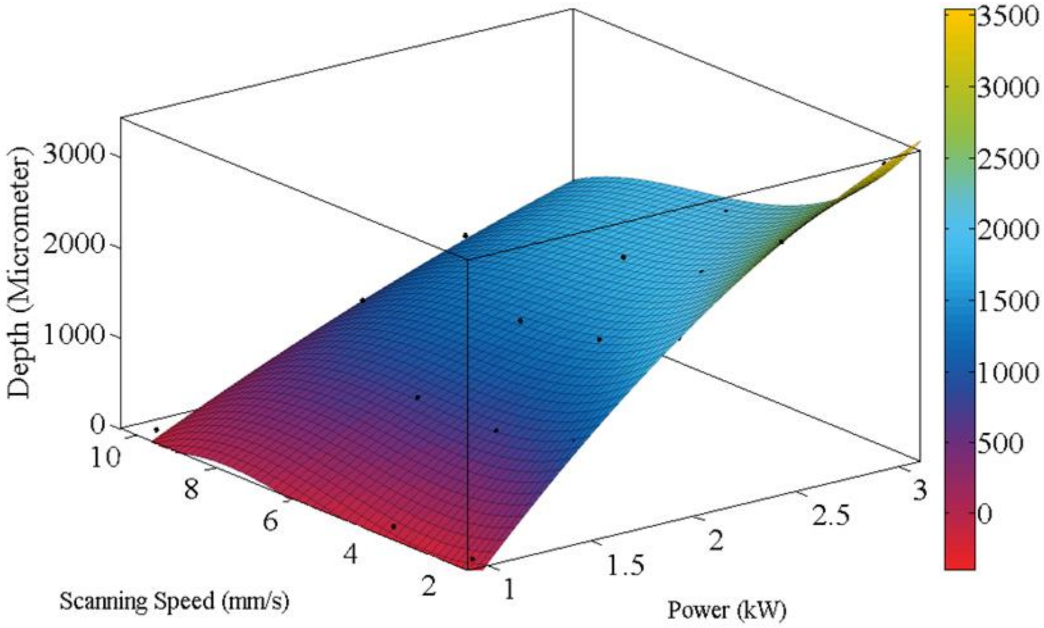

(**A**)

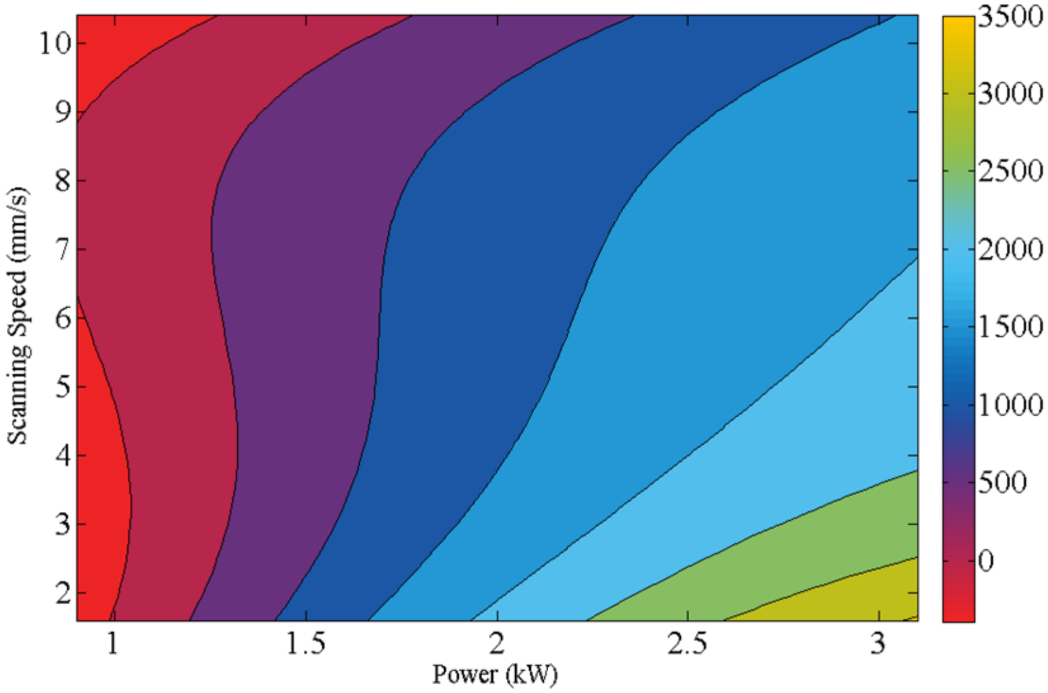

(**B**)

Figure 13. (**A**) The best curved surface (R-square: 0.9904; Adjusted R-square: 0.952; RMSE: 0.1674) and (**B**) contour plot for the depth (in micrometers) of deposited clad regarding the combination of the laser power and scanning speed.

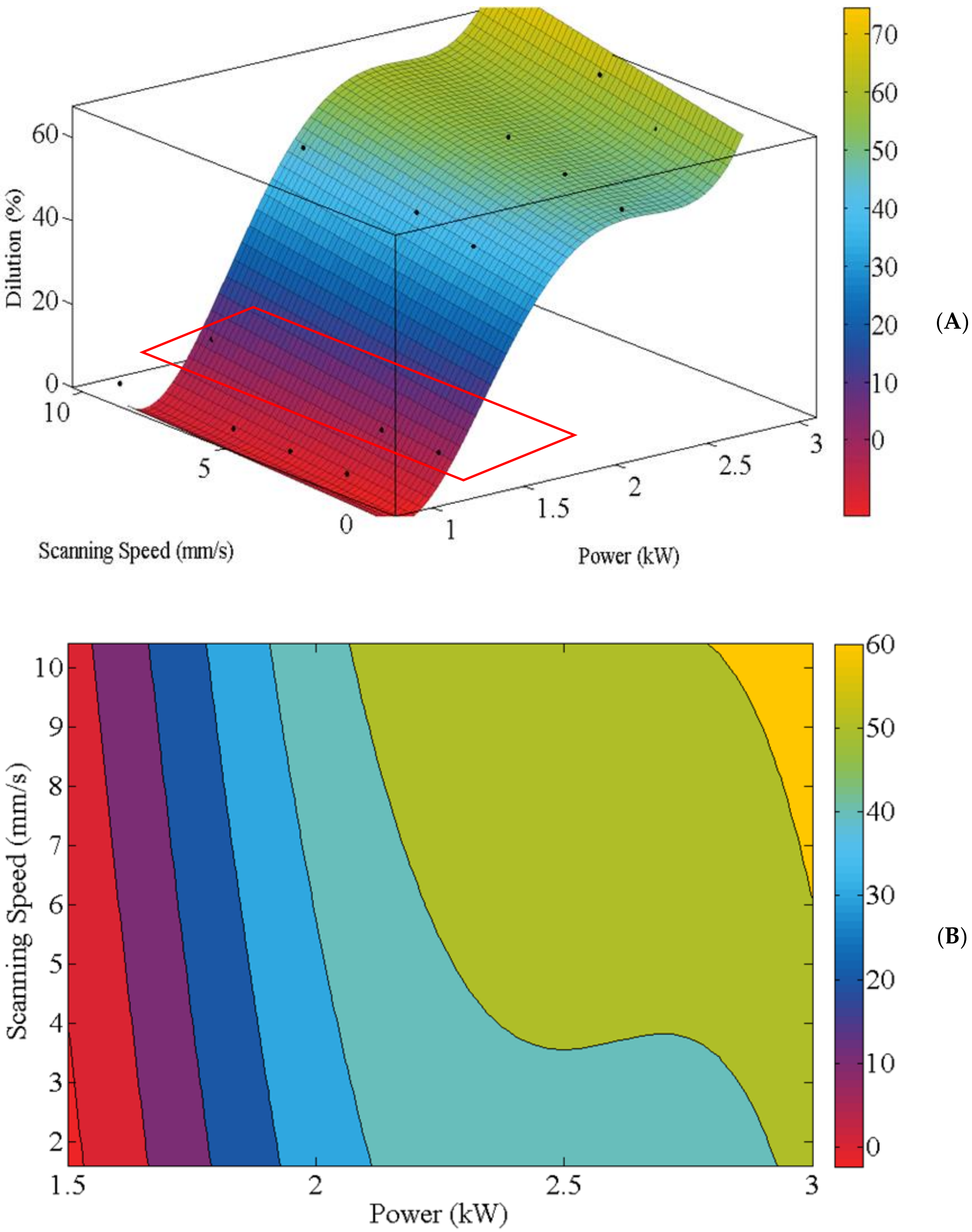

Figure 14. (**A**) The best curved surface (R-square: 0.9728; Adjusted R-square: 0.8641; RMSE: 0.347) and (**B**) contour plot for the dilution (in %) of deposited clad regarding the combination of the laser power and scanning speed.

Figures 15 and 16 illustrate derived Pareto frontiers [38] minimizing the three objective functions simultaneously for samples without preheating and with 300 °C preheating, respectively.

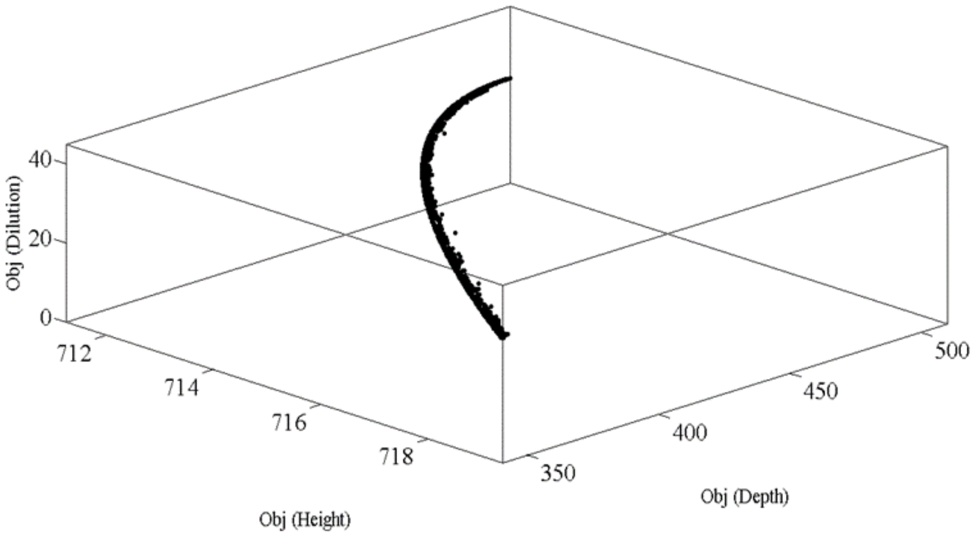

Figure 15. 3D Pareto frontier of the three objective functions including depth, dilution, and height of clads, with a feed rate of 15 g/min and without pre-heating.

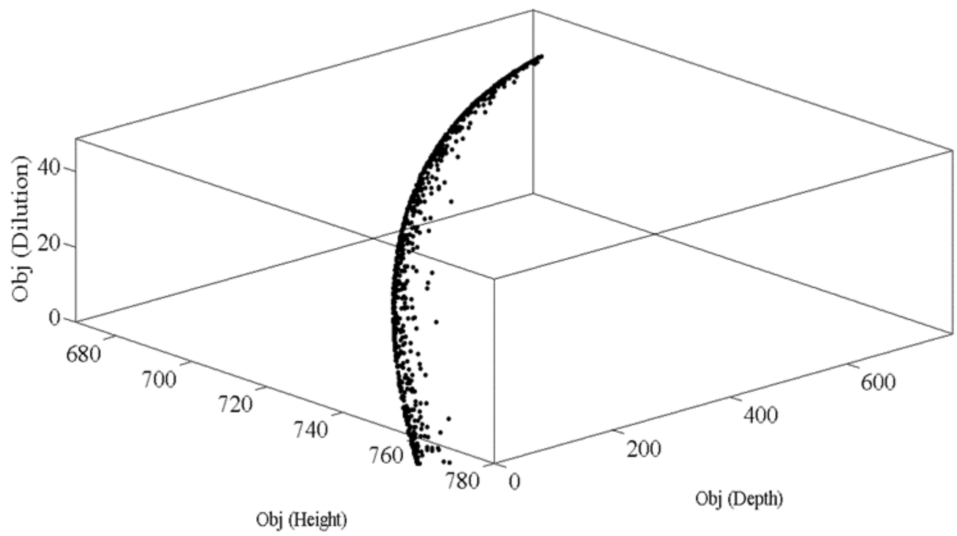

Figure 16. 3D Pareto frontier of the three objective functions including depth, dilution, and height of clads, with a feed rate of 15 g/min and with 300 °C pre-heating.

In this study, L3 norm Minimization technique [41] is used to minimize the distance from the Pareto set to an ideal solution, utopia point. Table 5 shows the best values for minimized outputs based on the inputs. For a feed rate of 15 g/min, the best processing conditions are a scan speed of 10 mm/s and a laser power of 1.5 and 1.7 kW for samples with and without preheating, respectively. These values correspond to 3340 and 2025 $(kW)^4.(mm/s)^2/(g/s)$, which are in accordance with those determined by using the empirical complex parameter $P^4.SS^2/FR$.

Table 5. Optimized value of the inputs and outputs for a feed rate of 15 g/min.

Conditions	Laser Power (kW)	Scan Speed (mm/s)	Height (μm)	Depth (μm)	Dilution (%)
Without preheating	1.70	10.000	719	348	28.3
With preheating	1.49	9.999	734	123	16.7

Conclusions

The present study analyzed the effect of laser power, scan speed, and feed rate on the deposition of AISI 431 steel powder (Metco 42C) on a 42CrMo4 steel substrate. The analysis of the clads revealed a martensitic structure with delta ferrite. This structure is susceptible to the appearance of cracks in the cladding area, this cracking being more common when the substrates were preheated to 300 °C. The metallurgical bonding of the clad to the substrate requires a power greater than 1 kW. Laser powers greater than 2 or 1.5 kW, for samples without or with preheating, respectively, induce dilutions greater than 30% with the consequent decrease in the yield of the deposition process. The increase in laser power and scan speed increases the possibility of cracking. The use of experimental complex parameters made it possible to define the conditions that prevent cracking and guarantee a sound clad with good deposition yield. The values obtained are 2000 and 5000 $(kW)^4.(mm/s)^2/(g/s)$ in samples with and without PHT, respectively. The use of a genetic optimization algorithm indicated that the best processing conditions were obtained with speeds of 10 mm/s, feed rate of 15 g/min, and laser powers of 1.5 and 1.7 kW for samples with and without preheating, respectively. These conditions agree with the ones resulting from the application of the complex parameters.

Author Contributions: A.A.F., M.F.V. and A.R.R. proposed the methodology and results data analyses followed in this research, A.A.F., J.P.S. and J.M.C. carried out the experimental tests, R.D. performed the genetic optimization and all authors participated in the discussion of results and writing of the manuscript. All authors have read and agreed to the published version of the manuscript.

Funding: This research was funded by FEDER through the program P2020|COMPETE, Projetos em Copromoção (project POCI-01-0247-FEDER-039848).

Institutional Review Board Statement: Not applicable

Informed Consent Statement: Not applicable

Data Availability Statement: Not applicable

Acknowledgements: The authors are grateful to CEMUP (Centro de Materiais da Universidade do Porto) for expert assistance with SEM, and to Project ADDing (POCI-01-0145-FEDER-030490), co-financed by FEDER through P2020|COMPETE and national funds through Fundação para a Ciência e a Tecnologia.

Conflicts of Interest: The authors declare no conflict of interest.

References

1. Alimardani, M.; Fallah, V.; Khajepour, A.; Toyserkani, E. The effect of localized dynamic surface preheating in laser cladding of Stellite 1. *Surf. Coat. Technol.* **2010**, *204*, 3911–3919, doi:10.1016/j.surfcoat.2010.05.009.
2. Leunda, J.; Navas, V.G.; Soriano, C.; Sanz, C. Effect of laser tempering of high alloy powder metallurgical tool steels after laser cladding. *Surf. Coat. Technol.* **2014**, *259*, 570–576, doi:10.1016/j.surfcoat.2014.10.028.
3. Dass, A.; Moridi, A. State of the Art in Directed Energy Deposition: From Additive Manufacturing to Materials Design. *Coatings* **2019**, *9*, 418, doi:10.3390/coatings9070418.
4. Thompson, S.M.; Bian, L.; Shamsaei, N.; Yadollahi, A. An overview of Direct Laser Deposition for additive manufacturing; Part I: Transport phenomena, modeling and diagnostics. *Addit. Manuf.* **2015**, *8*, 36–62, doi:10.1016/j.addma.2015.07.001.

5. Vilar, R.; Santos, E.; Ferreira, P.; Franco, N.; Da Silva, R. Structure of NiCrAlY coatings deposited on single-crystal alloy turbine blade material by laser cladding. *Acta Mater.* **2009**, *57*, 5292–5302, doi:10.1016/j.actamat.2009.06.049.
6. Fu, F.; Zhang, Y.; Chang, G.; Dai, J. Analysis on the physical mechanism of laser cladding crack and its influence factors. *Optik* **2016**, *127*, 200–202, doi:10.1016/j.ijleo.2015.10.043.
7. Hutasoit, N.; Luzin, V.; Blicblau, A.; Yan, W.; Brandt, M.; Cottam, R. Fatigue life of laser clad hardfacing alloys on AISI 4130 steel under rotary bending fatigue test. *Int. J. Fatigue* **2015**, *72*, 42–52, doi:10.1016/j.ijfatigue.2014.11.001.
8. Chen, J.-Y.; Conlon, K.; Xue, L.; Rogge, R. Experimental study of residual stresses in laser clad AISI P20 tool steel on pre-hardened wrought P20 substrate. *Mater. Sci. Eng. A* **2010**, *527*, 7265–7273, doi:10.1016/j.msea.2010.07.098.
9. Brandl, E.; Michailov, V.; Viehweger, B.; Leyens, C. Deposition of Ti–6Al–4V using laser and wire, part II: Hardness and dimensions of single beads. *Surf. Coat. Technol.* **2011**, *206*, 1130–1141, doi:10.1016/j.surfcoat.2011.07.094.
10. Le, T.-N.; Lo, Y.-L. Effects of sulfur concentration and Marangoni convection on melt-pool formation in transition mode of selective laser melting process. *Mater. Des.* **2019**, *179*, 107866, doi:10.1016/j.matdes.2019.107866.
11. Jiang, Y.; Cheng, Y.; Zhang, X.; Yang, J.; Yang, X.; Cheng, Z. Simulation and experimental investigations on the effect of Marangoni convection on thermal field during laser cladding process. *Optik* **2020**, *203*, 164044, doi:10.1016/j.ijleo.2019.164044.
12. Ju, J.; Zhou, Y.; Kang, M.; Wang, J. Optimization of Process Parameters, Microstructure, and Properties of Laser Cladding Fe-Based Alloy on 42CrMo Steel Roller. *Material* **2018**, *11*, 2061, doi:10.3390/ma11102061.
13. Huang, C.; Lin, X.; Yang, H.; Liu, F.; Huang, W. Microstructure and Tribological Properties of Laser Forming Repaired 34CrNiMo6 Steel. *Material* **2018**, *11*, 1722, doi:10.3390/ma11091722.
14. Dai, Q.-L.; Luo, C.-B.; You, F.-Y. Crack Restraining Methods and their Effects on the Microstructures and Properties of Laser Cladded WC/Fe Coatings. *Material* **2018**, *11*, 2541, doi:10.3390/ma11122541.
15. Ocylok, S.; Alexeev, E.; Mann, S.; Weisheit, A.; Wissenbach, K.; Kelbassa, I. Correlations of Melt Pool Geometry and Process Parameters During Laser Metal Deposition by Coaxial Process Monitoring. *Phys. Procedia* **2014**, *56*, 228–238, doi:10.1016/j.phpro.2014.08.167.
16. Ocelík, V.; De Oliveira, U.; De Boer, M.; De Hosson, J.T.M. Thick Co-based coating on cast iron by side laser cladding: Analysis of processing conditions and coating properties. *Surf. Coat. Technol.* **2007**, *201*, 5875–5883, doi:10.1016/j.surfcoat.2006.10.044.
17. de Oliveira, U.; Ocelík, V.; De Hosson, J. Analysis of coaxial laser cladding processing conditions. *Surf. Coat. Technol.* **2005**, *197*, 127–136, doi:10.1016/j.surfcoat.2004.06.029.

18. Huang, Y. Characterization of dilution action in laser-induction hybrid cladding. *Opt. Laser Technol.* **2011**, *43*, 965–973, doi:10.1016/j.optlastec.2010.12.005.
19. Gao, J.; Wu, C.; Hao, Y.; Xu, X.; Guo, L. Numerical simulation and experimental investigation on three-dimensional modelling of single-track geometry and temperature evolution by laser cladding. *Opt. Laser Technol.* **2020**, *129*, 106287, doi:10.1016/j.optlastec.2020.106287.
20. Zhao, Y.; Guan, C.; Chen, L.; Sun, J.; Yu, T. Effect of process parameters on the cladding track geometry fabricated by laser cladding. *Optik* **2020**, *223*, 165447, doi:10.1016/j.ijleo.2020.165447.
21. Bi, G.; Gasser, A.; Wissenbach, K.; Drenker, A.; Poprawe, R. Identification and qualification of temperature signal for monitoring and control in laser cladding. *Opt. Lasers Eng.* **2006**, *44*, 1348–1359, doi:10.1016/j.optlaseng.2006.01.009.
22. Hemmati, I.; Ocelík, V.; De Hosson, J.T.M. Microstructural characterization of AISI 431 martensitic stainless steel laser-deposited coatings. *J. Mater. Sci.* **2011**, *46*, 3405–3414, doi:10.1007/s10853-010-5229-2.
23. Altuncu, E.; Tarım, M. Laser Cladding of Martensitic Stainless Steels on Armor Steels. *Emerg. Mater. Res.* **2020**, *9*, 1–4, doi:10.1680/jemmr.18.00120.
24. Hemmati, I.; Ocelík, V.; De Hosson, J.T.M. The effect of cladding speed on phase constitution and properties of AISI 431 stainless steel laser deposited coatings. *Surf. Coat. Technol.* **2011**, *205*, 5235–5239, doi:10.1016/j.surfcoat.2011.05.035.
25. Li, L.; Shen, F.; Zhou, Y.; Tao, W. Comparative study of stainless steel AISI 431 coatings prepared by extreme-high-speed and conventional laser cladding. *J. Laser Appl.* **2019**, *31*, 042009, doi:10.2351/1.5094378.
26. Ravi, G.; Hao, X.; Wain, N.; Wu, X.; Attallah, M. Direct laser fabrication of three dimensional components using SC420 stainless steel. *Mater. Des.* **2013**, *47*, 731–736, doi:10.1016/j.matdes.2012.12.062.
27. Shen, F.; Tao, W.; Li, L.; Zhou, Y.; Wang, W.; Wang, S. Effect of microstructure on the corrosion resistance of coatings by extreme high speed laser cladding. *Appl. Surf. Sci.* **2020**, *517*, 146085, doi:10.1016/j.apsusc.2020.146085.
28. Sun, C.; Fu, P.-X.; Liu, H.-W.; Liu, H.-H.; Du, N.-Y. Effect of Tempering Temperature on the Low Temperature Impact Toughness of 42CrMo4-V Steel. *Metals* **2018**, *8*, 232, doi:10.3390/met8040232.
29. International Conference on Recent Trends in Physics 2016 (ICRTP2016). *J. Phys. Conf. Ser.* **2016**, *755*, 011001, doi:10.1088/1742-6596/755/1/011001.
30. BS EN 10269:2013. Steels and Nickel Alloys for Fasteners with Specified Elevated and or Low Temperature. BSI Standards Limited. ISBN 978 0 580 76784 5, **2013**.
31. Kurz, W.; Bezençon, C.; Gäumann, M. Columnar to equiaxed transition in solidification processing. *Sci. Technol. Adv. Mater.* **2001**, *2*, 185–191, doi:10.1016/s1468-6996(01)00047-x.
32. Niessen, F.; Tiedje, N.S.; Hald, J. Kinetics modeling of delta-ferrite formation and retainment during casting of supermartensitic stainless steel. *Mater. Des.* **2017**, *118*, 138–145, doi:10.1016/j.matdes.2017.01.026.

33. Tabernero, I.; Lamikiz, A.; Martínez, S.; Ukar, E.; de Lacalle, L.L. Modelling of energy attenuation due to powder flow-laser beam interaction during laser cladding process. *J. Mater. Process. Technol.* **2012**, *212*, 516–522, doi:10.1016/j.jmatprotec.2011.10.019.
34. Bennett, J.; Dudas, R.; Cao, J.; Ehmann, K.; Hyatt, G. Control of heating and cooling for direct laser deposition repair of cast iron components. In Proceedings of the 2016 International Symposium on Flexible Automation (ISFA), Cleveland, OH, USA, 1–3 August 2016; pp. 229–236.
35. Chen, Y.; Lu, F.; Zhang, K.; Nie, P.; Hosseini, S.R.E.; Feng, K.; Li, Z. Dendritic microstructure and hot cracking of laser additive manufactured Inconel 718 under improved base cooling. *J. Alloy. Compd.* **2016**, *670*, 312–321, doi:10.1016/j.jallcom.2016.01.250.
36. Su, J.; Qiu, X.; Xing, F.; Ruan, Y. Effect of Preheating Temperature on Microstructure and Properties of 42CrMo4/38MnVS6 Heterogeneous Laser Welded Joint. *Metals* **2019**, *9*, 870, doi:10.3390/met9080870.
37. Toyserkani, E.; Khajepour, A.; Corbin, S.F. *Laser Cladding*; CRC Press: Boca Raton, FL, USA, 2004.
38. Farshidianfar, M.H.; Khajepour, A.; Gerlich, A.P. Effect of real-time cooling rate on microstructure in Laser Additive Manufacturing. *J. Mater. Process. Technol.* **2016**, *231*, 468–478, doi:10.1016/j.jmatprotec.2016.01.017.
39. Nikam, S.H.; Jain, N.K.; Sawant, M.S. Optimization of parameters of micro-plasma transferred arc additive manufacturing process using real coded genetic algorithm. *Int. J. Adv. Manuf. Technol.* **2020**, *106*, 1239–1252, doi:10.1007/s00170-019-04658-2.
40. Zhang, K.; Chen, Y.; Zheng, J.; Huang, J.; Tang, X. Adaptive filling modeling of butt joints using genetic algorithm and neural network for laser welding with filler wire. *J. Manuf. Process.* **2017**, *30*, 553–561, doi:10.1016/j.jmapro.2017.10.025.
41. Kasprzak, E.; Lewis, K. Pareto analysis in multiobjective optimization using the collinearity theorem and scaling method. *Struct. Multidiscip. Optim.* **2001**, *22*, 208–218, doi:10.1007/s001580100138.

Article 4 - Deposition of Nickel-Based Superalloy Claddings on Low Alloy Structural Steel by Direct Laser Deposition

METALS

https://doi.org/10.3390/met11081326

metals

MDPI

Article

Deposition of Nickel-Based Superalloy Claddings on Low Alloy Structural Steel by Direct Laser Deposition

André Alves Ferreira [1,2,*], Rui Loureiro Amaral [2], Pedro Correia Romio [1], João Manuel Cruz [3], Ana Rosanete Reis [1,2] and Manuel Fernando Vieira [1,2,*]

Article 4 - Deposition of Nickel-Based Superalloy Claddings on Low Alloy Structural Steel by Direct Laser Deposition

André A. Ferreira [1,2,*], Rui L. Amaral [2], Pedro C. Romio [1], João M. Cruz [3], Ana R. Reis [1,2] and Manuel F. Vieira [1,2,*]

[1]Faculty of Engineering,University of Porto, R. Dr Roberto Frias, 4200-465 Porto, Portugal; pedro.romio@gmail.com (P.C.R.); areis@inegi.up.pt (A.R.R.)

[2]LAETA/INEGI—Institute of Science and Innovation in Mechanical and Industrial Engineering, R. Dr Roberto Frias, 4200-465 Porto, Portugal; ramaral@inegi.up.pt (R.L.A.)

[3]SERMEC-Group, R. de Montezelo 540, 4425-348 Porto, Portugal; joaocruz@sermecgroup.pt (J.M.C.)

*Correspondence: andreferreira@fe.up.pt (A.A.F.); mvieira@fe.up.pt (M.F.V.); Tel.: +351-910-461-480 (A.A.F.)

Abstract

In this study, direct laser deposition (DLD) of nickel-based superalloy powders (Inconel 625) on structural steel (42CrMo4) was analysed. Cladding layers were produced by varying the main processing conditions: laser power, scanning speed, feed rate, and preheating. The processing window was established based on conditions that assured deposited layers without significant structural defects and a dilution between 15 and 30%. Scanning electron microscopy, energy dispersive spectroscopy, and electron backscatter diffraction were performed for microstructural characterisation. The Vickers hardness test was used to analyse the mechanical response of the optimised cladding layers. The results highlight the influence of preheating on the microstructure and mechanical responses, particularly in the heat-affected zone. Substrate preheating to 300 °C has a strong effect on the cladding/substrate interface region, affecting the microstructure and the hardness distribution. Preheating also reduced the formation of the deleterious Laves phase in the cladding and altered the martensite microstructure in the heat-affected zone, with a substantial decrease in hardness.

Keywords: direct laser deposition; Inconel 625; parametrisation; microstructure; microhardness; preheating

Introduction

The laser-based additive manufacturing (LBAM) technologies applied in the production and repair of industrial components emerged in the late 1990s. Their use continues to extend to many industrial sector applications for components that operate in extreme conditions. LBAM technologies are unique and versatile in the manufacturing of parts with complex geometry, functionally graded or customised, producing an im-provement in properties that can be used for a variety of industrial applications, such as within the aerospace, metallurgy, energy, and automotive industries [1,2]. Direct laser deposition (DLD) is an LBAM technology used for the additive manufacturing of metal parts, reconstructions, and repairs. DLD consists of the supply, through a nozzle, of metallic powder (or wire) processed by a focused laser, creating a melt pool on the surface of a metallic substrate. Several processing variables directly or indirectly affect the quality and structural integrity of components, dictated by solidification and metallurgical bonding [3].

DLD involves interactions between the laser beam, powder, and substrate in an environment with local protection from inert gas. Laser power, scanning speed, beam size, and powder feed rate are parameters that play a dominant role in cladding geometry (height, width, and length), dilution, and metallurgical properties. Clad overlapping, gas flow rate, powder flow profile, powder quality (size, shape, and density), and preheating are important secondary parameters [4,5].

The success of DLD depends on the selection of processing conditions that guar-antee an effective bonding of the deposited material. This proper bonding produces adequate thermal delivery control, dense layers, a small heat-affected zone (HAZ), low dilution, minimal distortion, and good surface quality, with an attractive set of me-chanical properties as well as resistance to wear and corrosion [6–8]. A controlled DLD process can replace conventional processes (i.e., electric arc welding and thermal spraying) in order to repair industrial components. Traditional approaches present drawbacks in component repairs, such as the time required, the limited thickness of the deposition layers, the low metallurgical bond, the formation of porosities and cracks, and the distortion of substrates (caused by overheating of the components). Therefore, it is of industrial interest to develop high-efficiency and precision repair technologies to increase component life.

This additive manufacturing technology is considered the best strategy for reconstructing and repairing damaged components in terms of environmental benefit and economic feasibility. However, it is regarded as a complex process due to uncertainties in the quality and reliability of recovered industrial components [9], requiring further investigation to consolidate the results reported in this area. Although the equipment cost is high, DLD has successfully repaired dies, moulds, turbines, and gears. Adaptability for automation, ease of assembly of the laser on a CNC machine or robotic arm, and lower post-processing requirements are additional advantages of the DLD process [10,11].

DLD still has a way to go for broader industrial applications. Theoretical and experimental studies have developed relevant information about DLD; however, there are still many challenges, such as process optimisation, 3D reconstruction of highly complex structures, and substrate preheating effects, which need to be clarified. The production of wear-resistant claddings on low and medium carbon steel substrates is an application that can have many industrial applications, both in component repair and protective coating with a thick resistant layer.

Nickel-based superalloys are an excellent option for producing this wear-resistant layer. These alloys have been adopted in multiple applications due to their properties, such as mechanical behaviour at high temperatures, hardness, mechanical resistance, and good fatigue resistance, creep, and corrosion [12,13]. These properties are conferred by the structure and chemical composition of the alloy, mainly by elements such as molybdenum (Mo) and niobium (Nb), which form a solid solution in a nickel–chromium matrix [14]. While conventional manufacturing with these high-performance alloys has been difficult due to excessive tool wear and low material deposition rates, LBAM technologies can overcome these constraints, improving delivery times, and reducing manufacturing costs [15].

The use of nickel-based superalloys in DLD must consider the high cooling rates of the process, promoted by the localised thermal delivery induced by the laser beam, which can lead to the formation of metastable phases and the segregation of elements. These microstructural effects reduce the toughness and hardness of the coated components [16–19]. Preheating (PHT) is essential to control the cooling rate, minimising this effect. Increasing PHT temperature promotes the growth of the melt pool (depth and width), melting more substrate, thus increasing dilution [20–24]. PHT also prevents cladding delamination or cracking and reduces distortion and residual stresses due to the lower thermal gradient between the cladding and substrate [7,25,26].

In this study, Inconel 625, a nickel-based superalloy, powder was deposited on 42CrMo4 steel, while the process parameters were varied. 42CrMo4 steel is often used to produce components, such as gears and main shafts, and Inconel 625 is employed in the repair/remanufacturing of these components by SERMEC Group. Single layers were produced to evaluate the metallurgical bonding with a substrate; the influence of several processing parameters, such as laser power, scanning speed, and powder feed rate on the cladding quality, was evaluated considering the absence of cracks and structural imperfections. Preheating was performed on an optimised cladding condition in order to moderate the microstructure and mechanical responses. Microhardness profiles of claddings were obtained and correlated with the microstructures.

Materials and Methods

DLD System Setup

A laser system, LDF 3000–100, was used to produce DLD claddings. The system has a high-power fibre-coupled laser diode (wavelength 900–1030 nm, depending on the power), with a nominal beam power of 6000 W. The machine concept is a KUKA KR90 R3100 industrial robot, based on a 6-axis industrial robot. All axes are connected to the robot and laser control units, which command the temperature of the melt pool as well as the laser power. The powder was fed during the deposition process by a coaxial feeding system, as illustrated in Figure 1. The substrate was preheated (PHT) to 300 °C with a manual gas system. The temperature control of the preheated substrate was done by a digital pyrometer, for verification of the uniformity of the substrate surface temperature distribution. Preheating is intended to decrease the cooling rate in the melt pool and HAZ regions as well as eliminate moisture. Tests were performed on substrates after the production of clads, with and without PHT, to evaluate suscepti-bility to cracking and eventual formation of metastable phases.

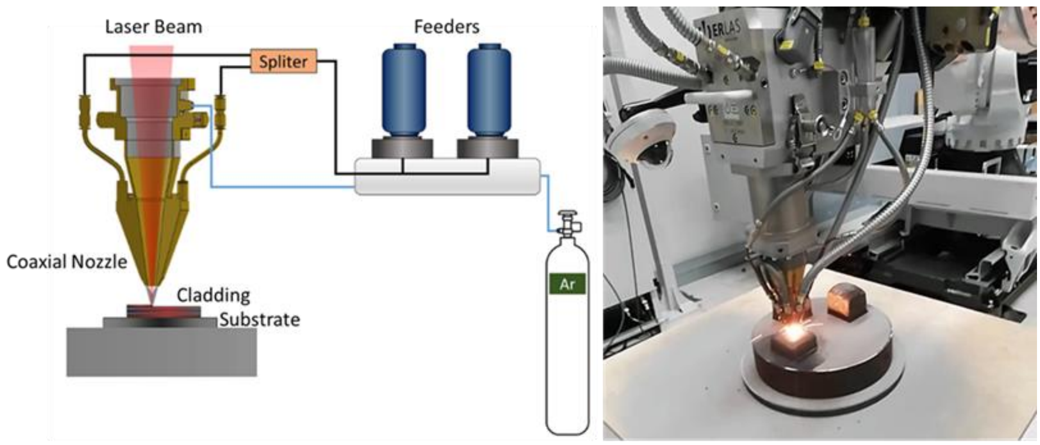

(A) (B)

Figure 1. (A) Schematic representation of the direct laser deposition system with two feeders; (B) system in operation.

Feedstock Powder and Substrate

A nickel-based superalloy (MetcoClad 625 from Oerlikon), similar to Inconel 625, produced by the gas- atomisation process, was used in this study. This powder was developed specifically for laser processing and presents a spherical morphology as well as particle sizes ranging between 45 and 90 μm. Figure 2 shows scanning electron microscopy (SEM) images of the morphology of the MetcoClad 625 powder.

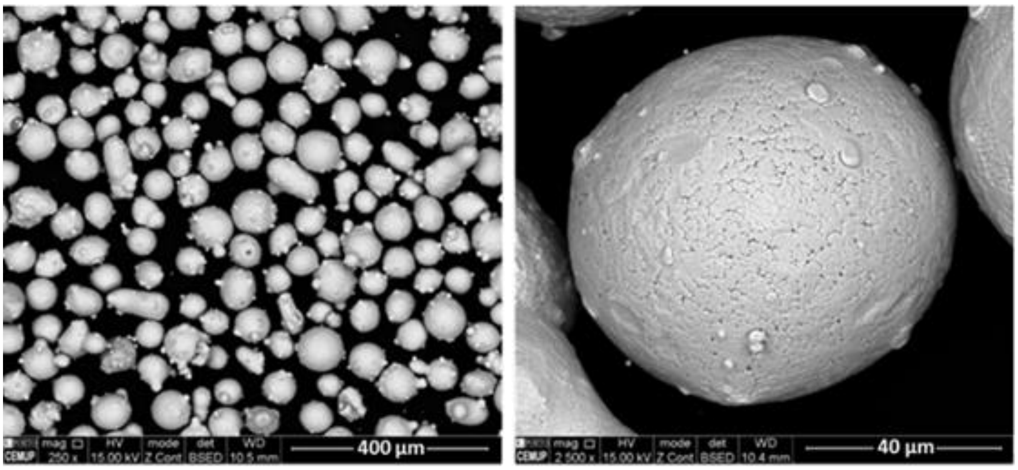

Figure 2. SEM images of MetcoClad 625 powder.

42CrMo4 steel, in the quenched and tempered condition, was used as a substrate for the DLD deposition. Specimens with dimensions of 100 mm × 120 mm × 15 mm were prepared for depositions. This steel is classified as a low alloy structural steel with high mechanical strength and toughness as well as good fatigue resistance and machinability, being widely used in the manufacturing of critical industrial components, such as gears, automotive components, wing generators, and drilling joints for deep wells [27]. Its mechanical and chemical properties are described in standard EN 10,269 [28]. The chemical composition of the MetcoClad 625 (M625) powder and 42CrMo4 steel are shown in Table 1.

Table 1. Chemical composition of M625 powder and 42CrMo4 steel (wt.%).

Material	Ni	Cr	Mo	Nb	Si	Mn	C	Fe
M625	60.8	21.3	9.2	4.6	-	-	-	4.1
42CrMo4	-	1.1	0.2	-	0.3	0.7	0.4	97.3

Process Parameters

The main process parameters (laser power, scanning speed, and feed rate) were considered to evaluate the effect of processing conditions on clads. The evaluation of the clad quality depends on clad characteristics, namely, absence of cracks or pores, good metallurgical bond (interfaces without microcracks, pores, and fragile phases, exhibiting good wettability), and dilution between 15 and 30%. The values of the tested parameters are shown in Table 2. All results are representative of single-layer samples. The terminology ILP_SS_FR was used to identify the samples, being I—M625 powder (Inconel powder); LP—laser power (kW); SS—scanning speed (mm/s); FR—feed rate (g/min). Eighteen combinations of different processing conditions were tested, with and without preheating (see Table 3). Before deposition, the substrates were cleaned with pure acetone.

Table 2. Process parameters tested for M625 deposition on 42CrMo4 substrate.

Process Parameters	Values
Laser power (LP)	1.0, 1.5, 2.0, 2.5, and 3.0 kW
Scanning speed (SS)	2.0, 4.0, 6.0, and 10.0 mm/s
Feed rate (FR)	10, 15, and 20 g/min

In all tests, a spot size of 2.5 mm and an offset in the Z-axis of 0.2 mm were used. High-purity argon (99.99%), with a 5.5 L/min flow rate, was used as the shielding gas for minimising contamination of the melt pool during the DLD process. Samples with and without PHT were cooled in air.

Mechanical and Microstructural Characterisation

Samples from each deposition were cut for microstructural and mechanical characterisation using a metallographic cut-off machine with refrigeration in order to avoid substrate and cladding overheating. Samples were mounted in resin and polished down to a 1 μm diamond suspension. Kalling's N°. 2 chemical etching ($CuCl_2$—5 g, hydrochloric acid—100 mL, and ethanol—100 mL) was used to reveal the micro-structures.

The measurements of the height, depth, and width of the claddings produced by the DLD technique were performed using a Leica DVM6 A 2019 digital microscope (DM) (Wetzlar, Germany). The Leica DM 4000 M optical microscope (OM) (Wetzlar, Germany) allowed for a microstructural analysis at low magnifications to evaluate, for example, the size of the heat-affected zone. A scanning electron microscope, FEI Quanta 400 FEG (ESEM, Hillsboro, OR, USA), equipped with energy-dispersive X-ray spectroscopy (EDX) (EDAX Genesis X4M, Oxford Instrument, Oxfordshire, UK) and electron backscatter diffraction (EBSD) (EDAX-TSL OIM EBSD, Mahwah, NJ, USA) was used for higher magnification observation and phase identification. For EBSD evaluation, the samples went through an additional polishing step, using a 0.06 μm silica colloidal suspension, for a superior surface finish and to remove polish-ing-induced plastic deformations, allowing Kikuchi patterns to be obtained [29]. EBSD allows for the obtaining of information on microstructural characteristics with a small interaction volume and a high resolution, for which TSL OIM Analysis 5.2 software was used. For all raw data obtained by EBSD, a dilatation clean-up routine was performed, with a grain tolerance angle of 15° and a minimum grain size of 10 points.

Quantitative image analysis was employed on optical images using the ImageJ software, version 1.51p (National Institutes of Health, Bethesda, MD, USA).

Vickers microhardness tests gave the mechanical characterisation. The tests were performed using a test force of 300 g for 15 s in a Struers Duramin 5 (Struers Inc., Cleveland, OH, USA) Vickers hardness tester. Each hardness value corresponds to the average of three indentations.

Results and Discussion

Processing Effects

The quality of cladding was first evaluated by inspection with a digital micro-scope (DM). The microstructural analysis of all the claddings produced did not detect cracks, pores, or inclusions of significant dimensions, an essential requirement for ob-taining high-performance deposits.

SEM characterisation confirmed the observations made by the DM. Figure 3 shows an SEM image of the cross-section of an M625 clad deposited on 42CrMo4 steel, representing the geometric aspects of cladding: height (h), width (w), depth (d), clad area (AC), melting area (AM), and wetting angle (ϴ). These geometric aspects were measured on all claddings using the ImageJ software. The results are shown in Table 3.

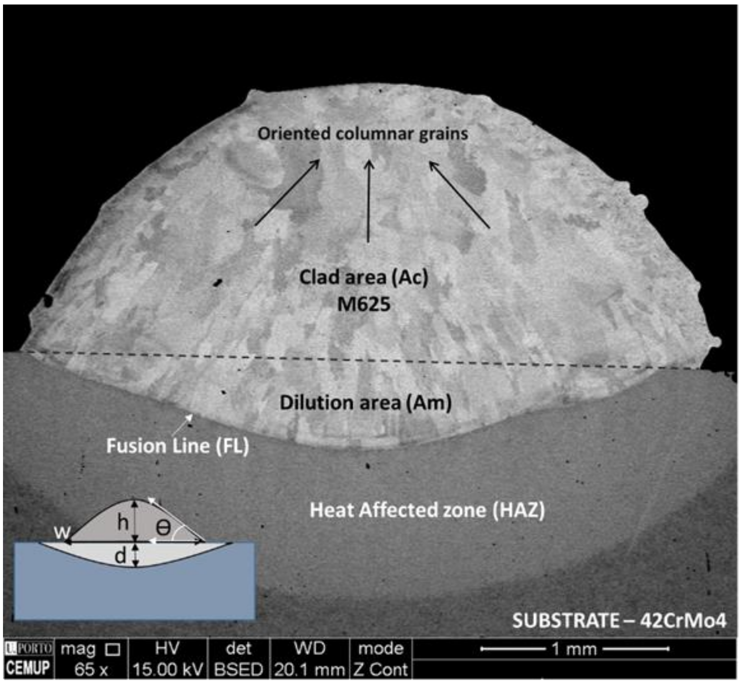

Figure 3. Cross-section of a single layer of M625 deposited on 42CrMo4: d—depth; h—height; w—width; ϴ—contact angle; AC—clad area; and AM—melting area.

This analysis of the geometry of the single-track deposits is critical as it provides information on process yield and cladding performance. For example, the contact angle is an essential parameter in assessing the quality of the cladding [30,31]. Higher beads can promote low wettability during the deposition of multi-tracks, hindering overlapping and generating discontinuities in the hatch spacing of the overlapping deposits, thus facilitating crack propagation. Typically, a contact angle greater than 90° is associated with lower-quality claddings [32]. Table 3 shows that depositions with higher heights have a high contact angle, as samples I1_2_15, I2_2_15, and I3_2_15 demonstrate.

Table 3. Dimensional analysis of claddings produced by DLD.

Sample	Cladding Dimensional Analysis						
	W (mm)	H (mm)	D (mm)	θ (°)	AC (mm^2)	AM (mm^2)	D (%)
I1_2_15	2.79	3.07	0.25	121	9.9	0.3	2.6
I1_6_15	3.07	1.22	0.06	64	3.0	0.0	1.3
I1.5_10_10	3.09	0.71	0.43	47	5.8	2.1	26.5
I1.5_10_15	3.11	1.03	0.23	64	2.3	0.2	7.3
I2_2_15	3.62	3.66	1.28	107	15.2	3.0	16.6
I2_4_15	3.50	2.47	1.12	88	7.2	2.4	25.0
I2_6_10	3.38	1.39	1.16	53	3.3	2.3	40.6
I2_6_15	3.61	1.47	0.51	65	4.5	1.3	22.0
I2_6_20	3.63	1.71	0.56	74	4.9	1.2	19.5
I2_10_10	3.20	1.20	0.72	58	2.7	1.1	29.1
I2_10_15	3.36	0.81	0.88	40	1.9	1.5	45.1
I2.5_10_10	3.33	0.86	1.04	49	2.1	2.3	52.1
I2.5_10_15	3.36	1.23	1.00	51	2.9	1.9	39.8
I3_2_15	5.05	3.40	2.06	99	15.4	6.6	29.9
I3_4_15	4.64	2.06	0.89	70	7.5	2.5	25.3
I3_6_10	3.89	1.85	1.08	74	6.2	2.8	30.8
I3_6_15	4.71	0.78	0.68	37	2.8	2.6	48.0
I3_6_20	3.94	1.55	1.34	69	4.6	3.3	41.6

The results presented in Table 3 show that the analysed processing parameters (laser power, scanning speed, powder feed rate, and preheating) strongly influence the production of the cladding and its bonding to the substrate. The selection of a processing window that guarantees a metallurgically bonded clad with good material yield is a fundamental task. This selection is difficult since the mutual interaction of the various parameters is complex. Thus, it is common to apply combined parameters in the DLD process to obtain a more accurate relationship between processing parameters and the clad characteristics [33].

One of the most used complex parameters is powder deposition density (PDD), which expresses the combined effect of feed rate, scanning speed, and laser spot size (φ) (Equation (1)) [34–36]. Figure 4 exposes the linear growth of the cladding area with the increase in the PDD parameter.

$$PDD\ (g/mm^2) = FR/(SS \times \varphi) \quad (1)$$

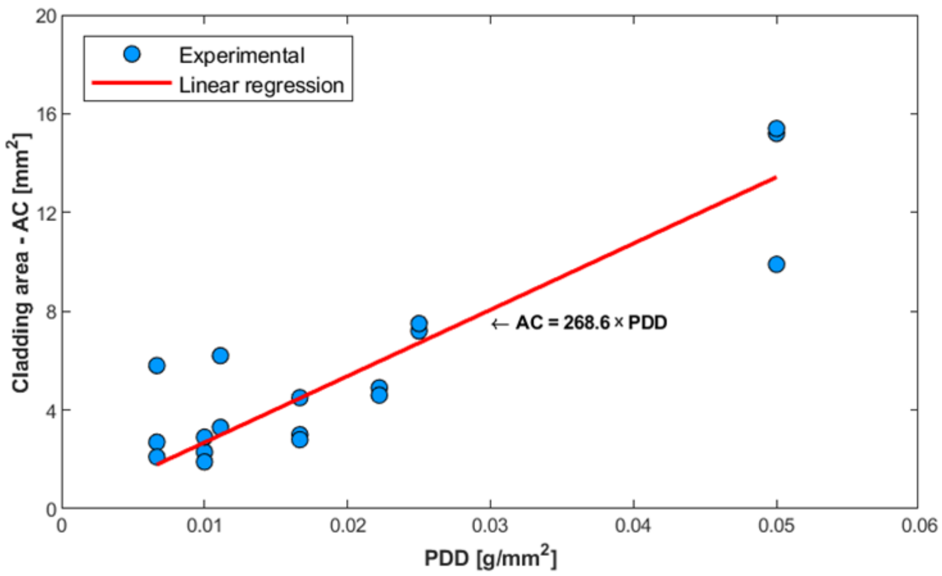

Figure 4. Dependence of cladding area on the value of the PDD complex parameter.

This parameter shows that by increasing the feed rate or decreasing the scanning speed, we can obtain claddings with a larger area, which was expected since both situations result in more powder supply in the same period of time. PDD is a valuable parameter, but this relationship is only valid for the cladding area and not for the total area of the deposit, including the area of the substrate that has been melted. This last area is vital because it affects the quality of the cladding.

Additionally, with the measured areas (Table 3), it was possible to calculate the dilution, which quantifies the relative amount of melted substrate during laser processing, according to Equation (2).

$$\text{Dilution (\%)} = AM/(AC + AM) \times 100 \quad (2)$$

A dilution ratio between 15 and 30% is sufficient to allow a good metallurgical bond between the substrate and the cladding. Higher dilution, which means a greater melting of the substrate, is undesirable since it reduces the deposition yield and induces considerable changes in the chemical composition of the deposited material, modifying the expected properties of the cladding.

The results obtained, and presented in Table 3, indicate that dilution increases with increased laser power, keeping the other processing variables constant. A laser power of 1.5 kW is enough to guarantee a dilution higher than 15% for almost all conditions (the only exception is the I1.5_10_15 sample).

Despite this apparent direct relation between laser power and dilution, the effect of other critical processing variables, namely the scanning speed and the feed rate, makes the establishment of relationships between processing condition and dilution complex. To overcome this difficulty, it is common to apply complex parameters, empirically adjusted, to the clad/substrate set under analysis to define the processing window [33,37,38].

Figure 5 shows a process window map, which associates laser power with the scanning speed and feeding rate ratio, as well as the dilution that is correlated with the laser power through complex parameter LP $(SS/FR)^{0.5}$; it is represented by two curves, one for 15% and the other for 30%. Additionally, as was also considered in the map, a vertical line that corresponds to the acceptable limit for the wetting angle is present.

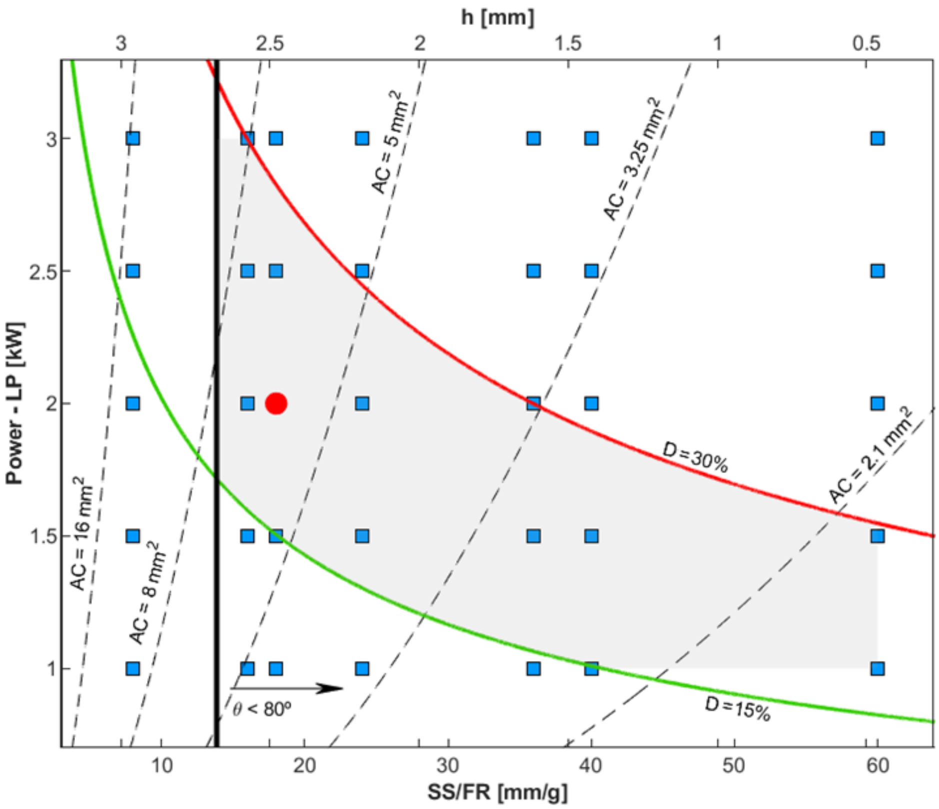

Figure 5. DLD process window map of M625 for additive manufacturing of single tracks. Red point represents the experimental I2_6_20 condition.

As seen in Figure 5, the shaded area, delimited by the previous conditions (dilution range, acceptable wetting angle, and process parameters), reveals the desirable practical manufacturing processing window of Inconel 625. In addition, the dilution increases proportionally with the increase in laser power and decreases with the ratio between scanning speed and feeding rate [39]. The flow of liquid metal in the melt pool is dominated by Marangoni's convection effect, caused by the surface tension gradient. As the temperature of the substrate increases, this effect becomes more evident. How-ever, in practice, the surface tension gradient (γ) $d\gamma/dT$ depends on both temperature (T) and composition. In this case, the most significant influence factor is the thermal gradient promoted between laser beam and substrate, as Le et al. [40] demonstrated, where the increase in the substrate temperature becomes more evident.

Laser power control allows the required good metallurgical integrity and dilution to be achieved [41], producing a cladding with a good metallurgical bond and uniform properties. Increasing the power of the laser promotes increased energy density as well as greater dilution and mixing between the substrate and the deposited powder, which is characteristic of the laser alloy process [42].

Considering the analyses performed, the I2_2_15, I2_4_15, I2_6_15, I2_6_20, I2_10_10, I3_2_15, and I3_4_15 conditions showed dilutions within the established range, between 16.6% and 29.9%, but a lower dilution value is preferable. Nevertheless, the I2_2_15, I2_4_15, and I3_2_15 samples presented poor wettability angles (107°, 88°, and 99°, respectively) that may lead, in future, to claddings with overlapping defects between strands. On the other hand, the four remaining conditions presented good wetting angles, but taking into account not only the quality of the process but also its efficiency, condition I2_6_20 (Figure 5 red point) is the only one that allows for the possibility of manufacturing a larger cladding area and consequently a higher cladding high, which has an inverse linear relationship with the SS/FR ratio. Considering this evaluation, the I2_6_20 condition will be used to perform the analyses throughout the following sections.

Microstructures and Mechanical Characterisation of the DLD Samples

Figure 6 shows the cladding microstructure formed adjacent to the substrate by the deposition of M625 on 42CrMo4 steel. This microstructure consists of columnar grains, mainly dendrites, and cellular morphologies in a few regions.

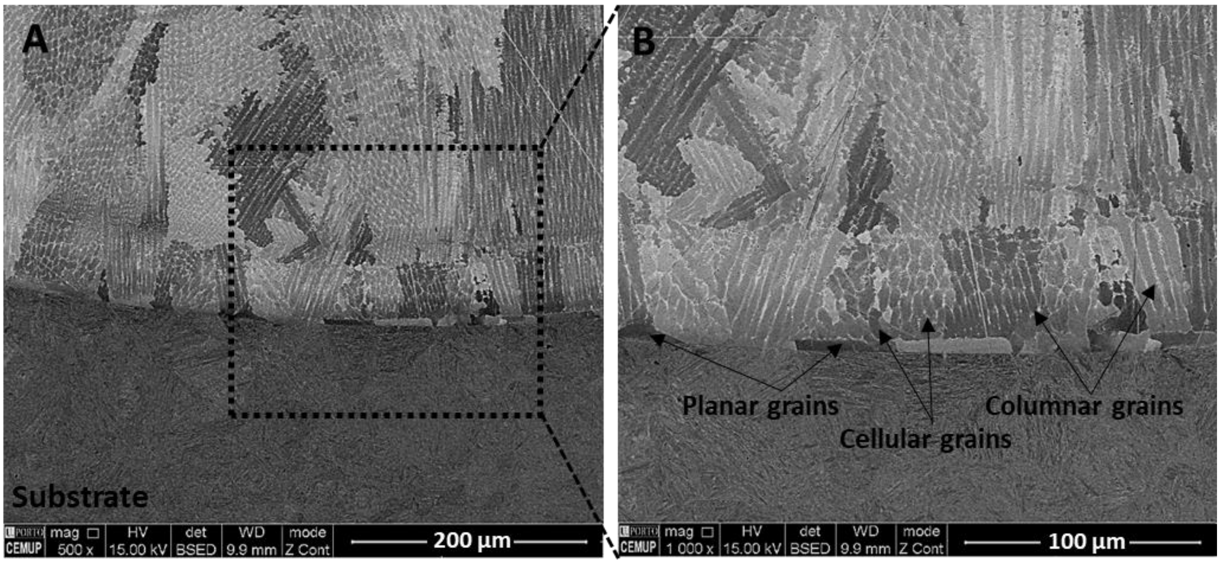

Figure 6. Microstructure of cladding produced by the I2_6_20 cladding condition on the preheated substrate, showing (**A**) substrate interface cladding zone. (**B**) A higher magnification illustration of the interface.

As shown in Figure 6B, on solidification a continuous thin layer, < 10 µm, consist-ing of planar grains formed in the vicinity of the substrate. This morphology evolves into columnar grains with continued solidification of the cladding. This microstructure is consistent with the results of a similar study in which martensitic stainless steel is deposited [43]. The very high thermal gradient in the contact zone of the melt pool with the cold substrate contributed to the formation of planar grains. The microstructure evolves into a columnar/dendritic structure due to a rapid decrease in the thermal gradient when more material solidifies. Moreover, columnar grains grow perpendicular to the substrate/solidified material, i.e., in the opposite direction of the primary heat dissipation source, as is usual in DLD solidification [44]. As seen in Figure 7, this columnar/dendritic structure is the characteristic microstructure of the cladding.

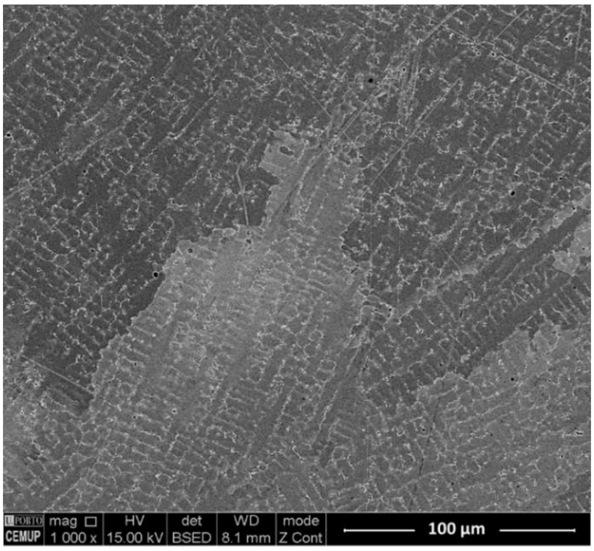

Figure 7. SEM image of the I2_6_20 cladding microstructure.

Figure 8 shows a high-magnification SEM image and elemental mapping of the microstructure of the I2_6_20 cladding. This microstructure consists of the γ matrix, bright zones (surrounded by a segregation zone), and rounded dark particles. The elemental mapping indicates that the bright zones are rich in Mo and Nb, indicating the formation of the Laves phase located at an the interdendritic region. Rounded dark particles are complex oxides dispersed in the γ matrix. Table 4 shows the chemical composition obtained by EDX analysis of the zones indicated in Figure 8.

The γ dendrites are formed during the solidification of nickel-based superalloys processed by DLD, segregating Nb and Mo into the liquid, thus creating the local conditions for forming the Laves phase. The final stage of non-equilibrium solidification thus gives rise to this microstructure consisting mainly of the γ matrix and Laves phase. A similar microstructure has been found in other nickel-based superalloy solidi-fication studies [45–51].

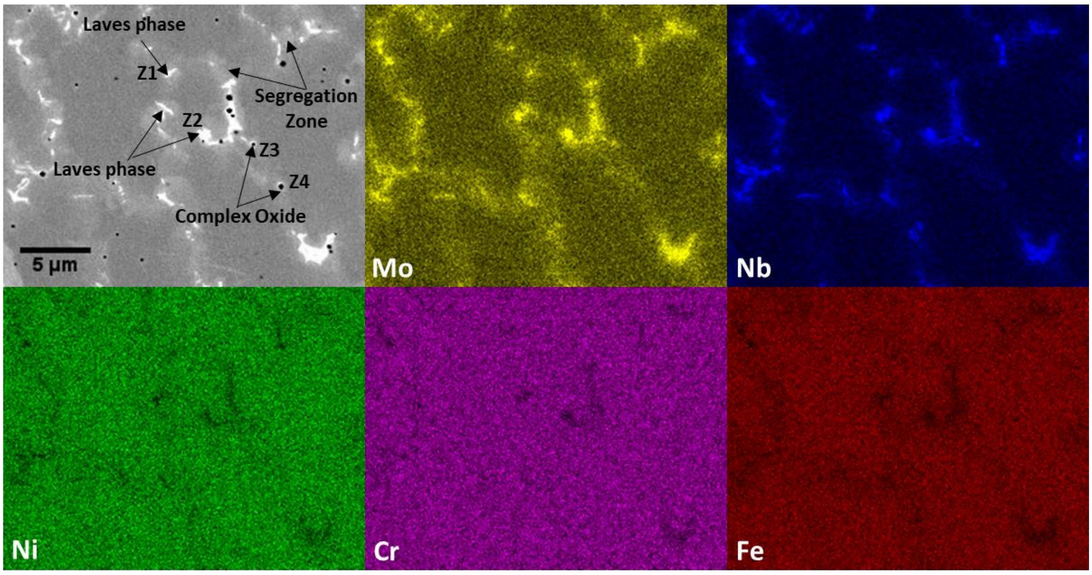

Figure 8. SEM image and the elemental maps obtained by EDX microanalysis showing segregation zones associated with the Laves phase and complex oxides.

Table 4. Chemical composition (%) of the zones indicated in Figure 8.

Phases	Zones	Ni	Cr	Mo	Nb	Si	Fe	Mn	Al	Ca	C	O
Laves phase	Z1	42.16	17.39	10.97	10.88	3.17	15.43	-	-	-	-	-
	Z2	42.29	17.91	10.62	10.34	2.63	16.21	-	-	-	-	-
Oxide	Z3	0.33	4.24	-	1.11	13.00	-	2.44	15.83	4.70	2.58	55.77
	Z4	0.71	4.38	-	1.18	14.71	-	1.78	14.58	6.91	-	55.75

Laves phase formation promotes the initiation and propagation of cracks, with a detrimental effect in mechanical response, reducing ductility, ultimate tensile strength, fracture resistance, and fatigue life [52,53]. Thus, this phase reduces the performance of Inconel 625, requiring control of morphology and distribution in the cladding.

A similar analysis was performed at the cladding/substrate interface, Figure 9. In the continuous thin layer adjacent to the substrate, characterized by planar grains (see Figure 6), the thermal gradient and growth rate are significantly different from those of the dendritic region, and the Laves phase was not detected.

Figure 9 shows that DLD deposition of M625 on the 42CrMo4 substrate led to cladding with a flat interface, with a thin continuous layer of planar γ grains, followed by γ dendrites and a dispersed Laves phase. As already mentioned, the appearance of the Laves phase in this region has a detrimental effect and should be minimized.

Therefore, another cladding was performed with the substrate preheated to 300 °C. This procedure leads to a decrease in the thermal gradient of the deposited layer, influencing the microstructure. Preheating (PHT) increases the interdiffusion of constit-uents of M625 and 42CrMo4 at the bonding interface and, by decreasing the substrate cooling rate, can also affect the microstructure and properties in the heat-affected zone.

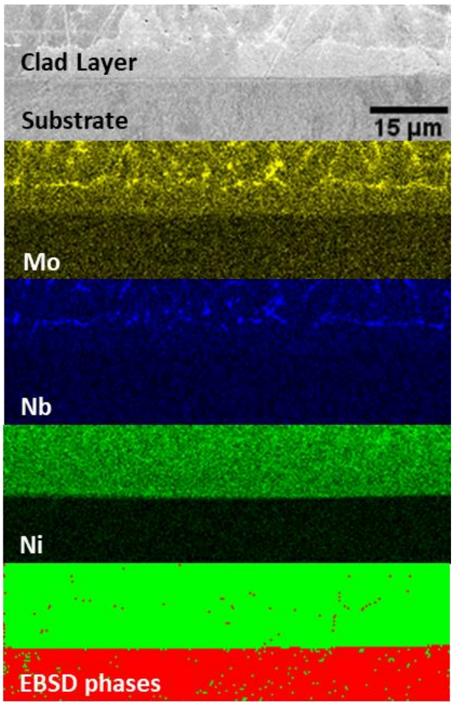

Figure 9. SEM image and elemental maps obtained by EDX microanalysis of M625 deposited on 42CrMo4 substrate. An EBSD image shows the phase distribution in this region: FCC phases in green and BCC phases in red.

The influence of PHT application on the cladding/substrate interface is shown in Figure 10. The thin layer of planar grains was not formed. Substrate heating significantly reduced the thermal gradient in the initial solidification phase of the melt pool, leading to the formation of dendrites throughout the cladding. Furthermore, it appears that PHT slightly increases the interdendritic spacing from 5–7 µm to 6–9 µm, meas-ured by ImageJ software in Figures 6 and 10, respectively. This observation confirms the decrease in the cooling rate allowing the growth of the interdendritic spacing. This feature is consistent with a study that indicates that lower cooling rates promote dendrite growth and decrease cellular grain formation in the initial stages of solidification [54].

Besides, the application of PHT has led to the reduction in Laves phases, this effect highlighted at the interface zone, as seen in Figure 11. A lower cooling rate effectively maintained the Nb and Mo in the γ matrix, avoiding segregation. Moreover, the elemental mapping and EBSD image in Figure 11 confirm a more intense interdiffusion at the interface, which is not as plane as it was without PHT, Figure 9. Diffusion of nickel, which is a gamma-phase stabilizer, to steel is associated with a greater amount of re-sidual austenite in this region. Thus, the application of preheating seems helpful for reducing the deleterious Laves phase and for enhancing metallurgical bonding.

The HAZ of 42CrMo4 steel is also a critical region, as substrate heating by the laser followed by rapid cooling leads to martensite formation, which can create cracks and allow for rapid crack propagation. Microstructural differences in HAZ caused by PHT were analysed by EBSD, as illustrated in Figure 12. This figure shows that PHT affects the HAZ microstructure, with larger (longer and wider) martensite laths caused by a slower cooling rate. Martensite with wider laths is associated with lower mechanical strength which, together with the more significant amount of residual austenite determined when using PHT, can reduce the brittleness of this region.

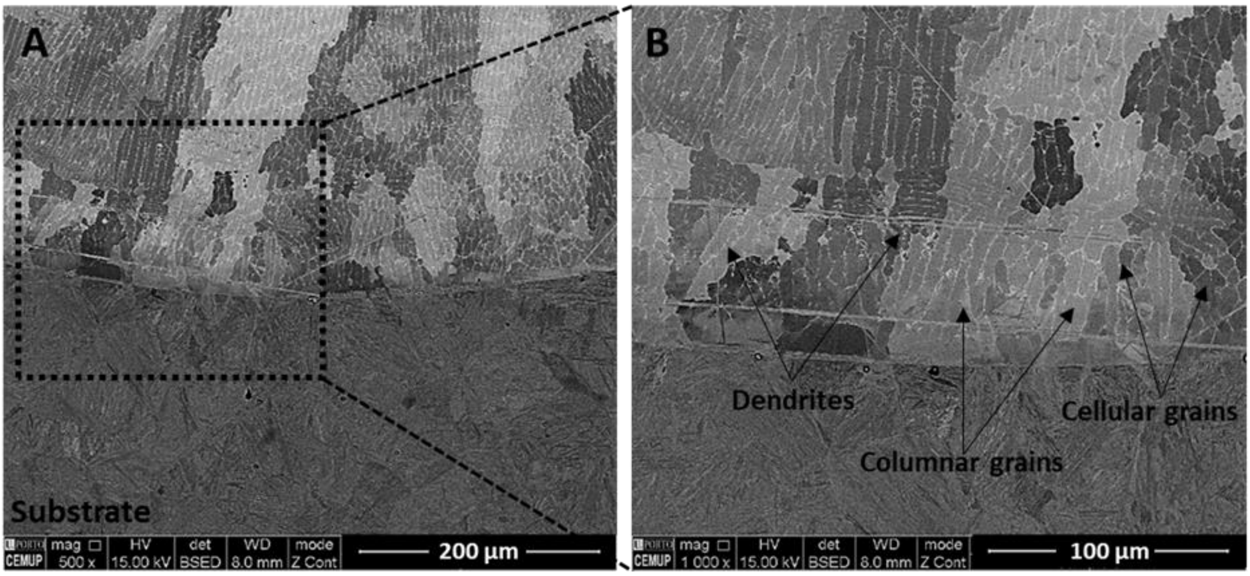

Figure 10. Microstructure of cladding produced by the I2_6_20 cladding condition on the preheated substrate, showing (**A**) substrate interface cladding zone. (**B**) A higher magnification illustration of the interface.

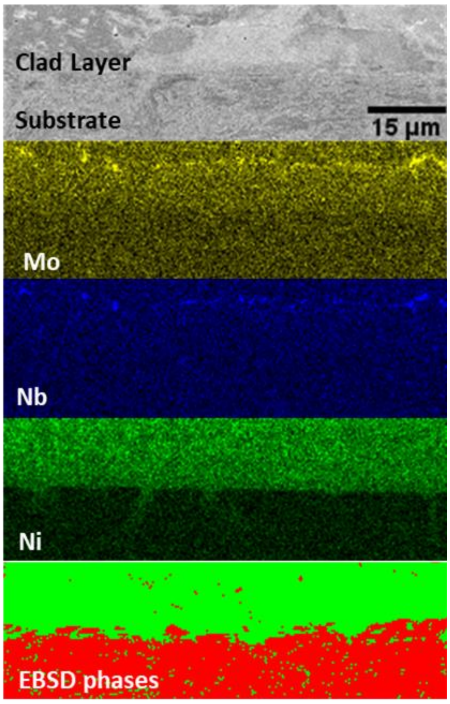

Figure 11. SEM image and elemental maps obtained by EDX microanalysis of M625 deposited on preheated (PHT) 42CrMo4 substrate. An EBSD image shows the phase distribution in this region: FCC phases in green and BCC phases in red.

Figure 12 also shows that no preferential crystalline orientation was formed in the HAZ of claddings without or with PHT.

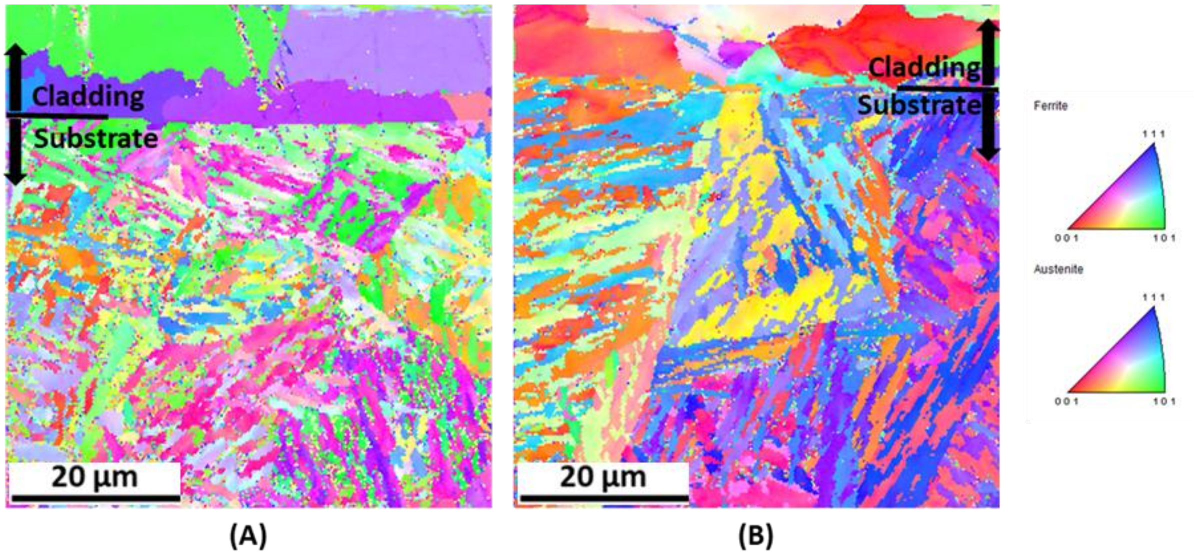

Figure 12. EBSD images of the I2_6_20/substrate interface region. (**A**) Without PHT; (**B**) with PHT.

Microhardness Measurements

The microhardness profile shown in Figure 13 shows that the hardness distribution in the cladding zone is uniform and independent of PHT, with an average hardness of 258 ± 2 HV and 253 ± 2 HV for the samples with and without preheating, respectively. A sharp transient zone with a pronounced hardness increase is measured in the HAZ of the sample without PHT (maximum hardness of 491 ± 23 HV). The application of PHT to the substrate before deposition produced a more uniform distribution of hardness in the HAZ (368 ± 25 HV), with a less sharp transient near the interface. Furthermore, the hardness peak has been eliminated, and the hardness values show less dispersion. These differences in hardness are attributed to changes in the microstructure induced by PHT, as seen in Figure 12, and its influence on chemical composition distribution, seen in Figures 9 and 11, and indicate that the HAZ region is less prone to cracking.

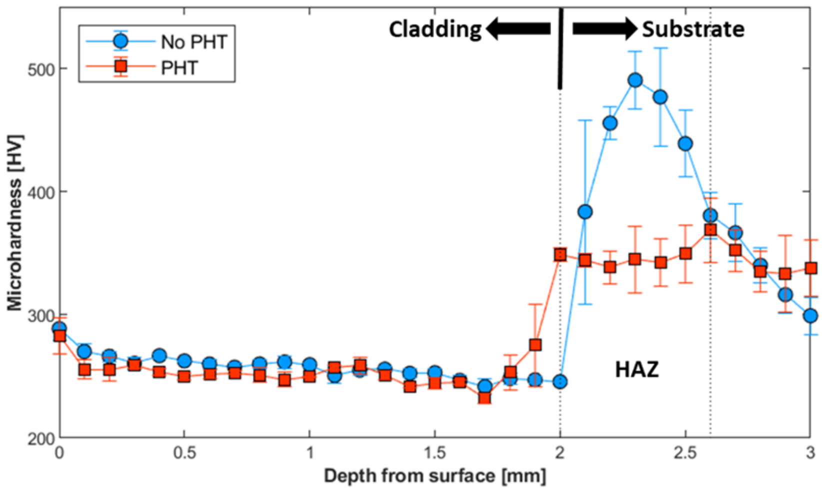

Figure 13. Microhardness profile of cladded samples applying the I2_6_20 condition with and without PHT.

Conclusions

The deposition of Inconel 625 claddings onto a 42CrMo4 steel substrate was performed using direct laser deposition (DLD) and varying processing conditions: laser power, scanning speed, feed rate, and preheating. Macro- and microstructural analysis, in addition to the hardness measurements, led to the following main conclusions:

- A DLD process window map considering processing variables shows that several combinations can be used. However, the cladding produced with 2 kW of laser power, a scanning speed of 6 mm/s, and a 20 g/min feed rate presented adequate dilution and wettability.

- The deposited layers were produced without significant structural defects such as cracks, pores, or other types of discontinuities.

- Substrate preheating to 300 °C influences the microstructure of the cladding/substrate interface, reducing the formation of the deleterious Laves phase.

- PHT also alters the hardness profile, mainly in the heat-affected zone, due to modification of the martensite microstructure and increased residual austenite.

Author Contributions: A.A.F., M.F.V., and A.R.R. proposed the methodology and results data analyses followed in this research; A.A.F., J.M.C., P.C.R., and R.L.A. carried out the experimental tests. All authors participated in the discussion of results and writing of the manuscript. All authors have read and agreed to the published version of the manuscript.

Funding: This research was funded by FEDER through the Operational Programme for Competitiveness and Internationalization (COMPETE 2020), Projetos em Copromoção (project POCI-01-0247-FEDER-039848).

Institutional Review Board Statement: Not applicable.

Informed Consent Statement: Not applicable.

Data Availability Statement: Not applicable.

Acknowledgments: The authors give their thanks to the CEMUP (Centro de Materiais da Universidade do Porto) for expert assistance with SEM.

Conflicts of Interest: The authors declare no conflict of interest.

References

1. Bian, L.; Shamsaei, N.; Usher, J.M. Laser-Based Additive Manufacturing of Metal Parts, 1st ed.; CRC Press: Boca RatonTaylor & Francis Group, FL, USA, 2018.
2. Ur Rahman, N.; Matthews, D.T.; de Rooji, M.; Khorasani, A.M.; Gibson, I.; Cordova, L.; Römer, G. An Overview: La-ser-Based Additive Manufacturing for High Temperature Tribology. Front. Mech. Eng. 2019, 5, 1–15, doi:10.3389/fmech.2019.00016.
3. Thompson, S.M.; Bian, L.; Shamsaei, N.; Yadollahi, A. An overview of Direct Laser Deposition for additive manufacturing; Part I: Transport phenomena, modeling and diagnostics. Addit. Manuf. 2015, 8, 36–62, doi:10.1016/j.addma.2015.07.001.
4. Song, L.; Bagavath-Singh, V.; Dutta, B.; Mazumder, J. Control of melt pool temperature and deposition height during direct metal deposition process. Int. J. Adv. Manuf. Technol. 2012, 58, 247–256, doi:10.1007/s00170-011-3395-2.
5. Petrat, T.; Graf, B.; Gumenyuk, A.; Rethmeier, M. Laser metal deposition as repair technology for a gas turbine burner made of inconel 718. Phys. Procedia 2016, 83, 761–768, doi:10.1016/j.phpro.2016.08.078.

6. Alimardani, M.; Fallah, V.; Khajepour, A.; Toyserkani, E. The effect of localised dynamic surface preheating in laser cladding of Stellite 1. Surf. Coatings Technol. 2010, 204, 3911–3919, doi:10.1016/j.surfcoat.2010.05.009.
7. Leunda, J.; García Navas, V.; Soriano, C.; Sanz, C. Effect of laser tempering of high alloy powder metallurgical tool steels after laser cladding. Surf. Coatings Technol. 2014, 259, 570–576, doi:10.1016/j.surfcoat.2014.10.028.
8. Dass, A.; Moridi, A. State of the art in directed energy deposition: From additive manufacturing to materials design. Coatings 2019, 9, 418, doi:10.3390/COATINGS9070418.
9. Lahrour, Y.; Brissaud, D. A Technical Assessment of Product/Component Re-manufacturability for Additive Remanufactur-ing. Procedia CIRP 2018, 69, 142–147, doi:10.1016/j.procir.2017.11.105.
10. Kush, M. Advanced Manufacturing Technologies Modern Machining Advanced Joining Sustainable Manufacturing; Springer Inter-national Publishing: New York, NY, USA, 2018; p. 294, doi:10.1007/978-3-319-56099-1.
11. Pinkerton, A.J.; Wang, W.; Li, L. Component repair using laser direct metal deposition. Proc. Inst. Mech. Eng. B J. Eng. Manuf. 2008, 222, 827–836, doi:10.1243/09544054JEM1008.
12. Vilar, R.; Almeida, A. Repair and manufacturing of single crystal Ni-based superalloys components by laser powder deposi-tion—A review. J. Laser Appl. 2015, 27, S17004, doi:10.2351/1.4862697.
13. Abioye, T.E.; McCartney, D.G.; Clare, A.T. Laser cladding of Inconel 625 wire for corrosion protection. J. Mater. Process. Technol. 2015, 217, 232–240, doi:10.1016/j.jmatprotec.2014.10.024.
14. Marchese, G.; Colera, X.G.; Calignano, F.; Lorusso, M.; Biamino, S.; Minetola, P.; Manfredi, D. Characterization and Com-parison of Inconel 625 Processed by Selective Laser Melting and Laser Metal Deposition. Adv. Eng. Mater. 2017, 19, 1–9, doi:10.1002/adem.201600635.
15. Gonzalez, J.A.; Mireles, J.; Stafford, S.W.; Perez, M.A.; Terrazas, C.A.; Wicker, R.B. Characterization of Inconel 625 fabricat-ed using powder-bed-based additive manufacturing technologies. J. Mater. Process. Technol. 2019, 264, 200–210, doi:10.1016/j.jmatprotec.2018.08.031.
16. Long, Y.T.; Nie, P.L.; Li, Z.G.; Huang, J.; Li, X.; Xu, X.M. Segregation of niobium in laser cladding Inconel 718 superalloy. Trans. Nonferrous Met. Soc. China 2016, 26, 431–436, doi:10.1016/S1003-6326(16)64131-6.
17. Xiao, H.; Li, S.; Han, X.; Mazumder, J.; Song, L. Laves phase control of Inconel 718 alloy using quasi-continuous-wave laser additive manufacturing. Mater. Des. 2017, 122, 330–339, doi:10.1016/j.matdes.2017.03.004.
18. Singh, G.; Vasudev, H.; Bansal, A.; Vardhan, S.; Sharma, S. Microwave cladding of Inconel-625 on mild steel substrate for corrosion protection. Mater. Res. Express 2020, 7, doi:10.1088/2053-1591/ab6fa3.
19. Feng, K.; Feng, K.; Chena, Y.; Denga, P.; Li, Y.; Zhao, H.; Lu, F.; Li, R.; Jian, H.; Li, Z. Improved high-temperature hardness and wear resistance of Inconel 625

coatings fabricated by laser cladding. J. Mater. Process. Technol. 2017, 243, 82–91, doi:10.1016/j.jmatprotec.2016.12.001.
20. Farahmand, P.; Kovacevic, R. Laser cladding assisted with an induction heater (LCAIH) of Ni-60%WC coating. J. Mater. Process. Technol. 2015, 222, 244–258, doi:10.1016/j.jmatprotec.2015.02.026.
21. Wang, Z.; Zhao, J.; Zhao, Y.; Zhang, H.; Shi, F. Microstructure and microhardness of laser metal deposition shaping K465/stellite-6 laminated material. Metals 2017, 7, 512, doi:10.3390/met7110512.
22. Bennett, J.; Dudas, R.; Cao, J.; Ehmann, K.; Hyatt, G. Control of Heating and Cooling for Direct Laser Deposition Repair of Cast Iron Components. In Proceedings of the International Symposium on Flexible Automation, ISFA 2016, Cleveland, OH, USA, 1–3 August 2016.
23. The Laser Repair Process of High-Speed Gear Transmission Body with Better Wear Resistance and Higher Hardness. CN 106222651 A, 14 December 2016.
24. Sadhu, A.; Choudhary, A.; Sarkar, S.; Nair, A.M.; Nayak, P.; Pawar, S.D.; Muvvala, G.; Pal, S.K.; Nath, A.K. A study on the influence of substrate preheating on mitigation of cracks in direct metal laser deposition of NiCrSiBC-60%WC ceramic coat-ing on Inconel 718. Surf. Coatings Technol. 2020, 389, 125646, doi:10.1016/j.surfcoat.2020.125646.
25. Shim, D.S.; Baek, D.S.; Lee, S.B.; Yu, J.H.; Choi, Y.S.; Park, S.H. Influence of heat treatment on wear behavior and impact toughness of AISI M4 coated by laser melting deposition. Surf. Coatings Technol. 2017, 328, 219–230, doi:10.1016/j.surfcoat.2017.08.059.
26. He, W.; Shi, W.; Li, J.; Xie, H. In-situ monitoring and deformation characterisation by optical techniques; part I: Laser-aided direct metal deposition for additive manufacturing. Opt. Lasers Eng. 2019, 122, 74–88, doi:10.1016/j.optlaseng.2019.05.020.
27. Sun, C.; Fu, P.X.; Liu, H.W.; Liu, H.H.; Du, N.Y. Effect of tempering temperature on the low temperature impact toughness of 42CrMo4-V steel. Metals 2018, 8, 232, doi:10.3390/met8040232.
28. Steels and Nickel Alloys for Fasteners with Specified Elevated and/or Low Temperature.; BSI. Standard, ISBN 978 0 580 76784 5, 2013. ; 2006.
29. Engler, O.; Randle, V. Introduction to texture analysis: Macrotexture, Microtexture and Orientation Mapping. 2010, 2st edi-tion, CRC Press: Taylor & Francis Group, FL, USA. Davies, E.R. Introduction to texture analysis. In Handbook of Texture Anal-ysis; Mirmehdi, M., Xie, X., Suri, J, Eds. Imperial College Press: London, UK, 2008.
30. Abioye, T.E.; Folkes, J.; Clare, A.T. A parametric study of Inconel 625 wire laser deposition. J. Mater. Process. Technol. 2013, 213, 2145–2151, doi:10.1016/j.jmatprotec.2013.06.007.
31. Toyserkani, E.; Khajepour, A.; Corbin, S. Laser Cladding.; 2004, 1st edition, CRC Press: Taylor & Francis Group, FL, USA. CRC Press: Boca Raton, FL, USA, 2017; vol. 11, no. 2.

32. Li, C.; Guo, Y.B.; Zhao, J.B. Interfacial phenomena and characteristics between the deposited material and substrate in selec-tive laser melting Inconel 625. J. Mater. Process. Technol. 2017, 243, 269–281, doi:10.1016/j.jmatprotec.2016.12.033.
33. Ferreira, A.A.; Darabi, R.; Sousa, J.P.; Cruz, J.M.; Reis, A.R.; Vieira, M.F. Optimization of direct laser deposition of a marten-sitic steel powder (Metco 42c) on 42CrMo4 steel. Metals 2021, 11, 672, doi:10.3390/met11040672.
34. Emamian, A.; Corbin, S.F.; Khajepour, A. In-Situ Deposition of Metal Matrix Composite in Fe-Ti-C System Using Laser Clad-ding Process. Met. Ceram. Polym. Compos. Var. Uses 2011, doi:10.5772/10593.
35. Farshidianfar, M.H.; Khajepour, A.; Gerlich, A.P. Effect of real-time cooling rate on microstructure in Laser Additive Manu-facturing. J. Mater. Process. Technol. 2016, 231, 468–478, doi:10.1016/j.jmatprotec.2016.01.017.
36. Emamian, A.; Corbin, S.F.; Khajepour, A. Effect of laser cladding process parameters on clad quality and in-situ formed mi-crostructure of Fe-TiC composite coatings. Surf. Coatings Technol. 2010, 205, 2007–2015, doi:10.1016/j.surfcoat.2010.08.087.
37. Ocelík, V.; de Oliveira, U.; de Boer, M.; de Hosson, J.T.M. Thick Co-based coating on cast iron by side laser cladding: Analysis of processing conditions and coating properties. Surf. Coatings Technol. 2007, 201, 5875–5883, doi:10.1016/j.surfcoat.2006.10.044.
38. de Oliveira, U.; Ocelík, V.; De Hosson, J.T.M. Analysis of coaxial laser cladding processing conditions. Surf. Coatings Technol. 2005, 197, 127–136, doi:10.1016/j.surfcoat.2004.06.029.
39. Liu, J.; Li, J.; Cheng, X.; Wang, H. Effect of dilution and macrosegregation on corrosion resistance of laser clad AerMet100 steel coating on 300M steel substrate. Surf. Coatings Technol. 2017, 325, 352–359, doi:10.1016/j.surfcoat.2017.04.035.
40. Le, T.N.; Lo, Y.L. Effects of sulfur concentration and Marangoni convection on melt-pool formation in transition mode of selective laser melting process. Mater. Des. 2019, 179, 107866, doi:10.1016/j.matdes.2019.107866.
41. Marya, M.; Singh, V.; Hascoet, J.-Y.; Marya, S. Metallurgical Investigation of the Direct Energy Deposition Surface Repair of Ferrous Alloys. J. Mater. Eng. Perform. 2018, 27, 813–824, doi:10.1007/s11665-017-3117-5.
42. Ocelík, V.; Hemmati, I.; De Hosson, J.T.M. The influence of processing speed on the properties of laser surface deposits. Surf. Contact Mech. Incl. Tribol. XII 2015, 1, 93–103, doi:10.2495/secm150091.
43. Hemmati, I.; Ocelík, V.; De Hosson, J.T.M. Microstructural characterisation of AISI 431 martensitic stainless steel la-ser-deposited coatings. J. Mater. Sci. 2011, 46, 3405–3414, doi:10.1007/s10853-010-5229-2.
44. Dinda, G.P.; Dasgupta, A.K.; Mazumder, J. Laser aided direct metal deposition of Inconel 625 superalloy: Microstructural evolution and thermal stability. Mater. Sci. Eng. A 2009, 509, 98–104, doi:10.1016/j.msea.2009.01.009.
45. Naghiyan Fesharaki, M.; Shoja-Razavi, R.; Mansouri, H.A.; Jamali, H. Microstructure investigation of Inconel 625 coating obtained by laser cladding and

TIG cladding methods. Surf. Coatings Technol. 2018, 353, 25–31, doi:10.1016/j.surfcoat.2018.08.061.
46. Xiao, H.; Li, S.M.; Xiao, W.J.; Li, Y.Q.; Cha, L.M.; Mazumder, J.; Song, L.J. Effects of laser modes on Nb segregation and Laves phase formation during laser additive manufacturing of nickel-based superalloy. Mater. Lett. 2017, 188, 260–262, doi:10.1016/j.matlet.2016.10.118.
47. Knorovsky, G.A.; Cieslak, M.J.; Headley, T.J. Inconel 718 A Solidification Diagram. Metall. Transactions A 1989, 20, 2149–2158.
48. Wang, L.; Dong, J.; Tian, Y.; Zhang, L. Microsegregation and Rayleigh number variation during the solidification of superal-loy Inconel 718. Mineral. Metall. Mater. 2008, 15, 594–599, doi:10.1016/S1005-8850(08)60111-5.
49. Dupont, J.N. Solidification of an Alloy 625 Weld Overlay. Metall. Mater. Trans. A 1996, 27, 3612–3620, doi:10.1007/bf02595452.
50. Cieslak, M.J.; Headley, T.J.; Kollie, T.; Romig, A.D. A Melting and Solidification Study of Alloy 625. Met. Mater. Trans. A 1988, 19, 2319–2331, doi:10.1007/bf02645056.
51. Nie, P.; Ojo, O.A.; Li, Z. Numerical modeling of microstructure evolution during laser additive manufacturing of a nick-el-based superalloy. Acta Mater. 2014, 77, 85–95, doi:10.1016/j.actamat.2014.05.039.
52. Xie, H.; Yang, K.; Li, F.; Sun, C.; Yu, Z. Investigation on the Laves phase formation during laser cladding of IN718 alloy by CA-FE. J. Manuf. Process. 2020, 52, 132–144, doi:10.1016/j.jmapro.2020.01.050.
53. Chen, Y.; Guo, Y.; Xu, M.; Ma, C.; Zhang, Q.; Wang, L.; Yao, J.; Li, Z. Study on the element segregation and Laves phase formation in the laser metal deposited IN718 superalloy by flat top laser and gaussian distribution laser. Mater. Sci. Eng. A 2019, 754, 339–347, doi:10.1016/j.msea.2019.03.096.
54. Porter, D.A.; Easterling, K.E.; Sherif, M.Y. Phase Transformations in Metals and Alloys. 2009, 3rd edition, CRC Press: Taylor & Francis Group, FL, USA.; CRC Press: Boca Raton, FL, USA, 2019, 53, 9.

Article 5 - Thermal Study of a Cladding Layer of Inconel 625 in Directed Energy Deposition (DED) Process Using a Phase-Field Model

The International Journal of Advanced Manufacturing Technology

https://doi.org/10.1007/s00170-021-08376-6

The International Journal of Advanced Manufacturing Technology (2022) 119:3975–3993
https://doi.org/10.1007/s00170-021-08376-6

ORIGINAL ARTICLE

Check for updates

Thermal study of a cladding layer of Inconel 625 in Directed Energy Deposition (DED) process using a phase-field model

Roya Darabi[1,2] · André Ferreira[1,2] · Erfan Azinpour[2] · Jose Cesar de Sa[2] · Ana Reis[1,2]

Article 5 - Thermal Study of a Cladding Layer of Inconel 625 in Directed Energy Deposition (DED) Process Using a Phase-Field Model

Roya Darabi*[1,2], André Ferreira[1,2], Erfan Azinpour[2], Jose Cesar de Sa[1], Ana Reis[1,2]

[1]Institute of Science and Innovation in Mechanical and Industrial Engineering (INEGI), FEUP campus, Rua Dr. Roberto Frias, 400, 4200-465, Porto, Portugal

[2]Faculty of Engineering of University of Porto (FEUP), Rua Dr. Roberto Frias, 4200-465, Porto, Portugal

*Corresponding Author: rdarabi@inegi.up.pt

Abstract

In an effort to simulate the involved thermal physical effects that occur in direct energy deposition (DED) a thermodynamically-consistent phase-field method is developed. Two state parameters, characterizing phase change and consolidation, are used to allocate the proper material properties to each phase. The numerical transient solution is obtained via a finite element analysis. A set of experiments for single tracks scanning were carried out to provide dimensional data of the deposited cladding lines. By relying on a regression analytical formulation to establish the link between process parameters and geometries of deposited layers from experiments, an activation of passive elements in the finite element discretization is considered. The single-track cladding of Inconel 625 powder on tempered steel 42CrMo4 was printed with different power, scanning speed and feed-rate to assess their effect on the morphology of the melt pool and the solidification cooling rate. The forecast capability of the developed model is assessed by comparison of the predicted dimensions of melt pools with experiments reported in the literature. In addition, this research correlated the used process parameter in the modelling of localized transient thermal with solidification parameters, namely, the thermal gradient (G) and the solidification rate (R). The numerical results report an inverse relationship between R with G, and

microstructure transition from the planar to dendrite by moving from the boundary to the interior of melt pool, which agree well with experimental measurements.

Keywords: Direct energy deposition. Additive manufacturing. Finite element method. Phase-field method. Melt pool morphology. Solidification

Nomenclature

e	Energy density	T_s	Solidus temperature
k	Thermal conductivity	A	Steepness changing phase parameter
U	Volumetric heat source	T_{vp}	Vaporized temperature
$\boldsymbol{n}$	Outward unit normal vector	T_{vl}	Temperature at the liquid-vapor transition
h	Heat convection	T_v	Average vaporization temperature
ε	Emissivity of the material	k_p	Thermal conductivity of powder
σ	Stefan-Boltzmann constant	k_d	Thermal conductivity of dense material
C_s	Volumetric heat capacities in the solid state	C_d	Volumetric heat capacities in the dense state
ϕ_f	Fusion phase parameter	ε_0	Initial powder porosity
ϕ_v	Vaporization phase parameter	f	Distribution of laser power
ψ	Consolidation parameter	P	Laser power
T	Temperature	r_l	Laser beam radius
$p(\phi_v)$	Vaporization thermodynamically consistent phase-field parameter	v	Laser scanning speed
$p(\phi_f)$	Fusion thermodynamically consistent phase-field parameter	E	Specific energy
L_f	Latent heat of fusion	D	Powder density
L_v	Latent heat of vaporization	H	Height of cladding lines
C_l	Volumetric heat capacities in the liquid state	W	Width of cladding lines
T_m	Average melting temperature	$w(\boldsymbol{x})$	Weighting function
T_l	Liquidus temperature	Δt	Time increment
		Δx	Mesh size

Introduction

Additive manufacturing (AM) is a transformative approach to industrial production that enables the creation of lighter and stronger parts with higher flexibility in the design to achieve desirable mechanical properties and high dimensional accuracy. The AM processes consolidate feedstock materials such as powder, wire or sheets into a dense metallic part by melting and solidification with the aid of an energy source such as laser, electron beam or electric arc, in a layer by layer manner[1][2]. Directed Energy Deposition (DED) covers a range of terminology including laser engineered net shaping products, directed light fabrication, direct metal deposition and 3D laser cladding [3]. DED is a complex printing process commonly used to repair or add additional material to existing components [4][5]. DED involves injecting a stream of metallic powder that is melted by a laser beam as a heat source in order to deposit material layer-by-layer on a built platform [6]. In DED process, solidification and solid-state transformations, upon heating and cooling, deeply affect the mechanical properties of deposited layer induced by the high-energy input and high cooling rate during the process [7]. The control of the involved physical phenomena like melting, phase changing, vaporization, and Marangoni convection is extremely difficult and sometimes impossible exclusively by means of experimental analyses [8]. Furthermore, it is rather time-consuming and expensive to produce DED fabricated parts. Computational simulation can give precious information on the complex process–structure–property relations and therefore be useful to its design and optimization. The phenomenon has a multi-scale inherent nature which is computationally complex and challenging that, so far, must be tackled at different stages. Temperature prediction and solid-liquid phase fields detection can be defined as the initial stage in the process simulation, that can then be utilized subsequently in thermal-mechanical and material microstructure evolution. The model needs to properly consider the material properties with respect to solid-liquid phase changing, powder-dense material status. Lee et al. presented enhanced models for temperature evolution and phase-dependent thermal conductivity and heat capacity in selective laser melting (SLM) process [9][10]. Roy et al. proposed a purely thermal model which explicitly incorporates two state variables for both the phase and the porosity in SLM. Their model has the ability to capture the consolidation of the material and allowed them to investigate the phase-dependent laser absorptivity [11]. It is worth noting that although a broad number of numerical modeling approaches for selective laser melting (SLM) can be found in recent years, capable of predicting the temperature field, melting and solidification [12] [13], there is a lack of the detailed studies on phase detecting on DED. The origin of this inattention comes from another existing challenge in DED simulation, including the dynamic incorporation of the additive material as the deposited layer into the numerical model. Through activation of a new set of elements in each time step of the finite element solution. Moreover, DED process has a highly localized thermal behavior which leads to undesirable microstructural features [14] and inconsistent mechanical properties of the fabricated parts. Nevertheless, some significant efforts have been made to simulate solidification kinetics [15] and investigation results on the correlation microstructural features and mechanical properties between thermal characterization of melt pool and solidification parameters, including thermal gradient G and solidification rate, have been reported [16]. The effect of increasing the laser speed and decreasing the power simultaneously on the melt pool size, thermal gradients and cooling rates were illustrated in [17]. Correlation between solidification parameters which can be derived from numerical thermal models based on the Finite Element Method (FEM) were reported in [18][19]. Subsequently, the microstructure was predicted using the solidification map of the specific material. Finally, indirect microstructure control was achieved by relating the predicted micro-structure to the derived melt pool dimensional map. In order to improve the accuracy of the analysis results for continuum-based simulation of the DED process, proper models for effective material properties are required. The thermal properties, including the conductivity and the specific heat capacity of the powder and dense material may be involved with the phase material characterization. Previous researches for effective modeling of material phase focused on the selective laser melting (SLM) process [9][11] [20][21]. At present, many scholars have carried out DED forming mechanism, microstructure and performance research on Inconel alloy, which is very common in aerospace applications. Ni-based alloy Inconel 625 has excellent thermal corrosion resistance, fatigue resistance, wear resistance and excellent strength at high temperatures for cladding purposes [22][23]. Clad layers exhibit good bonding between substrate and clad material, when at least a thin layer of the base material is melted. Accordingly, a layer-wise melt pool temperature tracking is beneficial in manipulating the process parameters and therefore adjusting the melt pool temperature[24][25].

To the best of the authors' knowledge, very little attention has been given, so far, to the development of a transient heat numerical model on DED process involving phase changing to predict of the melt pool boundary with varying laser power to extract the solidification parameters.

The present article focuses on the development of a thermal powder deposition evolution for DED process using the commercial FEM software ABAQUS. The transient heat transfer model associated with the phase field concept is implemented by user coding in FORTRAN language, taking into consideration the latent heat of fusion and vaporization. In the present model, the volume fraction of the deposited material is modeled based on the synergistic interactions from experiment-driven equations. Subsequently, the validation procedure is carried out based on experimentally measured melt pool dimensions related to single track fabrication of IN 625 on a 42CrMo4 baseplate. Then the calculated solidification parameters (G, R) were compared across the melt pool by changing laser power to shed light on its effect on the microstructure map.

The paper is organized as follows. Section 2 contains the numerical approach consisting of governing equations, describing the transient heat transfer model associated with the phase change concept, material allocations for both deposition and substrate with the concept of the phase-field model and heat source modeling. Section 3 presents the experimental study for single-track lines of IN625 on the tempered substrate 42CrMo4 with different power, scanning speed and feed rate to achieve various penetrations. In section 4, the thermal phenomena based on finite element formulation is implemented in ABAQUS through relevant user interface routines. Subsequently, in section 5 the results from the proposed numerical method are compared with experimental data to assess the efficiency of the model. In Section 6, conclusions are drawn and summarized.

Proposed Numerical Approaches

The direct energy deposition (DED) process modelling is presented in detail in the following sections, in terms of heat transfer constitutive equations, allocated material properties with respect to temperature and material states and energy source modelling;

Governing equation of thermal energy balance

The thermal energy balance equation based on first law of thermodynamic states that change in the total energy equals to the rate of work, which is done on the volumetric boundary of Ω . The adaption of energy balance considering the phase parameters, temperature, flux boundary and initial conditions are represented in Equations.1-3 [9][11][26];

$$\frac{de}{dt} = \nabla.[k(\psi)\nabla(T)] + U(\boldsymbol{x}, t) \quad \text{in } \Omega \qquad (1)$$

$$-[k(\psi)\nabla(T)].\boldsymbol{n} = \hat{q} \quad \text{on } \Gamma_2 \qquad (2)$$

$$\hat{q} = h(T - T_0) + \varepsilon\sigma(T^4 - T_0^4) \qquad (3)$$

where e, k, U are energy density, thermal conductivity and the volumetric heat source delivered from laser beam. with $\hat{q}$ prescribed heat flux vector on the surface boundary, which can include the heat loss for convection and radiation terms and $\boldsymbol{n}$ is the outward unit normal vector. The parameters $\varepsilon = 0.28$, $h = 10\left(\frac{W}{m^2K}\right)$ and $\sigma = 5.67 \times 10^{-8}$ $(\frac{W}{m^2K^4})$ are the emissivity of the material, heat convection and coefficient Stefan-Boltzmann constant respectively. In addition, the value of, 10 and 5.67×10^{-8} are dedicated to these values.

The energy density is expressed in terms of the temperature and state variables as below[9][11][26];

Here C_s , C_l and L_f, L_v are the volumetric heat capacities in the solid and liquid states, the latent heat of fusion-melting [27][28] and latent heat of vaporization respectively. T_m is the average melting temperature, taken as $T_m = 0.5 * (T_s + T_l)$, where T_l and T_s are liquidus and solidus temperatures [29].

The used function $p(\phi_{f\ or\ v})$ in Equation 4 is defined based on the thermodynamically consistent phase-field approach proposed by Wang et al. [26] such that $p(0) = 0$ and $p(1) = 1$ and $\frac{dp}{d\phi_{f\ or\ v}} = \frac{d^2p}{d^2\phi_{f\ or\ v}} = 0\ at\ \ \phi_{f\ or\ v} = 0$ and $\phi_{f\ or\ v} = 1$ [29], where $\phi_{f\ or\ v}$ is the phase parameter. It takes the following form:

$$p(\phi_{f\ or\ v}) = (\phi_{f\ or\ v})^3\left[10 - 15(\phi_{f\ or\ v}) + 6(\phi_{f\ or\ v})^2\right] \tag{5}$$

In Equation 5 the phase parameters ϕ_f, ϕ_v are defined as [9]:

$$\phi_f = \frac{1}{2}\left(\tanh\left(A\left(\frac{T - T_m}{T_l - T_s}\right) + 1\right)\right) \tag{6}$$

$$\phi_v = \frac{1}{2}\left(\tanh\left(A\left(\frac{T - T_v}{T_{vp} - T_{vl}}\right) + 1\right)\right) \tag{7}$$

where T_{vp} is the vaporized temperature, T_{vl} is the temperature at the liquid-vapor transition and T_v is the average vaporization temperature taken as $T_v = 0.5 * (T_{vl} + T_{vp})$.

Some conditions are considered: $\phi_f = 0$ if $T < T_s$ and $\phi_f = 1$ if $T_l < T$. When $T_s \leq T \leq T_l$ then $0 < \phi_f < 1$, representing the mushy region. Moreover, $\phi_v = 1$ if $T_{vp} < T$, indicating whether the material is vaporized or not. The parameter A determines the steepness of change transition [10]. The effect of the choice of A on the profile of the phase parameter $p(\phi_f)$ (for sharp transition $A = 10$ and for diffuse transition $A = 5$) is shown in Figure. 1.

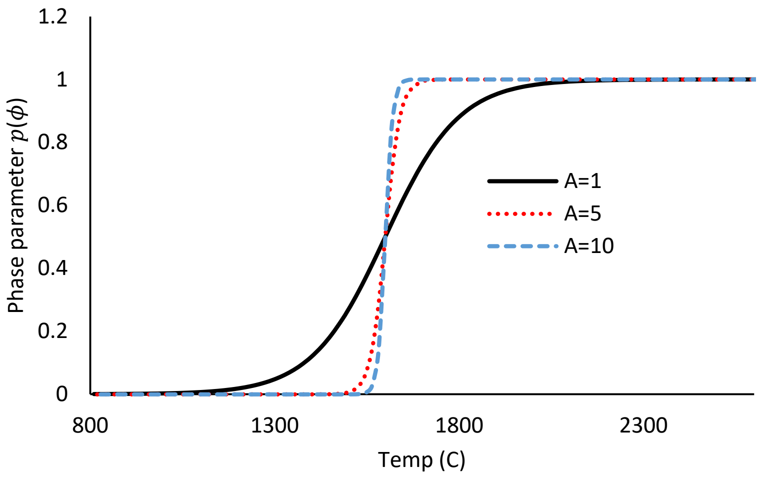

Figure 1. Effect of sharpness of transition in phase parameter

Regarding Equation 1, the thermal properties of the material, including volumetric heat capacity and thermal conductivity, are defined based on the consolidation parameter ψ as in Equation 8. This parameter always keeps the maximum values of ϕ_f to characterize the thermal history at each material point [9][10].

$$\psi(\boldsymbol{x}, t) = max\{\phi_f(\boldsymbol{x}, t + dt), \psi\ (\boldsymbol{x}, t)\} \tag{8}$$

When $\psi = 0$ the material is still in the powder state and $\psi = 1$ refers to the fully dense region. Table 1 shows the material state relation with the state variables.

Table 1. $\phi_f(T)$, $\psi(T)$ values for different states of the material

Powder	Solid porous	Mushy powder-melt	Liquid melt	Mushy melt-dense	Solid dense
$\phi_f(T) = 0$	$\phi_f(T) = 0$	$0 < \phi_f(T) \leq 1$	$\phi_f(T) = 1$	$0 \leq \phi_f(T) \leq 1$	$\phi_f(T) = 0$
$\psi(T) = 0$	$0 < \psi(T) < 1$	$0 < \psi(T) \leq 1$	$\psi(T) = 1$	$\psi(T) = 1$	$\psi(T) = 1$

According to Equation 8, ψ which is related to the history of the fusion phase parameter at each material point. The mentioned volumetric heat capacity $C_s(\psi)$ and thermal conductivity $k(\psi)$ in Equations 1 and 2 are determined by the degree of consolidation (ψ) defined in Equations 9-10 [9][11]:

$$k(\psi) = (1-\psi)k_p + \psi k_d \tag{9}$$

$$C_s(\psi) = (1-\varepsilon_0(1-\psi))C_d \tag{10}$$

where k_p and k_d are the thermal conductivity in the powder and dense material, respectively. The volumetric heat capacity depends on the consolidation ψ and C_d, the latter being the heat capacity of the fully dense material and ε_0 represents the initial porosity of powder and assumed 0.6. In general, the thermal conductivity and heat capacity are also temperature dependent. In the next section, the correlation between materials' thermo-physical properties with state variables are presented.

Material Properties Module

Nickel-based super alloy powder (MetcoClad625®) as cladding powder and 42CrMo4 tempering steel as substrate are considered in this research. MetcoClad625 is used as a blown powder cladding layer and tempering steel is employed as a solid substrate part. Figures 2 and 3 along with the Table 2 represent the thermo-physical material properties dependence on the temperature for MetcoClad625 (both powder and solid phase) and steel 42CrMo4. In the DED process, a great part of the blown powder particle undergoes a phase change and turns into a liquid state by a heat source, while the rest of the material remains in mushy powder-melt state. Thereafter, as the material cools down, the melted parts change to a solid state. Since the difference of material properties between the liquid area with mushy zones and the solid state is very large, the current state of the material should be identified in order to utilize appropriate properties according to the phase change history.

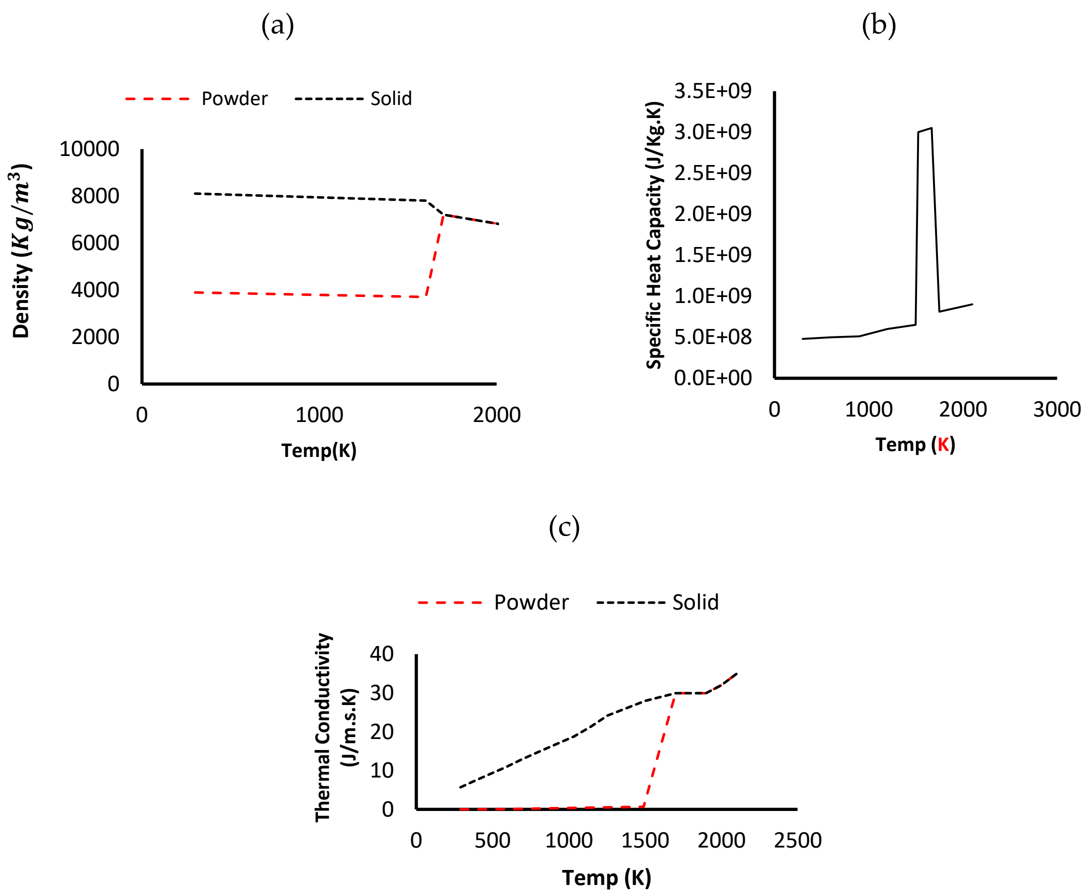

Figure 2. Temperature-dependent material properties of MetcoClad625 : (a) Density ($kg/\,m^3$), (b)Specific Heat Capacity ($J/kg.K$), (c) Thermal Conductivity ($J/m.s.K$)

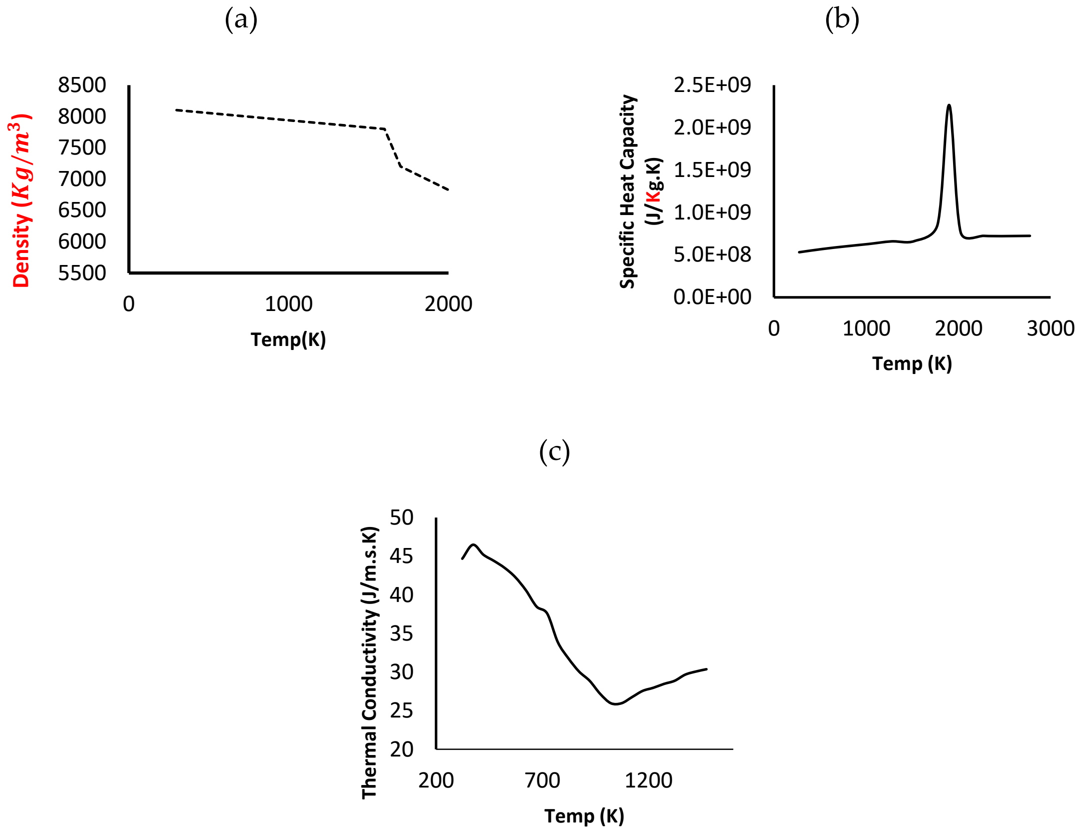

Figure 3 Temperature-dependent material properties of 42CrMo4 tempered Steel: (a) Density $(kg/\,m^3)$, (b)Specific Heat Capacity $(J/kg.K)$, (c) Thermal Conductivity $(J/m.s.K)$

Table 2. Thermo-physical properties of the material

	$T_s(K)$	$T_l(K)$	$L_f(kJ/kg)$	$T_{vp}(K)$	$T_{vl}(K)$	$L_v(kJ/kg)$
MetcoClad625	1563	1723	44.34	3580	3650	91.3
42CrMo4	1770	1920	25.72	3560	3680	104

Figure 4 shows the different phases throughout deposition process between solid and liquid phases.

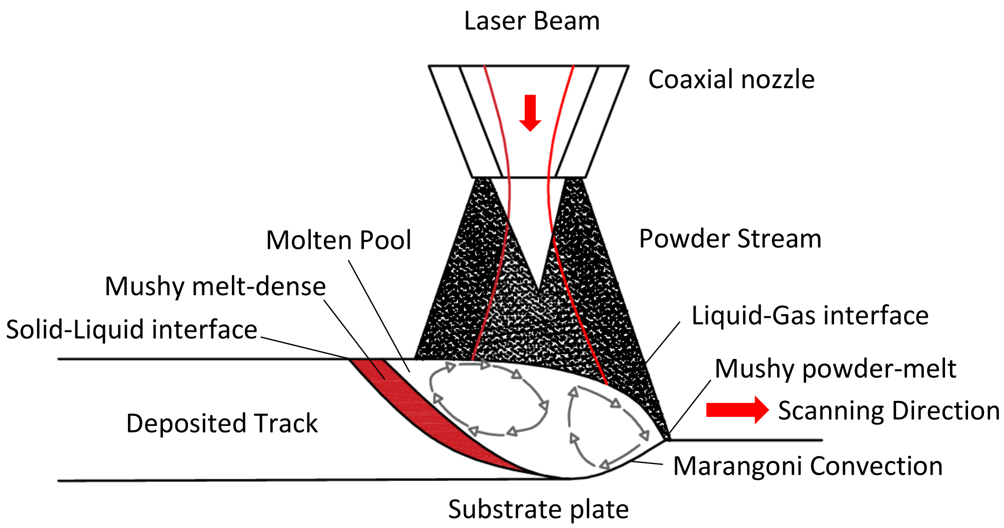

Figure 4. Intersection of different phases during direct energy deposition process

Heat Source Model

It is important to establish an appropriate heat source model of laser deposition simulations since the heat source not only influences the geometries of melt pools, but also it may have an impact on the mechanical performance of final products. Heat source models used in DED simulations are typically assumed [30][31], as the following two-dimensional exponentially decaying function of Equation 11 which is schematically represented in Figure 5,

$$U(x, y, z, t) = \frac{fP}{\pi {r_l}^2} \exp\left(-f \frac{x^2 + (y - v \cdot t)^2}{{r_l}^2}\right) \tag{11}$$

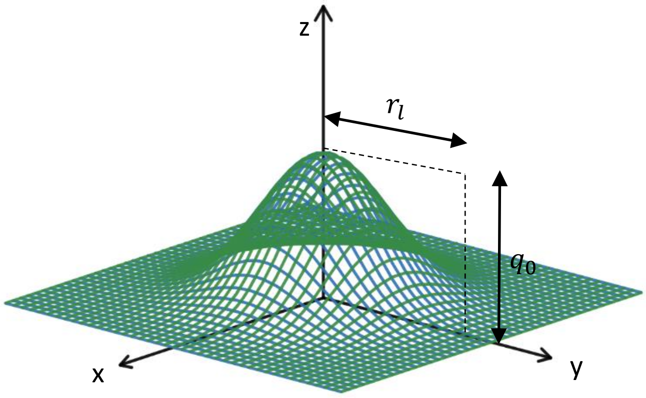

Figure 5. The schematic of heat source with exponentially decaying method

where P is the laser power, f is the distribution of power factor, r_l is laser beam radius corresponding to the distance between the beam center and the point at coordinates (x, y), v is the laser speed moving. Figure 6 illustrates the schematic profile of power density with respect to the distribution factor.

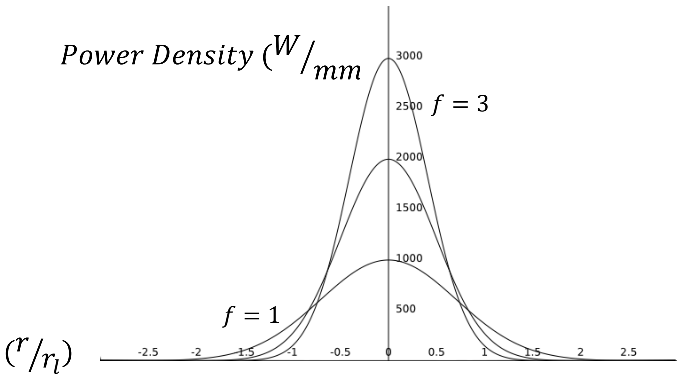

Figure 6 The power density distribution with a laser power of 2 kW according to different distribution factors

Experimental procedure

A tempered steel (42CrMo4) plate with size of $100mm \times 120mm \times 15mm$ was used as a substrate. In the preparation process, the surface was machined and then cleaned by ethanol. The used powder is commercially the gas-atomised Nickel-based super alloy (MetcoClad 625), similar to Inconel 625. Figure 7 shows the micrography of the powder. Laser cladding experiments were performed by a coaxial laser machine "LDF 3000 – 100" with a fibre-coupled high power laser diode (adjustable wavelength 900-1030 nm that changes depend on power), with 6000 W maximum beam power output. The laser machine was equipped with a 6-axes KUKA KR90 R3100 industrial robot. Based on Table 3, 18 different single tracks, 15 mm in length, were produced by altering three process parameters, namely laser powers P $(1, 1.5, 2, 2.5, 3$ kW$)$, scanning speeds $v\ (2, 4, 6, 10\ mm/s)$ and powder feed rates $F(10, 15, 20\ gr/min)$. All other parameters remained constant throughout the experiments: the laser spot diameter was 2.5 mm with a top-hat beam profile. A high purity argon (99.99%) as the shield gas, with a flow rate equal to 5.5 L/min, was utilized to minimize contamination and oxidisation. The single tracks were cross-sectioned, mounted in resin and polished down to 1 μm diamond suspension as a last stage. The geometry measurements of height, depth and width of the cladding lines produced by the DED technique were achieved using a Leica DVM6 A 2019 digital microscope. Figure 8 (a - f) shows the geometrical measures of the clad section of the molten pool for some samples using software ImageJ. Table 3 presents the measured value from designed experiments for Inconel 625 single tracks cladded on 42CrMo4 entirely.

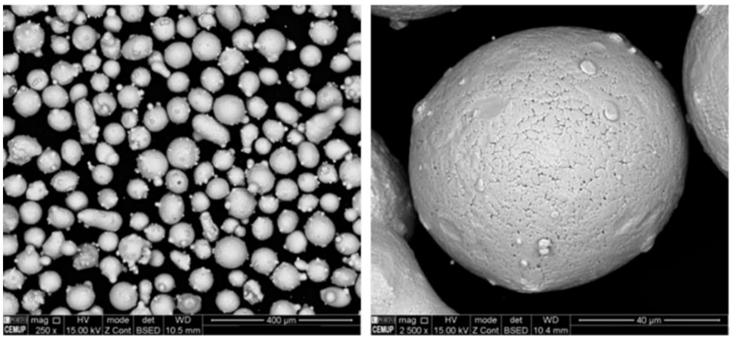

Figure 7. SEM micrograph of MetcoClad 625 powder

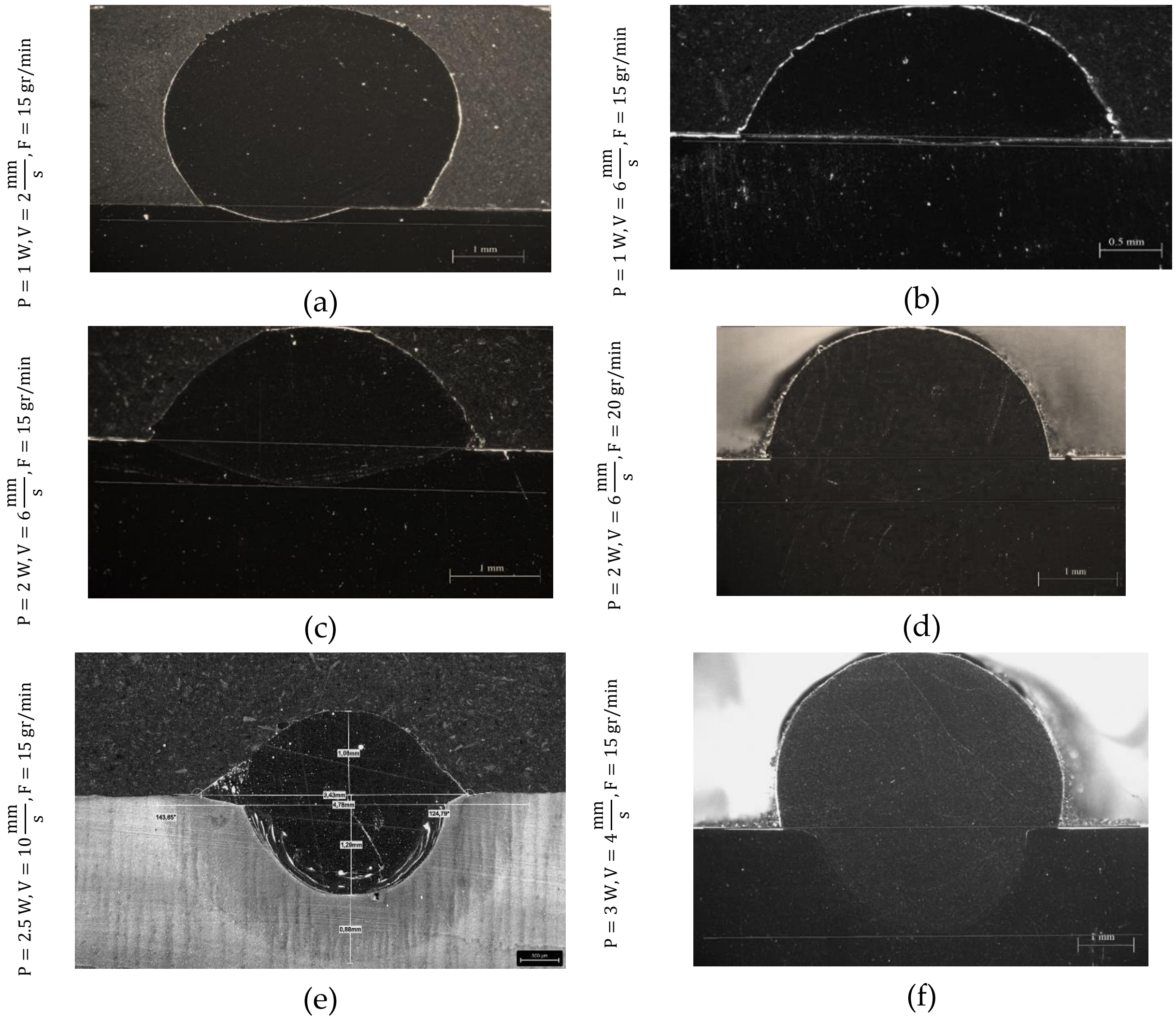

Figure 8 (a-e). Selection of the cross sections of Inconel 625 single tracks cladded on 42CrMo4 substrate

Table 3. Measured value sets for width, height and penetration depth in single clads Inconel 625 on 42CrMo4 substrate

#Set	1	2	3	4	5	6	7	8	9
Power-Velocity-Feed rate (P-V-F)	1_2_15	1_6_15	1.5_10_10	1.5_10_15	2_2_15	2_4_15	2_6_10	2_6_15	2_6_20
w (mm)	2.79	3.07	3.09	3.11	3.62	3.5	3.38	3.61	3.63
h (mm)	3.07	1.22	0.71	1.03	3.66	2.47	1.39	1.47	1.71
d (mm)	0.25	0.06	0.43	0.23	1.28	1.12	1.16	0.51	0.56
#Set	10	11	12	13	14	15	16	17	18
Power-Velocity-Feed rate (P-V-F)	2_10_10	2_10_15	2.5_10_10	2.5_10_15	3_2_15	3_4_15	3_6_10	3_6_15	3_6_20
w (mm)	3.2	3.36	3.33	3.46	5.05	4.64	3.89	4.71	3.94
h (mm)	1.2	0.81	0.86	1.23	3.4	2.06	1.85	0.78	1.55
d (mm)	0.72	0.88	1.04	1	2.06	0.89	1.08	0.68	1.34

The specific energy E and powder density D are calculated via Equations 12 and 13, where P, D_l, v and F are laser power, laser diameter, scanning speed and scanning feed rate respectively.

$$E(kW/mm^2) = {}^{P}/_{D_l * v} \tag{12}$$

$$D(gr/mm^2) = {}^{F}/_{D_l * v} \tag{13}$$

Then, the synergistic interaction between regression-based specific energy and powder density can be represented by Equations 14 and 15. Adjusted R-square values are 86.55% and 75.07% respectively for H (height of cladding layer) and W (width of cladding layer).

$$H\ (mm) = 0.51761 + 0.00025\ E + 0.01083\ D \tag{14}$$

$$W\ (mm) = 3.12365 + 0.00127\ E - 0.00654\ D \tag{15}$$

Numerical implementation with finite element method (FEM)

To obtain the thermal model for DED process, including subsequent results such as temperature, melt pool dimensions, interfacial phenomena, and a thermal finite element analysis framework was built using the commercial software ABAQUS/Standard. ABAQUS provides the interface for mesh designing, programming user-defined material behavior and boundary conditions. Hereby, the specific features and numerical models of DED introduced in Section 2 associated with experimental results, in section 3, are implemented using provided user subroutines as follows.

Finite element solution for heat transfer

Using the Galerkin weighted residual method it is possible to obtain from Equations 1 and 2 the following classical integral (weak) form as Equation 16;

$$\int_{\Omega} (w\, \dot{e}(T) + \nabla w \,.\, k(T)\, \nabla T - w\, U) d\Omega + \int_{\Gamma_2} w.\hat{q}\, d\Gamma_2 = 0 \quad (16)$$

where $w = w(\boldsymbol{x})$ is a weighting function, and from which, utilizing the finite element method, a system of ordinary differential equations can be written, in a matrix form as Equation 17:

$$\boldsymbol{C}(\boldsymbol{T})\, \dot{\boldsymbol{T}} + \boldsymbol{K}(\boldsymbol{T})\, \boldsymbol{T} = \boldsymbol{F} \quad (17)$$

In Equation 17, $\boldsymbol{T}$ is the nodal temperature vector, $\dot{\boldsymbol{T}}$ its time derivative, $\boldsymbol{C}(\boldsymbol{T})$ a temperature dependent equivalent capacity matrix, resulting terms that include temperature time derivative in Equation 16, $\boldsymbol{K}(\boldsymbol{T})$ is the equivalent conductivity matrix, resulting from terms that include temperature in Equation 16 and $\boldsymbol{F}$ is the equivalent time dependent heat source, resulting from independent terms in Equation 16.

Using an implicit time integration scheme to solve Equation 17, in which it is assumed that

$$\dot{\boldsymbol{T}}^{t+\Delta t} = \frac{1}{\Delta t}(\boldsymbol{T}^{t+\Delta t} - \boldsymbol{T}^{t}) \tag{18}$$

Then final nonlinear system of equations to be solved results in Equation 19;

$$\boldsymbol{C}\ \boldsymbol{T}^{t+\Delta t} + \Delta t\, \boldsymbol{K}\, \boldsymbol{T}^{t+\Delta t} = \Delta t\, \boldsymbol{F}^{t+\Delta t} + \boldsymbol{C}\, \boldsymbol{T}^{t} \tag{19}$$

The nonlinear system of equations is iteratively solved, within each time step, resorting to the Newton method, in a three-step procedure at each iteration i as below;

$$\boldsymbol{R}_i = \boldsymbol{C}\ \boldsymbol{T}_i^{t+\Delta t} + \Delta t\, \boldsymbol{K}\, \boldsymbol{T}_i^{t+\Delta t} - \Delta t\, \boldsymbol{F}^{t+\Delta t} - \boldsymbol{C}\, \boldsymbol{T}^{t} \tag{20}$$

$$\left(\frac{\partial \boldsymbol{C}}{\partial \boldsymbol{T}} + \Delta t \frac{\partial \boldsymbol{K}}{\partial \boldsymbol{T}}\right)\ \Delta \boldsymbol{T}_i = -\boldsymbol{R}_i \tag{21}$$

$$\boldsymbol{T}_{i+1}^{t+\Delta t} = \boldsymbol{T}_i^{t+\Delta t} + \Delta \boldsymbol{T}_i \tag{22}$$

Information on the residual force vector of Equation 20 and on the Jacobian matrix in Equation 22 must be given in the implementation of the method in ABAQUS. In particular a special care must be taken on the information from the definition of the terms resulting from the variation of internal energy density with temperature, $\frac{de}{dT}$, as depending on whether the value of ψ parameter is updated or not, the following energy density equations should be utilized as Equations 23 and 24:

$$\frac{de}{dT} = C_s(\psi) + \frac{dp(\phi_f)}{dT}\{L_f + [C_l - C_s(\psi)](T - T_m)\} + p(\phi_f)(C_l - C_s(\psi)) + L_v \frac{dp(\phi_v)}{dT} \tag{23}$$

$$\frac{de}{dT} = \frac{dC_s(\phi_f)}{dT}T + C_s(\phi_f) + \frac{dp(\phi_f)}{dT}\{L_f + [C_l - C_s(\phi_f)](T - T_m)\} - p(\phi_f)\frac{dC_s(\phi_f)}{dT}(T - T_m) + p(\phi_f)(C_l - C_s(\phi_f))L_v \frac{dp(\phi_v)}{dT} \tag{24}$$

Implementation

At present, there is no ready constitutive model in ABAQUS suitable for additive manufacturing simulation. The material phase change and taking into account the latent heat whether for fusion or vaporization into the thermal analysis, adding the deposited layers and the moving laser heat source are applied by resorting to the user-coded subroutines programmed in FORTRAN language. The user subroutine UEPACTIVATIONVOL is utilized to prescribe and update the following variables: height and width of cladding layer. Then, the user-defined subroutine DFLUX is called to define the non-uniform distributed heat source (U). In line with purpose of apply thermal constitutive behavior, UMATHT subroutine is used and following variables are needed to be updated incrementally;

- Internal thermal energy (enthalpy) per unit of mass: e
- Derivative of internal energy with respect to the temperature: $\frac{de}{dT}$
- Heat flux vector with respect to temperature: $\hat{q} = -k(\psi)\nabla(T)$
- Variation of heat flux vector to temperature: $\frac{\partial \hat{q}}{\partial T}$
- Variation of heat flux vector to the spatial gradient of temperature: $\frac{\partial \hat{q}}{\partial \frac{\partial T}{\partial x}}$ $(i = 1,2,3)$

Therefore, the material state can be defined by the state variables $\phi_{f\ or\ v}, \psi$ with respect to temperature. Finally, a USDFLD subroutine is developed to manage the material states at the end of each time increment. In Figure 9, a general flowchart summarizes the structure combination of used subroutines in ABAQUS.

Time and space discretization

The dimensional size of the modeled substrate is 100mm×120mm×15mm and the cladding lines are modeled with 5 mm×5 mm×100mm dimensions above the substrate as shown schematically in Figure 9. During the simulation, only a specific volume of the cladding line is activated based on the fed process parameters. This methodology makes the affordable balance for the computational time with the resolution of the results, thus making the simulation times reasonable. In this research, for both deposition layer and substrate, 3D thermal finite element mesh DC3D8 is utilized. The resolution of FEM model was selected to be high enough guarantee stabilization as well as an accurate cooling rate but keeping an affordable computational time. Thus artificial dispersion control introduces a stability limit on the size of the time increment and mesh size such that the local Courant number as Equation 25 [32].

$$C = |v| \frac{\Delta t}{\Delta x} \; meanwhile \; C \leq 1 \tag{25}$$

where $|v|$ is the velocity and Δt and Δx represent the time increment and characteristic element size in the direction of flow respectively. The larger elements were used far away from the scanned region to reduce calculation time in the substrate. Meanwhile, to ensure a good link between the clad layers surface and the substrate, the mesh is refined as much as to avoid numerical temperature fluctuation due to very high temperature gradient.

Initial and Thermal boundary condition

All the surfaces of the cladding welding line and the substrate were initially fixed at $T_0 = 298.15\,K$ and the sink temperature was also fixed at T_0 in the bottom of the baseplate. Besides, the tie constraint is applied between the top surface of baseplate and bottom surface of cladding layer to transfer the temperature between the contacted nodes.

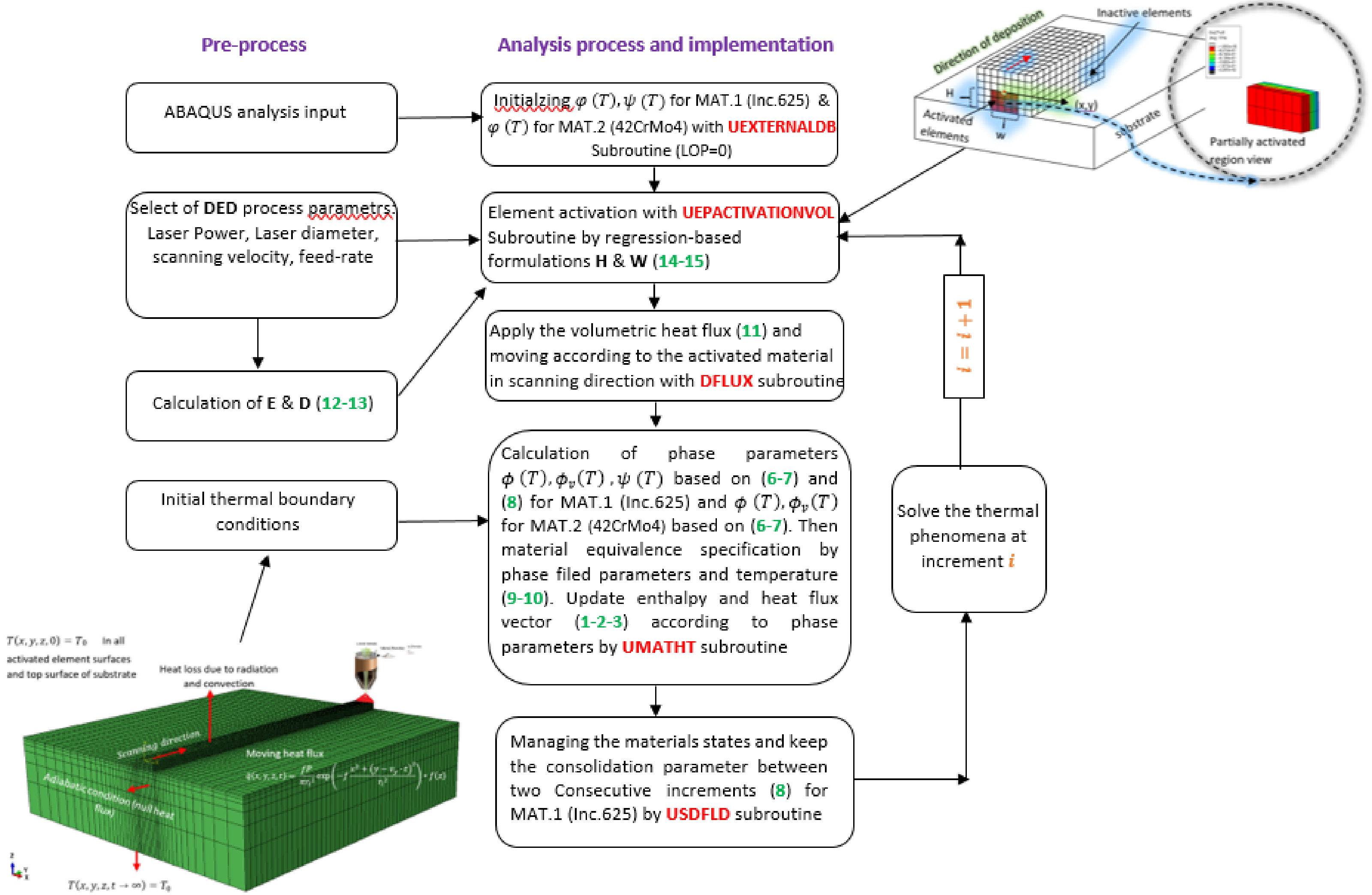

Figure 9 FE model structure and the subroutine for the material addition (UEPACATIVATION VOL), the material state variable for the degree of solidification (USDFLD), and heat flux application (DFLUX), solving thermal material constitutive behavior (UMATHT) combinations

Result and discussion

In this research, a numerical technique for the thermal part of DED process simulation using ABAQUS was proposed based on the phase-field concept. To demonstrate the thermal model and finite element implementation, firstly the data from experiments was used to predict of height and width of clad geometries, then compared the simulation in the area of melt pool with the experiments of the single laser tracks presented in section 3. The estimation of the temperature field, the spatial variation of the melt pool morphology, the effect of the process parameters on the phase changing, and interfacial solidification were investigated. The analysis of the calculation results are summarized in the following sections.

Sensitivity analysis to the time and space discretization

The direct energy deposition (DED) processes commonly produce materials with heterogeneities on different length scales, which calls for a requirement of adopting adequate meshes and timescales in simulations in order to achieve accurate results. Previous studies [33][34] showed the effect of the mesh size and time increment in additive manufacturing simulation resolution results. Discretization with finer meshes improves the accuracy but increases the cost of computation and therefore assigning the proper mesh size and time-step is an essential requirement. Hereby, mesh sensitivity analysis is conducted for a cladding line with $P = 1.5kW$,$SS = 10\frac{mm}{s}$ $and\ FR = 15\ gr/min$. Figure 10 (a-b) shows a comparative temperature-location for the points of interest in the building direction and the width of cladding lines at a distance of 1 mm from the edge of the starting point of printing ($y = 1\ mm$). Figure 10 (c) shows the temperature distribution, with time, for two grid refinement sizes with two time-steps. It reveals that sensitivity is greatly influenced by spatial discretization. The element size and Courant number were restricted to 0.2 mm and 1 respectively for the success of the simulation.

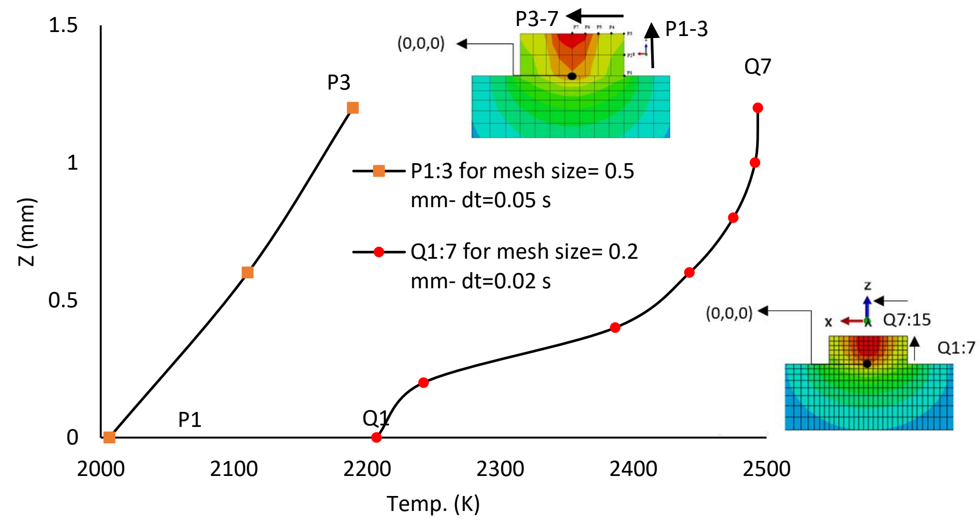

P3-7
P1-3
(0,0,0)
P3
Q7
P1:3 for mesh size= 0.5 mm- dt=0.05 s
Q1:7 for mesh size= 0.2 mm- dt=0.02 s
Q7:15
Q1:7
P1
Q1
Z (mm)
Temp. (K)
1.5
1
0.5
0
2000
2100
2200
2300
2400
2500

(a)

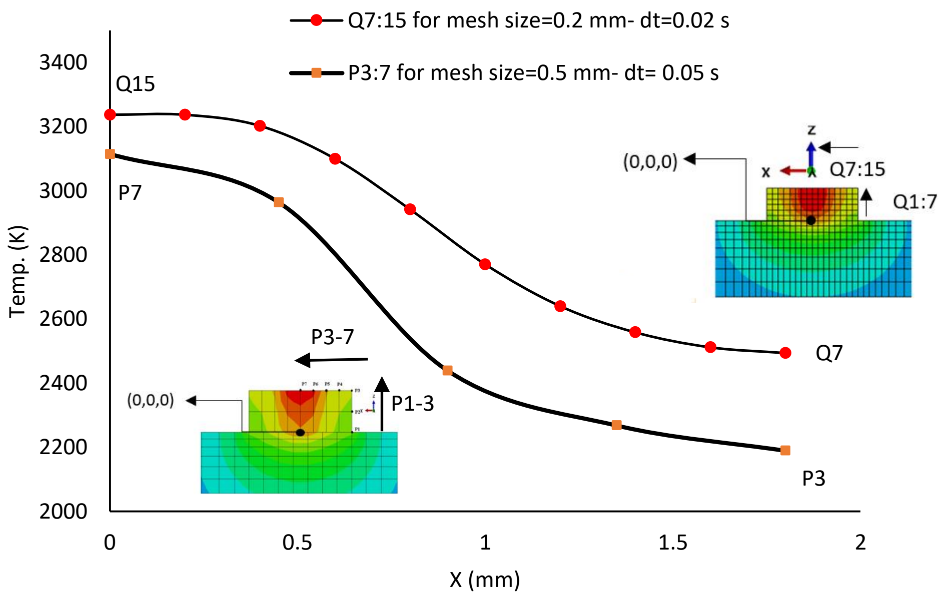

Q7:15 for mesh size=0.2 mm- dt=0.02 s
P3:7 for mesh size=0.5 mm- dt= 0.05 s
Q15
P7
Q7
P3
(0,0,0)
Q7:15
Q1:7
P3-7
P1-3
Temp. (K)
X (mm)
3400
3200
3000
2800
2600
2400
2200
2000
0
0.5
1
1.5
2

(b)

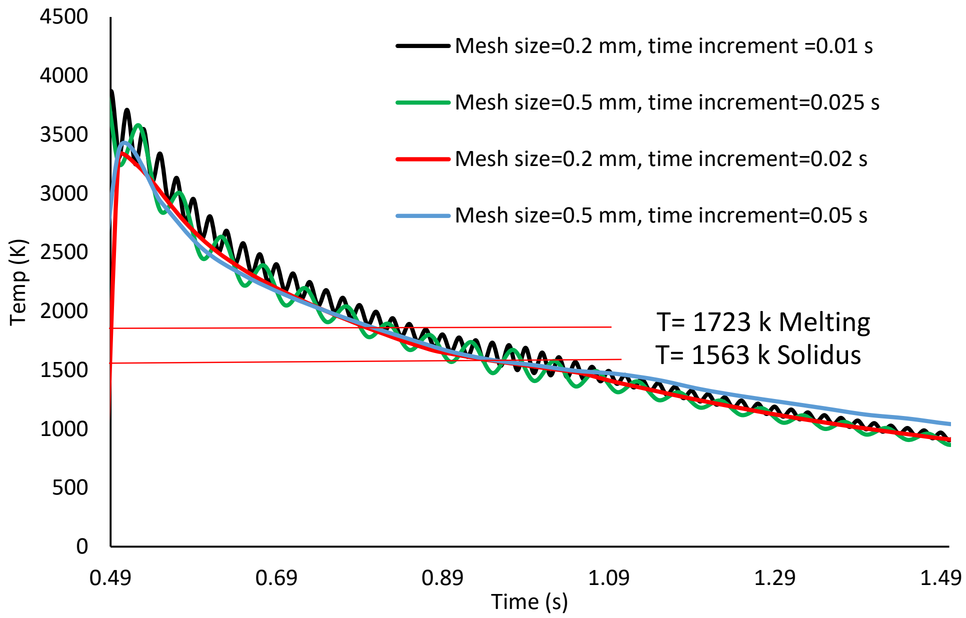

(c)

Figure 10. Comparison of the temperature distribution (a) in the building direction with respect to mesh size, (b) in the width direction with respect to mesh size, (c) effect of time-space sensitivity in the temperature distributing over time

Numerical model validation

Three single-track laser scans are simulated firstly to validate the proposed numerical model using the experimentally measured melt pool dimensions. The processing parameters used in the simulation of is shown in Table 3. The real scanning speed, feed rate, laser power are used in the numerical model to better mimic the real phenomena. The predicted melt pool dimension using the described numerical model and the experimental results are shown in Figures 11 and 12. The results show that both melt pool dimensions including width and depth increase as more laser power is used. In other words, by increasing the laser power, the heat per unit time increases as well, and so the melt pool volume increases. The predicted results are also in good agreement with the experimental data-driven. In particular, Table 4 illustrates the comparison between width, depth of melt pool area and height of cladding lines derived from associated regression-based information experimentally and numerically.

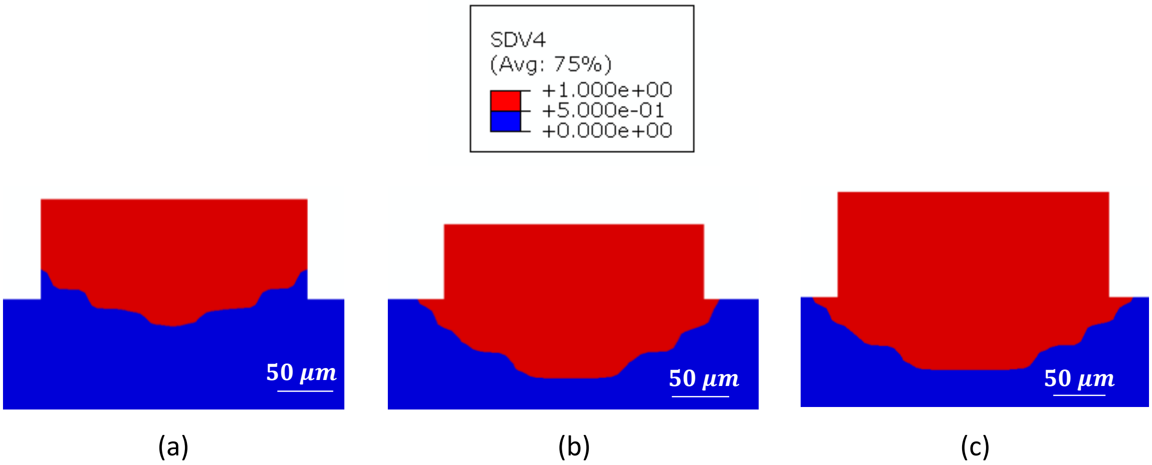

Figure 11. predicted melt pool morphology in Z direction for single-track with $SS = 10\ mm/s, FR = 15gr/min$ (a) $\boldsymbol{P = 1.5\ kW}$, (b) $\boldsymbol{P = 2\ kW}$, (c) $\boldsymbol{P = 2.5\ kW}$

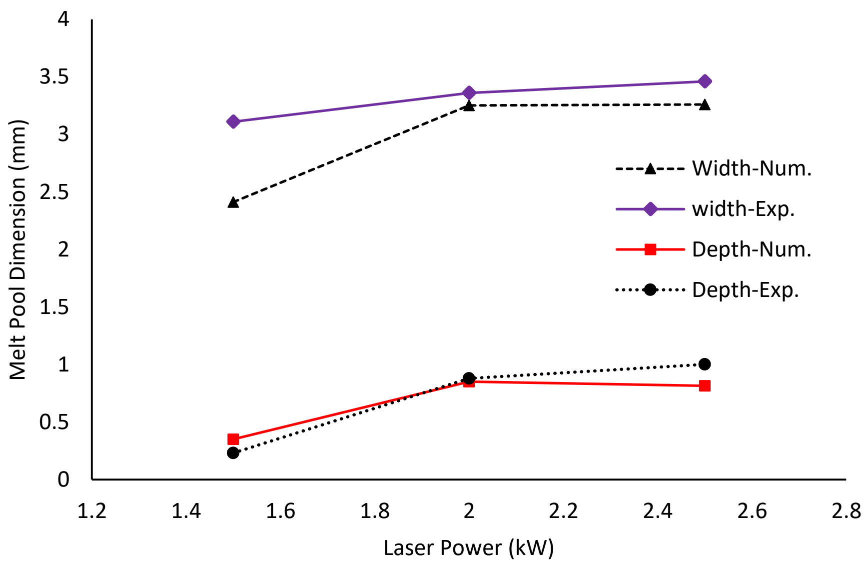

Figure 12. Predicted melt pool dimensions and the experimental results for single-track scan with the fixed scanning speed $SS = 10\ mm/s$and feed rate $FR = 15gr/min$ and varying the laser power

Table 4. Comparison of simulation results with experimental results

Process Parameters	Width (Exp.)	Width (Num.)	Depth (Exp.)	Depth (Num.)	Height (Exp.)	Height (Num.)
$P = 1.5\ kW, SS = 10\frac{mm}{s}, FR = 15\ gr/min$	3.11 mm	2.41 mm	0.23 mm	0.35 mm	1.03 mm	1.10
$P = 2.0\ kW, SS = 10\frac{mm}{s}, FR = 15\ gr/min$	3.36 mm	3.25 mm	0.88 mm	0.85 mm	0.81 mm	0.8
$P = 2.5\ kW, SS = 10\frac{mm}{s}, FR = 15\ gr/min$	3.46 mm	3.26 mm	1 mm	0.814 mm	1.23 mm	1.14

The red triangles and purple squares in Figure 13 show the average widths and depths of the simulated melt tracks at different scanning speeds. In the Figure, results from the simulation illustrate that both the width and depth of the melt track decrease with increasing scanning speed. Figure 14 provides evidence that by increasing the laser velocity the volume of the melt pool decrease. When the scanning speed is low, the laser remains longer around a local point, thereby generating more heat and resulting in a larger melt volume.

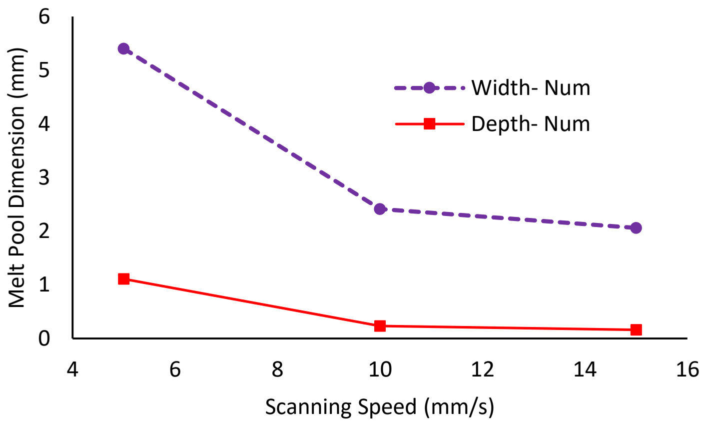

Figure 13. Predicted melt pool dimensions numerically for single-track scan with the fixed laser power $P = 1.5\ kW$ and feed rate $FR = 15 gr/min$ and varying the scan speed

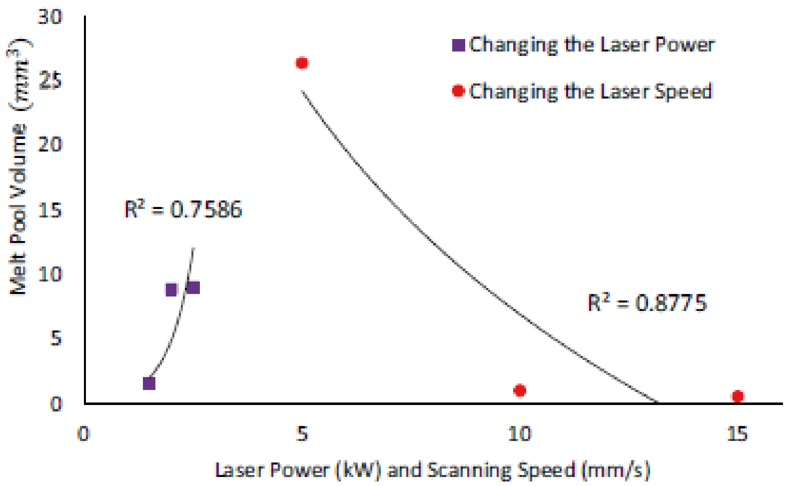

Figure 14. Melt pool volume in DED with different scanning speeds and powers

Transient heat model associated with phase field approach

The presented graphs in Figure 15 (a-c) show the obtained results from the proposed model with a phase-field approach for various laser power from 1.5 kW to 2.5 kW. The results indicate that by increasing the laser power the temperature value remarkably increases and even material vaporization occurs. For two laser powers $2kW$ and $2.5kW$ the temperature reaches vaporization.

The material phase variables include : ϕ_f , with red dotted lines, which represents the time of material changes from liquid to the solid phase, the parameter ϕ_v with purple dotted line which presents a time period of vaporization phase existence, and lastly, dedicated parameter ψ (black solid line) for tracking consolidation, between powder and melt states. Before laser reaches and starts melting ψ *and* $\phi_f = 0$, after melting the temperature rises and material state variable ϕ_f changes to 1 which means the material state is liquid.

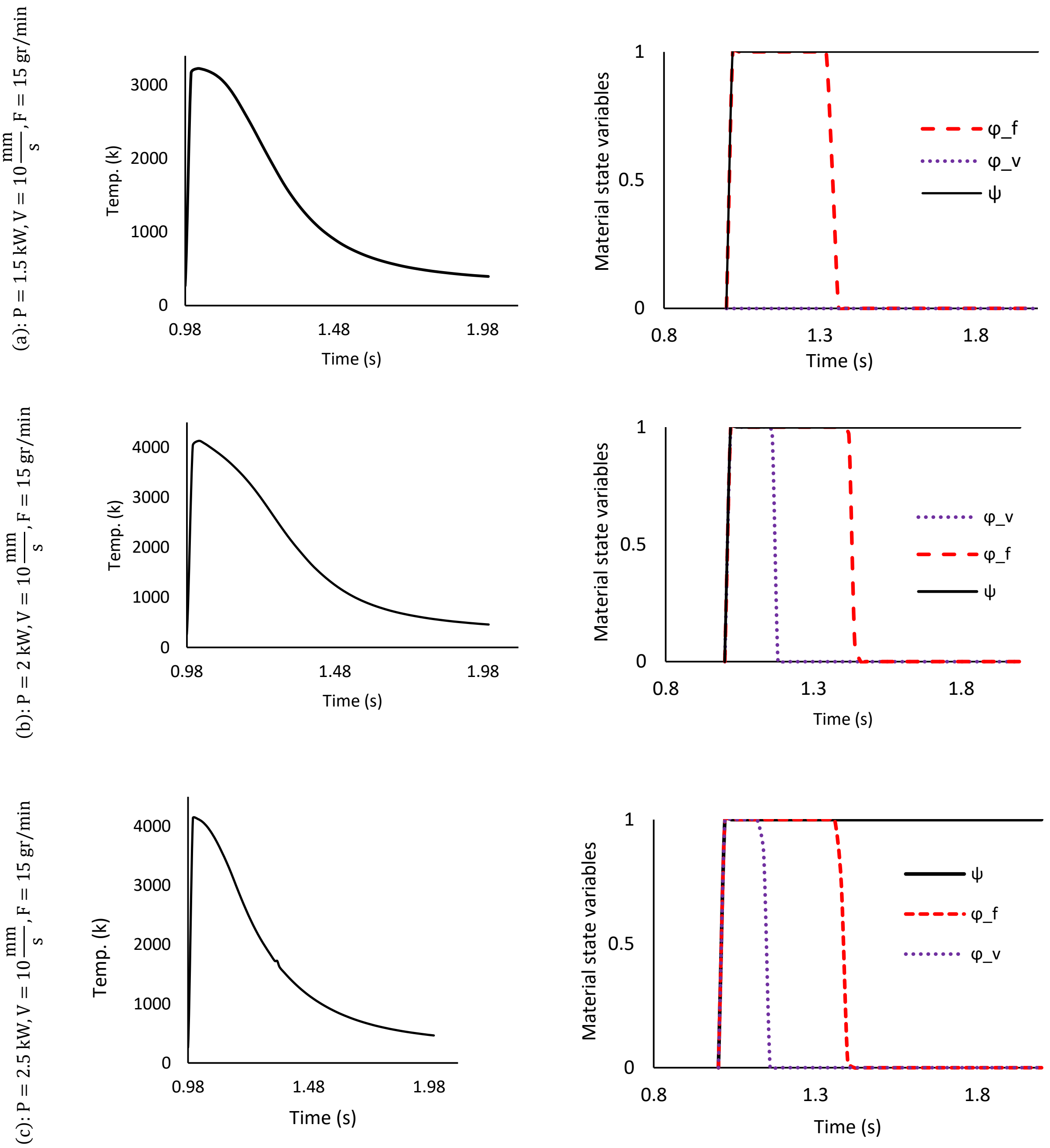

Figure 15. Temperature profile and material state variables with $SS = 10\,mm/s, FR = 15gr/min$ (a) $\boldsymbol{P = 1.5\ kW}$, (b) $\boldsymbol{P = 2\ kW}$, (c) $\boldsymbol{P = 2.5\ kW}$

Melt pool lifetime refers to the period of time the liquid phase is present. The melt pool lifetime can be observed in Figure 16 for three different laser power values, which is an important parameter that determines the stability of the track formation during the process [35]. This graph illustrates when the scanning speed and feed rate are fixed and the laser power increases, the melt pool life time increases, the reason is liquid phase lifetime is not only depended on the scanning speed but also to the heat supply and volume of the melt pool. The liquid phase lifetime for laser power 1.5 kW is 54 ms and increases to 64 ms with laser power 2.5 kW.

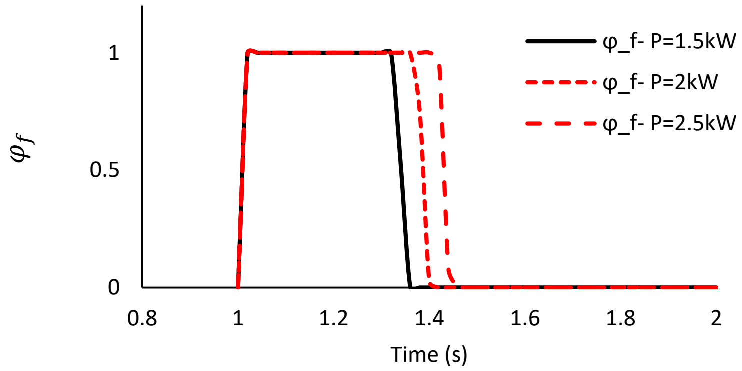

Figure 16. Liquid phase life-time comparison for changing laser powers from 1.5kW to 2.5kW versus time with the fixed scanning speed $SS = 10\ mm/s$and feed rate $FR = 15gr/min$

From Figure 17, the different lifetime of melt pool by varying the scanning speed while the laser power and feed rate keep fixed can be obtained. The results indicate that the melt pool lifetime tends to decrease gradually as the speed increase from 30 ms to 92 ms for 15 mm/s and 5mm/s respectively.

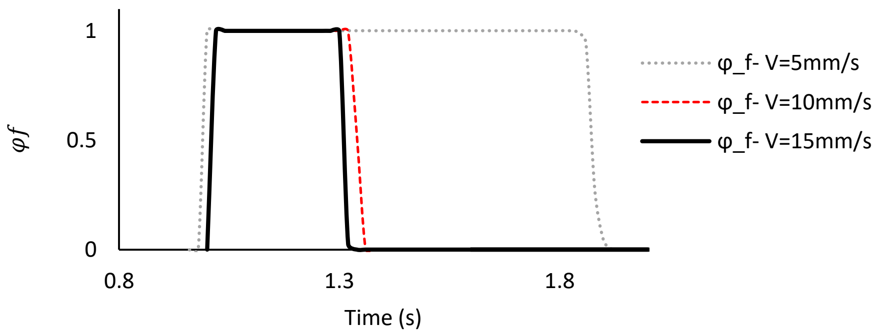

Figure 17. Liquid phase life-time comparison for changing laser scanning speed from 5 mms to 15 mm/s versus time with the fixed laser power $P = 1.5kW$ and feed rate $FR = 15gr/min$

Local temperature gradient and solidification rate $(\boldsymbol{G}, \boldsymbol{R})$

The temperature gradient G and solidification growth R are the most significant parameters in determining the solidification microstructure (e.g. planar, cellular, columnar dendritic, and equiaxed dendritic grain structure). A solidification micro graphical map for In 625 on 42CrMo4 demonstrating the variation in the morphology and size is presented in Figure 18. As can be seen the dendrite morphology, orientations, and micro segregation are different at different locations within the melt pool. This is primarily due to different positions and orientations of the initial nuclei combined with different thermal gradients and solidification velocities along the melt pool boundary.

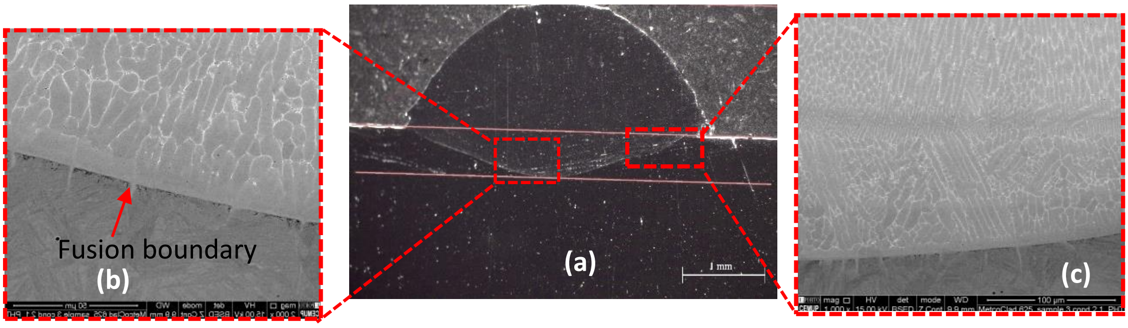

Figure 18. (a)Optical micrograph demonstrating transverse cross-sections of melt pool obtained under $\boldsymbol{P = 2\ kW, SS = 10\ mm/s, FR = 15 gr/min}$, (b) ,(c) enlarged views

In the presented model, G can be calculated from partial derivative of temperature with respect to each Cartesian coordinate as in Equation 22:

$$G = \sqrt{\left(\frac{\partial T}{\partial x}\right)^2 + \left(\frac{\partial T}{\partial y}\right)^2 + \left(\frac{\partial T}{\partial z}\right)^2} \quad (22)$$

The growth rate is geometrically derived as the projection of laser velocity v onto the normal vector of solidification front, using the angle θ, which is the local angle between the surface normal to the liquidus isotherm boundary and the welding direction as in Equation 23 and Figure 19;

$$R = |v|.\cos(\theta) \quad (23)$$

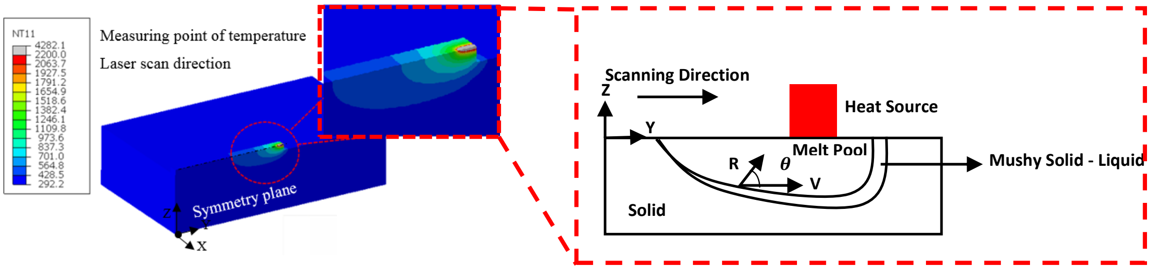

Figure 19. Schematic of solidification growth rate R in the melt pool with laser scanning V

The values of G and R were extracted from macro-scale simulation. The points of interested were selected on the trailing half of the melt pool which is the portion subject to solidification as the melt pool domain. In Figure 20 (a, b), the variation of the G and R along with the centerline of melt pool boundary with increasing depth is explicitly shown. The results reveal that there is an inverse relationship between R and G. The maximum R is calculated near the top of the melt pool (with a low solidification front depth) while the minimum is found near the bottom of the melt pool (with a high solidification front depth). In contrast, the maximum G is calculated at the bottom of the melt pool as the minimum G is observed at the top. In the bottom region is exposed at high G and low R and hence corresponds to the planar grains as shown in Figure 18 (b) SEM microstructure evidence. On the other hand, the top regions tend relatively lower G and higher R with the dendrite structure from Figure 18 (c).

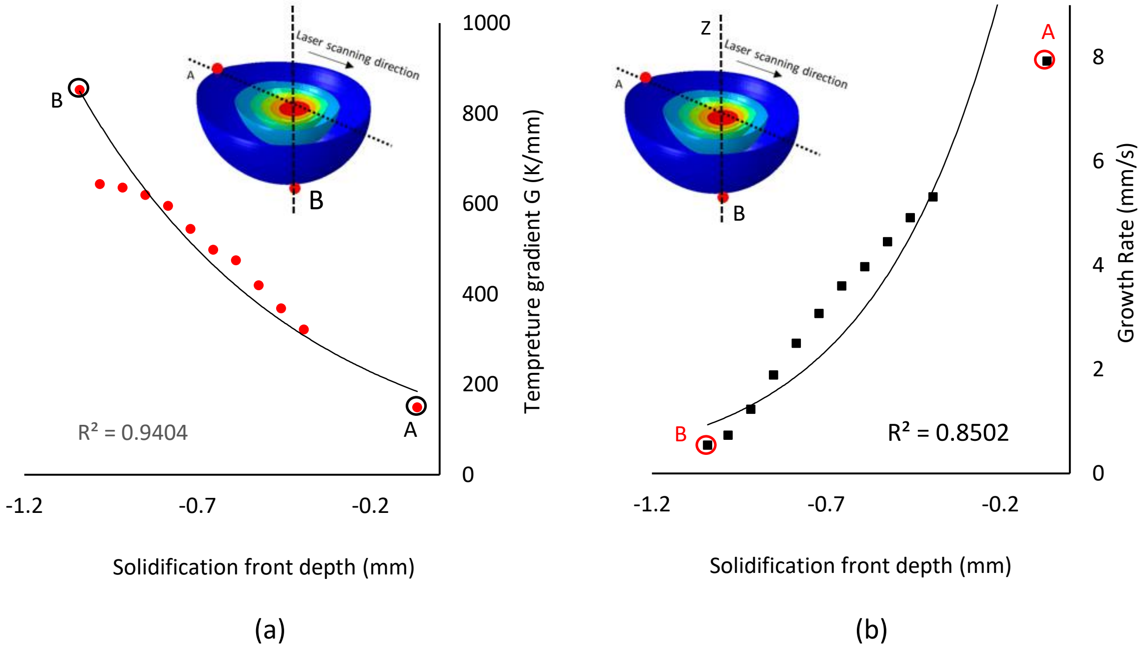

Figure 20. The calculated (a): G and (b): R, along the centerline of the melt pool surface; Variation in relation with the solidification front depth for one set of parameters $\boldsymbol{P = 2\ kW, SS = 10\ mm/s, FR = 15 gr/min}$

Figure 21 (a,b) illustrates the cooling rate for two set of parameters including (a): $\boldsymbol{P = 2\ kW, SS = 10\ mm/s, FR = 15gr/min}$ and (b): $\boldsymbol{P = 1.5\ kW, SS = 10\ mm/s, FR = 15gr/min}$. It can be seen how the cooling rate, $\dot{T} = G \times R$, varies as a function of the melt pool depth for both cases; the dotted rectangular views emphasize the highest and lowest cooling rate along with the location of the melt pool boundary. Simulation results show that cooling rate increases from bottom to top along the melt pool boundary. The predicted cooling rate varies by changing the laser power. The cooling rate increases with decreasing the laser power [26][36] and consequently differences in cooling rate leads to variety of solidified microstructures.

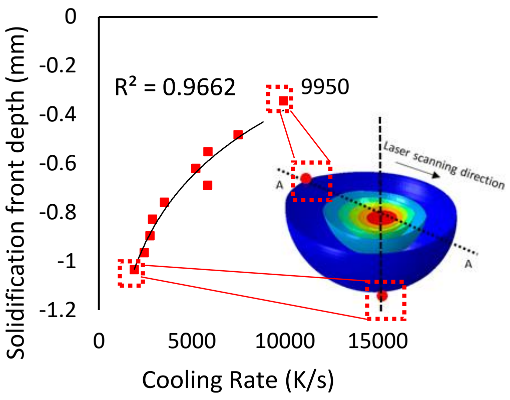

(a)

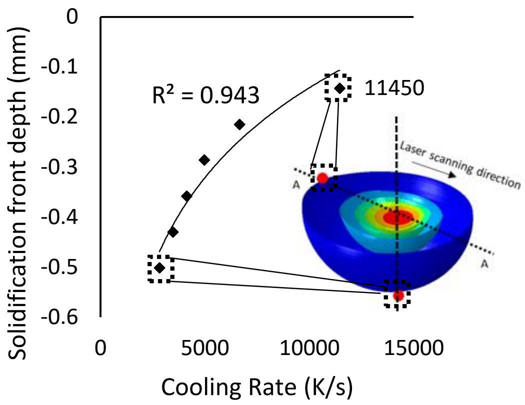

(b)

Figure 21. The predicted cooling rates at varying solidification front depths for two sets of process parameters; (a) $\boldsymbol{P = 2\ kW, SS = 10\ mm/s, FR = 15 gr/min}$, (b) $\boldsymbol{P = 1.5\ kW, SS = 10\ mm/s, FR = 15 gr/min}$

Conclusion

In the present study, a computational framework for the transient heat phenomena in DED process is developed by coupling a finite element based on phase-field model. In the proposed model three state variables ϕ_f, ϕ_v ,and ψ are defined to track and capture the phase of materials between molten, solid, and even vaporized conditions to allocate the proper thermal-physical material properties. The proposed model is implemented in the commercial finite element software ABAQUS-standard. The capability of numerical model is investigated by comparing melt pool dimensions, including width and depth from simulation for single cladding lines, with the experimental data. Three different laser power values were applied to quantify their effect on the melt pool morphology. The melt pool width and depth have a tendency of becoming greater when a higher laser power is applied. Moreover, the numerical results showcases the inverse correlation between the scanning speed the melt pool volume. The investigation is further proceeded to detect the solidification parameters, the temperature gradient and the growth rate. To achieve this goal, the temperature variation as well as the liquidus isotherm boundary surface information is utilized to calculate these parameters along the solidification front depth path. The planar to dendrite transition was predicted by moving from melt pool boundary to the interior of melt pool. Furthermore, an inverse relationship between R and G, can be seen and maximum R is calculated near the top of the melt pool, while the minimum is found near the bottom of the melt pool, which is in agreement with a solidification map obtained by SEM. Finally, the cooling rate increases from the bottom to the top of melt pool and decreasing laser power leads to an increase of the range of the cooling rate.

Acknowledgements - The corresponding author would like to thank Professor Manuel F. Vieira and Dr. Omid Emadinia for supporting experiments and constructive comments on the solidifcation concept.

Author contribution - Roya Darabi: conceptualization, investigation, writing—original draft, writing—review and editing. Andre Ferreira: Conceiving, planning and conducting the experiments. Erfan Azinpour: writing—review and editing. Jose Cesar de Sa: conceptualization, investigation, review and editing, funding acquisition. Ana Reis: conceptualization, investigation, review and editing, funding acquisition

Funding - This work was supported by Fundo Europeu de Desenvolvimento Regional (FEDER) through Programa Operacional Competitividade e Internacionalização (COMPETE 2020) and national funds through Fundação para a Ciência e a Tecnologia (FCT), Portugal, Grant number: ADDing (POCI-01-0145-FEDER-030490) and Project GEAR3D (POCI-01-0247-FEDER-039848), co-financed by FEDER through P2020|COMPETE

Availability of data and materials - It has been confirmed that data is open and transparent.

Declarations

Ethics approval - Not applicable.

Consent to participate - Not applicable.

Consent for publication - Not applicable.

Conflict of interest - The authors declare no competing interests.

References

1. DebRoy T, Wei HL, Zuback JS, et al (2018) Additive manufacturing of metallic components – Process, structure and properties. Progress in Materials Science 92:112–224. doi: 10.1016/j.pmatsci.2017.10.001

2. Azinpour E, Darabi R, Cesar de Sa J, et al (2020) Fracture analysis in directed energy deposition (DED) manufactured 316L stainless steel using a phase-field approach. Finite Elements in Analysis and Design 177:103417. doi: 10.1016/j.finel.2020.103417

3. Gardan J (2016) Additive manufacturing technologies: State of the art and trends. International Journal of Production Research 54:3118–3132. doi: 10.1080/00207543.2015.1115909

4. Gibson DG, Glass JI, Lartigue C, et al (2010) Creation of a bacterial cell controlled by a chemically synthesized genome. Science 329:52–56. doi: 10.1126/science.1190719

5. Somashekara MA, Naveenkumar M, Kumar A, et al (2017) Investigations into effect of weld-deposition pattern on residual stress evolution for metallic additive manufacturing. International Journal of Advanced Manufacturing Technology 90:2009–2025. doi: 10.1007/s00170-016-9510-7

6. Gu DD, Meiners W, Wissenbach K, Poprawe R (2012) Laser additive manufacturing of metallic components: Materials, processes and mechanisms. International Materials Reviews 57:133–164. doi: 10.1179/1743280411Y.0000000014

7. Feenstra DR, Banerjee R, Fraser HL, et al (2021) Critical review of the state of the art in multi-material fabrication via directed energy deposition. Current Opinion in Solid State and Materials Science 25:100924. doi: 10.1016/j.cossms.2021.100924

8. Fallah V, Alimardani M, Corbin SF, Khajepour A (2011) Temporal development of melt-pool morphology and clad geometry in laser powder deposition. Computational Materials Science 50:2124–2134. doi: 10.1016/j.commatsci.2011.02.018

9. Lee KH, Yun GJ (2020) A novel heat source model for analysis of melt Pool evolution in selective laser melting process. Additive Manufacturing 36:101497. doi: 10.1016/j.addma.2020.101497

10. Lee KH, Yun GJ (2021) Prediction of melt pool dimension and residual stress evolution with thermodynamically-consistent phase field and consolidation models during re-melting process of SLM. Computers, Materials and Continua 66:87–112. doi: 10.32604/cmc.2020.012688

11. Roy S, Juha M, Shephard MS, Maniatty AM (2018) Heat transfer model and finite element formulation for simulation of selective laser melting. Computational Mechanics 62:273–284. doi: 10.1007/s00466-017-1496-y

12. Markl M, Körner C (2016) Multiscale Modeling of Powder Bed-Based Additive Manufacturing. Annual Review of Materials Research 46:93–123. doi: 10.1146/annurev-matsci-070115-032158

13. Proell SD, Wall WA, Meier C (2020) On phase change and latent heat models in metal additive manufacturing process simulation. Advanced Modeling and Simulation in Engineering Sciences. doi: 10.1186/s40323-020-00158-1

14. Darabi R, Azinpour E (2021) Fracture Prediction Based on Evaluation of Initial Porosity Induced By Direct Energy Deposition. doi: 10.13052/ejcm2642-2085.29233

15. Wolff SJ, Lin S, Faierson EJ, et al (2017) A framework to link localized cooling and properties of directed energy deposition (DED)-processed Ti-6Al-4V. Acta Materialia 132:106–117. doi: 10.1016/j.actamat.2017.04.027

16. Farshidianfar MH, Khajepour A, Gerlich AP (2016) Effect of real-time cooling rate on microstructure in Laser Additive Manufacturing. Journal of Materials Processing Technology 231:468–478. doi: 10.1016/j.jmatprotec.2016.01.017

17. Wang Z, Palmer TA, Beese AM (2016) Effect of processing parameters on microstructure and tensile properties of austenitic stainless steel 304L made by directed energy deposition additive manufacturing. Acta Materialia 110:226–235. doi: 10.1016/j.actamat.2016.03.019

18. Hagenlocher C, Fetzer F, Weller D, et al (2019) Explicit analytical expressions for the influence of welding parameters on the grain structure of laser beam welds in aluminium alloys. Materials and Design 174:107791. doi: 10.1016/j.matdes.2019.107791

19. Karayagiz K, Johnson L, Seede R, et al (2020) Finite interface dissipation phase field modeling of Ni–Nb under additive manufacturing conditions. Acta Materialia 185:320–339. doi: 10.1016/j.actamat.2019.11.057

20. Ho S, Eun J, Park G, et al (2021) Thermal Analysis for Simulation of Metal Additive Manufacturing Process Considering Temperature- and History-Dependent Material Properties. International Journal of Aeronautical and Space Sciences 22:52–63. doi: 10.1007/s42405-020-00283-6

21. Kundakcioglu E, Lazoglu I, Rawal S (2016) Transient thermal modeling of laser-based additive manufacturing for 3D freeform structures. The International Journal of Advanced Manufacturing Technology 493–501. doi: 10.1007/s00170-015-7932-2

22. Liu J, Xu Y, Ge Y, et al (2020) Wire and arc additive manufacturing of metal components: a review of recent research developments. International Journal of Advanced Manufacturing Technology 111:149–198. doi: 10.1007/s00170-020-05966-8

23. Qiu Z, Wu B, Zhu H, et al (2020) Microstructure and mechanical properties of wire arc additively manufactured Hastelloy C276 alloy. Materials and Design. doi: 10.1016/j.matdes.2020.109007

24. Hofman JT, De Lange DF, Pathiraj B, Meijer J (2011) FEM modeling and experimental verification for dilution control in laser cladding. Journal of Materials Processing Technology 211:187–196. doi: 10.1016/j.jmatprotec.2010.09.007

25. Rezaeifar H, Elbestawi MA (2021) On-line melt pool temperature control in L-PBF additive manufacturing. International Journal of Advanced Manufacturing Technology 112:2789–2804. doi: 10.1007/s00170-020-06441-0

26. S.L.Wang, R.F.Sekerka, A.A.Wheeler, B.T.Murray, S.R.Coriell, R.J.Braun GBM (1993) Thermodynamically-Consistent Phase-Field Models for Solidification. Physica D: Nonlinear Phenomena 69:189–200. doi: https://doi.org/10.1016/0167-2789(93)90189-8

27. Reis A, Xu Z, Tol R V., Neto R (2012) Modelling feeding flow related shrinkage defects in aluminum castings. Journal of Manufacturing Processes 14:1–7. doi: 10.1016/j.jmapro.2011.05.003

28. Reis A, Houbaert Y, Xu Z, et al (2008) Modeling of shrinkage defects during solidification of long and short freezing materials. Journal of Materials Processing Technology 202:428–434. doi: 10.1016/j.jmatprotec.2007.10.030

29. Guo Z, Lin P (2015) A thermodynamically consistent phase-field model for two-phase flows with thermocapillary effects. Journal of Fluid Mechanics 766:226–271. doi: 10.1017/jfm.2014.696

30. Zhang Z, Huang Y, Rani Kasinathan A, et al (2019) 3-Dimensional heat transfer modeling for laser powder-bed fusion additive manufacturing with volumetric heat sources based on varied thermal conductivity and absorptivity. Optics and Laser Technology 109:297–312. doi: 10.1016/j.optlastec.2018.08.012

31. Roberts IA, Wang CJ, Esterlein R, et al (2009) A three-dimensional finite element analysis of the temperature field during laser melting of metal powders in additive layer manufacturing. International Journal of Machine Tools and Manufacture 49:916–923. doi: 10.1016/j.ijmachtools.2009.07.004

32. Katopodes ND, Method EE, Size S, et al low-Water Flow Methods for Two-Dimensional Shal- Courant Number.

33. Deering RA (2018) Additive Manufacturing Part Level Distortion Sensitivity Analysis within Abaqus on a Thin Walled, Tubular Structure. Additive Manufacturing Symposium 14.

34. Yashchuk I (2018) A multiscale finite element framework for additive manufacturing process modeling.

35. Haley JC, Zheng B, Bertoli US, et al (2019) Working distance passive stability in laser directed energy deposition additive manufacturing. Materials and Design 161:86–94. doi: 10.1016/j.matdes.2018.11.021

36. Ali H, Ghadbeigi H, Mumtaz K (2018) Processing Parameter Effects on Residual Stress and Mechanical Properties of Selective Laser Melted Ti6Al4V. Journal of Materials Engineering and Performance 27:4059–4068. doi: 10.1007/s11665-018-3477-5

Chapter 4

MECHANICAL AND MICROSTRUCTURAL PROPERTIES OF INCONEL 625 PRODUCED BY DIRECT LASER DEPOSITION (DLD)

Article 6 - Mechanical and Microstructural Characterisation of Bulk Inconel 625 Produced by Direct Laser Deposition

Journal Materials Science and Enginnering: A

https://doi.org/10.1016/j.msea.2022.142777

ELSEVIER

Materials Science and Engineering: A

Available online 8 February 2022, 142777

In Press, Journal Pre-proof

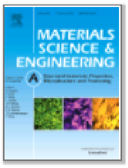

Mechanical and microstructural characterisation of bulk Inconel 625 produced by direct laser deposition

André A. Ferreira [a, b], Ana R. Reis [a, b], Rui L. Amaral [b], João M. Cruz [c], Pedro C. Romio [a], Jorge O. Seabra [a, b], Manuel F. Vieira [a, b]

Article 6 - Mechanical and Microstructural Characterisation of Bulk Inconel 625 Produced by Direct Laser Deposition

André A. Ferreira[1,2], Ana R. Reis[1,2], Rui L. Amaral[2], João M. Cruz[3], Pedro C. Romio[1], Jorge O. Seabra[1,2], Manuel F. Vieira[1,2]

[1]Faculty of Engineering of the University of Porto, 4200-465 Porto, Portugal
[2]LAETA/INEGI—Institute of Science and Innovation in Mechanical and Industrial Engineering, 4200-465 Porto, Portugal
[3]SERMEC-Group, 4425-348 Folgosa-Maia, Portugal
*Corresponding author: Department of Metallurgical and Materials Engineering, University of Porto, Porto, 4200-465 Portugal E-mails addresses: andreferreira@fe.up.pt (A. A. Ferreira) and mvieira@fe.up.pt (M. F. Vieira).

Abstract

Direct laser deposition (DLD) is an advanced additive manufacturing (AM) technology with growing industrial importance. In the present study, the mechanical and microstructural characterisation of a bulk produced by DLD depositing a nickel superalloy (type Inconel 625) on 42CrMo4 structural steel was performed. Optimised processing parameters (laser power, scanning speed and feed rate) were used for deposition and remained constant during bulk production. The bulk showed structural integrity, with no cracking or unmelted particles. Successive layers were deposited on a pre-heated substrate to reduce the cooling rate and minimise both the formation of metastable phases in the heat-affected zone and the dimensions of the deleterious phases in bulk. The bulk microstructure mainly consists of a coarse columnar/dendritic structure, and the longitudinal section microstructure revealed the layer-by-layer deposition pattern. Microstructural and mechanical characterisation demonstrated that a sound bulk was formed, with mechanical properties similar to wrought Inconel 625. These results contribute to the recognition of DLD as a suitable technique for the repair and remanufacturing of industrial components.

Keywords: Inconel 625; direct laser deposition; additive manufacturing; pre-heating; microstructure; mechanical evaluation

Introduction

Laser-Based Additive Manufacturing (LBAM) are emerging technologies with applications for various industrial sectors, including medical implants, automotive and aerospace parts, with complex geometries and structures [1]. Direct Laser Deposition (DLD) is an LBAM technology used to manufacture, reconstruct, or repair metal parts. DLD consists of the supply, through a nozzle, of metallic powder (or wire) processed by a focused laser, creating a melt pool on the surface of a metallic substrate that interacts with the substrate to form a cladding. Several processing variables directly or indirectly affect the quality and structural integrity of the cladding, dictated by solidification and metallurgical bonding [2]. DLD is a process that also enables the production of functionally graded materials [3]. Unlike conventional coating/repair production techniques such as welding, DLD can fabricate 3-D components with complex features directly from the CAD model. The goal of the process is the controlled melting of metal powders and their layered deposition, producing claddings with excellent metallurgical bonding and density, small heat-affected zone (HAZ), low dilution, minimal distortion, and precise deposition, making the technique fundamental in the repair of high value-added components [4], [5]. Deposits produced by DLD exhibit an attractive set of mechanical properties and wear and corrosion resistance [6]. The production of wear-resistant coatings on low- and medium-carbon steel substrates is an application that can have many industrial applications, both in component repair and in protective coating with a thick, tough layer.

Nickel-based superalloys, such as Inconel 625, have been widely adopted in multiple fields due to their versatile capabilities and their wide range of applications. These materials are used primarily in power generation aircraft and turbines, rocket engines and other challenging environments, including industrial furnace components, chemical power plants, marine systems, nuclear power plants and many other fields where high temperature corrosion resistance is generally required [7], [8]. Conventional component manufacturing using these high-performance alloys is difficult due to excessive tool wear and low material removal rates. In fact, nickel-based superalloys are very attractive materials for various industrial sectors due to their high-temperature ductility, hardness, mechanical strength, fatigue and creep resistance, and excellent oxidation and corrosion resistance in aggressive environments [9], [10]. Powder-based LBAM technologies can remove these constraints, improving lead times and reducing manufacturing costs [11].

Inconel 625 is one of the main nickel superalloys whose properties are mainly derived from the addition of elements such as molybdenum (Mo) and niobium (Nb), which strengthen by solid solution the nickel-chromium matrix [12]–[14]. Further strengthening is achieved by intermetallic phases, namely the gamma double prime (γ''-Ni3Nb), and by carbide precipitation [12], [15]. The formation of topologically close-packed (TCP) phases, such as σ (FeCr, FeCrMo, CrCo), μ and Laves, is detrimental for nickel superalloys application. These phases are brittle and detrimental to these superalloys' mechanical properties and creep resistance [16]. A high refractory elements content can cause the extensive formation of TCP phases during prolonged exposure to high temperatures; this formation is dependent on the material's microstructure [17]. Laser processing of Inconel 625 alloy shows complex structures involving cellular grains, typical columnar dendrites and equiaxial grains [18].

The use of nickel-based superalloys in DLD must consider the effect of high cooling rates promoted by the localised thermal delivery induced by the laser beam. However, the rapid cooling rate and repeated heating/cooling cycles during laser processing induce intense thermal stresses that can exceed the yield point of cladding materials

[19]. The high temperature of the laser beam creates a large temperature gradient between the centre and edges of the weld pool, producing surface tension gradients that are similar to those observed during laser welding [20]. This effect can influence the formation of intermetallics and TCP phases. The cooling rate directly influences the resulting microstructure and mechanical properties of the deposited component, being more dependent on the scanning speed than laser power [21]. High cooling rate and low G/R ratio (temperature gradient to growth rate ratio)promotes the formation of dendrites with smaller arms and discrete Laves phase particles. In contrast, low cooling rate and high G/R ratio tend to produce coarse dendrites and particles of continuously distributed Laves phase [22]–[24]. Similar effects of metastable phases (martensite) formation in the heat-affected some (HAZ) and near the melt line were observed for depositions performed on structural steel [25].

Pre-heating (PHT) the substrate is essential to control the cooling rate, minimising this detrimental effect. Increasing the PHT temperature also promotes melt pool growth (depth and width), melting more substrate, thus increasing dilution [26]–[28]. PHT also prevents cladding delamination or cracking and reduces distortion and residual stresses due to the lower thermal gradient between the coating and substrate [6], [29], [30]. Another factor to be observed is that the deposition of multiple layers of Inconel 625 by DLD allows the minimization of distortion, reducing the deflection of the coating [31].

The industrial importance of the Inconel 625 alloy and its complexity being unquestionable, it is essential to determine the conditions for its deposition by DLD. The influence of process parameters, such as laser power, scanning speed, powder feed rate, and pre-heating on single layers, was analysed in a previous study [25]. This work explores the deposition of multiple layers of Inconel 625 superalloy powder, forming a bulk, on a pre-heated steel substrate. The quality of the bulk was evaluated by the absence of cracks and structural imperfections, and its mechanical properties were determined to assess the feasibility of using these bulks for the repair/remanufacturing of industrial components.

Experimental Procedure

DLD System Setup

A laser system, LDF 3000 - 100, was used to produce the DLD claddings. The system has a high power fibre-coupled laser diode (wavelength 900-1030 nm, depending on power), with a nominal beam power of 6000 W. The machine concept is based on a six-axis industrial robot, a KUKA KR90 R3100, which can be placed on a linear table with a 4 m working range. All axes are connected to the robot and laser control units, which control the temperature in the molten pool and the laser power. A coaxial feeding system supplied the addition powder during the deposition process.

Powder and Substrate Characteristics

Nickel-based superalloy powder, supplied by the Oerlikon company under the trade designation MetcoClad 625 (Inconel 625), produced by the gas atomised process, was used in this study. The powders present a spherical morphology and particle size with a nominal range from 45 to 90 μm. Figure 1 shows an image of the powder obtained by scanning electron microscopy (SEM).

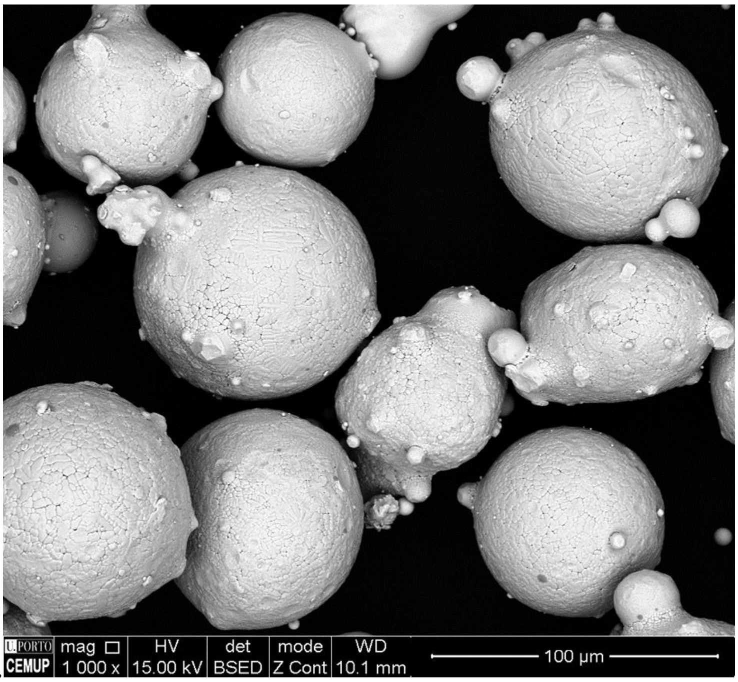

Figure 1. SEM micrograph of MetcoClad 625 powder.

42CrMo4 steel was the substrate for the cladding deposition. The steel was machined in plates with dimensions equal to 100 mm x 120 mm x 15 mm. Mechanical and chemical properties and additional information are described in the standard in EN 10269 [32]. Table 1 shows the chemical composition of MetcoClad 625 (M625) powder and 42CrMo4 steel.

Table 1. Chemical composition of M625 powder and 42CrMo4 steel (wt.%).

Raw Material	C	Cr	Ni	Mn	Mo	Nb	Si	P	S	Fe
M625	-	21.3	60.8	-	9.2	4.6	-	-	-	4.1
42CrMo4	0.42	1.11	-	0.67	0.19	-	0.28	0.025	0.015	Balance

Samples Production

The successive depositions of M625 for the bulk production were carried out with a coaxial nozzle. The deposition conditions were defined in previous study [25], in which the influence of the following three independent processing variables was analysed: laser power (LP), scanning speed (SS), and powder feed rate (FR). Processing optimisation allowed selecting the conditions for the production of the M625 bulk, expressed as values of two combined process parameters (parameters based on previous studies [33], [34], allowing a more general approach, and non-machine specific). The two parameters selected were the specific energy, $E_{specific}$ (= LP / φ*SS), and the powder density, G (= FR / φ*SS);φ is the spot size diameter of the laser beam on the substrate. The optimized combined parameters for M625 solid production through DLD are $E_{specific}$ = 133.3 J/mm^2 and G = 16.7 x 10^{-3} g/mm^2. Before deposition, the substrates were cleaned with pure acetone and pre-heated to approximately 300 °C by an oxy torch to eliminate moisture and decrease the cooling rate in the melt pool and adjacent regions of the substrate (thus reducing the detrimental effect of the HAZ). The temperature was selected following welding practices for 42CrMo4 steel and controlled with a digital pyrometer. Furthermore, for bulk production, the M625 powder deposition strategy selected was the zigzag-XY tool path, as shown in Figure 2. This deposition strategy was chosen due to minimize the possibility of porosity formation and allow obtaining good mechanical properties [35].

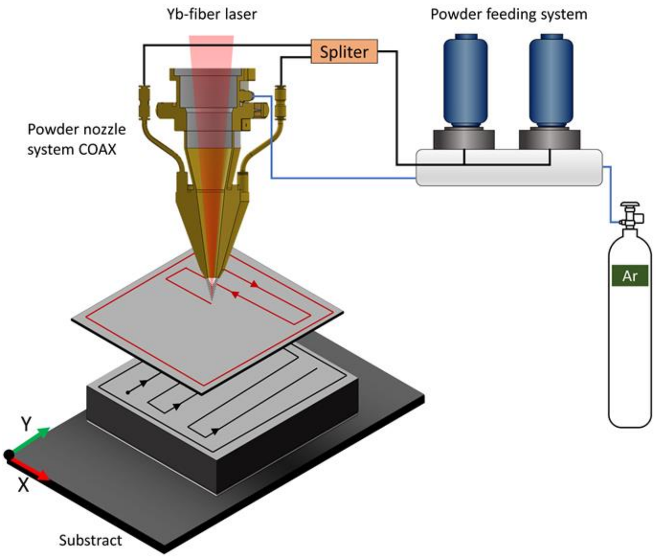

Figure 2. Schematic diagram of the strategy for the M625 bulk production by DLD.

In all tests, a spot size of 2.5 mm, and an offset in the Z-axis of 0.2 mm were used. High purity argon (99.99%) was applied as shielding gas, with a flow rate of 5.5 L/min, minimising the contamination of the melt pool during the DLD process. During the deposition and production of the M625 bulk, the distance between substrate and nozzle was 13 mm. The samples were air-cooled to room temperature. Figure 3 shows a bulk produced by the DLD technique with the respective measurements.

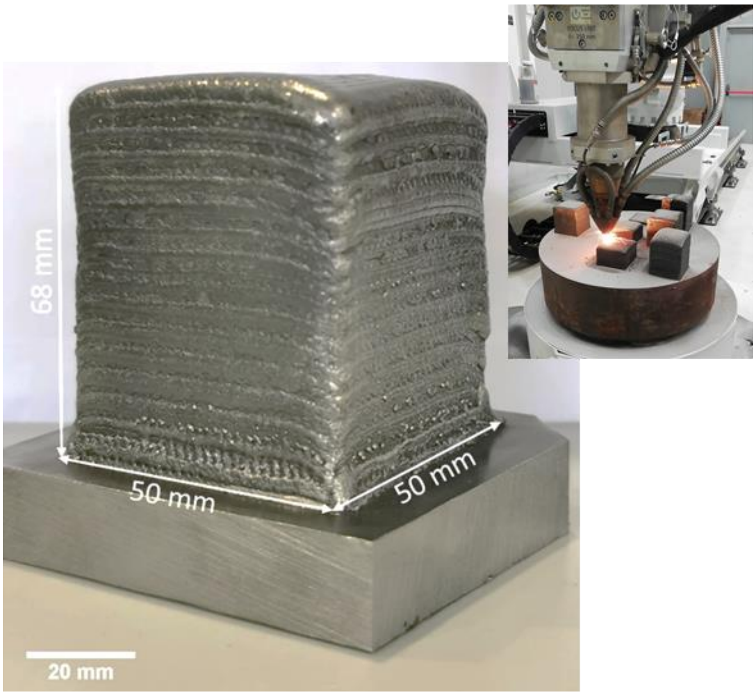

Figure 3. Bulk produced by direct laser deposition (DLD) using Inconel 625 powder deposited on 42CrMo4 steel substrate.

Microstructural and Mechanical Characterisation

The M625 bulk was cut for microstructural and mechanical characterisation using a metallographic cut-off machine with refrigeration to avoid substrate and cladding overheating. Samples were mounted in resin and polished down to 1 μm diamond suspension. An additional polishing step was performed with 0.06 μm silica colloidal suspension for a superior surface finishing and polishing-induced plastic deformation removal.

Chemical and microstructural characterisations were performed using a scanning electron microscope (SEM) equipped with Energy Dispersive X-Ray Spectroscopy (EDX) and a Digital Microscope (DM).

Vickers microhardness evaluation was performed on a fully automated microindenter . The HV hardness maps were obtained from a sample taken from the bulk, applying a load of 300 g and a dwell time of 15 s. This procedure scanned a 10 × 2.4 mm area of with 0.5 mm as the distance between the centres of two adjacent indentations.

Uniaxial tension tests were carried out on an electromechanical uniaxial testing system with a 5 kN load cell and a 0.5 mm/min strain rate. The surface strains were measured by digital image correlation (DIC), a non-contact method, using correlation softwareVIC-2D 6. The DIC images were captured with a telecentric lens and a 5 MPixel camera (acA2440-75um, 2448x2048 pixels. The experimental work plan was carried out using a 5 kN electromechanical testing system designed expressly for this type of request (Figure 4) [36]. The specimens were tested at room temperature with a constant crosshead speed of 0.5 mm/min, which corresponds to an initial strain rate of 0.0037 s^{-1}. Wire electrical discharge machining was used to extract the specimens with a thickness of 1.4 mm, according to the geometry indicated in Figure 4.

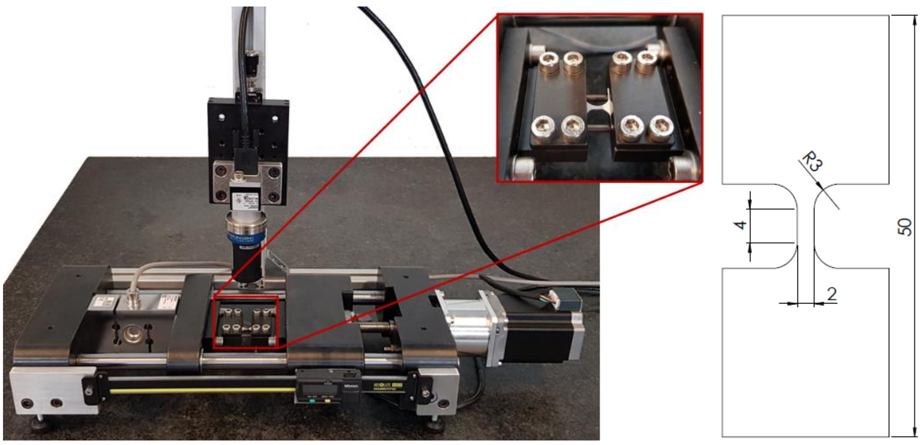

Figure 4. Uniaxial tensile test setup and sample dimensions (in mm).

Micro-abrasion wear tests evaluated the bulk wear rate with a micro-scale abrasion tester, using a fixed rotating ball configuration. The wear craters were measured with a 3D Optical profilometer, and the volume of the worn material was calculated.

Results and Discussion

Microstructure

The bulk deposited by DLD evidenced a layered macrostructure appearance, as shown in Figure 2. From the cladding/substrate set, sections perpendicular to the substrate were prepared for microstructural observation. The observation of these sections revealed that the bulk was free from cracks, voids between the deposited layers, and no unmelted particles were observed along with the structure. No porosities with deleterious dimensions were identified during the DM and SEM analysis. It also presented an excellent metallurgical bonding to the substrate, as illustrated in Figure 5.

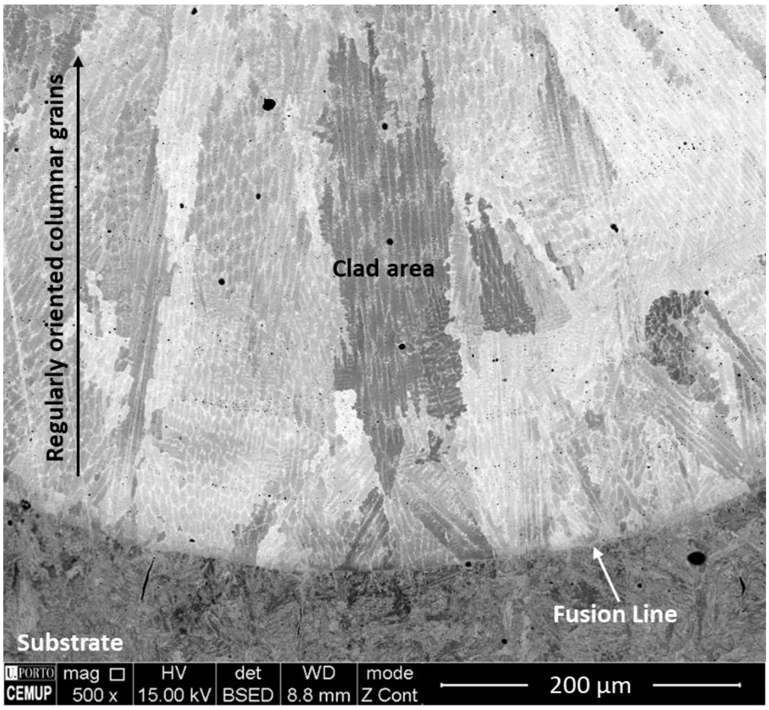

Figure 5. Microstructure obtained by scanning electron microscopy (SEM) of the M625 solid produced by direct laser deposition (DLD).

As indicated in previous studies [25][37], PHT promotes the formation of cellular or equiaxial grains in the region adjacent to the substrate (as illustrated in Figure 3), a condition not observed in samples without PHT, where the formation of planar grains occurs. The microstructure in the bulk consists mainly of a columnar/dendritic structure, which exhibits a coarse grain, and the longitudinal section microstructure revealed the layer-by-layer deposition pattern. The dendritic growth is approximately parallel to the direction of heat flow, showing similar direction in all single layers. A more detailed description of the microstructure of claddings produced with M625 is presented in [25]. The transition region between two depositions produced by DLD and the columnar/dendritic microstructure evolution characteristic of these regions are shown in Figure 6.

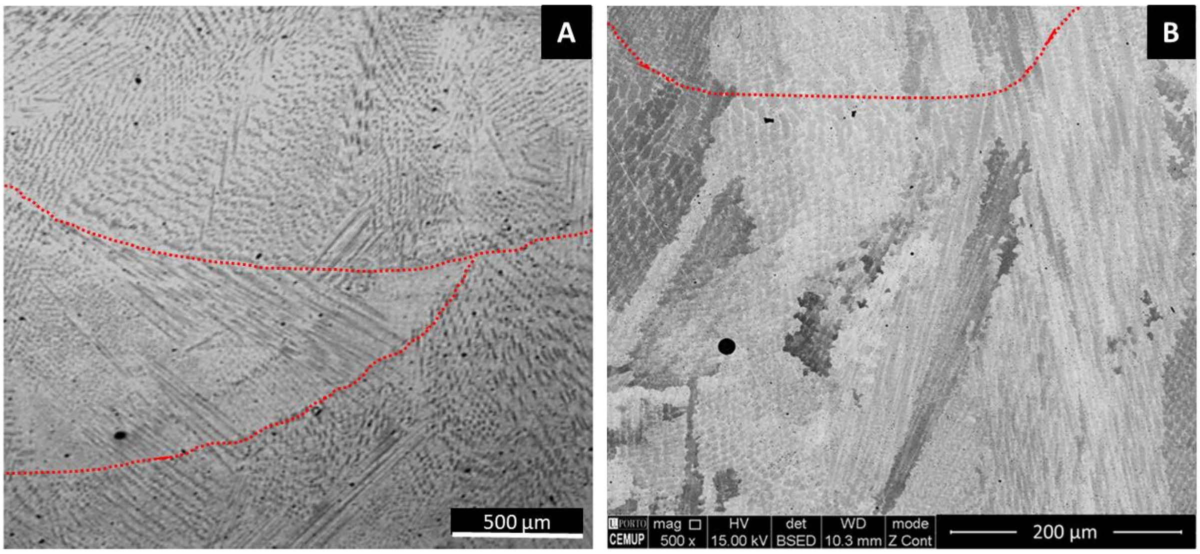

Figure 6. Microstructure images of M625 claddings obtained by (A) Digital Microscopy and (B) Scanning Electron Microscopy. Red lines indicate transition regions between consecutive claddings.

Figure 4 shows no discontinuities between layers and a small dilution zone, a consequence of the remelting provoked by the deposition of the new layer. Figure 4B illustrates columnar/dendritic grains continuity across the interface, evidencing epitaxial growth. The material on which the layer is deposited (substrate or previously deposited layer) acts as a heat sink during the laser processing of materials. Due to this factor, the grains are columnar and present a directional growth parallel to the heat flow direction. Epitaxial growth is promoted by nucleation in partially remelted surface grains, either from the substrate or from the solidified deposited layer. Figure 7 is an Inverse Pole Figure (IPF), obtained by the EBSD technique, showing this epitaxial growth that is most evident in the transition from the first layer to the second layer of M625.

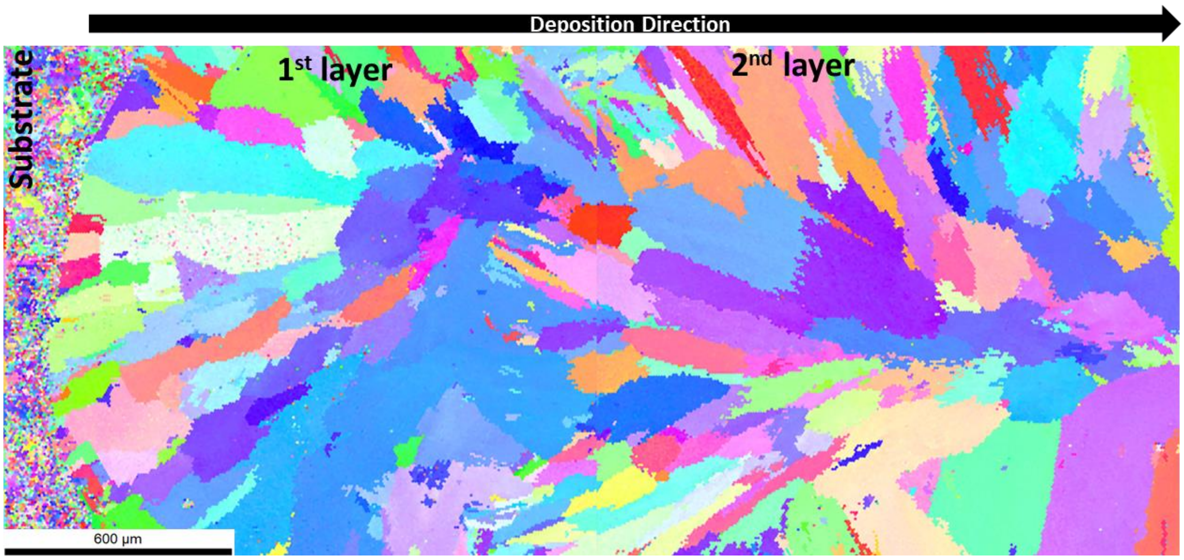

Figure 7. Inverse Pole Figure (IPF), obtained by the EBSD technique, showing the epitaxial growth

The formation of deleterious phases during the DLD deposition process was investigated. Nickel-based superalloys consist basically of an austenitic matrix (FCC), carbides (MC, $M_{23}C_6$, ...), Laves phase (Nb-Mo-Cr-Fe-Ni), and complex oxides, as shown in Figure 8 and Table 2. These phases are typical of this superalloy [38], [39] and have been detected across the entire M625 bulk; the γ'' (Ni_3Nb) phase was not detected.

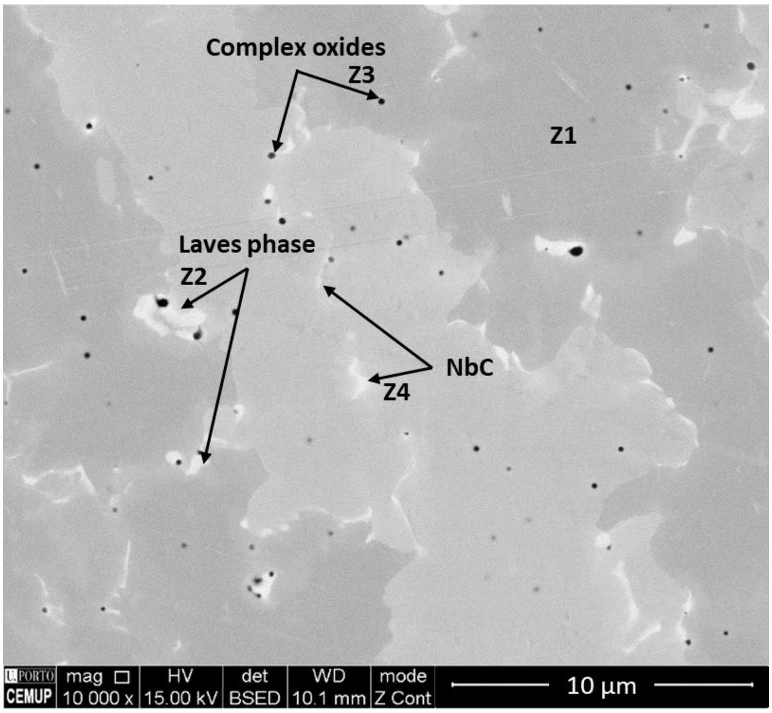

Figure 8. Microstructural constituents in the matrix and interdendritic zones of M625 bulk.

Table 2. Chemical composition of the phases identified in solid M625 by EDX.

Phases	**Chemical Composition (at%)**								
	Ni	Fe	Cr	Mo	Nb	Si	Al	O	C
Matrix (Z1)	51.91	23.19	19.76	4.39	-	0.75	-	-	-
Laves phase (Z2)	42.2	15.64	17.91	10.54	10.19	3.52	-	-	-
Complex Oxide (Z3)	20.86	9.11	14.68	7.1	4.97	5.41	4.96	27.15	5.76
NbC (Z4)	-	-	-	-	56.3	-	-	-	43.7

Superalloy solidification begins with the formation of γ dendrites, which during their formation, reject elements, like niobium, molybdenum and carbon to the liquid, resulting in the formation of carbides and Laves phase during the final stage of solidification [40]. The segregation of niobium is much more pronounced when compared to molybdenum and is, therefore, the main problem related to superalloy solidification [41].

Laves phase formation (Zone Z2) is highly undesirable since it promotes cracking, deteriorating mechanical properties and fatigue life [42]. As mentioned in a previous study [25], the PHT promotes a lower cooling rate, allowing higher diffusion of Nb and Mo to the γ matrix, thus reducing segregation and decreasing the size of this phase.

The formation of complex oxides was also detected across the bulk (Z3 zone). The presence of these inclusions is not necessarily detrimental because the chromium content in the complex oxides is not higher than in the matrix, thus maintaining the possibility of the formation of chromium oxides that increase the resistance to hot corrosion [43].

Zone Z4 is formed by the precipitation of NbC in the intragranular region of the austenitic matrix. The formation of NbC in higher proportions provides an opportunity to selectively control the hardness and wear resistance [44].

Uniaxial Tensile Test

The mechanical characterisation of the M625 material was obtained by performing uniaxial tensile tests on miniaturised specimens. Specimens were obtained in two different loading directions, horizontal and vertical, which are parallel and perpendicular to the base plane, respectively. Several tests were also performed for each direction to guarantee that the results were repeatable. The experimental conditions of the test are listed in Table 3.

Table 3. Experimental conditions of uniaxial tensile tests.

Property	Value
Loading direction	2
Crosshead speed (grip) [mm/min]	0.5
Data acquisition [Hz]	10
Clip gage initial length – l_0 [mm]	3
Temperature [°C]	21
Relative humidity [%]	52

The digital image correlation (DIC) technique was used to determine the material strains by measuring the elongation in the uniform section of the specimen. The DIC system comprises a camera connected to a software application that analyses the collected images and calculates the strain field. As shown in Figure 4, the first step is to set the camera in the test environment at a certain distance from the specimen.

The average speckle size is less than 15 μm due to the size of the in-plane uniform area. The strain field (logarithmic Hencky strains) was computed using the commercial software, with a step size of 7 and a set size of 25 for the chosen region of interest. Figure 9 shows the engineering and true stress-strain flow curves acquired from the executed uniaxial tensile tests.

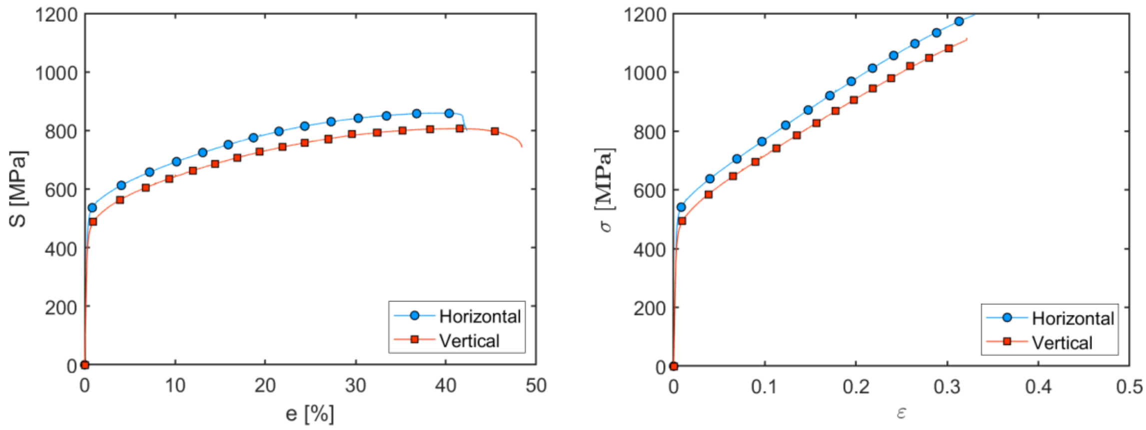

Figure 9. Miniaturised uniaxial tensile test results for Inconel 625 considering different loading directions: engineering (left) and true (right) stress-strain curves.

As seen in Figure 9, the obtained results from the uniaxial tensile tests suggest that the mechanical properties, more specific the material yield and ultimate tensile strength, are dependent on the loading direction relative to the deposition strategy. The samples taken perpendicularly to the layer deposition plane exhibit lower yield stress values and ultimate tensile strength. Although there is a difference of around 60 MPa in strength for the entire strain range, the amount of ductility is not much affected, showing good plastic deformation capacity, characteristic of this type of alloy and already reported in previous studies [45], [46].

Table 4 summarises the fundamental mechanical properties obtained from the uniaxial tensile tests. It contains the mean values of properties, such as yield stress ($Rp_{0.2}$), and ultimate tensile strength (Rm), as well as the uniform (e_u) and total elongation (e_t) calculated for each loading direction (horizontal and vertical). Additionally, Figure 10 presents the strain field contours obtained from the digital image correlation of the horizontal and vertical specimens, at different stages of the miniaturised uniaxial tensile tests.

Table 4. Summary of Inconel 625 mechanical properties (average values and corresponding standard deviation).

Loading direction	**$R_{p0.2}$ [MPa]**	**R_m [MPa]**	**e_u [%]**	**e_t [%]**
Horizontal	512.4 (0.26)	860.1 (0.25)	39.1 (0.29)	42.3 (0.51)
Vertical	449.1 (1.16)	807.1 (2.43)	40.5 (2.55)	46.8 (1.73)

The obtained values demonstrate a good agreement of the tensile characteristics over the whole bulk and repeatability between different tests. As previously stated, the specimens oriented vertically yielded significantly lower than the horizontally extracted ones but had comparable elongation values. This anisotropic behaviour between in-build direction (vertical) and horizontal direction was already reported in prior work [47].

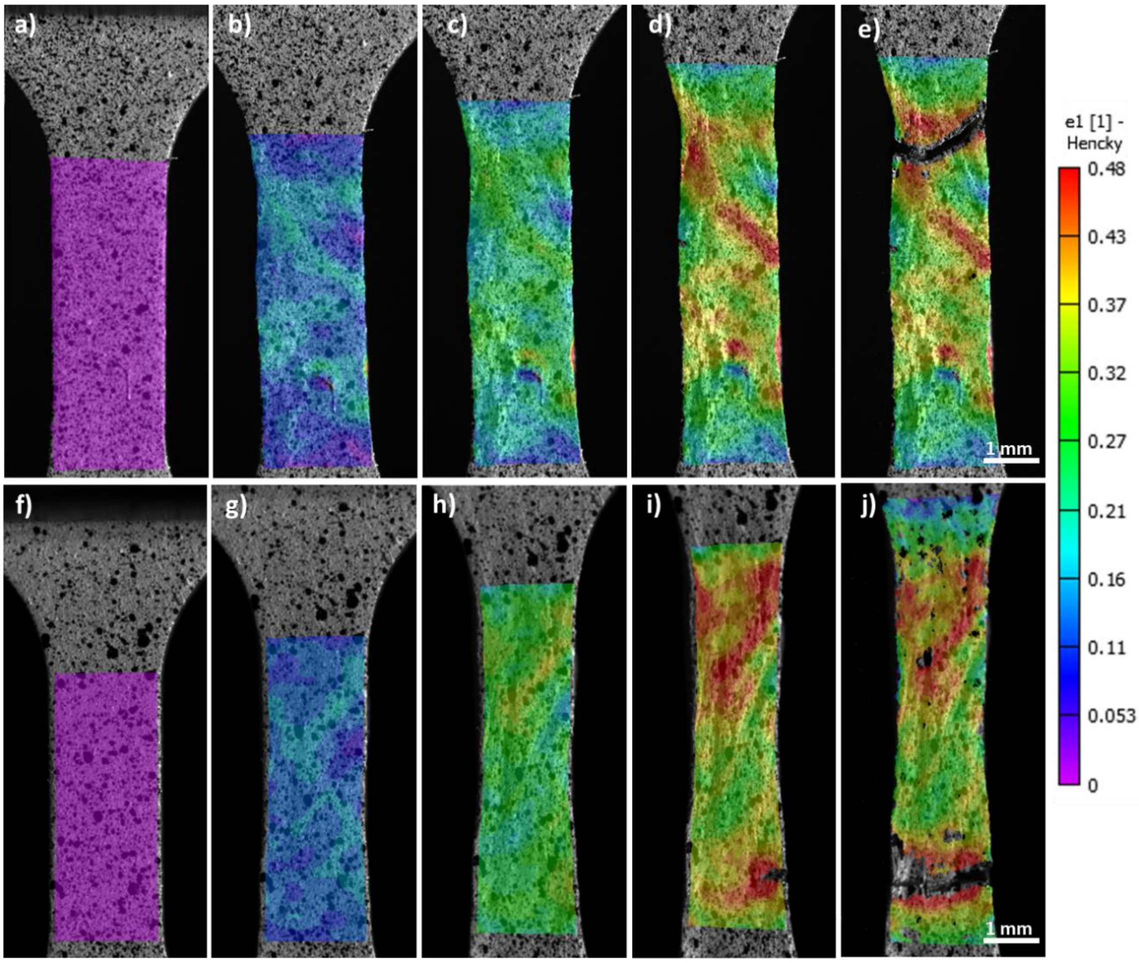

Figure 10. Digital image correlation results (contours correspond to logarithmic Hencky strain along loading direction): a-e) horizontal specimen; f-j) vertical specimen.

A comparison was also done with the mechanical properties specified in standards for different applications of this nickel-based superalloy to evaluate the deposited material's performance in this study. The minimum values specified in the standards for the forging and casting processes are listed in Table 5. Regarding the M625 material, only the lowest obtained value from the two loading directions was considered.

Table 5. Comparison of M625 mechanical properties with forging and casting standard requirements.

Material	$R_{p0.2}$ [MPa]	R_m [MPa]	A [%]
M625 (present study)	449	807	42
NW6625 (forging) [48]	415	830	30
NC6625 (casting) [49]	275	485	25

As can be seen, the mechanical properties of M625 deposited material are significantly superior than those required for the equivalent casting alloy, but at the same level regarding the specifications of the forging alloy. Through this comparison and the experimental tests, it is possible to demonstrate that using the defined process and conditions will result in a final product with good quality and excellent mechanical characteristics.

When employing the additive manufacturing process, good adhesion and bonding to the material substrate is another goal. However, to assess this characteristic, samples were taken in the transition zone between the substrate and M625. The transition zone is positioned in the centre area of the uniform section of the miniaturised specimen, as illustrated in Figure 11. The evolution of force with the specimen elongation is presented in Figure 12, and a comparison with the engineering stress-strain curves is already shown in Figure 9.

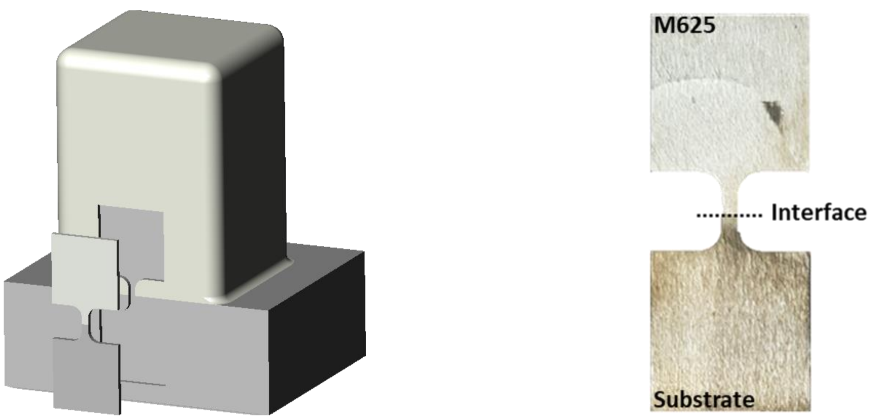

(A) Extraction scheme of interface specimen (b) Experimental specimen

Figure 11. Definition of interface specimen between substrate and M625.

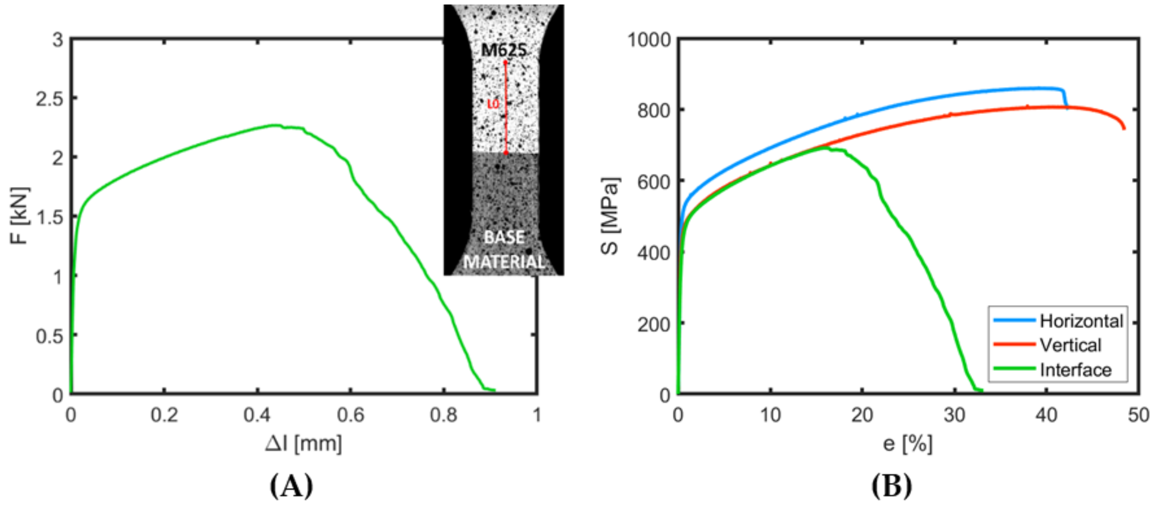

Figure 12. (A) Evolution of force (F) with elongation (Δl) obtained from interface specimen between the substrate and Inconel M625 and (B) comparison of engineering stress-strain curves.

Usually, one of the output results of this standardised test is the stress-strain curve, however since the deformation of the specimen is not uniform (Figure 13) due to different mechanical properties (e.g. modulus of elasticity, yield stress, etc.) and the material that undergoes plastic deformation is only M625, an extensometer was consider only in such zone (Figure 11).

As shown in Figure 12B, the mechanical behaviour of the interface specimen is identical to the behaviour of the vertical specimen, because both were taken from the bulk sample in the same orientation. However, due to the geometric constraints, the material's plastic deformation is more localized. Similar low elongation values were also exhibited by the welded joints with strength mismatch to localized plastic deformation [50]. Also, the fracture only occurs in the M625 (Figure 13h), which means that the adhesion and bonding to the substrate is very good, since the fracture occurred outside the transition zone, validating the used conditions and process parameters. This mechanical response of the tensile specimens is an excellent indication of the correct choice of processing parameters and of the influence of preheating the substrate, minimising the probability of brittle metastable phases in the bonding zone and HAZ.

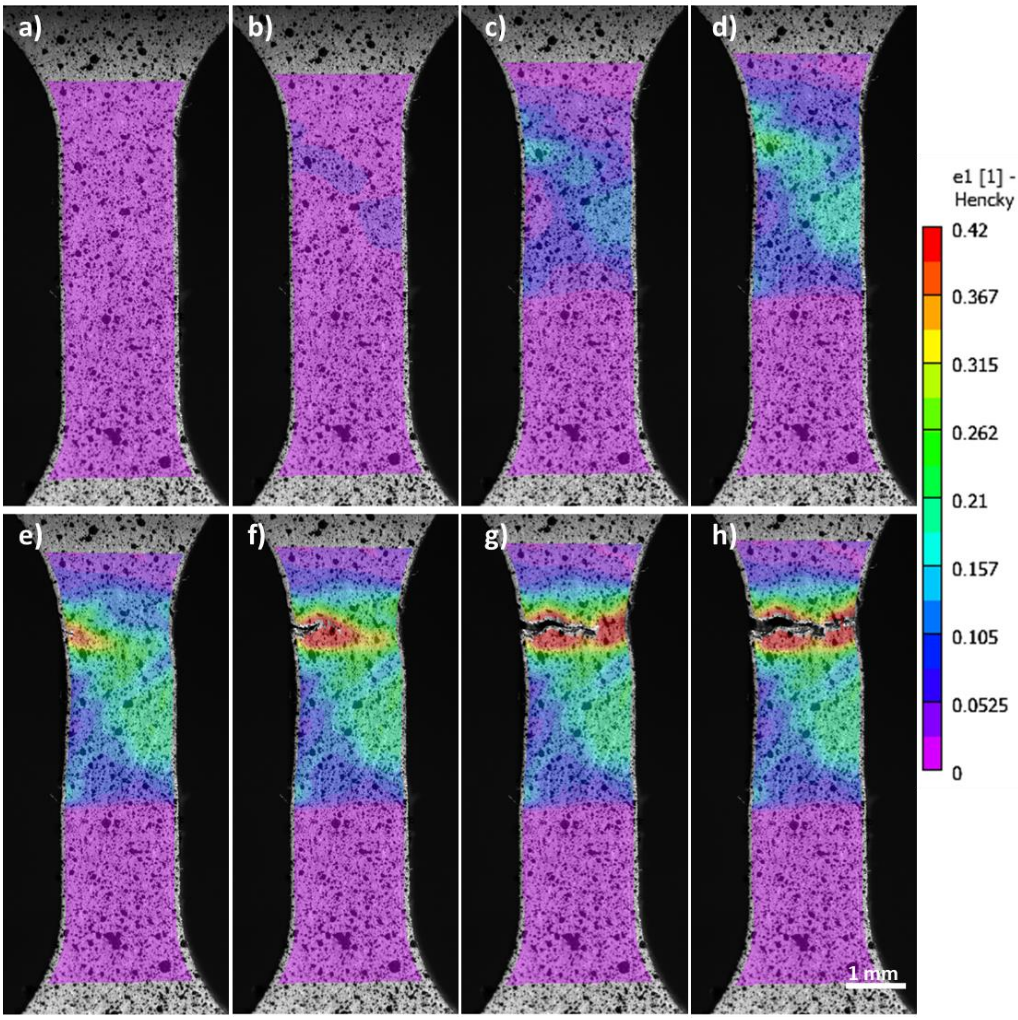

Figure 13. Digital image correlation results obtained for the interface specimen (contours correspond to logarithmic Hencky strain along loading direction).

Fracture Surface Analysis

Fracture surface analysis was performed on the specimens for the two different loading directions, horizontal and vertical. Figure 14 shows micrographs obtained by SEM to determine the fracture mode of the specimens produced from the bulk of M625 produced by DLD. Table 6 shows the chemical composition of the zones identified in Figure 14.

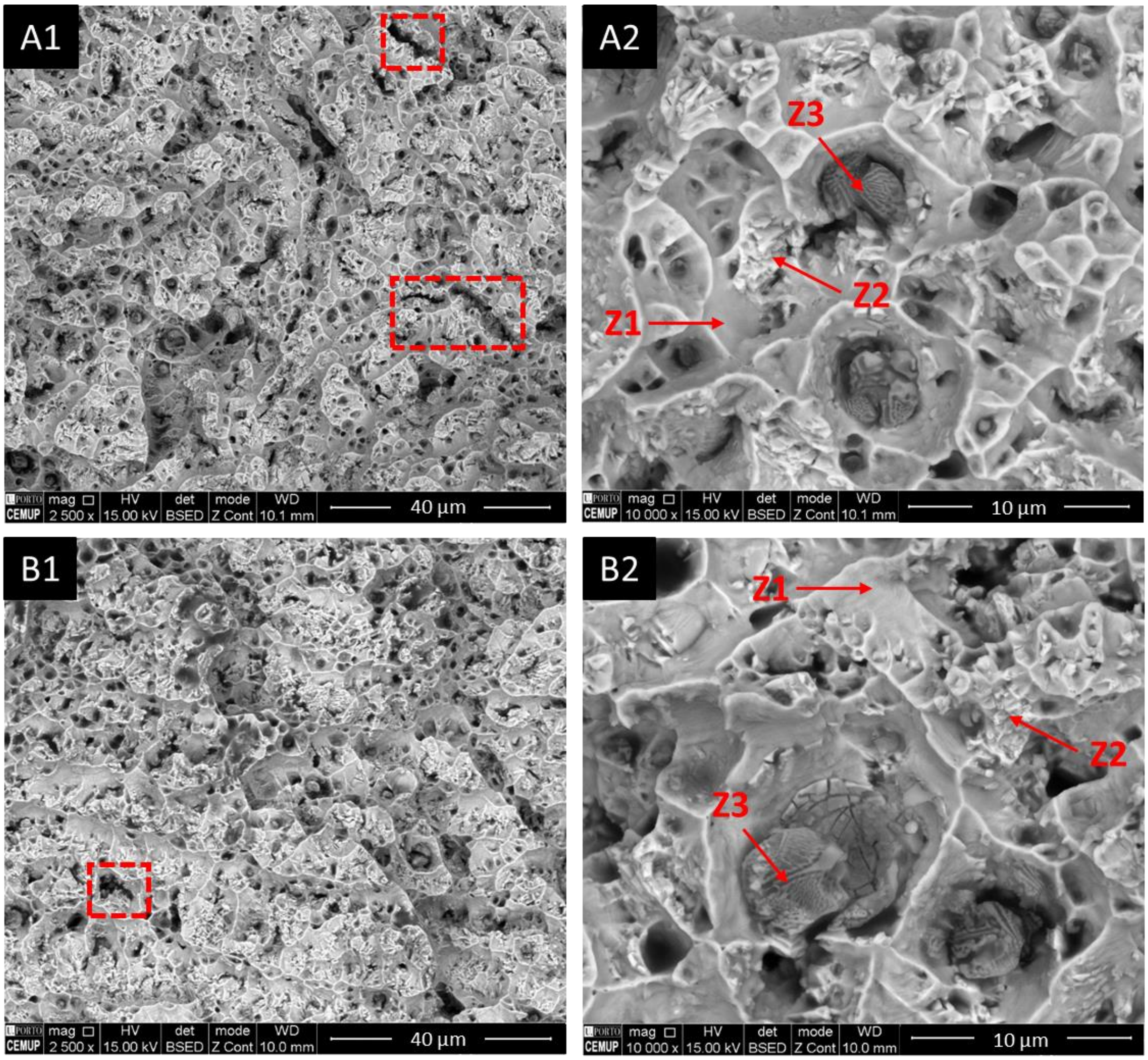

Figure 14. Tensile specimen fractography tested to failure. A1 and A2 are SEM micrographs of the fracture surface for the horizontal sample. B1 and B2 for vertical sample.

Table 6. Phase chemical analysis by EDX – horizontal and vertical fractography. samples.

Elements	Horizontal (A2)			Vertical (B2)		
	Z1	Z2	Z3	Z1	Z2	Z3
Ni	67.26	54.84	22.44	68.36	58.64	4.26
Cr	23.83	24.65	30.28	24.22	25.51	26.85
Mn	-	-	7.19	-	-	9.41
Mo	5.98	7.78	1.66	4.12	5.93	0.49
Nb	1.97	11.89	3.64	1.53	9.29	1.88
Fe	0.96	0.84	0	0.71	0.63	-
Si	-	-	6.61	1.06	-	15.4
O	-	-	28.18	-	-	41.71

The micrographs of the fracture surfaces, show microvoids (dimples) which are typical of ductile failure mode (ductile fracture), corroborating the ductility values measured in the tensile tests. Figures 14 A1 and B1 show, in the red hatched regions, the presence of micro-cracks in regions of elemental micro-segregation. According to Table 6, the main phases observed in these regions are the Laves phase (Z2) and complex oxides (Z3).

The micrographs indicate that some dimples start in complex oxides, which are particles of high mechanical resistance and non-deformable surrounded by a ductile matrix, leading to decohesion in the interface zone. Subsequent microcracking propagates through the Laves phase that is an intermetallic harder and less suitable for plastic deformation than the matrix.

Microhardness

To analyse the microhardness variation, a sample was taken from the centre of the M625 bulk, approximately 16 mm long and 12 mm wide. As a reference, the end closest to the top of the bulk was designated as the top of the specimen. After polishing, three series of indentations were performed. In each series, 20 hardnesses were performed 0.5 mm apart, thus analysing the hardness in different layers. The results obtained are shown in Figure 15.

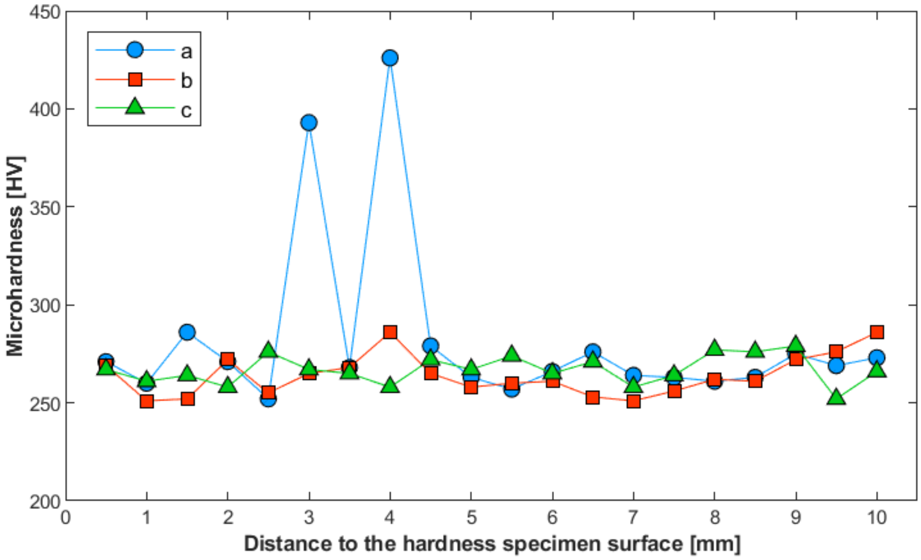

Figure 15. Microhardness profile on samples taken from the M625 solid. a, b and c indicates three series of indentations tests.

The results reveal sample microhardness in the range of 251-286 HV0.3 in most of the indentations performed. The microhardness average and standard deviation were 271 HV0.3 and 27.5 HV0.3, respectively, indicating a rather homogeneous hardness throughout the bulk. However, two indentations with values equal to 393 and 426 HV0.3 were obtained, related to regions with a higher concentration of secondary phases, such as the Laves phase, which increases the bulk hardness.

This distribution of hardness is consistent with the results of tensile tests, particularly with the homogeneous distribution of strain in the bulk. Microhardness analysis at the M625/substrate interface and adjacent areas was reported in a previous study [25]. The microhardness obtained in the M625 bulk is in agreement with the references [51][52][53].

Wear Analysis

The wear test performance was evaluated using the Abrasive Wear Rate (see Equation 3).

$$K = \frac{V}{S \cdot N} \tag{1}$$

where, K is the Abrasive Wear Rate [$mm^3.N^{-1}.mm^{-1}$], V is the worm volume [mm^3], S is the sliding distance [mm], and N is the normal load [N]. Both the calculated worm volume (V) (Equation 4) and the measured value obtained by optical profiler characterisation were used.

$$V = \frac{\pi \cdot b^4}{64 \cdot R} \tag{2}$$

where, b is the crater diameter [mm], and R is the radius of the ball [mm].

The micro-abrasion tests used a slurry of SiC powder (F1000) with 2% v/v concentration. The ball used on the tests was a 25.4 mm diameter hardened steel (SAE 52100), with rotation speed fixed at 85 rpm and a constant load of 0.25 N [54]. Three different test times were selected (15, 30 and 60 minutes) to evaluate the wear behaviour. Table 7 summarises the results.

Table 7. Micro-abrasion wear test results

			Calculated Volume		**Measured Volume**	
Tests [min]	S [mm]	b [mm]	V [mm^3]	K [$mm^3 \cdot N^{-1} \cdot mm^{-1}$]	V [mm^3]	K [$mm^3 \cdot N^{-1} \cdot mm^{-1}$]
15 min	203480.956	1.400	0.014857	5.841×10^{-7}	0.009060	3.562×10^{-7}
30 min	406962.912	1.558	0.022800	4.482×10^{-7}	0.014980	2.945×10^{-7}
60 min	813924.825	1.917	0.052236	5.134×10^{-7}	0.036650	3.602×10^{-7}

Figure 16 presents the volume of worn material as a function of the sliding distance (S) and normal load (N), considering the volume calculated by Equation (2) and the volume obtained by the optical profiler characterisation, illustrated in Figures 17 and 18 for 15 and 60 minutes test, respectively. As expected, the wear behaviour showed a linear development, representing a constant wear rate throughout the tests. Nevertheless, the Abrasive Wear Rate (K) for the volume calculated by Equation (1) was 45% higher than the value measured, which might be related to the assumption that the worm region is perfectly spherical, while in practice, there is a slight deviation and not uniform wear [54]. Microstructural observations evidenced that scratching was the abrasive wear mode.

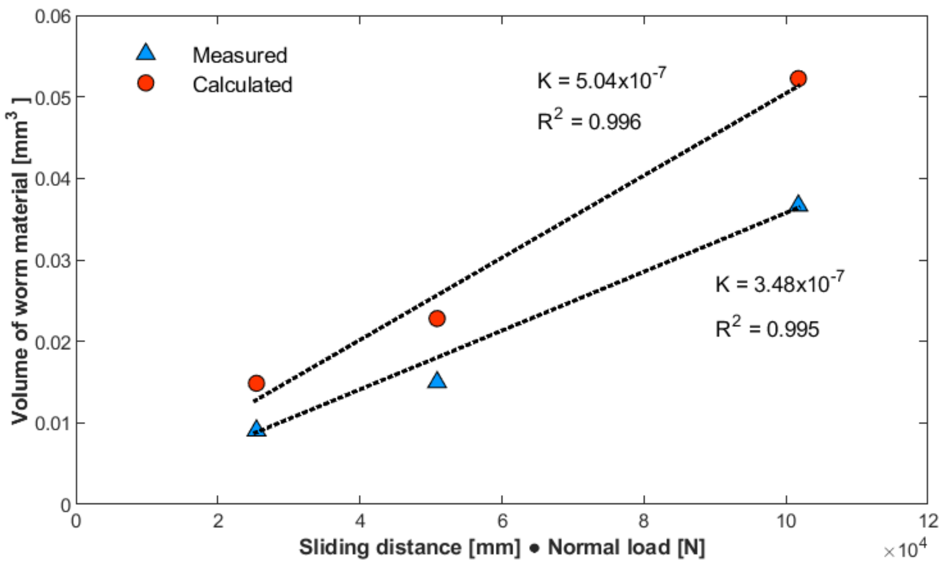

Figure 56. Volume of worn material as a function of the sliding distance (S) and normal load (N)

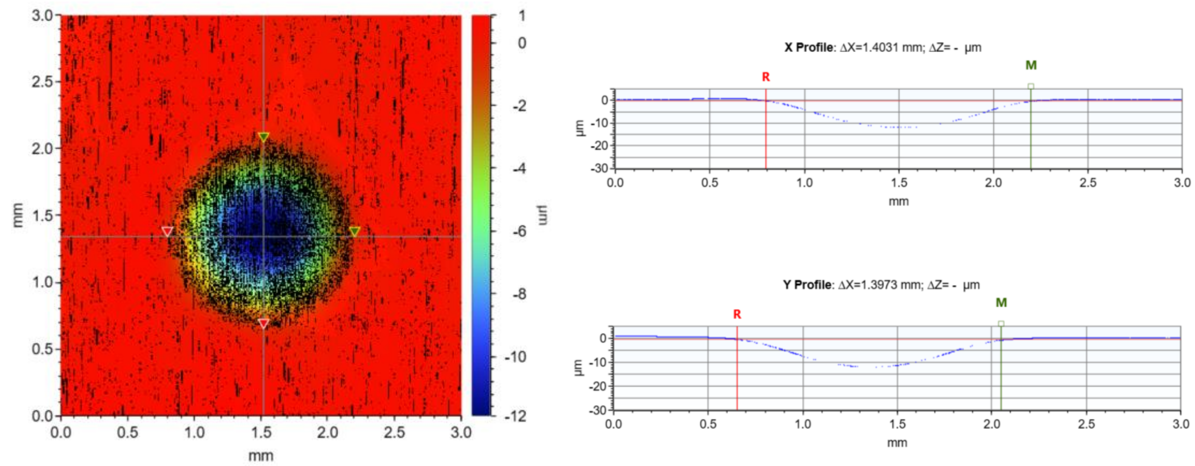

Figure 17. Worn crater optical characterisation for 15 minutes test

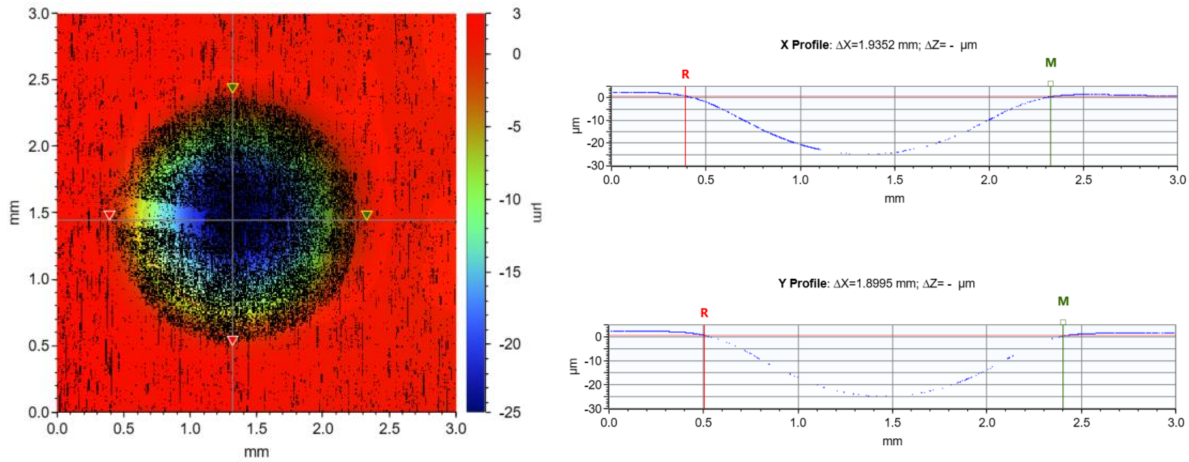

Figure 18. Worn crater optical characterisation for 60 minutes test

Conclusions

In the present study, a nickel superalloy bulk was successfully produced using a direct laser deposition technique. To construct the bulk, successive Inconel 625 (M625) powder layers were deposited on a 42CrMo4 structural steel substrate pre-heated to 300 °C. The main conclusions, which were drawn from the microstructural and mechanical analyses, are the following:

- The bulk produced by DLD did not present relevant defects, such as cracks or porosities, which could compromise its structural integrity.
- Columnar dendrites are the main microstructural feature seen throughout the entire bulk. Laves phase, carbides and complex oxides resulting from microsegregation were detected.
- Expressive hardness variations were not observed along the samples taken from the bulk.
- Tensile tests demonstrated that the ductility and tensile strength were similar to a forged Inconel 625. The metallurgical bonding of the bulk to the substrate is continuous and without metastable phases (martensite). Tensile samples

with an M625/steel interface in the central region suffer rupture by the M625 (less resistant material) away from the interface.

- Tensile samples with their length parallel to the substrate surface are slightly more strong and less ductile than those with length perpendicular to that surface, indicating a texture effect, which can be correlated to the epitaxial growth of columnar grains.
- The wear behaviour showed a linear development, representing a constant wear rate throughout the tests, and the worn surfaces showed abrasive wear.

These conclusions are excellent indications of the high quality of deposited layers that can be used for the repair/remanufacturing of components.

Funding: This research was funded by FEDER through the program P2020|COMPETE, Projetos em Copromoção (project POCI-01-0247-FEDER-039848).

Institutional Review Board Statement: Not applicable

Informed Consent Statement: Not applicable

Data Availability Statement: Not applicable

Acknowledgements: The authors are grateful to CEMUP (Centro de Materiais da Universidade do Porto) for expert assistance with SEM.

Conflicts of Interest: The authors declare no conflict of interest.

References

[1] L. E. Criales, Y. M. Arısoy, T. Özel, Sensitivity analysis of material and process parameters in finite element modeling of selective laser melting of Inconel 625, *Int. J. Adv. Manuf. Technol.*,vol. 86 (2016) 2653–2666, https://doi.org/10.1007/s00170-015-8329-y.

[2] S. M. Thompson, L. Bian, N. Shamsaei, A. Yadollahi, An overview of Direct Laser Deposition for additive manufacturing; Part I: Transport phenomena, modeling and diagnostics, *Addit. Manuf.*, 8 (2015) 36–62, https://doi.org/10.1016/j.addma.2015.07.001.

[3] N. Shamsaei, A. Yadollahi, L. Bian, S. M. Thompson, An overview of Direct Laser Deposition for additive manufacturing; Part II: Mechanical behavior,

process parameter optimization and control, *Addit. Manuf.*, 8 (2015) 12–35, https://doi.org/10.1016/j.addma.2015.07.002.

[4] C. P. Paul, P. Ganesh, S. K. Mishra, P. Bhargava, J. Negi, A. K. Nath, Investigating laser rapid manufacturing for Inconel-625 components, *Opt. Laser Technol.*, 39, (4) (2007) 800–805, https://doi.org/10.1016/j.optlastec.2006.01.008.

[5] L. Costa, Laser powder deposition, 4 (2009) 264–279, https://doi.org/10.1108/13552540910979785.

[6] J. Leunda, V. García Navas, C. Soriano, C. Sanz, Effect of laser tempering of high alloy powder metallurgical tool steels after laser cladding, *Surf. Coatings Technol.*, 259 (2014) 570–576, https://doi.org/10.1016/j.surfcoat.2014.10.028.

[7] G. R. Thellaputta, P. S. Chandra, C. S. P. Rao, Machinability of Nickel Based Superalloys: A Review, *Mater. Today Proc.*, 4 (2) (2017) 3712–3721, https://doi.org/10.1016/j.matpr.2017.02.266.

[8] G. Li, J. Huang, Y. Wu, An investigation on microstructure and properties of dissimilar welded Inconel 625 and SUS 304 using high-power CO_2 laser, *Int. J. Adv. Manuf. Technol.*, 76 (2015) 1203–1214, https://doi.org/10.1007/s00170-014-6349-7.

[9] R. Vilar, A. Almeida, Repair and manufacturing of single crystal Ni-based superalloys components by laser powder deposition—A review, *J. Laser Appl.*, 27 (2015) S17004, https://doi.org/10.2351/1.4862697.

[10] T. E. Abioye, D. G. McCartney, A. T. Clare, Laser cladding of Inconel 625 wire for corrosion protection, *J. Mater. Process. Technol.*, 217 (2015) 232–240, https://doi.org/10.1016/j.jmatprotec.2014.10.024.

[11] J. A. Gonzalez, J. Mireles, S. W. Stafford, M. A. Perez, C. A. Terrazas, R. B. Wicker, Characterization of Inconel 625 fabricated using powder-bed-based additive manufacturing technologies, *J. Mater. Process. Technol.*, 264 (2019) 200–210, https://doi.org/10.1016/j.jmatprotec.2018.08.031.

[12] G. Marchese, X. G. Colera, F. Calignano, M. Lorusso, S. Biamino, P. Minetola, D. Manfredi, Characterization and Comparison of Inconel 625 Processed by Selective Laser Melting and Laser Metal Deposition, *Adv. Eng. Mater.*, 19 (3) (2017) 1–9, https://doi.org/10.1002/adem.201600635.

[13] G. P. Dinda, A. K. Dasgupta, J. Mazumder, Laser aided direct metal deposition of Inconel 625 superalloy: Microstructural evolution and thermal stability, *Mater. Sci. Eng. A*, 509 (2009) 98–104, https://doi.org/10.1016/j.msea.2009.01.009.

[14] K. Löhnert , F. Pyczak, Microstructure evolution in the nickel base superalloy Allvac® 718Plus™, *7th Int. Symp. Superalloy 718 Deriv. 2010*, 2 (2010) 877–891, https://doi.org/10.1002/9781118495223.ch67.

[15] G. Marchese, E. Bassini, M. Calandri, E. P. Ambrosio, F. Calignano, M. Lorusso, D. Manfredi, M. Pavese, S. Biamino, P. Fino, Microstructural investigation of as-fabricated and heat-treated Inconel 625 and Inconel 718 fabricated by direct metal laser sintering: contribution of Politecnico di Torino and Istituto Italiano di Tecnologia (IIT) di Torino, *Met. Powder Rep.*, 71 (4) (2016) 273–278, https://doi.org/10.1016/j.mprp.2016.06.002.

[16] J. Belan, GCP and TCP Phases Presented in Nickel-base Superalloys, *Mater. Today Proc.*, 3 (4) (2016) 936–941, https://doi.org/10.1016/j.matpr.2016.03.024.

[17] R. Sowa, S. Arabasz, M. Parlinska-Wojtan, Classification and microstructural stability of high generation single crystal Nickel-based superalloys, *Zast. Mater.*, 57 (2) (2016) 274–281, https://doi.org/10.5937/zasmat1602274s.

[18] X. Xu *et al.*, "Research on microstructures and properties of Inconel 625 coatings obtained by laser cladding with wire," *J. Alloys Compd.*, 715 (2017) 362–373, https://doi.org/10.1016/j.jallcom.2017.04.252.

[19] Y. Li, K. Chen, R. L. Narayan, U. Ramamurty, Y. Wang, J. Long, N. Tamura, X. Zhou, Multi-scale microstructural investigation of a laser 3D printed Ni-based superalloy, *Addit. Manuf.*, 34 (2020) 101220, https://doi.org/10.1016/j.addma.2020.101220.

[20] M. Scendo, K. Staszewska-Samson, H. Danielewski, Corrosion behavior of inconel 625 coating produced by laser cladding, *Coatings*, 11 (7) (2021) https://doi.org/10.3390/coatings11070759.

[21] G. Muvvala, D. Patra Karmakar, A. K. Nath, Online monitoring of thermo-cycles and its correlation with microstructure in laser cladding of nickel based super alloy, *Opt. Lasers Eng.*, 88 (2017) 139–152, https://doi.org/10.1016/j.optlaseng.2016.08.005.

[22] Y. C. Zhang, Z. G. Li, P. L. Nie, and Y. X. Wu, Effect of ultrarapid cooling on microstructure of laser cladding IN718 coating, *Surf. Eng.*, 29 (6) (2013) 414–418, https://doi.org/10.1179/1743294413Y.0000000142.

[23] Y. T. Long, P. L. Nie, Z. G. Li, J. Huang, X. Li, X. M. Xu, Segregation of niobium in laser cladding Inconel 718 superalloy, *Trans. Nonferrous Met. Soc. China (English Ed.)*, 26 (2) (2016) 431–436, https://doi.org/10.1016/S1003-6326(16)64131-6.

[24] P. Nie, O. A. Ojo, Z. Li, Numerical modeling of microstructure evolution during laser additive manufacturing of a nickel-based superalloy, *Acta Mater.*, 77 (2014) 85–95, https://doi.org/10.1016/j.actamat.2014.05.039.

[25] A. A. Ferreira, R. L. Amaral, P. C. Romio, J. M. Cruz, A. R. Reis, M. F. Vieira, Deposition of nickel-based superalloy claddings on low alloy structural steel by direct laser deposition, *Metals.*, 11, (8) (2021),

https://doi.org/10.3390/met11081326.

[26] A. Sadhu, A. Choudhary, S. Sarkar, A. M. Nair, P. Nayak, S. D. Pawar, G. Muvvala, S. K. Pal, A. K. Nath, A study on the influence of substrate pre-heating on mitigation of cracks in direct metal laser deposition of NiCrSiBC-60%WC ceramic coating on Inconel 718, *Surf. Coatings Technol.*, 389 (2020) 125646, https://doi.org/10.1016/j.surfcoat.2020.125646.

[27] K. H. G. Bennett, Jennifer; Dudas, Rory; Cao, Jian; Ehmann, Control of Heating and Cooling for Direct Laser Deposition Repair of Cast Iron Components, *Int. Symp. Flex. Autom. ISFA 2016*, (2016) 1–3, https://doi.org/10.1109/ISFA.2016.7790166

[28] A. A. Ferreira, R. Darabi, J. P. Sousa, J. M. Cruz, A. R. Reis, and M. F. Vieira, Optimization of direct laser deposition of a martensitic steel powder (Metco 42C) on 42CrMo4 steel, *Metals*, 11 (4) (2021) 1–18, https://doi.org/10.3390/met11040672.

[29] W. He, W. Shi, J. Li, H. Xie, In-situ monitoring and deformation characterization by optical techniques; part I: Laser-aided direct metal deposition for additive manufacturing, *Opt. Lasers Eng.*, 122 (2019) 74–88, https://doi.org/10.1016/j.optlaseng.2019.05.020.

[30] D. S. Shim, G. Y. Baek, S. B. Lee, J. H. Yu, Y. S. Choi, S. H. Park, Influence of heat treatment on wear behavior and impact toughness of AISI M4 coated by laser melting deposition, *Surf. Coatings Technol.*, 328 (2017) 219–230, https://doi.org/10.1016/j.surfcoat.2017.08.059.

[31] J. C. Heigel, P. Michaleris, T. A. Palmer, In situ monitoring and characterization of distortion during laser cladding of Inconel® 625, *J. Mater. Process. Technol.*, 220 (2015) 135–145, https://doi.org/10.1016/j.jmatprotec.2014.12.029.

[32] British Standard, BS EN 10269:2006 Steels and nickel alloys for fasteners with specified elevated and / or low temperature, (2006).

[33] X. Wu, B. Zhu, X. Zeng, X. Hu, K. Cui, Critical state of laser cladding with powder auto-feeding, *Surf. Coatings Technol.*, 79 1–3 (1996) 200–204, https://doi.org/10.1016/0257-8972(95)02452-2.

[34] E. Toyserkani, A. Khajepour, and S. Corbin, "Laser Cladding," *New York*, 11 (2) (2017) 221, https://doi.org/10.2351/1.521888.

[35] L. Thivillon, P. Bertrand, B. Laget, I. Smurov, Potential of direct metal deposition technology for manufacturing thick functionally graded coatings and parts for reactors components, *J. Nucl. Mater.*, 385 (2) (2009) 236–241, https://doi.org/10.1016/j.jnucmat.2008.11.023.

[36] D. J. Cruz, S. P. Shamchi, A. D. Santos, R. L. Amaral, P. J. Tavares, P. M. G. P.

Moreira, Development of a mini-tensile approach for sheet metal testing using Digital Image Correlation, *Procedia Struct. Integr.*, 25 (2020) 316–323, https://doi.org/10.1016/j.prostr.2020.04.036.

[37] M.-S. Pham, B. Dovgyy, P. A. Hooper, C. M. Gourlay, A. Piglione, The role of side-branching in microstructure development in laser powder-bed fusion, *Nat. Commun.*, (2020) 1–12, https://doi.org/10.1038/s41467-020-14453-3.

[38] M. Naghiyan Fesharaki, R. Shoja-Razavi, H. A. Mansouri, H. Jamali, Microstructure investigation of Inconel 625 coating obtained by laser cladding and TIG cladding methods, *Surf. Coatings Technol.*, 353 (2018) 25–31, https://doi.org/10.1016/j.surfcoat.2018.08.061.

[39] H. Xiao, S. M. Li, W. J. Xiao, Y. Q. Li, L. M. Cha, J. Mazumder, L. J. Song, Effects of laser modes on Nb segregation and Laves phase formation during laser additive manufacturing of nickel-based superalloy, *Mater. Lett.*, 188 (2017) 260–262, https://doi.org/10.1016/j.matlet.2016.10.118.

[40] G. A. Knorovsky, M. J. Cieslak, T. J. Headley, “INCONEL 718: A Solidification Diagram,” Metall Mater Trans A, 20 (1989) 2149–2158, https://doi.org/10.1007/BF02650300.

[41] L. Wang, J. Dong, Y. Tian, L. Zhang, “Microsegregation and Rayleigh number variation during the solidification of superalloy Inconel 718,” *J. Univ. Sci. Technol. Beijing (Mineral Metall. Mater).*, 15 (5) (2008) 594–599, https://doi.org/10.1016/S1005-8850(08)60111-5.

[42] H. Xie, K. Yang, F. Li, C. Sun, Z. Yu, Investigation on the Laves phase formation during laser cladding of IN718 alloy by CA-FE, *J. Manuf. Process.*, 52 (2020) 132–144, https://doi.org/10.1016/j.jmapro.2020.01.050.

[43] M. Naghiyan Fesharaki, R. Shoja-Razavi, H. A. Mansouri, H. Jamali, Evaluation of the hot corrosion behavior of Inconel 625 coatings on the Inconel 738 substrate by laser and TIG cladding techniques, *Opt. Laser Technol.*, 111 (2019) 744–753, https://doi.org/10.1016/j.optlastec.2018.09.011.

[44] K. Shah, I. ul Haq, A. Khan, S. A. Shah, M. Khan, A. J. Pinkerton, Parametric study of development of Inconel-steel functionally graded materials by laser direct metal deposition, *Mater. Des.*, 54 (2014) 531–538, https://doi.org/10.1016/j.matdes.2013.08.079.

[45] J. R. Poulin, V. Brailovski, P. Terriault, Long fatigue crack propagation behavior of Inconel 625 processed by laser powder bed fusion: Influence of build orientation and post-processing conditions, *Int. J. Fatigue*, 116 (2018) 634–647, https://doi.org/10.1016/j.ijfatigue.2018.07.008.

[46] J. Nguejio, F. Szmytka, S. Hallais, A. Tanguy, S. Nardone, M. Godino Martinez, “Comparison of microstructure features and mechanical properties for additive

manufactured and wrought nickel alloys 625, *Mater. Sci. Eng. A*, 764 (2019) 138214, https://doi.org/10.1016/j.msea.2019.138214.

[47] Y. Hu, X. Lin, Y. Lib, Y. Ou, X. Gao, Q. Zhang, W. Li, W. Huang, Microstructural evolution and anisotropic mechanical properties of Inconel 625 superalloy fabricated by directed energy deposition, *J. Alloys Compd.*, 870 (2021) 159426, https://doi.org/10.1016/j.jallcom.2021.159426.

[48] ISO Standard, ISO 9725:2017 Nickel and nickel alloy forgings, (2017).

[49] ISO Standard, ISO 12725:2019 Nickel and nickel alloy castings, (2019).

[50] A. Moteshakker, I. Danaee, S. Moeinifar, A. Ashrafi, Hardness and tensile properties of dissimilar welds joints between SAF 2205 and AISI 316L, *Sci. Technol. Weld. Join.*, 21, (1) (2016) 1–10, https://doi.org/10.1179/1362171815Y.0000000062.

[51] W. Yangfan, C. Xizhang, S. Chuanchu, Microstructure and mechanical properties of Inconel 625 fabricated by wire-arc additive manufacturing, *Surf. Coatings Technol.*, 374 (2019) 116–123, https://doi.org/10.1016/j.surfcoat.2019.05.079.

[52] K. Feng, Y. Chen, P. Deng, Y. Li, H. Zhao, F. Lu, R. Li, J. Huang, Z. Li, Improved high-temperature hardness and wear resistance of Inconel 625 coatings fabricated by laser cladding, *J. Mater. Process. Technol.*, 243 (2017) 82–91, https://doi.org/10.1016/j.jmatprotec.2016.12.001.

[53] Q. Jiang, P. Zhang, Z. Yu, H. Shi, S. Li, D. Wu, H. Yan, X. Ye, J. Chen, Microstructure and Mechanical Properties of Thick-Walled Inconel 625 Alloy Manufactured by Wire Arc Additive Manufacture with Different Torch Paths, *Adv. Eng. Mater.*, 23 (1) (2021) 1–13, https://doi.org/10.1002/adem.202000728.

[54] British Standard, BS EN 1071-6:2007 Advanced technical ceramics - Ceramic composites - Methods of test for reinforcements - Part 6: Determination of the abrasion resistance of coatings by a micro-abrasion wear test, (2007).

Chapter 5

FUNCTIONALLY GRADED MATERIAL PRODUCED BY DIRECT LASER DEPOSITION (DLD)

Article 7 - Inconel 625 / AISI 413 Stainless Steel Functionally Graded Material Produced by Direct Laser Deposition

Materials

https://doi.org/10.3390/ma14195595

materials

Article

Inconel 625/AISI 413 Stainless Steel Functionally Graded Material Produced by Direct Laser Deposition

André Alves Ferreira [1,2,*], Omid Emadinia [2], João Manuel Cruz [3], Ana Rosanete Reis [1,2] and Manuel Fernando Vieira [1,2,*]

Article 7 - Inconel 625 / AISI 413 Stainless Steel Functionally Graded Material Produced by Direct Laser Deposition

André Alves Ferreira[1,2], Omid Emadinia[2], João Manuel Cruz[3], Ana Rosanete Reis[1,2], Manuel Fernando Vieira[1,2]

1Faculty of Engineering, University of Porto, R. Dr. Roberto Frias, 4200-465 Porto, Portugal; areis@inegi.up.pt (A.R.R.)
2LAETA/INEGI—Institute of Science and Innovation in Mechanical and Industrial Engineering, R. Dr. Roberto Frias, 4200-465 Porto, Portugal; oemadinia@inegi.up.pt (O.E.)
3SERMEC-Group, R. de Montezelo 540, 4425-348 Maia, Portugal; joaocruz@sermecgroup.pt (J.M.C)
*Correspondence: andreferreira@fe.up.pt (A.A.F.); mvieira@fe.up.pt (M.F.V.); Tel.: +3519-1046-1480 (A.A.F.)

Abstract

Functionally graded material (FGM) based on Inconel 625 and AISI 431 stainless steel powders was produced applying the direct laser deposition (DLD) process. The FGM starts with layers of Inconel 625 and ends with layers of 431 stainless steel having three intermediate zones with the composition (100-X)% Inconel 625-X% 431 stainless steel, X = 25, 50, and 75, in that order. This FGM was deposited on a 42CrMo4 steel substrate, with and without preheating. Microstructures of these FGMs were evaluated considering the distribution of chemical composition and grain structure. Microstructures mainly consisted of columnar grains independent of preheating condition; epitaxial growth was observed. The application of a non-preheated substrate caused the formation of planar grains in the vicinity of the substrate. In addition, hardness maps were produced. The hardness distribution across these FGMs confirmed a smooth transition between deposited layers; however, the heat-affected zone was greatly influenced by preheating condition. This study suggests that an optimum Inconel 625/AISI 431 FGM obtained by DLD should not exceed 50% AISI 431 stainless steel.

Keywords: functionally graded material; direct laser deposition; microstructure; chemical composition; hardness.

Introduction

Functionally Graded Materials (FGMs) can be considered as a particular class of composites with a spatial variation of composition/microstructure along a specific direction. However, FGMs may not encompass sharp distinguishable interfaces as observed in traditional composite materials [1]. The application of FGMs can overcome challenges that exist in conventional materials and processing. It enables designers to use two complex materials that would be difficult to bond, creating compositional gradients that allow for a gradual transition between both materials without discontinuities that jeopardize the structural integrity of the component. This setting leads to fewer internal stresses and cracking, consequently improving strength [2,3].

Functionally Graded Additive Manufacturing (FGAM) concept can be developed, i.e., the production of FGMs that are different in distribution or composition through a layer-by-layer approach [4,5]. Regarding this concept, the application of direct laser deposition (DLD), also designated by laser metal deposition (LMD), will be noticeable for depositing gradients of metals and alloys on a substrate. Densification will be obtained by solidifying consecutive melt pools generated by the laser [6]. This technique has the advantage of locally synthesizing metal/alloy gradients by mixing different powders with the desired compositions, gradually varying the mixture at intended locations [7]. However, the production of FGM components can face challenges such as the control of mixing, melting, and cooling rate, subsequently forming intermetallic phases and cracking. The lack of bonding between tracks/layers may happen, that is, caused by un-melted particles due to using dissimilar powders that have different properties.

Regarding the DLD process, laser/substrate relative velocity; laser scanning pattern; laser power; laser beam diameter; hatch spacing; powder feed rate; powders composition, powder gradient variation, and preheating conditions are vital parameters that must be considered [7,8]. Moreover, laser deposited materials experience complicated thermal history, presenting rapid solidification, high cooling rates, steep thermal gradients, and cyclic reheating and cooling. These conditions can produce non-equilibrium microstructures with variations layer to layer or even within individual layers. Therefore, the deposition process should be optimised considering the characteristics of input materials [9,10].

The production of FGM by DLD has been the subject of study by several research groups. However, these products are currently limited to small samples. The construction of a component with functional gradient properties depends not only on the position of materials but also on optimising process parameters required to control the microstructure and improve the mechanical properties in multi-material with functional gradient. High performance and versatility FGMs can meet performance requirements and have been widely used in the fields of aerospace, biological, electromagnetic, nuclear, and photoelectric engineering [7,11].

This process uses a deposition system equipped with two or more powder feeders and can create dissimilar gradients traditionally difficult to reach. The ability to mix two or more types of powders and control the feed rate of each flow makes DLD a flexible process for manufacturing complex components for the innovative development of alloys and formation of materials with a gradient of functionality [4,12,13]. This method makes it possible to produce materials with a gradient at the microstructure level; this gradient achieved due to the reduced and localised melting and the strong mixing movement in the melt. Thus, materials can be adapted for flexible, functional performance in particular applications. Besides, additive manufacturing technology (AM) has surpassed the prototyping concept to produce solid components for end-users.

Regarding the production of FGM by the DLD technique, some studies mentioned the use of different systems. For the SS316/ Inconel 625 system, there was an increase of mechanical and wear resistance due to the formation of secondary phases with the increase of Inconel 625 alloy content [11,14–16]. The increase in wear and hardness was also observed in the SS316/ Inconel 718 system [17]. The FGM produced using

SS410/ Inconel 625 materials demonstrated that the depositions were defected free and with good integrity along with the entire interface [18]. The effect of preheating on FGM was evaluated using the Inconel 625/ Ti6Al4V system, which was shown to promote the formation of thinner and more uniform secondary phases and free of cracks [19]. It is worth noting that there are many investigations producing FGMs using nickel superalloys in recent years. For these alloys, a percentage increase of alloying elements, such as Cr and Mo, promote the increase of mechanical strength and wear and corrosion resistance.

Recognising the importance of Metallic FGM and its complexity, this article explores the deposition of Inconel 625 superalloy powder gradually mixed with 431 stainless steel alloy, evaluating the influence of compositional variation as well as preheating on the microstructure and mechanical proprieties. The former condition was performed by preheating the substrate metal used for deposition. Although several investigations allocated the production of gradient materials using Inconel 625 superalloy with other alloys [14–16], to the knowledge of authors, the production of FGM consisting of Inconel 625 and SS431 has not been reported yet.

Experimental Procedure

This study included the production of compositional gradients as functionally graded material (FGM) using Inconel 625 powder (a nickel-based superalloy supplied as MetcoClad 625 by Oerlikon Metco, so-called M625 in this study) mixed with AISI 431 stainless steel powder (a martensitic stainless steel supplied as Metco 42C from the same supplier, so-called M42C) in gradient. According to the supplier's data sheets, M625 has particle size range of 45 - 90 μm, M42C is in a size range of 45 - 106 μm, the chemical composition of these alloys being presented in Table 1. Moreover, Figure 1 illustrates the morphology of these powders, the M625 particles are seen in spherical form, and M42C particles have irregular shape (non-spherical). Microscopic characterizations in this study involved a scanning electron microscopy (SEM), FEI-

Quanta 400 FEG equipment FEG (ESEM, Hillsboro, OR, USA), using secondary electron (SEM/SE) and backscattered electron (SEM/BSE) imaging modes. Moreover, semi-quantitative chemical analysis was performed by energy dispersive X-ray spectroscopy (EDX) (EDAX Genesis X4M, Oxford Instrument, Oxfordshire, UK). Structural analysis such as crystallographic information was performed by electron backscatter diffraction (EBSD) (EDAX-TSL OIM EBSD, Mahwah, NJ, USA) technique applying inverse pole figure (IPF) maps.

In this study, the substrate used for deposition was 42CrMo4 steel, machined plates in 100 x 120 x 15 mm, supplied in quenched and tempered condition. This steel is a low alloy structural steel, presenting high strength and toughness, with good fatigue behaviour and machinability [20,21]. Thus, it is widely used for manufacturing industrial components such as gears, automotive components, and drilling joints [21,22]. In the current study, the production of FGM was performed on two substrates: 1) one substrate in room temperature, 2) another one preheated to 300 °C by a manual gas system. For the latter condition, the temperature was controlled by a digital thermometer since it is essential to have a uniform temperature distribution in the substrate surface. The application of without and with preheating procedures (so-called without and with PHT in this study) aimed to evaluate the effect of cooling rate on the evolution of microstructure in deposited layers and substrate.

Table 1. Chemical composition (wt. %) of the FGM powder alloys used in this study.

Powders	Fe	Ni	Cr	Mo	Nb	Si	C
M42C	78.6	1.9	17.3	-	-	2.0	0.2
M625	4.1	60.8	21.3	9.2	4.6	-	-

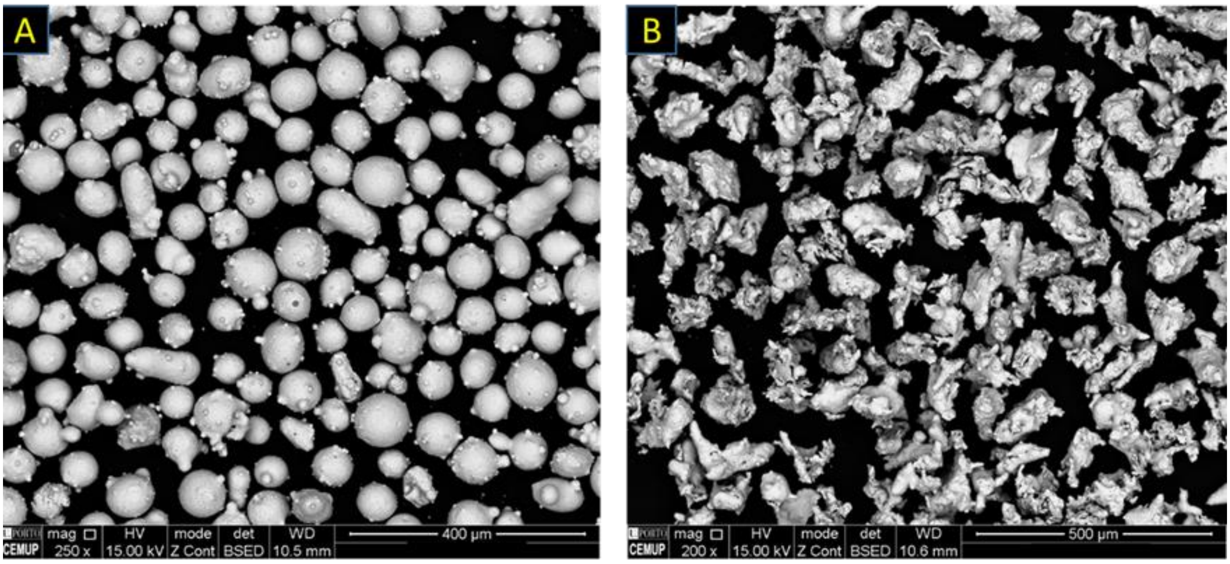

Figure 1. The morphology of (A) M625 and (B) M42C powders illustrated by SEM/BSE technique.

The consolidation of powders, required for the FGM production, was achieved by direct laser deposition (DLD) technique using a six-axis robot (KUKA KR90 R3100 model) connected to robotic and laser control units, this arrangement provided the temperature control in the melt pool. This system was equipped with a Laser system (LDF 3000 – 100), a fibre-coupled laser diode providing a wavelength range of 900-1030 nm reaching a nominal beam power of 6000 W.

The depositions started with 100% M625 on the 42CrMo4 substrates (without PHT and PHT conditions), followed by depositing layers of 75% M625-25% M42C, 50% M625-50% M42C, 25% M625-75% M42C, and ended to 100% M42C. Feeding of powder mixtures was performed in a coaxially delivering mode for constructing compositional gradients. Moreover, argon shield gas, with 99.99% purity, was used as protection gas with a flow rate equal to 5.5 l/min to minimise contamination and oxidation of the melt pool during the DLD process. For the deposition of M625 layers, the following processing conditions were used: laser power (LP) = 2000 W, scanning speed (SS) = 6 mm/s, and feeding rate (FR) = 15 g/min. The last layers (100% M42C) were deposited with the condition: LP = 1500 W, SS = 10 mm/s, and FR = 15 g/min. These procedures were carried out applying a spot size equal to 2.5 mm; the trajectory of depositions involved continuously parallel depositing applying a 40% overlapping between tracks, followed by depositing successive layers rotated in 90° in each layer. Afterwards, printed specimens, without PHT and PHT conditions, were cooled down to room temperature. The application of these conditions were based on previous studies [23,24]. Process optimisation is essential since FGMs produced by laser deposition present microstructural variations across layers affected by different parameters such as thermal gradients, these effects are caused by remelting and reheating cycles or cooling rate [9].

Regarding microscopic characterisations, FGM specimens, with and without PHT, were prepared using conventional metallographic techniques. However, an additional polishing step, using a 0.06 μm silica colloidal suspension, was needed for EBSD analysis, allowing to obtain Kikuchi patterns [25].

Similar FGM specimens were used for microhardness test using a fully automated DURASCAN 70 microindenter - EMCO TEST (EMCO-TEST PRÜFMASCHINEN GMBH, Kuchl, Austria). The HV hardness maps were produced by 700 indentations, applying a load of 300 g, considering 0.1 mm as the distance between the centres of every two adjacent indentations. This procedure scanned an area of 5.7 x 1.1 mm.

Results and discussion

Microstructural and Chemical Evaluations

The microstructure of a FGM specimen, from 100% M625 to 100% M42C, is illustrated in Figure 2. In this microstructure are observed some inclusions and porosities, apparently reduced by the increase in M42C alloy. However, this addition has ended up with the formation of cracks; the morphology of these defects reveal that they formed in the last layers, 100% M42C, and propagated to the layers beneath, that is 25% M625-75%M42C.

M42C deposits are prone to cracking, and strict control of processing conditions is mandatory [23,26]. The main reason for cracking is the stresses caused by processing conditions, namely the different coefficients of thermal expansion, nucleating microcracks in the brittle martensite. In this case, this was even more critical as the first layers remelted the top surface of 25% M625-75% M42C layer, and unexpected phases may have formed, increasing the brittle character of this region.

The inclusions (round black spots) are mainly complex oxides formed along the FGM, and the irregular porosities are likely caused by elemental segregation [27,28].

Figure 3 illustrates a higher magnification of the black rectangle in Figure 2 where an irregular porosity was detected. The morphology of the microstructure shown in the SEM image of Figure 3 consists of a dendritic structure embedding interdendritic regions. The elemental maps show a matrix homogeneous in Fe, Ni and Cr and zones rich in Nb and Mo (white regions in SEM image). In regions with higher segregation, remelting occurs during the next deposition, since every layer is highly affected by the heat conducted from successive deposition, and liquation cracks formed and remained in the FGM [28,29]. This can explain why this defect decrease with increasing amount of M42C powder.

Figure 2. Microstructural evolution across the longitudinal section of the FGM specimen, SEM/BSE image.

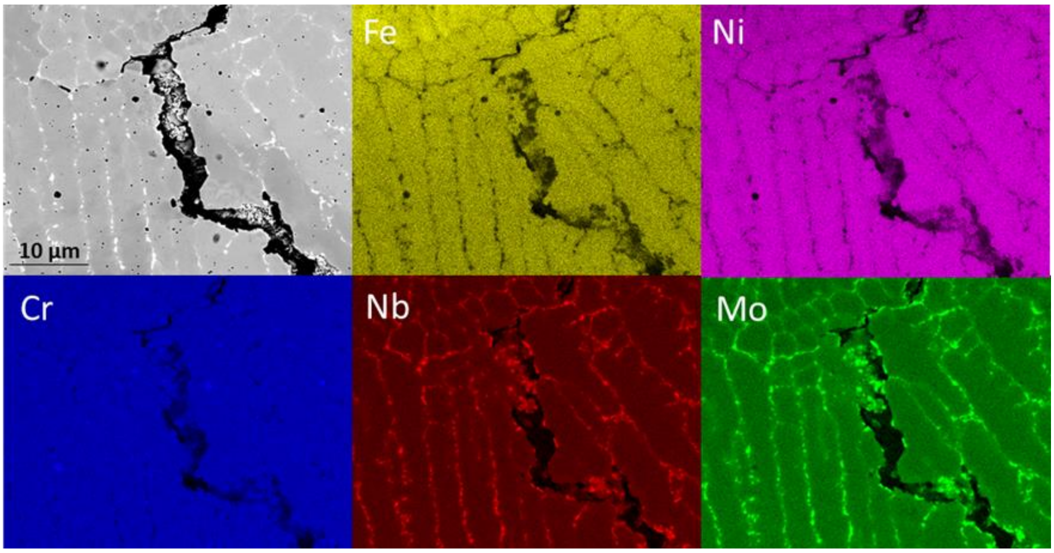

Figure 3. SEM image and EDS elemental maps of a discontinuity observed in 75% M625 + 50% M42C layer, illustrated as black square inset in Figure 2.

This second phase can be Laves phase resulting from the microstructural segregation of Nb and Mo elements from the liquid due to rapid solidification during deposition. The formation of Laves phase, or even of carbides, in the austenitic matrix has been observed in several studies [30-34]. Its presence was also revealed by microscopic observations and EDS analysis in a similar study on laser cladding of Inconel 625 alloy [24]. The amount of Laves phase can be reduced by post-deposition heat treatments that homogenize the material by reducing chemical composition gradients [35].

The formation of secondary phases in FGM depends on the processing history [36], being possible to minimize the proportion of Laves phase in the microstructure by preheating the substrate [24]. The application of PHT reduces the cooling rate of the deposited material, allowing the diffusion of Nb and Mo elements in the matrix, thus reducing the amount of Laves phase. The effect of Laves phase in the dendritic structure on the material hardness is not consensual. It has been reported that phase Laves can either increase hardness [32] or decrease it [37], in this case, due to the reduction of carbides in the matrix as a consequence of Nb and Mo segregation.

Figure 4 illustrates several details of the FGM microstructure. The images show that the microstructure is predominantly composed of columnar dendrites, a characteristic of laser-deposited structures [38,39]. This structure is formed since the thermal gradient and the solidification rate favour columnar-dendritic solidification morphology. There are two narrow zones of the cladding where planar and equiaxed morphologies can occur; a planar zone forms at the interface with the substrate due to the very high thermal gradient, and equiaxed morphology can be observed near the surface of the melt pool, resulting from the decreasing thermal gradient as the cladding solidifies. Typically, in this process, columnar grains grow parallel to the main flow of heat across the material being solidified.

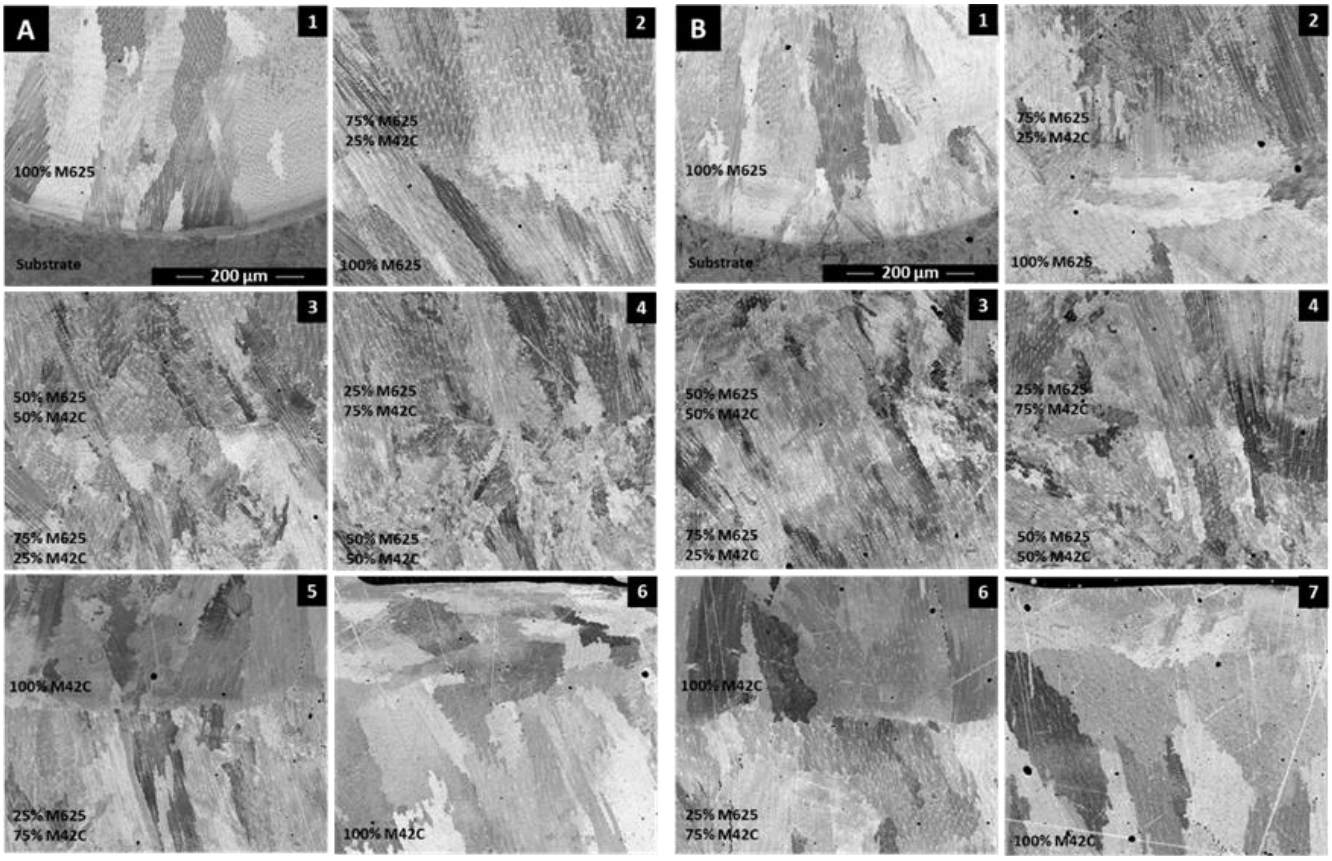

Figure 4. Microstructural evolution in the transversal cross section of FGMs produced (A) without, and (B) with the application of PHT (SEM/BSE images).

During the deposition of several layers of the same material, each new layer remelts the surface of the last deposited, replacing the zone of equiaxed grains with columnar ones. As a result, the equiaxed region is limited to the upper surface of the cladding. However, Figures 4.A4 and 4.B4 evidenced some equiaxed grains appearing inside the FGM, mainly in the upper region of the 50% M625 + 50% M42C zone. This effect can be explained by the composition of the liquid formed and the difficulty in solute redistribution, which can cause the appearance of equiaxed morphology, as reported in other studies [33,40].

SEM images of Figures 4.A1 and 4.B1 reveal a dilution zone resulting from the melting of the substrate during laser processing and ensuring the bonding between cladding and substrate. Moreover, well-bonded layers are seen all across the FGM, Figure 4.A2 to 4.A6 and 4.B2 to 4.B6. The remelting of the upper region of the last deposited layer and the mixing with melted powders ensure the bonding between these layers and a continuous chemical composition gradient across the entire FGM, as shown in Figure 5.

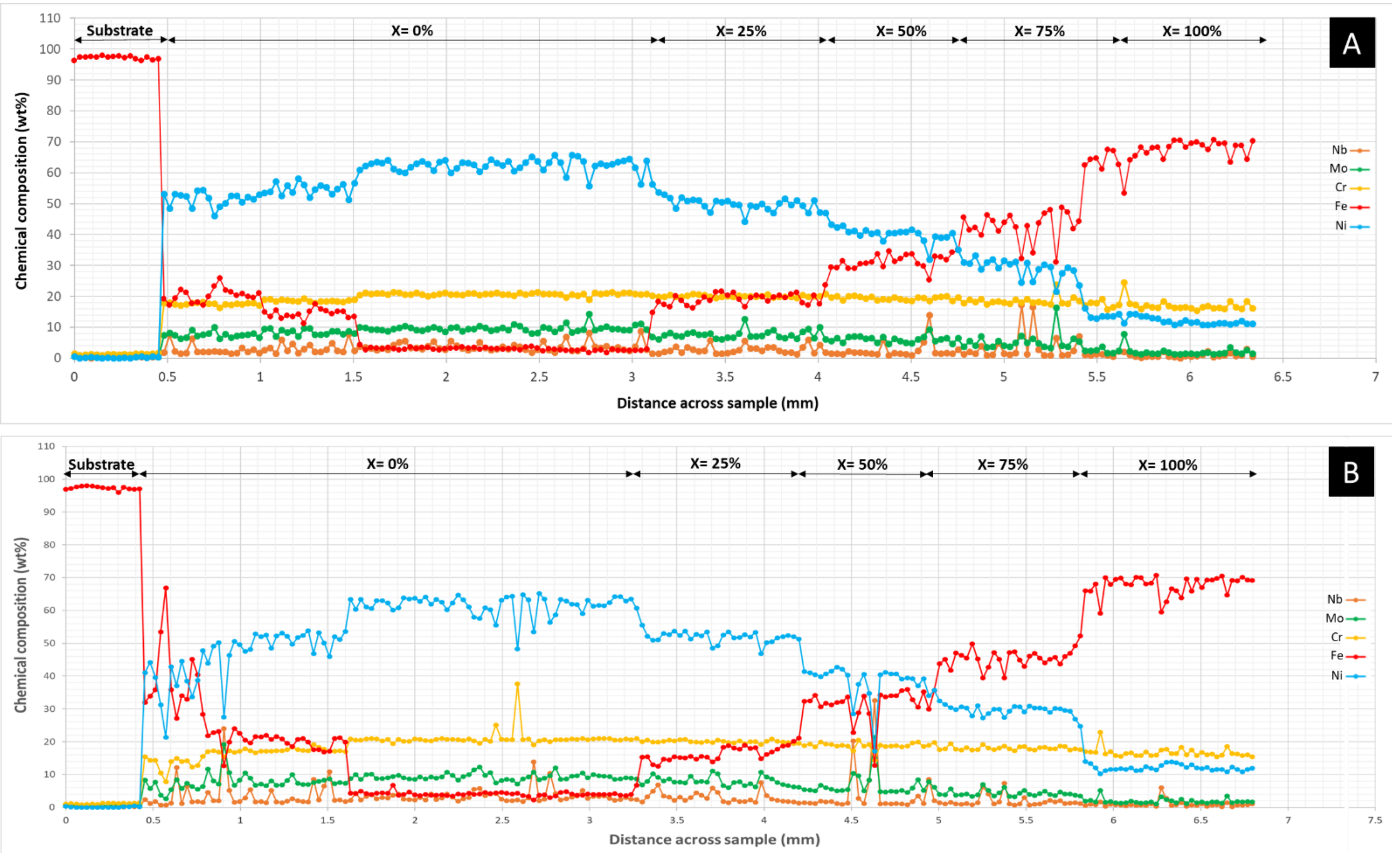

Figure 5. FGM linear chemical analysis - (A) without PHT and (B) with PHT. The composition of each FGM zone is (100-X)% M625 + X% M42C.

The presence of Fe from the substrate in the first M625 layers is more pronounced in the PHT condition. This difference is caused by the thermal energy having caused a higher dilution of the preheated substrate, with more Fe incorporating the melt pool, as observed in other studies [23]. As shown in Figure 5, the fluctuation of Fe concentration in the PHT condition implies the depletion of the Ni, Cr, and Mo. However, Fe from the substrate melt depletes at about 1.5 mm of the FGM regardless of preheating conditions; afterward, the Fe concentration increases with increasing M42C powder. Regarding other elements, the Cr distribution seems constant throughout the FGM, this homogeneity resulting from this element existing in both M625 and M42C powders in similar amounts. Some fluctuations in Nb and Mo profiles are stronger for the PHT condition in layers close to the substrate, up to about 1.5 mm; as expected, concentrations of these elements decrease with increasing M42C. This increment in steel powder is also associated with a decrease in Ni.

Figures 6.A and 6.B revealed an influence of PHT on the microstructure of the first M625 layers, i.e., in the substrate vicinity. Without PHT, a layer with almost 50 μm of planar grains was formed, while with PHT, only columnar structures are observed. As already mentioned, this zone of planar grains is formed due to the very high thermal gradient in the contact zone of the melt pool with the cold substrate; PHT significantly reduces this gradient, and solidification conditions lead to the formation of columnar structures. These observations are consistent with similar studies [41,24]. This layer with planar grains has been interrupted by proceeding the solidification, that means, the solid-liquid interface growth rate and thermal gradient in the melt pool changed in favour of columnar-dendritic growth.

The microstructural evolution in the FGM were evaluated in detail through localized chemical analysis using EDS. The EDS analysis of zones illustrated in Figures 6.A and 6.B and presented in Table 2, also confirmed that preheating caused the increase of Fe in the 100% M625 layers of the FGM (zones Z1 and Z3), and strongly promoted the diffusion of alloying elements of the M625 layer into the substrate with PHT (zones Z2 and Z4). This diffusion of Ni, Mo, Nb and Cr into the preheated substrate, associated with the depletion of Fe, can affect the mechanical properties, such as hardness, of the substrate in the diffused zone.

Figures 6.C and 6.D give more details into the formation of secondary phases in FGMs. The EDS analysis of the round dark zones, identified as zones Z5 and Z8, are complex oxides with a composition $(Cr, Ni, Fe, Nb, Mo, Mn, Si)_xO_y$. The microstructures also reveal the presence of lighter (white and grey) regions. The results of Table 2 confirm that these regions are mainly Laves phase and carbides. Comparison of the chemical composition of the zones indicated in figures 6.C (Z6 and Z7) and 6.D (Z9) shows that preheating affects their composition by increasing the iron content and decreasing the nickel content, in accordance with Figure 5.

PHT effect on the segregation for the interdendritic zones of Nb and Mo elements, which are the main compositional elements of the Laves phase, is not apparent throughout the FGM. However, close to the interface, this variation seems evident due to the decrease of Laves phase by PHT effect, as observed comparing Zones 1 in Figures 6.A and 6.B. This effect is, in part, is explained by the increase in Fe content in the cladding. Furthermore, the volume fraction of the Laves phase depends on the alloy solidification process, and higher cooling rates in this region, typical of the cladding without PHT, reduce the time for Nb and Mo diffusion and lead to their accumulation in the interdendritic spaces.

Typically, in the DLD process, the interface and heat-affected zone (HAZ) are critical regions. In fact, the heat input in these regions is much smaller than in conventional welding processes due to the localized molten region created by the laser. Consequently, the cooling rate is very high at the beginning of cladding solidification, promoting a significant microstructural change in the HAZ. This change can increase the hardness and decrease the toughness in the substrate HAZ.

In this study, preheating the substrate to a temperature of 300 °C promoted not only a microstructural change at the interface, inhibiting the formation of the planar grain layer (Figure 6), but also in the HAZ, causing the formation of coarser structures and reducing the formation of martensite, as shown in Figure 7. Thus, PHT leads to a microstructure that can reduce crack formation/propagation conditions during the in-service use of the coated steel. Figure 7 also showed a more intense diffusion at the interface of the FGM produced with a pre-heated substrate, with the mutual interpenetration of the substrate and cladding leading to a diffuse interface.

Previous studies confirmed that PHT positively influenced the microstructure and the mechanical properties in substrates processed by DLD [42]. In addition, it promoted a reduction of residual stresses of about 40%, as well as the reduction and attenuation of distortions [43], permitting a better distribution of stresses between the cladding and the substrate, as well as preventing the formation of intermetallic phases (as secondary phases), decreasing hardness, and improving mechanical properties.

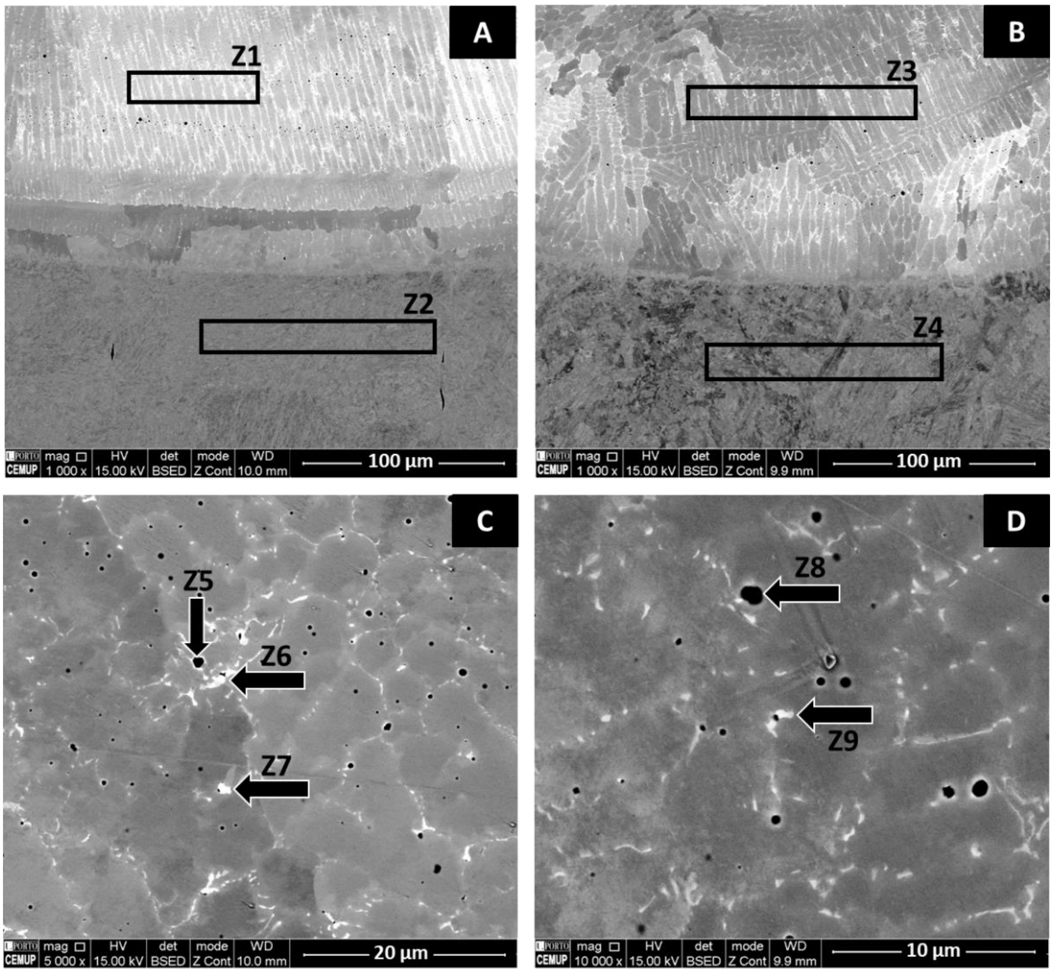

Figure 6. SEM/BSE images showing: (A) and (B) the FGM/substrate interface; (C) and (D) higher magnification images for secondary phases analysis from the 50% M625 + 50% M42C layers. (A) and (C) are from FGM produced without PHT, and (B) and (D) with PHT.

An EBSD analysis was performed to observe the morphology and grain distribution of the FGMs, as illustrated in Figure 8. As expected, considering SEM/BSE images of Figures 6.A and 6.B, there is a layer with smaller and equiaxed grains in the vicinity of the substrate. This smaller grain size is more evident in the sample without PHT due to the influence of the cold substrate. However, the microstructure in both FGMs is mainly composed of columnar grains that grow perpendicular to the substrate, i.e., in the direction of deposition and heat flow. The growth of columnar-dendritic structures along the deposition direction occurs when the temperature gradient component in that direction is larger than other temperature components in the melt pool [44,45].

Table 2. The EDS analysis (wt.%) performed on the FGMs zones illustrated in Figure 6.

Figure_Zone	C	O	Si	Nb	Mo	Cr	Fe	Ni	Mn
Z1	0.9	-	0.5	2.9	7.8	16.6	22.3	49.0	-
Z2	0.9	-	0.3	0.0	0.0	1.5	97.3	0.0	-
Z3	0.7	-	0.5	2.7	6.2	13.6	37.1	39.2	-
Z4	0.7	-	0.4	1.2	3.2	6.9	69.1	18.5	-
Z5	0.7	16.9	0.4	9.2	5.2	28.2	8.8	22.5	8.1
Z6	1.8	-	2.3	12.0	24.4	14.3	10.5	34.7	-
Z7	0.7	-	2.4	11.8	24.3	15.3	10.0	35.5	-
Z8	1.1	12.9	8.3	6.3	6.4	19.9	12.0	27.5	5.6
Z9	1.0	-	1.8	5.2	26.2	16.0	13.9	35.9	-

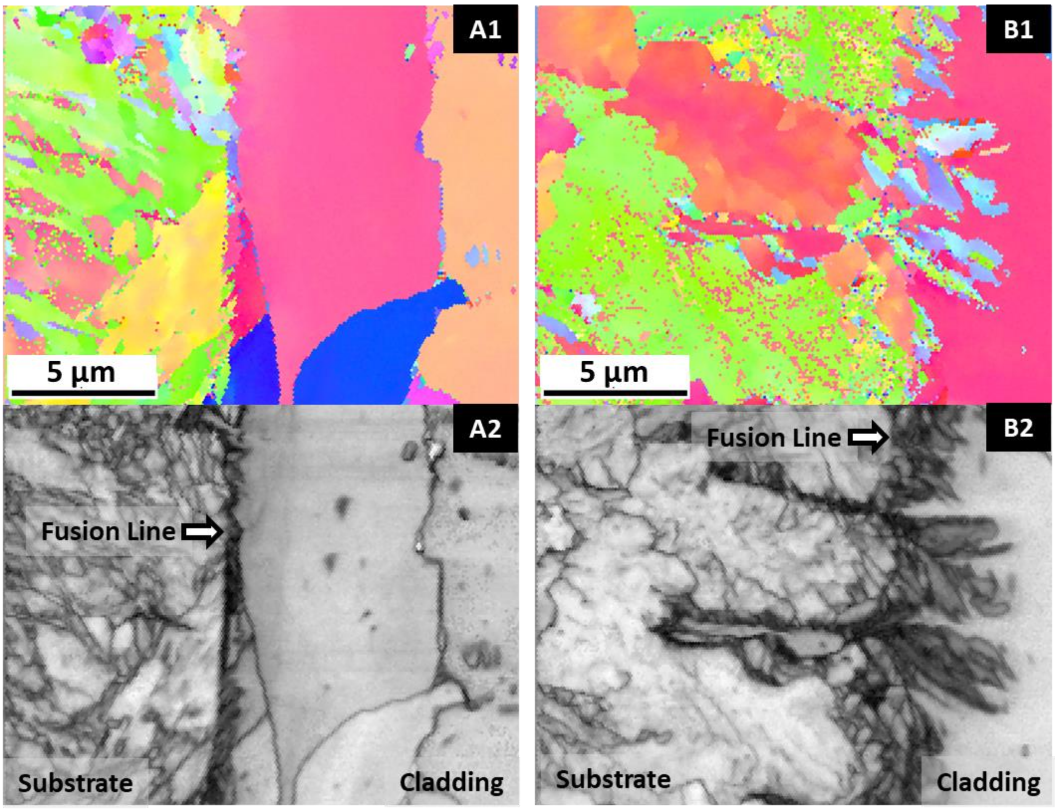

Figure 7. Morphology of the cladding/substrate interface with substrate and HAZ observed by EBSD technique: (A1 and A2) without PHT and (B1 and B2) with PHT, showing grain maps and SEM images, respectively.

In the layers deposited with the 50% M625 + 50% M42C powder mixture, there is a zone with equiaxed grains, probably formed by the complex chemical composition and the heat accumulation, which induced a partial reduction of the high thermal gradient. However, this localized microstructural alteration is again replaced by columnar grains, not being maintained until the last deposited layers, contrary to what has been seen in other studies [41]. It should also be noted that the size of columnar grains decreases as more layers are deposited.

For the first two compositions (100% Mg25 and 75% M625 + 25% M42C), the grains of the FGM without PHT, Figure 8A, are thicker and longer than those of the FGM with PHT, Figure 8B, which shows another effect of reducing the thermal gradient by the application of PHT.

EBSD images also show that some grains form in one region and spread to the next, with different compositions. This indicates epitaxial growth in successive layers. This type of growth, which favours the bonding between layers, occurs because the deposition of a new layer remelts the surface of the previous one. This remelting/solidification process allows the grains from the previous deposition to act as nucleation sites for the solidification of new grains.

The images in Figure 8 do not show the formation of a preferential orientation in the microstructure since no colour is dominant in these inverse-pole-figures.

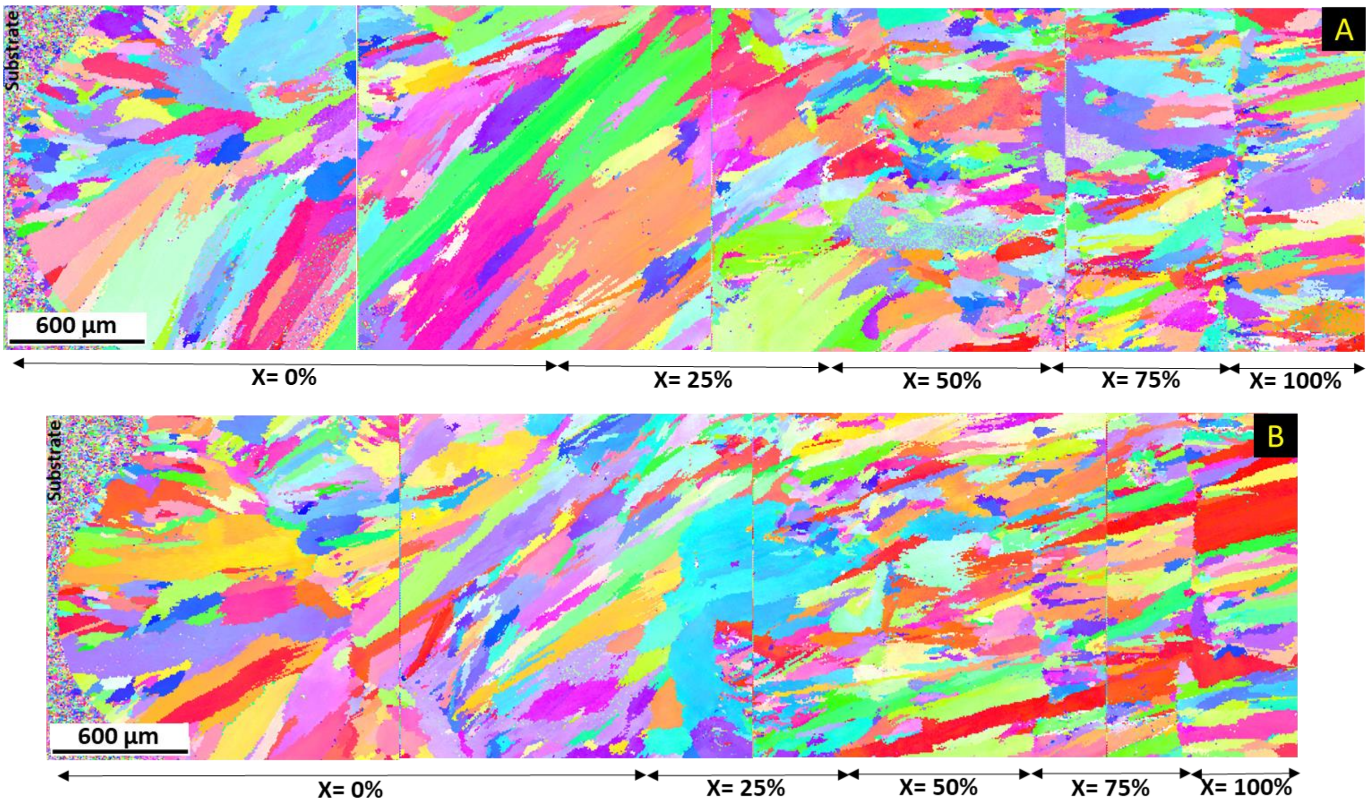

Figure 8. EBSD inverse-pole-figure (IPF) map of the cross-section of FGMs (A) without PHT and (B) with PHT showing the morphology and orientation of grains. The composition of each FGM zone is (100-X)% M625 + X% M42C.

Microhardness Mapping

In this study, the composition gradient from the substrates to the upper layers, with a continuous increase in the amount of martensitic steel, should show an evolution of hardness along with the deposited layers. In fact, previous studies on the deposition of monolayers of these materials indicate average hardness values greater than 500 HV for M42C [23] and approximately 250 HV for M625 [24]. However, no marked variation in hardness was measured across the FGMs, as illustrated in the microhardness maps shown in Figure 9. The figure also shows no significant differences in FGMs processed with and without PHT, which proves that the influence of PHT on the microstructure is not very significant, except for the planar morphology of the first deposited layers.

The relatively low hardness of the M42C-rich layers is explained by a slower cooling rate in these layers, which are the last to be deposited, inhibiting an extensive martensitic transformation, and by these layers having about 10 wt.% Ni, which, being one austenite stabilizer, also hinders the martensitic transformation. Finally, except for the last layer, all others undergo a self-tempering process of the martensite that may have formed.

Figure 9 reveals that the hardest zone obtained is in the heat-affected zone (HAZ) of the FGM produced without PHT, meaning that preheating application promoted a reduction in the cooling rate in the substrate, reducing the formation of martensite in this zone, as already discussed.

The higher hardness of the FGM with PHT (indicated by a red arrow) was measured in the M625 region, which can be attributed to compositional fluctuations leading to a local concentration of hard Laves phase/carbides.

This evolution of hardness shows that up to 50% of M42C powder, which is significantly less expensive, can be added to M625 powder without inducing significant changes in hardness and microstructure, as discussed above. Larger amounts of M42C should not be added as they can lead to cracking.

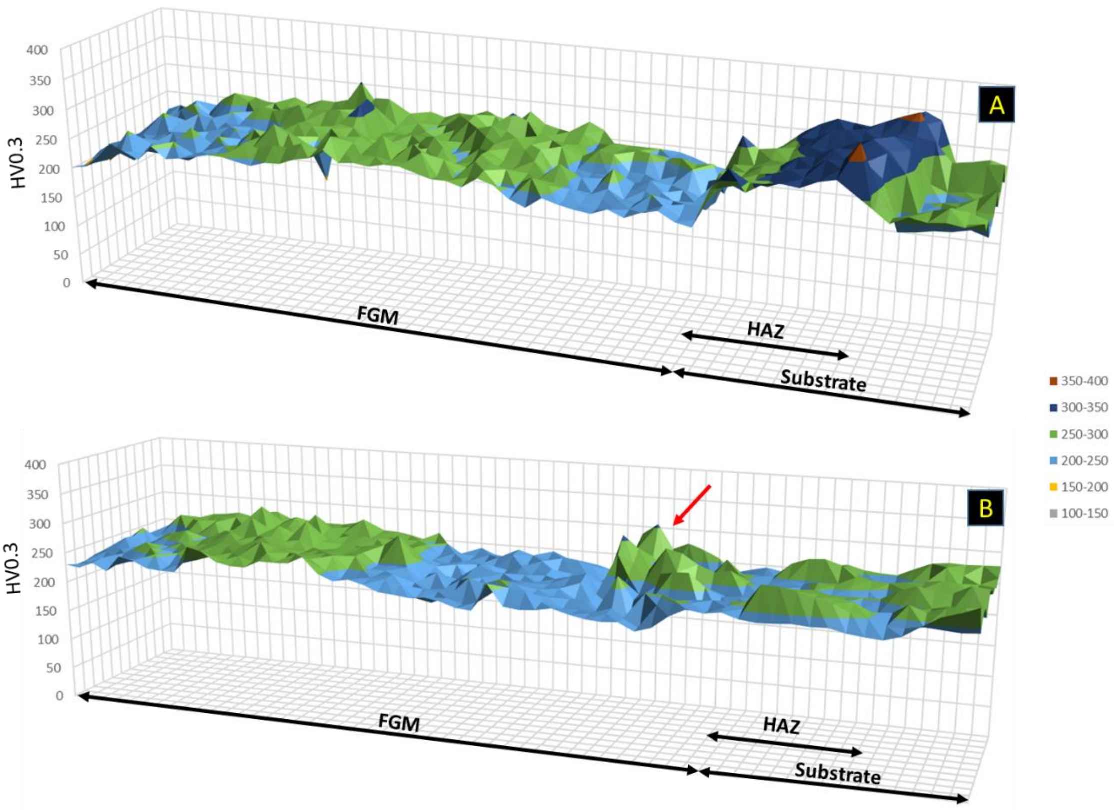

Figure 9. FGM microhardness mapping - (A) without PHT and (B) with PHT.

Conclusions

In this study, the production of functionally graded material (FGM) by direct laser deposition (DLD) technique was evaluated. The deposition started with layers of nickel-based superalloy (M625 powders) and ended with layers of martensitic stainless steel (M42C powders). Three mixtures of powders were used in intermediate deposits, sequentially increasing by 25 wt. % the amounts of M42C powder. Moreover, the influence of preheating the 42CrMo4 steel substrate on the microstructural and hardness evolution in FGMs were evaluated. The main conclusions of this study are as follows:

- Cracking-free production of the Inconel 625/AISI 431 steel FGM, applying DLD, is only verified up to a certain composition. The addition of stainless steel cannot exceed 50 wt. %.

- The metallurgical bonding of deposits to substrates and between the various layers of the FGM is ensured by the diffusion in the liquid state of the alloy constituents, the remelting effect, and epitaxial growth.
- The grain microstructure in Inconel 625/AISI 431 FGM is essentially columnar, regardless of preheating.
- Preheating influenced the microstructural evolution and microhardness in the substrate and the first deposited layers; the region of planar grains observed in the vicinity of the substrate only formed without preheating. A marked increase in grain size and a reduction in martensite was observed in the preheated substrate HAZ, decreasing the hardness of this region.

Author Contributions: Conceptualisation, A.A.F, A.R.R. and M.F.V.; methodology, A.A.F and J.M.C; validation, O.E. and M.F.V.; formal analysis, A.A.F.; investigation, A.A.F and M.F.V.; resources, A.R.R., M.F.V. and J.M.C.; writing—original draft preparation, A.A.F; review and editing, O.E. and M.F.V.; visualisation, A.A.F.; supervision, A.R.R. and M.F.V.; project administration, M.F.V. and J.M.C.; funding acquisition, A.R.R., M.F.V. and J.M.C. All authors have read and agreed to the published version of the manuscript.

Funding: This research was funded by FEDER through the program P2020|COMPETE, Projetos em Copromoção (project POCI-01-0247-FEDER-039848).

Acknowledgements: The authors are grateful to CEMUP (Centro de Materiais da Universidade do Porto) for expert assistance with SEM.

Conflicts of Interest: The authors declare no conflict of interest.

References

42. Sobczak, J. J.; Drenchev, L. Metallic Functionally Graded Materials: A Specific Class of Advanced Composites. *J. Mater. Sci. Technol.*, **2013**, 29, 297–316, doi: 10.1016/j.jmst.2013.02.006.
43. Durejko, T.; Zietala, M.; Polkowski, W.; Czujko, T. Thin wall tubes with Fe3Al/SS316L graded structure obtained by using laser engineered net shaping technology. *Mater. Des.*, **2014**, 63, 766–774, doi: 10.1016/j.matdes.2014.07.011.
44. Sarathchandra, D. T.; Kanmani Subbu, S.; Venkaiah, N. Functionally graded materials and processing techniques: An art of review. *Mater. Today Proc.*, **2018**, 5, 21328–21334, doi: 10.1016/j.matpr.2018.06.536.
45. Zhang, B.; Jaiswal, P.; Rai, R.; Nelaturi, S. Additive Manufacturing of Functionally Graded Material Objects: A Review. *J. Comput. Inf. Sci. Eng.*, **2018**, vol. 18, 1215–1231, doi: 10.1115/1.4039683.
46. Loh, G. H.; Pei, E.; Harrison, D.; Monzón, M. D. An overview of functionally graded additive manufacturing. *Addit. Manuf.*, **2018**, 23, 34–44, doi: 10.1016/j.addma.2018.06.023.
47. Yan, L.; Chen, Y.; Liou, F. Additive manufacturing of functionally graded metallic materials using laser metal deposition. *Addit. Manuf.*, **2020**, 31, 100901, doi: 10.1016/j.addma.2019.100901.
48. Mahamood, R. M. Laser Metal Deposition of Metals and Alloys. *Springer International Publishing*, **2018**.
49. Thompson, S. M.; Bian, L.; Shamsaei, N.; Yadollahi, A. An overview of Direct Laser Deposition for additive manufacturing; Part I: Transport phenomena, modeling and diagnostics. *Addit. Manuf.*, **2015**, 8, 36–62, doi: 10.1016/j.addma.2015.07.001.
50. Costa, L.; Vilar, R. Laser powder deposition. *Rapid Prototyping Journal*, **2009**, 4, 264–279, doi: 10.1108/13552540910979785.
51. Reichardt, A. Additive Manufacturing of Metal-based Functionally Graded Materials by Ashley Reichardt A dissertation submitted in partial satisfaction of the requirements for the degree of Doctor of Philosophy in Engineering – Nuclear Engineering in the Graduate Division. **2017**.
52. Chen, B.; Su, Y.; Xie, Z.; Tan, C.; Feng, J. Development and characterization of 316L/Inconel625 functionally graded material fabricated by laser direct metal deposition. *Opt. Laser Technol.*, **2020**, 123, doi: 10.1016/j.optlastec.2019.105916.
53. Carroll, B. E.; Otis, R. A.; Borgonia, J. P.; Suh, J.; Dillon, R. P.; Shapiro, A. A.; Hofmann, D. C.; Liu, Z; Beese, A. M. Functionally graded material of 304L stainless steel and inconel 625 fabricated by directed energy deposition: Characterization and thermodynamic modeling. *Acta Mater.*, **2016**, 108, 46–54, doi: 10.1016/j.actamat.2016.02.019.
54. Dass, A.; Moridi, A. State of the art in directed energy deposition: From additive manufacturing to materials design. *Coatings*, **2019**, 7, doi: 10.3390/COATINGS9070418.
55. Koike, R.; Unotoro, I.; Kakinuma, Y.; Aoyama, T.; Oda, Y.; Kuriya, T.; Fujishima, M. Evaluation for mechanical characteristics of Inconel625-SUS316L joint

produced with direct energy deposition. *Procedia Manuf.*, **2017**, 14, 105–110, doi: 10.1016/j.promfg.2017.11.012.
56. Meera Mirzana, I.; Krishana Mohana Rao, G.; Ur Raheman, S.; Zaki Ahmed, M. Fabrication and Micro-structural study of Functionally Graded Material Disc of SS316/IN625. *Mater. Today Proc.*, **2016**, 3, 4236–4241, doi: 10.1016/j.matpr.2016.11.103.
57. Zhang, X.; Chen, Y.; Liou, F. Fabrication of SS316L-IN625 functionally graded materials by powder-fed directed energy deposition. *Sci. Technol. Weld. Join.*, **2019**, 24, 504–516, doi: 10.1080/13621718.2019.1589086.
58. Liang, X.; Wu, D.; Li, Q.; Jiang, L. Laser rapid manufacturing of stainless steel 316L/Inconel718 functionally graded materials: Microstructure evolution and mechanical properties. *Int. J. Opt.*, **2010**, 1–6, doi: 10.1155/2010/802385.
59. Weng, F.; Liu, Y.; Chew, Y.; Wang, L.; Lee, B. Y.; Bi, G. Repair feasibility of SS416 stainless steel via laser aided additive manufacturing with SS410/Inconel625 powders. *IOP Conf. Ser. Mater. Sci. Eng.*, **2020**, 744, doi: 10.1088/1757-899X/744/1/012031.
60. Meng, W.; Zhang, W.; Zhang, W.; Yin, X.; Guo, L.; Cui, B. Additive fabrication of 316L/Inconel625/Ti6Al4V functionally graded materials by laser synchronous preheating. *Int. J. Adv. Manuf. Technol.*, **2019**, 104, 2525–2538, doi: 10.1007/s00170-019-04061-x.
61. Su, J.; Qiu, X.; Xing, F.; Ruan, Y. Effect of preheating temperature on microstructure and properties of 42CrMo4/38mnvs6 heterogeneous laser welded joint. *Metals* (Basel)., **2019**, 9, doi: 10.3390/met9080870.
62. Sun, C.; Fu, P. X.; Liu, H. W.; Liu, H. H.; Du, N. Y. Effect of tempering temperature on the low temperature impact toughness of 42CrMo4-V steel. *Metals* (Basel)., **2018**, 8, doi: 10.3390/met8040232.
63. B. Standard, “Steels and nickel alloys for fasteners with specified elevated and / or low temperature,” **2006**.
64. Ferreira, A. A.; Darabi, R.; Sousa, J. P.; Cruz, J. M.; Reis, A. R.; Vieira, M. F. Optimization of direct laser deposition of a martensitic steel powder (Metco 42c) on 42CrMo4 steel. *Metals* (Basel)., **2021**, 11, 1–18, doi: 10.3390/met11040672.
65. Ferreira, A. A.; Amaral, R. L.; Romio, P. C.; Cruz, J. M.; Reis, A. R.; Vieira, M. F. Deposition of Nickel-Based Superalloy Claddings on Low Alloy Structural Steel by Direct Laser Deposition. *Metals* (Basel)., **2021**, 11, 1326, doi: 10.3390/met11081326.
66. Davies, E. R. Introduction to texture analysis. *Taylor & Francis Group,* **2008**.
67. Ocelík, V.; Hemmati, I.; De Hosson, J. T. M. The influence of processing speed on the properties of laser surface deposits. *Surf. Contact Mech. Incl. Tribol. XII*, **2015**, 1, 93–103, doi: 10.2495/secm150091.
68. Guo, Q.; Chen, S.; Wei, M.; Liang, J.; Liu, C.; Wang, M. Formation and Elimination Mechanism of Lack of Fusion and Cracks in Direct Laser Deposition 24CrNiMoY Alloy Steel. *J. Mater. Eng. Perform.*, **2020**, 29, 6439–6454, doi: 10.1007/s11665-020-05163-4.
69. Chen, Y.; Lu, F.; Zhang, K. Nie, P. Hosseini, S. R. E.; Feng, K.; Li, Z. Dendritic microstructure and hot cracking of laser additive manufactured Inconel 718 under

improved base cooling. *J. Alloys Compd.*, **2016**, 670, 312–321, doi: 10.1016/j.jallcom.2016.01.250.
70. Chen, Y. Guo, Y.; Xu, M.; Ma, C.; Zhang, Q.; Wang, L.; Yao, J.; Li, Z. Study on the element segregation and Laves phase formation in the laser metal deposited IN718 superalloy by flat top laser and gaussian distribution laser. *Mater. Sci. Eng. A*, **2019**, 754, 339–347, doi: 10.1016/j.msea.2019.03.096.
71. Long, Y. T.; Nie, P. L.; Li, Z. G.; Huang, J.; Li, X.; Xu, X. M. Segregation of niobium in laser cladding Inconel 718 superalloy. *Trans. Nonferrous Met. Soc. China,* **2016**, English Ed., 26, 431–436, doi: 10.1016/S1003-6326(16)64131-6.
72. Xiao, H.; Li, S.; Han, X.; Mazumder, J.; Song, L. Laves phase control of Inconel 718 alloy using quasi-continuous-wave laser additive manufacturing. *Mater. Des.*, **2017**, 122, 330–339, doi: 10.1016/j.matdes.2017.03.004.
73. Singh, G.; Vasudev, H.; Bansal, A.; Vardhan, S.; Sharma, S. Microwave cladding of Inconel-625 on mild steel substrate for corrosion protection. *Mater. Res. Express*, **2020**, 7, doi: 10.1088/2053-1591/ab6fa3.
74. Wang, L.; Dong, J.; Tian, Y.; Zhang, L. Microsegregation and Rayleigh number variation during the solidification of superalloy Inconel 718. *Mineral Metall. Mater.*, **2008**, 15, 594–599, doi: 10.1016/S1005-8850(08)60111-5.
75. Knorovsky, G. A.; Cieslak, M. J.; Headley, T. J. INCONEL 718 A Solidification Diagram. **1989**, vol. 20.
76. Petrzak, P.; Kowalski, K.; Blicharski, M. Analysis of phase transformations in Inconel 625 alloy during annealing. *Acta Phys. Pol. A*, **2016**, 130, 1041–1044, doi: 10.12693/APhysPolA.130.1041.
77. Reichardt; A.; Shapiro, A. A.; Otis, R.; Dillon, R. P.; Borgonia, J. P.; McEnerney, B. W.; Hosemann, P.; Beese, A. M. Advances in additive manufacturing of metal-based functionally graded materials. *Int. Mater. Rev.*, **2020**, 0, 1–29, doi: 10.1080/09506608.2019.1709354.
78. Feng, K.; Feng, K.; Chena, Y.; Denga, P.; Li, Y.; Zhao, H.; Lu, F.; Li, R.; Jian, H.; Li, Z. Improved high-temperature hardness and wear resistance of Inconel 625 coatings fabricated by laser cladding. *J. Mater. Process. Technol.*, **2017**, 243, 82–91, doi: 10.1016/j.jmatprotec.2016.12.001.
79. Li, S.; Wei, Q.; Shi, Y.; Chua, C. K.; Zhu, Z.; Zhang, D. Microstructure Characteristics of Inconel 625 Superalloy Manufactured by Selective Laser Melting. *J. Mater. Sci. Technol.*, **2015**, 31, 946–952, doi: 10.1016/j.jmst.2014.09.020.
80. Zhaoyang, L.; Jiayang, S. Characterization of Microstructure, Precipitations and Microsegregation in Laser Additive Manufactured Nickel-Based Single-Crystal Superalloy," *Materials* (Basel)., **2020**, 13, 2300; https://doi.org/10.3390/ma13102300
81. Kurz, W.; Bezençon, C.; Gäumann, M. Columnar to equiaxed transition in solidification processing. *Sci. Technol. Adv. Mater.*, **2001**, 2, 185–191, doi: 10.1016/S1468-6996(01)00047-X.
82. Hemmati, I.; Ocelík, V.; De Hosson, J. T. M. Microstructural characterization of AISI 431 martensitic stainless steel laser-deposited coatings. *J. Mater. Sci.*, **2011**, 46, 3405–3414, doi: 10.1007/s10853-010-5229-2.
83. Ding, C.; Cui, X.; Jiao, J.; Zhu, P. Effects of substrate preheating temperatures on the microstructure, properties, and residual stress of 12CrNi2 prepared by laser

cladding deposition technique," *Materials* (Basel)., vol. 11, no. 12, **2018**, doi: 10.3390/ma11122401.
84. Corbin, D. J.; Nassar, A. R.; Reutzel, E. W.; Beese, A. M.; Michaleris, P. Effect of substrate thickness and preheating on the distortion of laser deposited Ti-6Al-4V. *J. Manuf. Sci. Eng. Trans. ASME*, **2018**, 140, 6, doi: 10.1115/1.4038890.
85. Guo, P.; Zou, B.; Huang, C.; Gao, H. Study on microstructure, mechanical properties and machinability of efficiently additive manufactured AISI 316L stainless steel by high-power direct laser deposition. *J. Mater. Process. Technol.*, **2017**, 240, 12–22, doi: 10.1016/j.jmatprotec.2016.09.005.
86. Wang, Q.; Zhang, S.; Zhang, C.; Wu, C.; Wang, J.; Chen, J.; Sun, Z. Microstructure evolution and EBSD analysis of a graded steel fabricated by laser additive manufacturing. *Vaccum*, **2017**, 141, 68–81, doi: 10.1016/j.vacuum.2017.03.021.

Article 8 - Mechanical and Microstructural Characterisation of Inconel 625 - AISI 431 Steel Bulk produced by Direct Laser Deposition

Journal of Materials Processing Technology

https://doi.org/10.1016/j.jmatprotec.2022.117603

Journal of Materials Processing Tech. 306 (2022) 117603

ELSEVIER

Contents lists available at ScienceDirect

Journal of Materials Processing Tech.

journal homepage: www.elsevier.com/locate/jmatprotec

Mechanical and microstructural characterisation of Inconel 625 - AISI 431 steel bulk produced by direct laser deposition

André A. Ferreira[a,b,*], Omid Emadinia[b], Rui L. Amaral[b], João M. Cruz[c], Ana R. Reis[a,b], Manuel F. Vieira[a,b]

[a] Faculty of Engineering of the University of Porto, 4200-465 Porto, Portugal
[b] LAETA/INEGI-Institute of Science and Innovation in Mechanical and Industrial Engineering, 4200-465 Porto, Portugal
[c] SERMEC-Group, 4425348 Folgosa-Maia, Portugal

Article 8 - Mechanical and Microstructural Characterisation of Inconel 625 - AISI 431 Steel Bulk produced by Direct Laser Deposition

André A. Ferreira[1,2], Omid Emadinia[2] , Rui L. Amaral[2], João M. Cruz[3], Ana R. Reis[1,2], Manuel F. Vieira[1,2]

[1]Faculty of Engineering of the University of Porto, 4200-465 Porto, Portugal
[2]LAETA/INEGI—Institute of Science and Innovation in Mechanical and Industrial Engineering, 4200-465 Porto, Portugal
[3]SERMEC-Group, 4425-348 Folgosa-Maia, Portugal
*Corresponding author: Department of Metallurgical and Materials Engineering, University of Porto, Porto, 4200-465 Portugal E-mails addresses: andreferreira@fe.up.pt (A. A. Ferreira)

Abstract

The direct laser deposition process successfully produced a bulk material by mixing 50% Inconel 625 powders (M625) with 50% AISI 431 steel powders (M42C). The properties of this new material, such as tensile strength and wear resistance, were evaluated. The microstructure was also analysed using scanning electron microscopy. Moreover, the formation of defects and second phases in the bulk material were investigated by applying a tomography analysis. M625-M42C bulk material shows tensile strength and abrasive wear behaviour similar to Inconel 625 alloy, suggesting a potential replacement material for the more expensive Inconel 625. This study is focused on an innovative material, which had not yet been produced as a bulk, allowing the evaluation of the mechanical and metallurgical characteristics promoted by this mixture of powders. In addition, this deposition methodology seems very interesting for cladding or repair objectives since the failure did not happen at the transition interface between deposited bulk and substrate.

Keywords: bulk, Inconel 625, AISI 431, powder mixing; direct laser deposition; microstructure; chemical composition; hardness.

Introduction

Direct Laser Deposition (DLD), as an additive manufacturing process, is a technique that has been investigated in depth in recent years. Hu et al. (2021) demonstrated that the DLD technique provides a high laser power density, enabling the production of unlimited-sized components. Thompson et al. (2015) showed that the technique provides the potential to (i) rapidly prototype metal parts, (ii) produce complex and customised parts and (iii) coat/repair metal components. This advanced process produces components layer by layer, and, according to Zhang et al., 2018, it enables fabricating new materials to meet an intended function. Densification is achieved by solidifying consecutive melt pools generated by laser as a heat source. Walker et al. (2017) cites that the DLD process is an innovative factor for the production of novel materials., where the proper mixing of powders that must be in accordance with the components metallurgical, mechanical, chemical, and tribological requirements. Recently, Yan et al. (2020) provided an overview of the progress in metallic Functionally Graded Materials (FGM) fabricated by DLD emphasizing the complexity of the process.

DLD depositions are, in fact, a complex process that involves the interaction between laser and metal (powders, wire or a combination of both), melt pool movements, rapid unbalanced solidification and phase transformations, as evidenced in the study of Wang et al. (2017). Mahamood (2018) demonstrated that the technique has the advantage of locally synthesising compositional gradients by mixing different powders, gradually varying the mixture at intended locations, thus generating parts with graded material properties. In the DLD process, high cooling rates caused by the localised heat inputs of the laser beam are observed. This rapid cooling causes metallurgical defects associated with metastable phases in the deposited material and the heat-affected zone (HAZ). Martin et al. (2022) demonstrated that the DLD technique could be combined with other additive manufacturing processes, such as Powder Bed Fusion (PBF), to produce hybrid structures.

Brandl et al. (2011) demonstrated that preheating (PHT) of the substrate is one of the processes to reduce the cooling rate and decrease the hardness in HAZ. Dass and Morid (2019) proved that PHT reduces the sharp thermal gradients. The laser absorption rate by the substrate is higher when there is preheating, according to research conducted by Su et al., (2019). As stated by Jiang et al. (2020), PHT improves stress distribution and prevents the formation of hard structures that are detrimental to the mechanical properties of the cladding. Meng et al. (2019) analysed the production of a gradient material using the Inconel 625/Ti6Al4V system. They demonstrated that preheating promotes the formation of thinner, more uniform and free of cracks secondary phases. The effect of preheating was discussed in two previous studies. According to Ferreira et al. (2021c), PHT promotes an increase in dilution in relation to samples without PHT, and this increase causes a decrease in the yield of the deposition process. Ferreira et al. (2021a) analysed the influence of substrate preheating to 300 °C on the microstructure of the cladding/substrate interface, showing that it reduces formation of hard and brittle phase and the hardness profile, mainly in the heat-affected zone.

The production of Functionally Graded Additive Manufacturing (FGAM) materials is, as mentioned, one of the major advantages of DLD. FGAM allow achieving spatially variable properties through gradual changes in composition or structure. The design, development, and applicability of FGAM by Direct Laser Deposition (DLD) is an important alternative for producing high-performance materials, mainly for the aerospace, automotive, medical, and energy sectors. FGAM can provide settings impossible to be achieved by traditional materials and processing. Allowing bonding two complex and incompatible materials by creating compositional gradients that function as transition layers between the two materials, this process minimises internal stresses and cracks, consequently improving mechanical strength, as evidenced by Durejko et al. (2014). FGAM allow the production of materials with mechanical (Su et al., 2020), magnetic (Zhang et al., 2018) or thermal (Soodi et al., 2013) properties varying throughout the component. Popovich et al. (2017) concluded that microstructural and chemical changes promote physical and mechanical properties alterations in the FGAM during DLD. Sarathchandra et al. (2018) recently reviewed this topic and identified that there is still a gap to understand microstructure, phase transformations, manufacturing process modelling and process optimisation in order to achieve better results.

Several studies have analysed the production of gradient materials using Inconel 625 superalloy with steels, mainly austenitic stainless steel. Mirzana et al. (2016) produced sound discs through the DLD process with two different materials, AISI 316 steel and Inconel 625, obtaining a microstructure that revealed a uniform variation of properties in the interface region, low distortion. The mechanical properties of an Inconel 625 - AISI 316L gradient material were evaluated by Koike et al. (2017) who showed that the bonding interface presented comparative mechanical strength and hardness similar to those of AISI 316L. An analogous mechanical behaviour was obtained by Zhang et al. (2019), when analyzing a FGM produced using AISI 316L and Inconel 625 powders. Clare et al. (2022) reviewed the metallurgical and mechanical characteristics of mixtures of materials by different additive manufacturing techniques; these new materials could respond to challenges posed by different industrial sectors. However, bulk production with tailored composition for the repair or remanufacturing of components is an approach that has not yet been studied. A new combination of powders can produce less expensive materials with enhanced mechanical strength and wear and corrosion resistance.

In this sense and recognising the importance and complexity of developing this type of solution, this study explores the production of a bulk composed of 50% Inconel 625 (M625) and 50% AISI 431 steel (M42C) deposited on a preheated substrate. In a previous study by Ferreira et al. (2021a), an FGAM using the same powders was produced, with deposition of initial layers of M42C, followed by layers of M625-25% M42C, M625-50% M42C, M625-75% M42C and ending in 100 % M42C. A metallurgical and mechanical analysis of the FGAM allowed the selection of the best composition for industrial applications. The microstructural analysis shows that several phases, with different chemical compositions, are formed as the mixture of powders varies, being also dependent on the manufacturing conditions. Inconel 625 + 50% AISI 431 steel ensures a cladding free of cracks and porosities, with a hardness similar to that of Inconel 625, and with less amount of this material, being, therefore, the least expensive. In this study, this composition was selected to produce a massif to analyse the structural integrity of this new material, its mechanical response and wear resistance.

Experimental Procedure

Direct laser deposition (DLD) technique, assembled with a six-axis robot (KUKA KR90 R3100 model), and equipped with a Laser system (LDF 6000 – 100), a fibre-coupled laser diode providing a wavelength range of 900-1030 nm and reaching a nominal beam power of 6000 W, was applied for the powder consolidation and production of blocks. The laser beam was delivered through an optical fiber of 1.0 mm in diameter, and with a beam quality of 100 mm*rad. The materials produced in this study include blocks of equimassic mixture of Inconel 625, so-called M625, and AISI 431 stainless steel, as M42C; and of individual alloys as references. The particles range size for M625 and M42C are 45 - 90 μm and 45 - 106 μm, respectively. Figure 1 illustrates the morphology of these powders, the M625 particles are seen in spherical form, and M42C particles have an irregular shape (non-spherical). Powders and steel substrates chemical composition is presented in Table 1. The particle size and chemical composition of the powders referred to are those indicated in the supplier's datasheets.

Table 2. Chemical composition (in wt%) of M625, M42C powders and 42CrMo4 steel.

Raw Material	C	Cr	Ni	Mn	Mo	Nb	Si	P	S	Fe
M625	-	21.3	60.8	-	9.2	4.6	-	-	-	4.1
M42C	0.18	17.3	1.9	-	-	-	0.24	-	-	Balance
42CrMo4	0.42	1.11	-	0.67	0.19	-	0.28	0.025	0.015	Balance

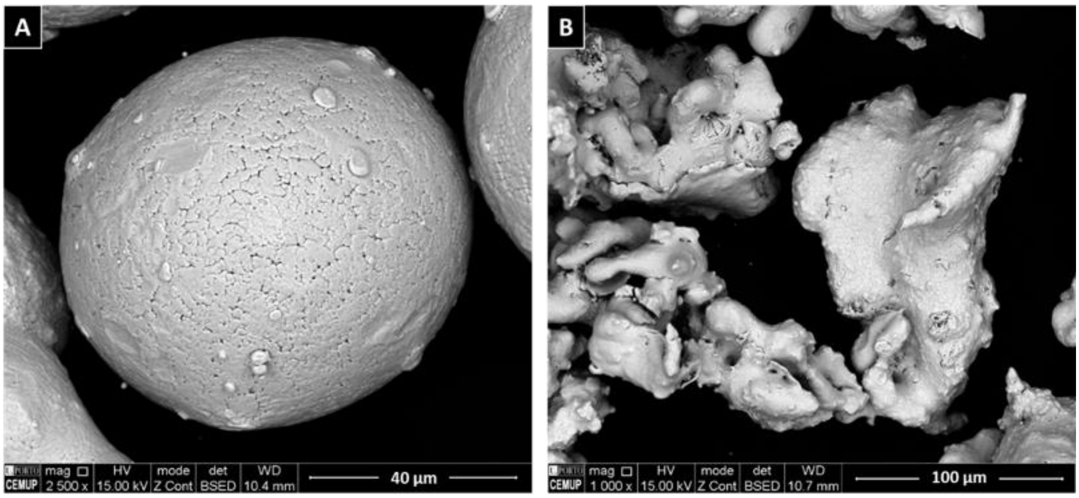

Figure 1. SEM/BSE technique illustrates the morphology of (A) M625 and (B) M42C powders.

Before deposition, the substrates, 42CrMo4, were cleaned with pure acetone and heated to approximately 300 °C by an oxy torch. This preheating condition was applied to eliminate moisture and decrease the cooling rate in the melt pool and adjacent regions of the substrate (thus reducing the detrimental effect of the HAZ). Successive depositions of an equimassic mixture of M625 and M42C powders (M625-M42C) were made to produce a bulk material. The powders were mixed and transported by a mixer attached to the feeders. Deposition was carried out through a one-step process with a coaxial powder nozzle. The nozzle had a self-contained powder feeder, a shield gas channel and four carrier gas channels. In addition, argon gas with 99.998% purity was used as shielding gas with a flow rate equal to 9.1667x10-5 m^3/seg (5.5 l/min) to minimise the contamination and oxidation of the melt pool during the DLD process. Furthermore, for bulk production, the Inconel 625 (M625) +

50% AISI 431 (M42C) powder deposition strategy selected was the zigzag-XY tool path, as shown in Figure 2.

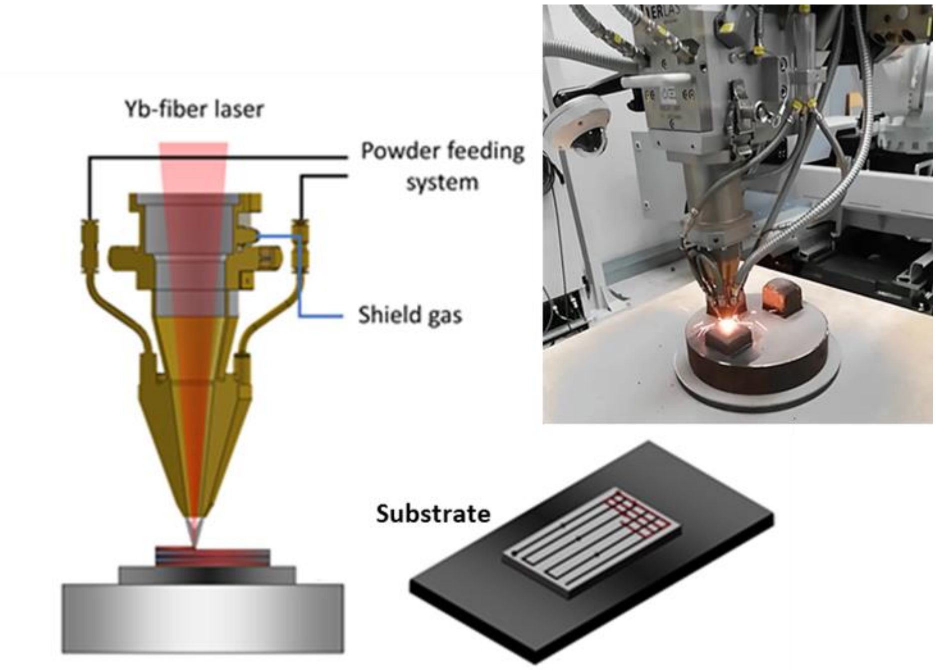

Figure 2. Schematic diagram of the strategy for the Inconel 625 (M625) + 50% AISI 431 (M42C) bulk production by DLD. An image during the production of a bulk is also shown.

These two combined parameters, specific energy [J/mm^2] and powder density G [g/mm^2], lead to a simpler and more general (non-machine specific) approach to the process, where LP is the laser power on the substrate [W], SS is the scanning speed [mm/s], φ is the radius of the laser beam on the substrate [mm], and FR the powder feed rate [g/min]:

$$E_{\text{specific}} = \frac{\text{LP}}{\varphi * SS} \tag{1}$$

$$G = \frac{\text{FR}}{\varphi * SS} \tag{2}$$

The combined parameters applied for depositing in the current study are presented in Table 2. These combined parameters were applied based on a previous study developed by Toyserkani et al. (2017). Nonetheless,in all tests, a spot size of 2.5 mm, and an offset in the Z-axis of 0.2 mm were applied; the coaxial powder flow had a focal distance of 13 mm. The trajectory of depositions involved continuously parallel depositing applying a 40% overlapping between tracks, followed by depositing successive layers rotated at 90° in each layer. The depositions were carried out in order to produce layers with similar thicknesses; the average layer thickness is 1.47 mm. Figure 3 shows a block produced by the DLD technique.

Table 3. Combined parameters for bulk production by DLD.

Combined parameters	50% M625 + 50% M42C
$E_{specific}$ [J/mm²]	60
G [g/mm²]	0.01

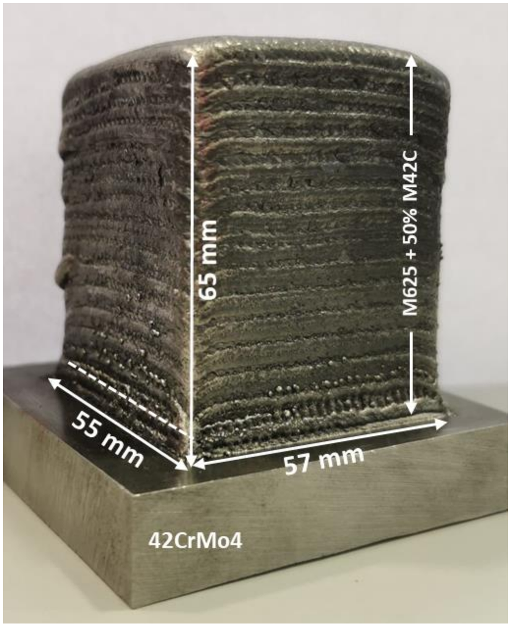

Figure 3. New material M625-M42C bulk, produced by DLD on 42CrMo4 substrate.

The bulk was cut for microstructural characterisation using a metallographic cut-off machine with refrigeration to avoid substrate and cladding overheating. Samples were mounted in resin and polished down to 1 μm diamond suspension. An additional polishing step was performed, using a 0.06 μm silica colloidal suspension for a superior surface finish and polishing-induced plastic deformation removal. Chemical compositions and microstructure were systematically investigated using scanning electron microscope (SEM) FEI Quanta 400 FEG (ESEM, Hillsboro, OR, USA) equipped with Energy Dispersive X-Ray Spectroscopy (EDX) (EDAX Genesis X4M, Oxford Instrument, Oxfordshire, UK).

Uniaxial tension tests were performed accordingly to Džugan et al. (2015), using an electromechanical uniaxial testing system (MSTD, INEGI, Portugal) with a 5 kN load cell at a 0.5 mm/min strain rate. Digital image correlation (DIC), a non-contact method to measure surface strains, was used to calculate surface strains using correlation software (VIC-2D 6, Correlated Solutions, Inc., USA). The DIC images were captured with a telecentric lens (Infaimon OPE-TC-23-09, 45 mm) and a 5 MPixel camera (Basler acA2440-75um, 2448x2048 pixels). Hardness tests were carried out, applying a load of 30 kgf per indentation, using EMCO M4U Universal machine (EMCO-TEST PRÜFMASCHINEN GMBH, Kuchl, Austria).

The abrasive resistance analysis was performed (1071-6:2007, 2010) applying the ball-cratering method, considered as a micro-abrasion test. A homogeneous slurry of SiC in distilled water, 2 vol.%, was used, continuously stirred during the test to ensure the dispersion of particles in the slurry. The ball test was a 25.4 mm diameter hardened steel (SAE 52100), the rotation was performed at a fixed speed of 85 rpm applying a constant load of 0.25 N, delivering the slurry at the contact surface through a roller pump. The specimens were subjected to this test in four individual rotations, for 30, 60, 120 and 240 minutes, corresponding to 203.48 m, 406.96 m, 813.92 m, and 1627.85 m of sliding distances. Micro-abrasion wear tests were performed to evaluate the bulk wear rate with the PLINT TE 66 Micro-Scale Abrasion Wear Tester (Phoenix Tribology, England) with a fixed rotating ball configuration. The worn surfaces were observed using LEICA DMV6 digital microscopy, equipped with LAS X software for image viewing and extracting crater profiles. The measurements were made using image processing software (ImageJ). Afterwards, the worn volume, V in mm3, was calculated using V=π×b4/(64×R) equation in which "b" is the crater mean diameter (mm) and R is the steel ball radius (mm). The abrasive wear rate, K in mm3·N−1·mm−1, was calculated through K=VxS−1×N−1 where S is the sliding distance (mm) and N is the applied load (N) (1071-6:2007, 2010).

X-ray computed tomography (X-Ray CT) (Nikon XT H 225, England) was used to investigate the distribution and size of discontinuities along with three cylindrical samples, with approximate dimensions of 9.93 x 23.68 mm, taken from the bulk produced with M625 + 50% M42C. The scanning time for each sample was 2 h and 12 min, using a 1mm silver filter. The source was an X-ray tube using an accelerated voltage of 225 kV and amperage of 116 μA. For this experiment, the effective voxel resolution was 17 mm. The dataset obtained from the X-Ray CT test was reconstructed using the manufacturers Inspect-X software. In addition, the data was imported into the myVGL 3.4.1 software (Volume Graphics GmbH, Germany), allowing three-dimensional visualisation, segmentation and quantification of the distribution of discontinuities.

Results and Discussion

Microstructure of the bulk material

Figure 4 illustrates the microstructure of the produced bulk material in different regions, consisting of dendrites, cellular and elongated morphologies, and discontinuities smaller than 0.1 mm. Microscopic observations did not detect non-fused particles that could act as weak points and diminish the mechanical properties of the produced material. According to Figure 4, with different magnificato, the main discontinuities observed in the bulk microstructure were inclusions of oxides, carbides and second phases precipitated in the interdendritic spaces, described in detail in the previous study by Ferreira et al. (2021b). Inclusions are typically submicrometer and may reach a few micrometres.4. The formation of these inclusions is directly related to the metallurgical interactions that occurred between the constituents. However, microscopic observations did not reveal the presence of any porosity in the microstructure of the bulk material.

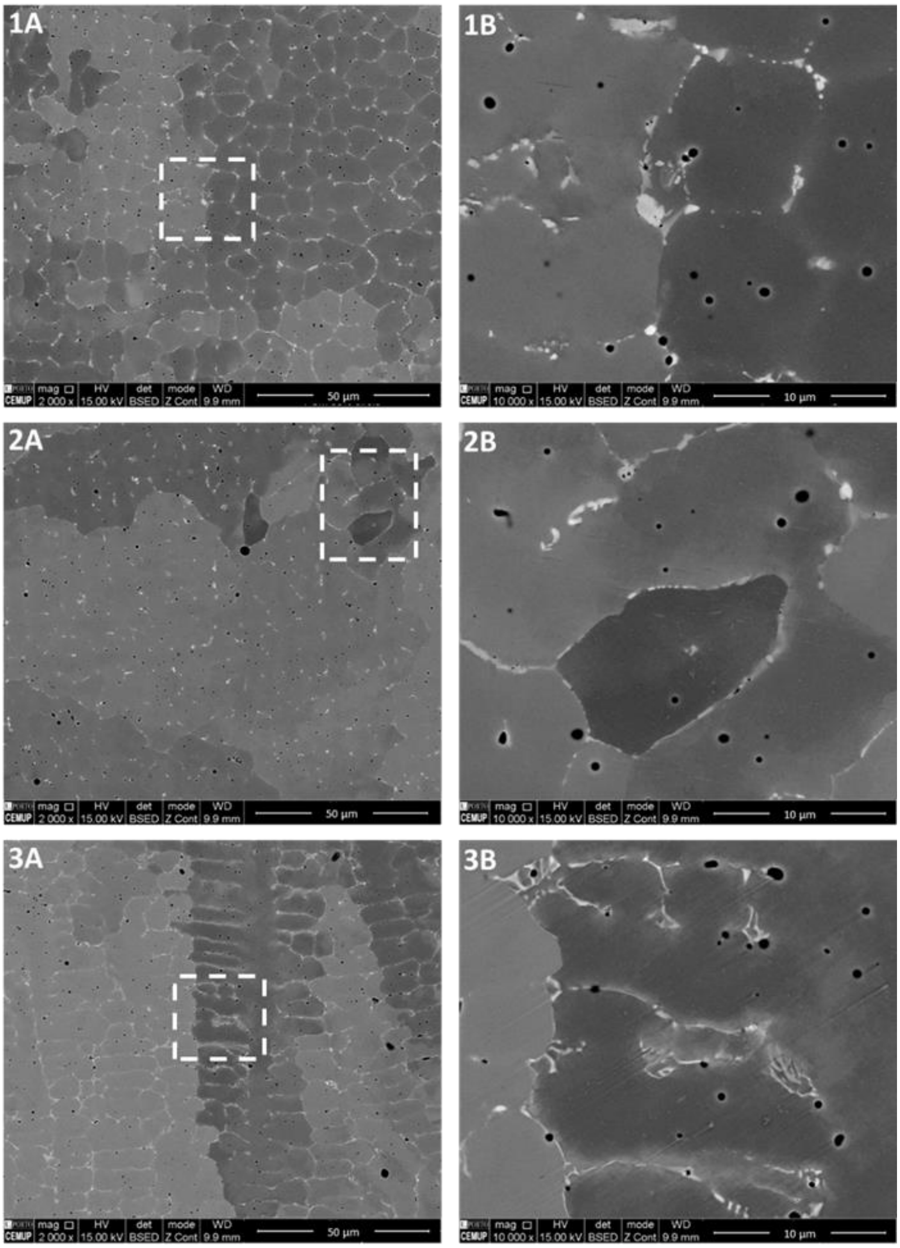

Figure 4. SEM images from the bulk material, M625 + 50% M42C produced by DLD, showing the microstructure and some inclusions.

Computerised Tomography

The structural integrity of the bulk material produced in the current study was confirmed by performing a 3D computerised tomography, X-ray scanning CT.

According to Du Plessis et al. (2018), this analysis is a non-destructive evaluation technique that allows the identification of internal discontinuities in components, the 3D images from the internal structure of the specimens are obtained applying X-ray radiation passing through the object and then being detected by an adequate detector. Proper radiations include the electromagnetic spectrum from microwaves to gamma rays or particles including protons, neutrons and electrons, which can produce 3D images with a spatial resolution larger than 1 micron (De Chiffre et al., 2014). The specimen preparation is not critical, and multiple scans can be performed for the same specimen under different conditions.

Discontinuities observed in the microstructure, Figure 5, are not detected by X-ray CT analysis. Figure 5A shows the generated profile from the bulk material, a cylindrical specimen approximately 23.68 mm long and 9.93 mm in diameter. The top view that corresponds to the volume obtained from the cylindrical body is shown in Figure 5B. Thus, it is possible to observe that a high-dense bulk has been produced, free of cracks and with a small distribution of discontinuities in volume.

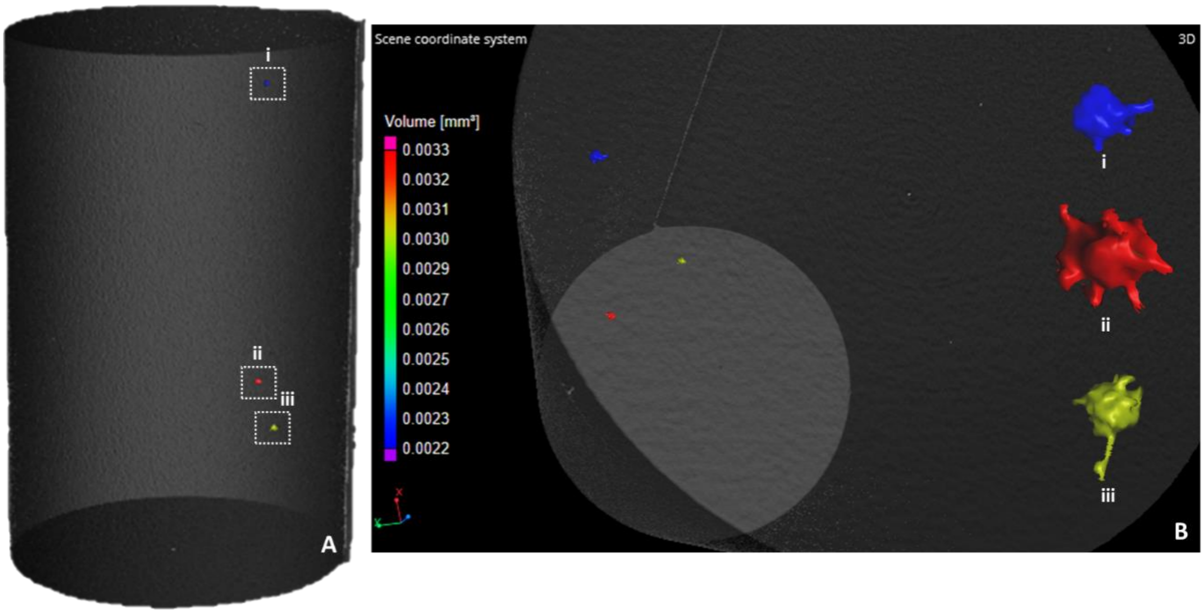

Figure 5. 3D visualisation of the bulk material produced in the current study: (A) a cylindrical specimen (B) the top view of the specimen.

According to data obtained from the myVGL software, the total analysed volume of the bulk specimen was 1130.15 mm^3, with a defect volume of 0.0085 mm^3. The detected discontinuities, with dimensions greater than 0.1 mm and with maximum sphericity of 0.66, can include porosities and/or inclusions, though microscopy observations did not reveal any porosity, Figure 4. The formation of these discontinuities is related to the interaction of elements susceptible to oxidation during laser processing. Porosities and inclusions can contribute to the occurrence of an early fracture, reducing ductility, thus decreasing the mechanical properties.

Uniaxial Tensile Test

Figure 6 illustrates the geometry of the specimens and the uniaxial tensile test setup, a 5 kN testing system developed by Cruz et al. (2020). The tests were performed at room temperature with a constant crosshead speed of 0.5 mm/min, corresponding to an initial strain rate of 3.7x10-3 s^{-1}.

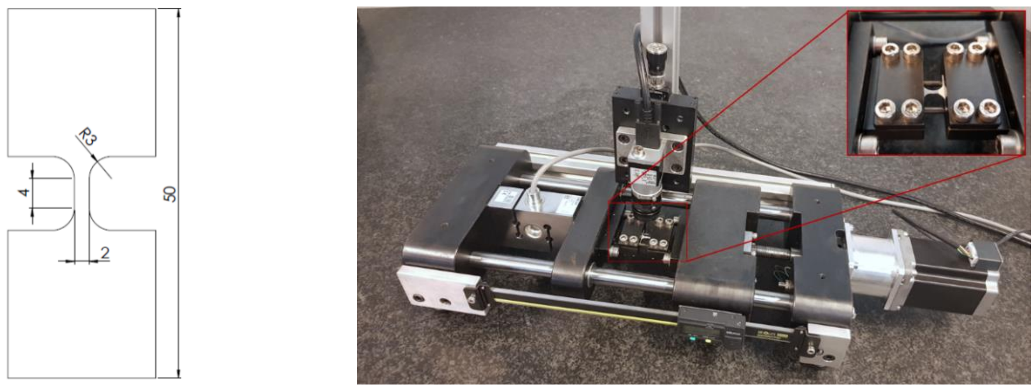

(A) (B)

Figure 6. (A) The design of the tensile specimens, dimensions are in mm, and (B) the uniaxial tensile test equipment and sample

Figure 7 presents the tensile specimen preparation from produced bulk material. Tensile specimens with a thickness of 1.4 mm were extracted using wire electrical discharge machining process, parallel and perpendicular to the building direction.

Moreover, a set of specimens was prepared consisting of bulk material and the substrate, with the interface in the middle of the gauge length (Figure 7B). Several tests were conducted for each direction to ensure the repeatability of the results. Table 3 list the test conditions.

Table 3. Uniaxial test conditions.

Property	Value
Maximum load [kN]	5
Crosshead speed (grip) [mm/min]	0.5
Data acquisition [Hz]	10
Clip gage initial length – l**0** [mm]	3
Temperature [°C]	23
Relative humidity [%]	54

The measurement of elongation in the gauge length applying the digital image correlation (DIC) approach allowed the determination of material strain during the tensile test. A camera is coupled with dedicated software analysing the collected images and computing the strain field captured by the DIC system. The strain field (logarithmic Hencky strains) in the filmed area was computed using a commercial software VIC-2D 6 with a step size of 7 and a set size of 25.

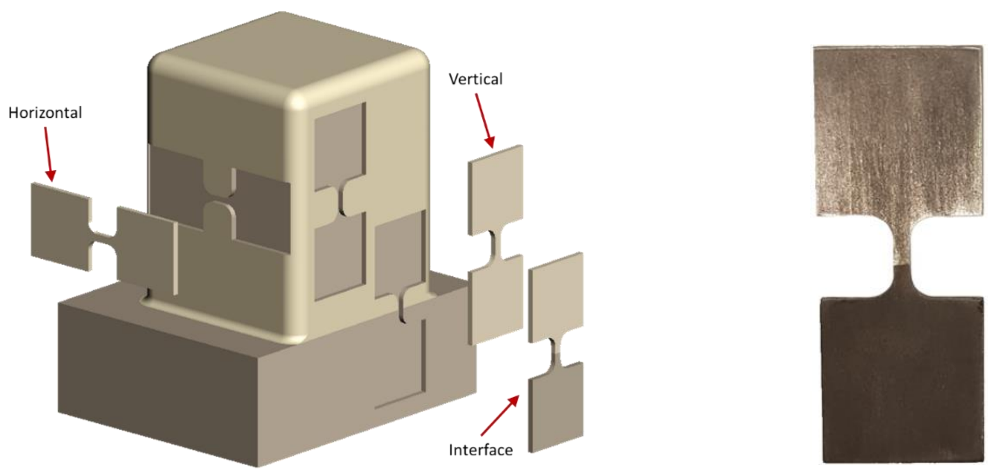

(A) (B)

Figure 7. The strategy used to produce specimens from the bulk material: (A) extraction scheme and (B) a real image of a specimen encompassing interface in the gauge length.

The engineering and true stress-strain flow curves obtained from the uniaxial tensile tests are shown in Figure 8. In addition, Figure 9 presents the mean values of fundamental properties calculated for each loading direction (horizontal and vertical).

As shown in Figure 8, the acquired data indicates a high consistency in mechanical characteristics across the entire bulk, with identical hardening behaviour observed in different tests. The vertically extracted specimens have a slightly lower yield stress than the horizontally oriented specimens; however, they have a greater ultimate tensile strength and better reproducibility. The difference in ultimate tensile strength (UTS), which is larger than 60 MPa, can be explained by the lower elongation of horizontal specimens (Figure 9), resulting in early fracture and lower UTS values. Figure 10 presents several images illustrating the strain field evolution of a horizontal sample during the tensile test.

Additionally, a comparison of these specimens flows stress-strain curves (Figure 11) with the behaviour of additive manufactured M625 and M42C specimens, was performed for a better interpretation of the acquired data. The specimens were extracted from a similar 3D feature to the Figure 3 and produced under identical experimental conditions by Ferreira et al. (2021c) and Ferreira et al. (2021a).

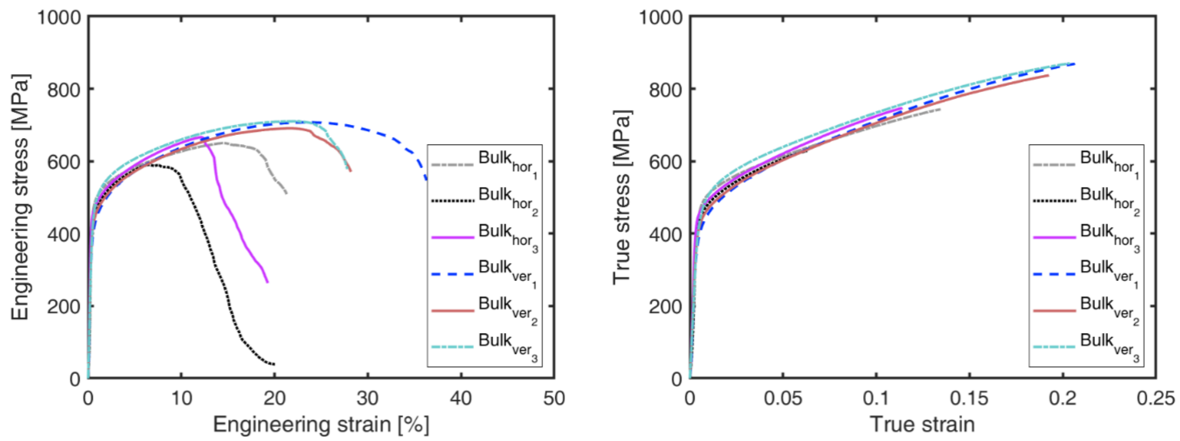

(A) (B)

Figure 8. Engineering (A) and true (B) stress-strain curves of bulk material obtained from the uniaxial tensile test for different loading directions.

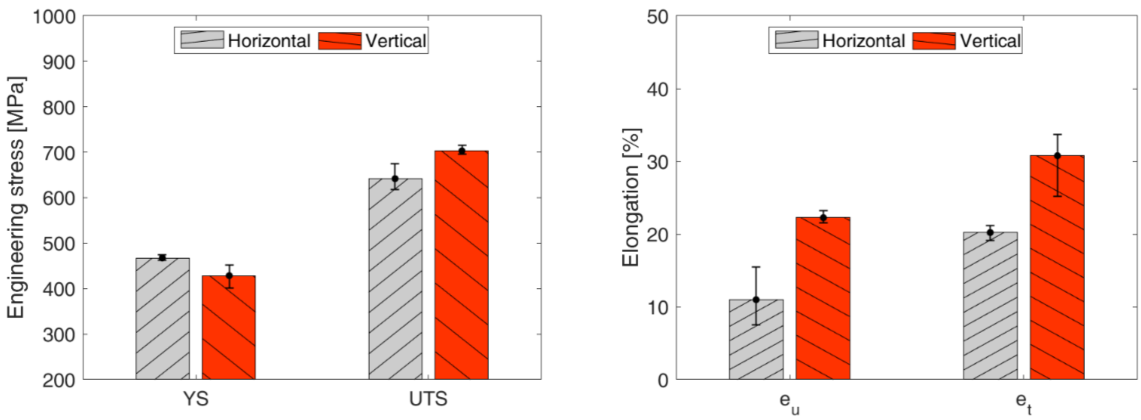

Figure 9. Mechanical properties of bulk material obtained from tensile tests for different loading directions (average values): yield stress (YS), UTS, uniform elongation (e_u) and total elongation (e_t).

As seen in Figure 11, the results of the uniaxial tensile tests indicate that the mechanical hardening behaviour of this new bulk material is comparable with that of M625, when subjected along the vertical direction. The M625 has a predominant mechanical advantage over the M42C. The bulk shows a lower plastic deformation capacity before fracture compared with M625, which is consistent with the lack of ductility in M42C.

The anisotropic response is another characteristic that can be observed when these materials are evaluated separately, dependent on the loading direction relative to the deposition building direction. However, the M625-M42C bulk material shows a closer trend for both types, taken perpendicular (vertical) and parallel (horizontal) to the building deposition, especially in yield stress. Concerning the plastic deformation of vertical specimens, the new bulk material has a closer value to the M625 alloy. The primary mechanical parameters obtained from the uniaxial tensile tests are summarised in Table 4.

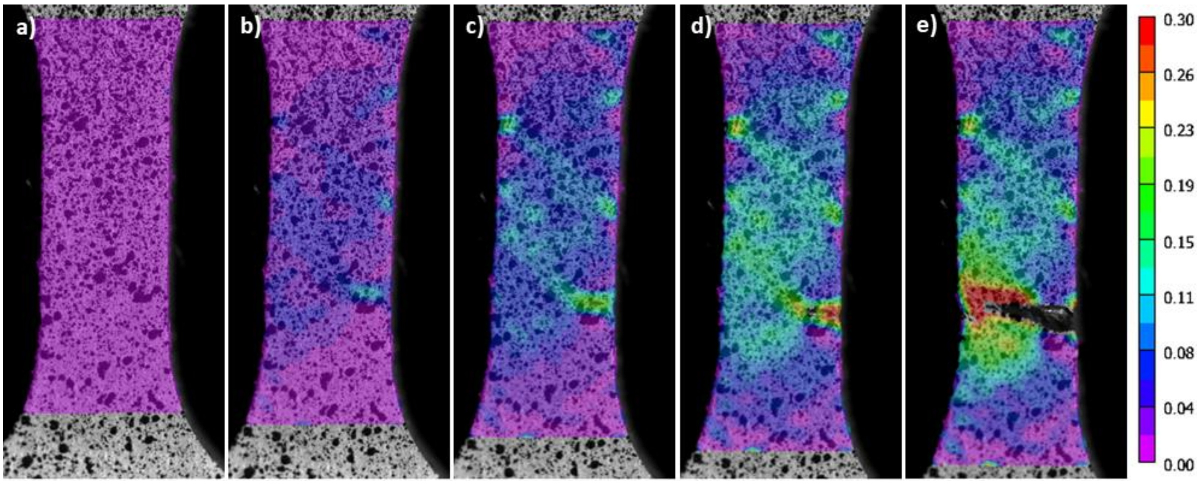

Figure 10. Logarithmic strain field illustrated along loading direction on a horizontal specimen: a) e=0%, b) e=3.5% c) e=10.6% d) e=18.1% e) e=22.6%.

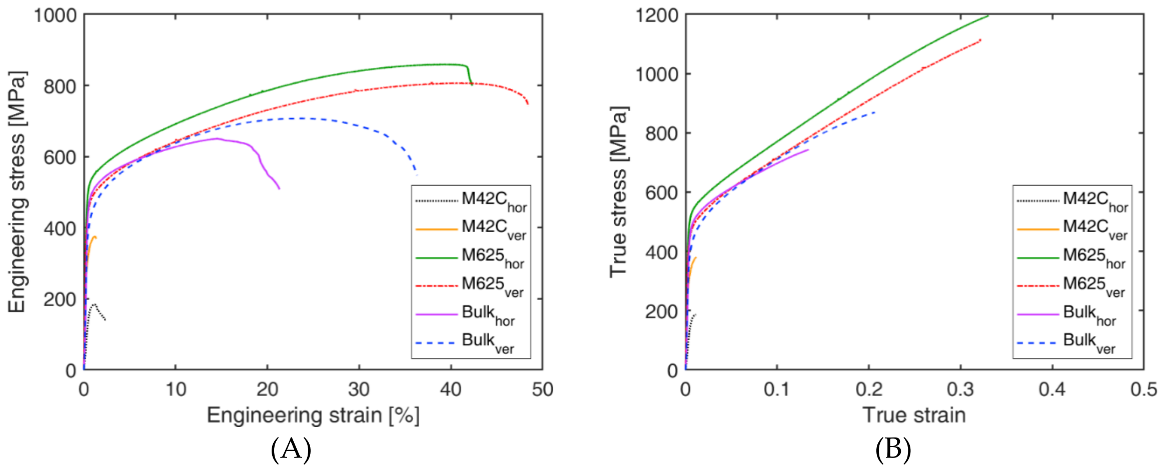

Figure 11. Comparison of (A) engineering and (B) true stress-strain curves for different loading directions of three materials: the bulk (M625-M42C) material, M42C and M625 alloys.

DLD process is reliable for cladding purposes, requiring an adequate metallurgical bonding to the substrate material. Hence, the uniaxial test was performed for specimens that include the bonding interface in the gauge length, shown in Figure 7. Figure 12A exhibits the force vs elongation in a specimen that includes this interface. The corresponding stress-strain curve is compared with the bulk material in horizontal and vertical conditions. As seen in Figure 12B, the mechanical response of this specimen is an intermediate. The vertical and interface specimens present a similar behaviour because both were extracted from the bulk material in the same orientation. Moreover, the strain field of this specimen, for different moments of the tensile test, illustrates that the failure occurred out of the interface region, Figure 13. Thus, the bonding between the bulk material and the substrate is acceptable.

Table 4. Mechanical properties of M42C and M625 alloys and of the bulk material.

Material	Loading direction	YS [MPa]	UTS [MPa]	e_u [%]	e_t [%]
M42C	Horizontal	173.1	186.1	1.2	2.4
	Vertical	298.8	375.9	1.2	1.4
M625	Horizontal	512.4	860.1	39.1	42.3
	Vertical	449.1	807.1	40.5	46.8
Bulk (M625-M42C)	Horizontal	467.4	641.9	11.0	20.2
	Vertical	428.6	703.0	22.3	30.8

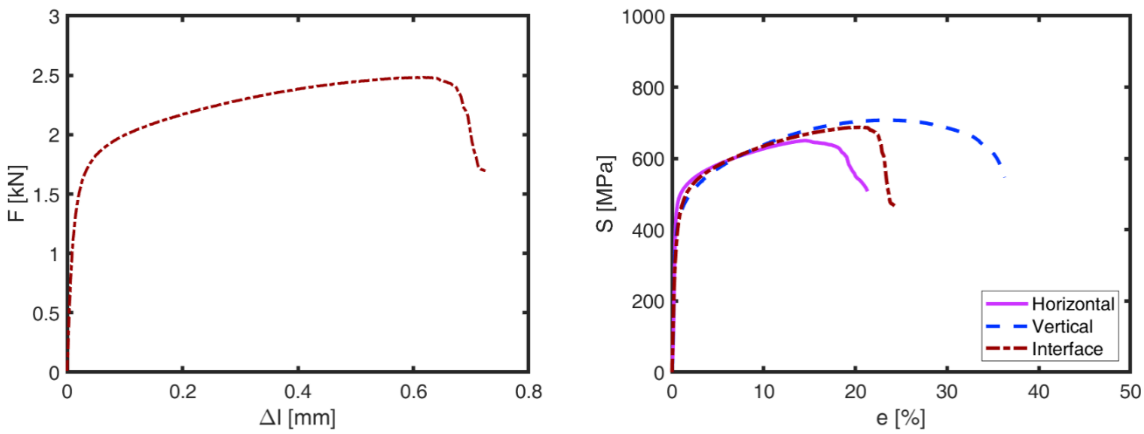

(A) (B)

Figure 12. (A) Evolution of force (F) with elongation (Δl) obtained from the specimen containing interface between the substrate and the bulk material; (B) comparison of engineering stress-strain curves.

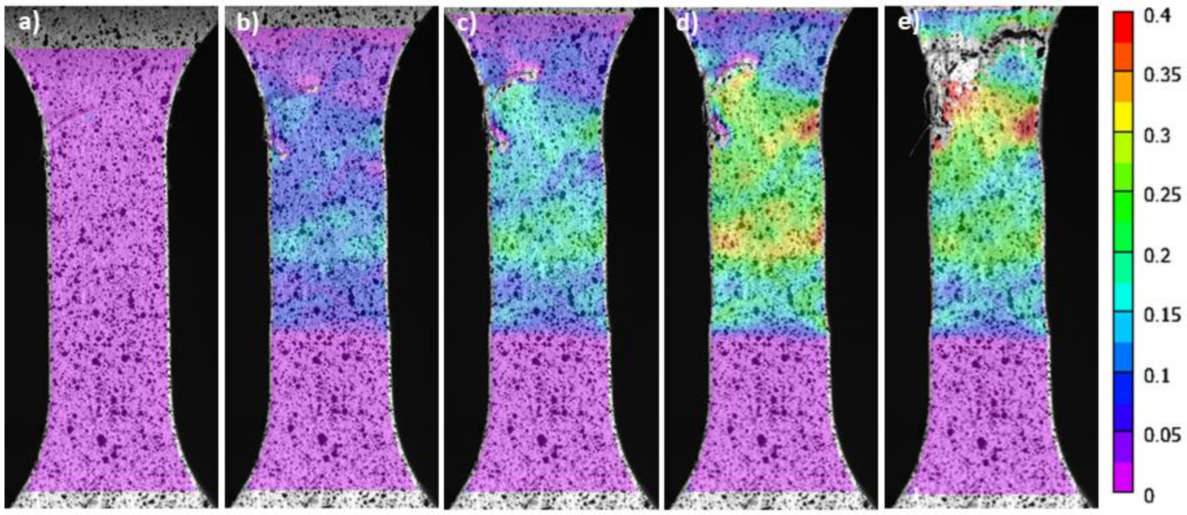

Figure 13. Logarithmic strain field along loading direction obtained for the interface sample: a) e=0%, b) e=3.3% c) e=10.5% d) e=17.9% e) e=23.6%.

The fracture surfaces of tensile specimens, taken horizontally and vertically, were analysed using a scanning electron microscope (SEM). Figure 14 shows the morphology of the fracture surfaces. Fractography analysis was performed on the M42C alloy (Figures 13A and 14B), M625 (Figures 14C and 14D), and the bulk material (Figures 14E and 14F) produced in the current study. This analysis aimed to determine the fracture mode occurred during the uniaxial tensile test.

According to BS EN 10088-5:2009, for martensitic stainless steel such as AISI 431 (X17CrNi16-2), the minimum values to be considered are 600 MPa of yield strength (YS), 800-950 MPa of the tensile strength (UTS) and 14% of elongation at failure. These properties were not obtained in this material processed by DLD, presented in Table 4. The fracture surface of 100% M42C alloy, Figures 14A and 14B, shows cleavages that are characteristics of transgranular fracture, representing a brittle failure. The failure in M42C alloy was independent of sample direction. Although the vertical specimen of this alloy presented higher yield strength than the sample obtained from the horizontal direction, the material at both directions shows similar elongation. The difference in the Ys and UTS can be attributed to the stronger integrity obtained in the building direction. Moreover, the weak properties of the horizontal specimen can be assigned to discontinuities such as complex oxides, cracks, and slag accumulation in the overlapping zones. The performance of EDX local analysis, Table 5, on some zones at the fracture surfaces, yellow insets are shown in Figure 14A and 14B, confirms the presence of complex oxides (Fe, Cr, Si)xOy.

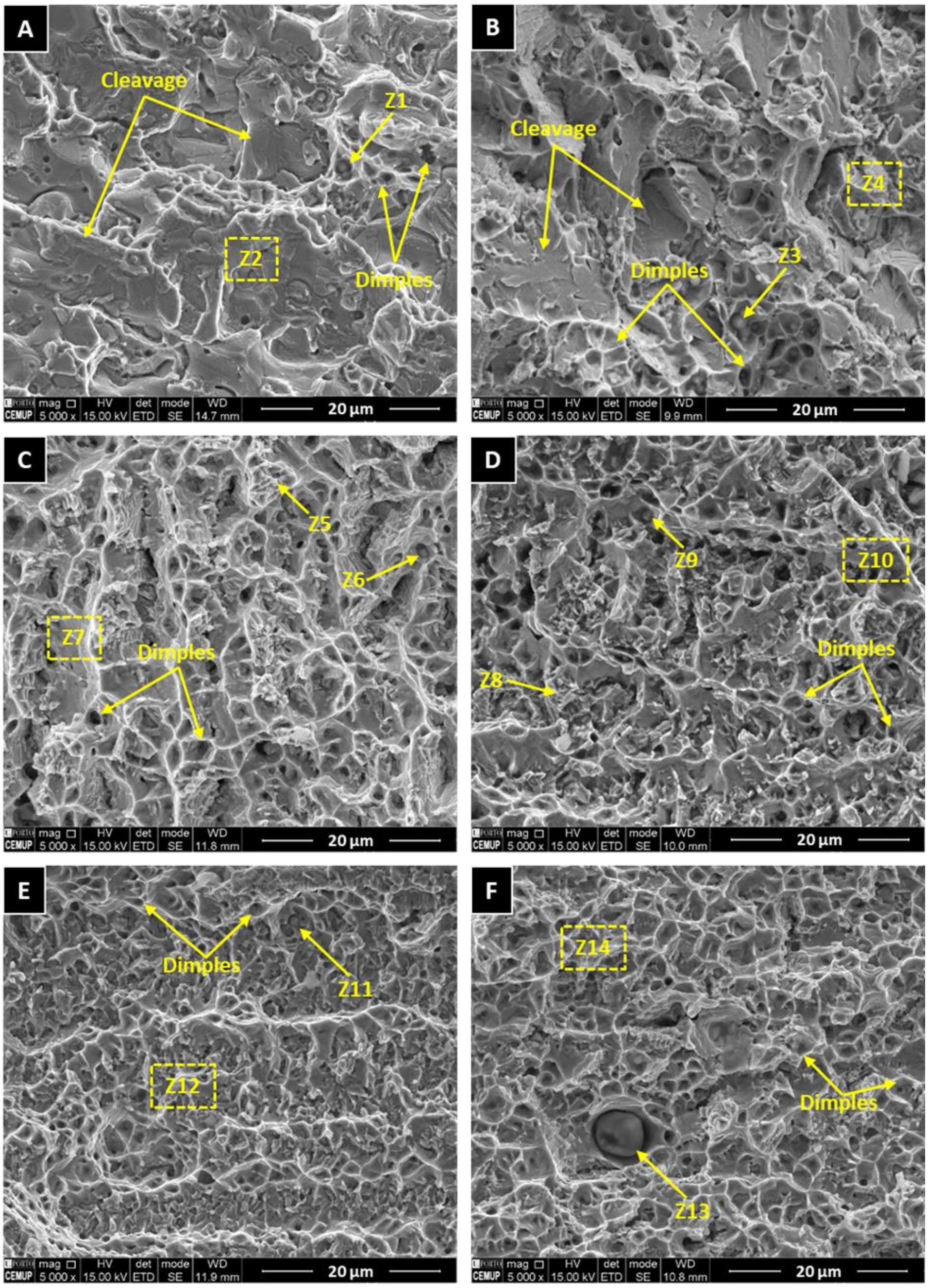

Figure 14. Fractography of tensile specimens: (A) horizontal and (B) vertical M42C specimens; (C) horizontal and (D) vertical of M625; (E) horizontal and (F) vertical of the bulk material.

Table 5. Chemical composition obtained by EDX analysis from the zones highlighted by yellow insets in Figure 13.

Zones	Chemical composition (at %)									
	Ni	Fe	Cr	Mo	Mn	Nb	Si	Al	Ca	O
Z1	1.02	50.15	14.85				13.73			20.25
Z2	1.84	76.63	19.05				2.48			
Z3	0.5	25.62	17.17		2.07		17.38			37.26
Z4	1.8	77.58	17.78				2.84			
Z5	52.08	0.84	24.65	7.78		11.89	2.76			
Z6	22.44		30.28	1.66	7.19	3.64	6.61			28.18
Z7	65.66	0.75	24.51	5.88		1.85	1.35			
Z8	58.63	0.63	25.51	5.93		7.11	2.19			
Z9	16.03		30.82	1.06	10.13	1.2	11.62			29.14
Z10	65.37	0.96	23.83	5.98		1.97	1.89			
Z11	5.85	9.12	14.27	1.03	3.49	2.41	18.87	0.32		44.64
Z12	30.05	39.9	21.56	3.95		1.41	2.36	0.77		
Z13	1.49	2.63	10.28			3.59	26.86	0.69	2.08	52.38
Z14	68.35	0.72	24.22	4.12		1.53	1.06			

Regarding the fractography of the 100% M625 alloy produced and tested in this study, Figure 14C and 14D, respectively horizontal and vertical directions, dimples are observed as the characteristic of ductile failure mode, associated with good bulk toughness and tensile strength, as presented in Table 4.

The insets are shown in Figures 14C, and 14D represent the matrix (Z7 and Z10) and Laves phase (Z5 and Z8), as their chemical compositions are presented in Table 5, appearing adjacent to the dimples. It is possible that these microconstituents, with high hardness, act as stress concentration zones and crack initiation under stress. Sui et al. (2019) demonstrated that the finer the dimension of the Laves phase, the better the material behaviour in tension. Complex multimetallic oxides (Z6 and Z9) were also identified in this alloy. EDX analysis of these oxides identified a high amount of chromium, silicon, manganese, and niobium, which is related to the affinity of these elements with oxygen. However, Wang et al. (2019) demonstrated that these complex oxides are not necessarily detrimental since they can promote an increase in bulk resistance at high temperatures. Matrix chemical composition is described by Z7 and Z10 zones (Table 5).

The information provided in Table 4 presented that the new bulk material, M625 + 50% M42C, is stronger with more capacity for withstanding plastic deformation in the vertical direction than the horizontal one. Figures 14E and 14F illustrate the fractography consistent with this characteristic, appearing larger dimples in the vertical specimen. Nevertheless, the new bulk material showed a ductile failure mode in both directions, similar to the M625 alloy. Although large oxide particles are seen in the fractured surface, zone Z13 in Figure 14F, the bulk material in a vertical direction withstander tensile stresses near the M625 alloy.

Abrasion wear characteristics

According to hardness measurements (M42C 508 ± 4 HV30, M625 319 ± 8 HV30, and Bulk 222 ± 9 HV30), it is expected that the harder the material, the smaller the worn volume. Abrasive wear analysis was performed on similarly produced M42C alloy, M625 and the bulk materials. Figure 15A and 15B shows the craters that appeared on the surface of the bulk after 4h. As seen in Figures 16A and 16B, this behaviour is influenced by the chemical composition and the sliding distance. In the current study, the hardest material, M42C, did not show a good wear abrasive resistance to sliding distance, whereas the bulk material appears as good as Inconel 625 alloy. The former behaviour can be attributed to the alloy microstructure, such as cracking, as presented in a previous study by Ferreira et al. (2021b). As seen in Figure 16A, the Inconel 625 alloy and the bulk material tend to erode less than the M42C alloy within long distances. Although the worn volume increases continuously with sliding distance, Figure 16B confirms that the wear rate decreases with this distance.

These results are noteworthy since the bulk material shows an abrasive wear resistance behaviour similar to the M625 alloy, a more expensive material. Thus, the bulk material produced in the current study is proposed to substitute Inconel for the repair and remanufacturing of components.

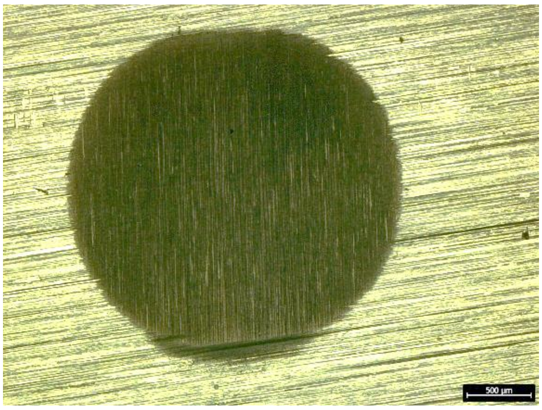

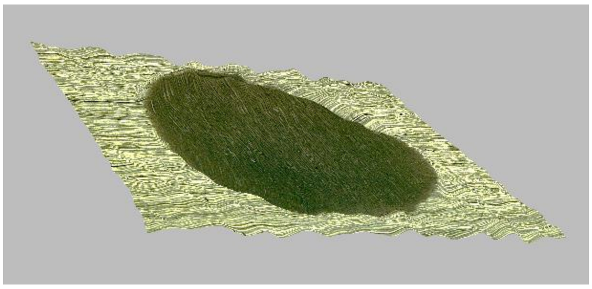

(A) (B)

Figure 15. Worn craters of 1627.8 m sliding distance (equivalent to 4h) for the bulk (A) OM image, and (B) a 3D image of the similar crater.

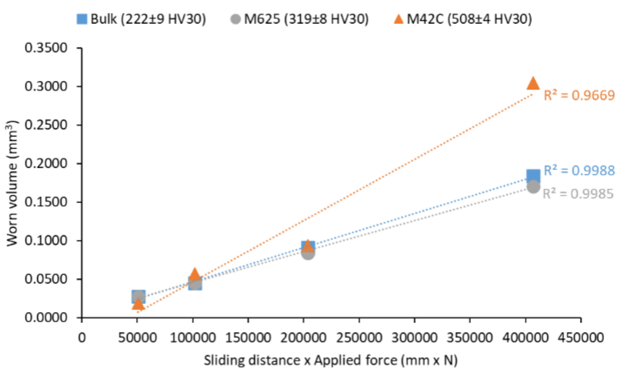

(A)

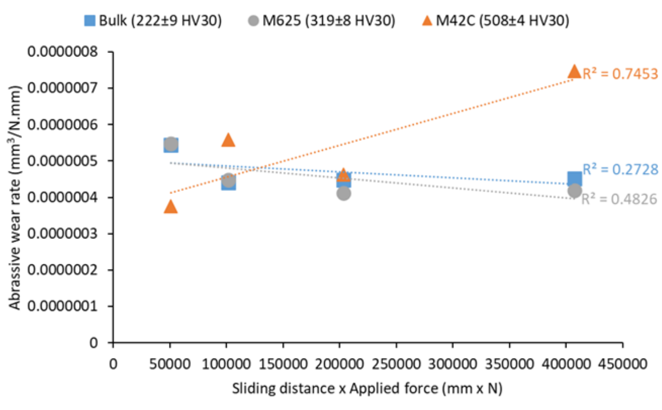

(B)

Figure 16. (A) the worn volume and (B) wear rate as a function of the sliding distance under 0.25 N, constant load.

Conclusions

A bulk material composed of 50% Inconel 625 mixed with AISI 431 alloy was successfully produced by laser direct deposition process. Moreover, individual blocks of Inconel 625 and AISI 431 alloys were similarly produced and served as references.

The 41CrMo4 steel was used as deposition substrates, preheated to 300 °C. Uniaxial tensile test was conducted, and a digital image correlation methodology was implemented to evaluate plastic deformation behaviours. Abrasive wear resistance was performed using ball cratering analysis. Microstructure observations were performed for microstructure analysis, such as fracture surface, wear measurements, and phase formations. The formation of defects and second phases in the bulk material was investigated by tomography analysis. The achievements of this study are summed up as follows:

- The mechanical behaviour of the bulk deposited material is not very far from the Inconel 625; the worst results were obtained for the M42C alloy.
- The UTS and elongation of the bulk material are higher in the direction parallel with building construction than in the horizontal direction.
- Fracture analysis supports the plastic deformation behaviour of the M625 and of the bulk materials when exposed to uniaxial stress respectively in parallel with the building direction, and perpendicular direction, i.e., the presence of dimples seemed more dominant than cleavages face in these materials.
- The bulk material has good bonding with the substrate alloy since the fracture happed to the deposited material.
- The bulk material illustrates a similar behaviour in the abrasive wear test as the M625 alloy.
- Tomography analysis detected a few discontinuities having a dimension less than 0.1 mm.
- Scanning electron microscopy analyses revealed the presence of submicrometer second phases such as oxides or carbides precipitated at the interdendritic spaces.

Funding: This research was funded by FEDER through the program P2020|COMPETE, Projetos em Copromoção (project POCI-01-0247-FEDER-039848).

Institutional Review Board Statement: Not applicable

Informed Consent Statement: Not applicable

Data Availability Statement: Not applicable

Acknowledgements: The authors are grateful to CEMUP (Centro de Materiais da Universidade do Porto) for expert assistance with SEM.

Conflicts of Interest: The authors declare no conflict of interest.

References

Brandl, E., Michailov, V., Viehweger B., Leyens, C., 2011. Deposition of Ti-6Al-4V using laser and wire, part II: Hardness and dimensions of single beads. Surface and Coatings Technology, 206(6), 1130–1141. https://doi.org/10.1016/j.surfcoat.2011.07.094.

British Standards Institution 1071-6, 2007. Advanced technical ceramics - Ceramic composites - Methods of test for reinforcements - Part 6: Determination of the abrasion resistance of coatings by a micro-abrasion wear test.

British Standards Institution EN 10088-5, 2009. Stainless Steels - Part 5: Technical delivery conditions for bars, rods, wire, sections and bright products of corrosion resisting steels for construction purposes.

De Chiffre, L., Carmignato, S., Kruth, J.-P., Schmitt, R., Weckenmann, A., 2014. Industrial applications of computed tomography. CIRP Annals - Manufacturing Technology, 63(2), 655–677. https://doi.org/10.1016/j.cirp.2014.05.011.

Clare, A. T., Mishra, R. S., Merklein, M., Tan, H., Todd, I., Chechik, L., Li, J., Bambach, M., 2022. Alloy design and adaptation for additive manufacture. Journal of Materials Processing Technology, 299. https://doi.org/10.1016/j.jmatprotec.2021.117358

Cruz, D. J., Shamchia, S.P., Santosa, A.D., Amaral, R. L., Tavares, P. J., Moreira, P.M.G.P, 2020. Development of a mini-tensile approach for sheet metal testing using Digital Image Correlation. Procedia Structural Integrity, 25(2019), 316–323. https://doi.org/10.1016/j.prostr.2020.04.036.

Dass, A., Moridi, A., 2019. State of the art in directed energy deposition: From additive manufacturing to materials design. Coatings, 9(7), 1–26. https://doi.org/10.3390/coatings9070418.

Du Plessis, A., Yadroitsev, I., Yadroitsava, I., Le Roux, S.G., 2018. X-Ray Microcomputed Tomography in Additive Manufacturing: A Review of the Current Technology and Applications. 3D Printing and Additive Manufacturing, 5(3), 227–247. https://doi.org/10.1089/3dp.2018.0060.

Durejko, T., Zietala, M., Polkowski, W., Czujko, T., 2014. Thin wall tubes with Fe3Al/SS316L graded structure obtained by using laser engineered net shaping technology. Materials and Design, 63, 766–774. https://doi.org/10.1016/j.matdes.2014.07.011.

Džugan, J., Prochazka, R., Konopik, P., 2015. Micro-Tensile Test Technique Development and Application to Mechanical Property Determination, ASTM International, STP157620140022. https://doi.org/10.1520/STP157620140022

Ferreira, A.A., Amaral, R.L., Romio, P.C., Reis, A.R., Vieira, M.F., 2021a. Deposition of nickel-based superalloy claddings on low alloy structural steel by direct laser deposition. Metals, 11(8). https://doi.org/10.3390/met11081326.

Ferreira, A.A., Emadinia, O., Cruz, J.M., Reis, A.R., Vieira, M.F., 2021b. Inconel 625/AISI 413 Stainless Steel Functionally Graded Material Produced by Direct Laser Deposition. Materials, 14(19), 5595. https://doi.org/10.3390/ma14195595.

Ferreira, A.A., Darabi, R., Sousa, J.P. Cruz, J.M., Reis, A.R., Vieira, M.F., 2021c. Optimisation of direct laser deposition of a martensitic steel powder (Metco 42c) on 42crmo4 steel. Metals, 11(4), 1–18. https://doi.org/10.3390/met11040672.

Hu, J., Zhu, H., Zhang, J., Ouyang, M., Qiu, C., Duan, J., 2021. Effects of TiC addition on microstructure, microhardness and wear resistance of 18Ni300 maraging steel by direct laser deposition. Journal of Materials Processing Technology, 296, 117213. https://doi.org/10.1016/j.jmatprotec.2021.117213.

Jiang, Y., Cheng, Y., Zhang, X., Yang, J., Yang, J., Cheng, Z., 2020. Simulation and experimental investigations on the effect of Marangoni convection on thermal field during laser cladding process. Optik, 203(December 2019), 164044. https://doi.org/10.1016/j.ijleo.2019.164044.

Koike, R., Unotoro, I., Kakinum, Y., Aoyama, T., Oda, Y., Kuriya, T., Fujishima, M., 2017. Evaluation for mechanical characteristics of Inconel625-SUS316L joint produced with direct energy deposition. Procedia Manufacturing, 14, 105–110. https://doi.org/10.1016/j.promfg.2017.11.012.

Mahamood, R. M., 2018. Laser Metal Deposition of Metals and Alloys. DOI: https://doi.org/10.1007/978-3-319-64985-6.

Martin, N., Hor, A., Copin, E., Lours, P., Ratsifandrihana, L., 2022. Correlation between microstructure heterogeneity and multi-scale mechanical behavior of hybrid LPBF-DED Inconel 625. Journal of Materials Processing Technology, 303, 117542. https://doi.org/10.1016/j.jmatprotec.2022.117542.

Meera Mirzana, I., Rao, G.K.M., Rahemana, S., Ahmeda, M.Z., 2016. Fabrication and Micro-structural study of Functionally Graded Material Disc of SS316/IN625. Materials Today: Proceedings, 3(10), 4236–4241. https://doi.org/10.1016/j.matpr.2016.11.103.

Meng, W., Zhang, W., Zhang, W., Yin, X., Guo, L., Cui, B., 2019. Additive fabrication of 316L/Inconel625/Ti6Al4V functionally graded materials by laser synchronous preheating. International Journal of Advanced Manufacturing Technology, 104(5–8), 2525–2538. https://doi.org/10.1007/s00170-019-04061-x.

Popovich, V. A., Borisov, E.V., Popovich, A.A., Sufiiarov, V.Sh., Masaylo, D.V., Alzina, L., 2017. Functionally graded Inconel 718 processed by additive manufacturing: Crystallographic texture, anisotropy of microstructure and mechanical properties. Materials and Design, 114, 441–449. https://doi.org/10.1016/j.matdes.2016.10.075.

Sarathchandra, D. T., Kanmani Subbu, S., Venkaiah, N., 2018. Functionally graded materials and processing techniques: An art of review. Materials Today: Proceedings, 5(10), 21328–21334. https://doi.org/10.1016/j.matpr.2018.06.536.

Soodi, M., Masood, S. H., Brandt, M., 2013. Thermal expansion of functionally graded and wafer-layered structures produced by laser direct metal deposition. International Journal of Advanced Manufacturing Technology, 69(9–12), 2011–2018. https://doi.org/10.1007/s00170-013-5157-9.

Su, J., Qiu, X., Xing, F., Ruan, Y., 2019. Effect of preheating temperature on microstructure and properties of 42CrMo4/38MnVS6 heterogeneous laser welded joint. Metals, 9(8). https://doi.org/10.3390/met9080870.

Su, Y. Chen, B., Tan, C., Song, X., Feng, J., 2020. Influence of composition gradient variation on the microstructure and mechanical properties of 316 L/Inconel718 functionally graded material fabricated by laser additive manufacturing. Journal of Materials Processing Technology, 283 (January). https://doi.org/10.1016/j.jmatprotec.2020.116702.

Sui, S. Tan, H., Chen, J., Zhong, C., Li, Z., Fan, W., Gasser, A., Huang, W., 2019. The influence of Laves phases on the room temperature tensile properties of Inconel 718 fabricated by powder feeding laser additive manufacturing. Acta Materialia, 164, 413–427. https://doi.org/10.1016/j.actamat.2018.10.032.

Thompson, S. M., Bian, L., Shamsaei, N., Yadollahia, A., 2015. An overview of Direct Laser Deposition for additive manufacturing; Part I: Transport phenomena, modeling and diagnostics', Additive Manufacturing, 8, 36–62. https://doi.org/10.1016/j.addma.2015.07.001.

Toyserkani, E., Khajepour, A., Corbin, S., 2017. Laser Cladding. New York, 11(2), 221. ISBN 0-8493-2172-7.

Walker, K. F., Lourenço, J.M., Sun, S., Brand, M., Wang, C.H., 2017. Quantitative fractography and modelling of fatigue crack propagation in high strength AerMet®100 steel repaired with a laser cladding process. International Journal of Fatigue, 94, 288–301. https://doi.org/10.1016/j.ijfatigue.2016.06.031.

Wang, Q., Zhang, S., Zhang, C., Wu, C., Wang, J., Chen, J., Sun, Z., 2017. Microstructure evolution and EBSD analysis of a graded steel fabricated by laser additive manufacturing. Vaccum, 141, 68–81. https://doi.org/10.1016/j.vacuum.2017.03.021.

Wang, R., Dong, T., Di, Y., Wang, H., Li, G., Liu, L., 2019. High temperature oxidation resistance and thermal growth oxides formation and growth mechanism of double-layer thermal barrier coatings. Journal of Alloys and Compounds, 798, 773–783. https://doi.org/10.1016/j.jallcom.2019.05.052.

Yan, L., Chen, Y., Liou, F., 2020. Additive manufacturing of functionally graded metallic materials using laser metal deposition. Additive Manufacturing, 31(November 2019), 100901. https://doi.org/10.1016/j.addma.2019.100901.

Zhang, B., Jaiswal, P., Rai, R., Nelaturi, S., 2018. Additive Manufacturing of Functionally

Graded Material Objects: A Review. Journal of Computing and Information Science in Engineering, 18(4), 1215–1231. https://doi.org/10.1115/1.4039683.

Zhang, X., Chen, Y., Liou, F., 2019. Fabrication of SS316L-IN625 functionally graded materials by powder-fed directed energy deposition. Science and Technology of Welding and Joining, 24(5), 504–516. https://doi.org/10.1080/13621718.2019.1589086.

Chapter 6

ONGOING WORKS AND PROPOSALS FOR FURTHER RESEARCH

Ongoing Works and Proposals for Further Research

Preliminary tooth reconstruction

In order to validate the concept developed throughout this research, rebuilding tests of a previously selected gear were initiated. This step aims to evaluate the reconstruction process of spur gears through the characterization of geometric properties, mechanical properties and functional aspects. Figure 1 shows the gear (FZG pinion type C14) chosen for the laboratory tests for rebuilding the teeth.

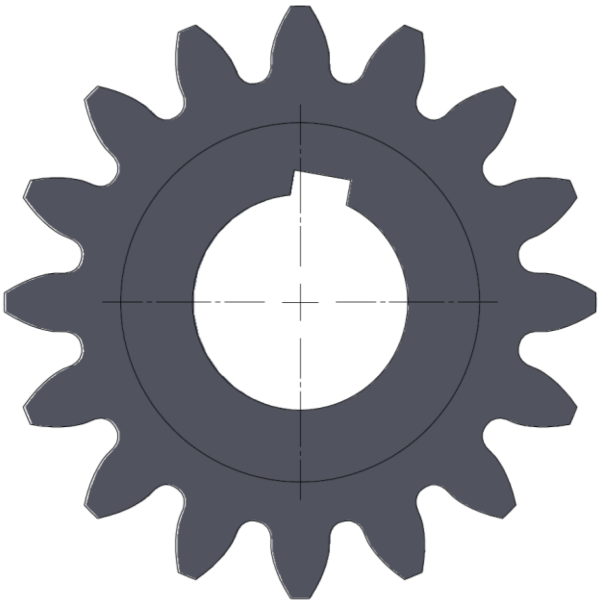

Figure 1. Schematic of the FZG Pinion Type C14.

The gear used for the development of the laboratory scale research is manufactured in 42CrMo4 and carburized to produce a 60 HRC surface hardness. The mating wheel is of the same type but with 24 teeth, and the Pinion geometric characteristics are shown in Table 1.

Table 1. FZG Pinion Type C14

Tooth Characteristic	Value
Module	4,5 mm
Number of Teeth	16
Reference Chainring	ISO53 – 20°
Primary Cut Diameter	72,000 mm
Tooth Offset Coefficient	+0,1817
Tangential dimension k Teeth (k = 3)	$34{,}779^{-0{,}017}_{-0{,}141}$ mm
Class DIN	5b24
Between Shaft	$91{,}5 \pm 0{,}01$ mm
Number of Teeth Mating Whee	24

The gear repair process is shown in Figure 2. Figure 2A shows the cuts performed on the gear, where region 1 was machined to remove all the tooth. In region 2, partial tooth removal was performed. Meanwhile, in region 3, total removal and deepening of the cut allowed for greater interaction and dilution of the material deposited with the substrate. Figure 2B shows the repair via Direct Laser Deposition, and Figure 2C shows the restored geometry after machining.

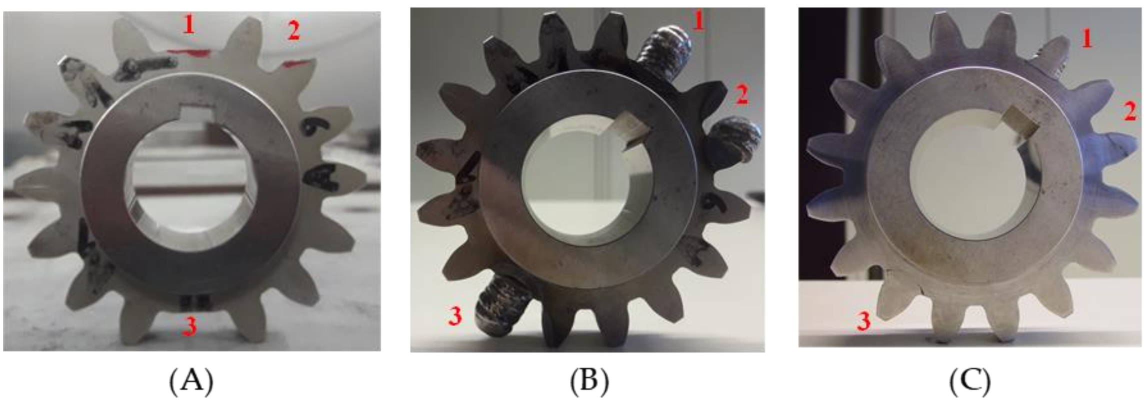

Figure 2. FZG Type C14 Pinion. (A) cuts, (B) repair via Direct Laser Deposition and (C) geometry restoration.

Initially, the reconstruction was made using Inconel 625 (M625), deposited with the conditions and parameters described in chapters 3 and 4. The tests are being carried out at the Tribology, Vibrations and Industrial Management Unit of the Mechanical

Engineering Department of the Faculty of Engineering of the University of Porto. After these tests, similar procedure will be performed with the 50% M625 + 50% M42C powder mixture, using the same type of gear.

Initial laboratory-scale testing allows project risk to be mitigated by iteratively producing successive test elements and validating them. Laboratory specimens/prototypes of a more functional character will be built throughout the project to verify structures, materials, manufacturing procedures and connection between systems. The final tests will be executed on an industrial scale, reconstructing one or more gear teeth to be tested on SERMEC Group's test bench, as shown in Figure 3.

Figure 3. Test bench SERMEC Group.

SERMEC has a 2 MW test bench capable of testing transmission elements (gears, shafts, etc.) in accordance with standards and thus comparing performances between new and repaired components. This comparison will attest to the compliance with the imposed safety criteria and industrial validation

New Materials Development

The development of innovative materials for the various industrial sectors to repair large components pushes the boundaries of material properties to extreme levels, being one of the motivations throughout this research. Another factor is the hardness that the gearing must have on the outer layer, and the neighbouring teeth have a hardness around 60 HRC, obtained through thermochemical treatments.

Due to this fact, a new FGM was produced by mixing M625 and NiCrWMo alloy. The FGM was characterized by microstructural analysis and microhardness mapping, and some results are presented below.

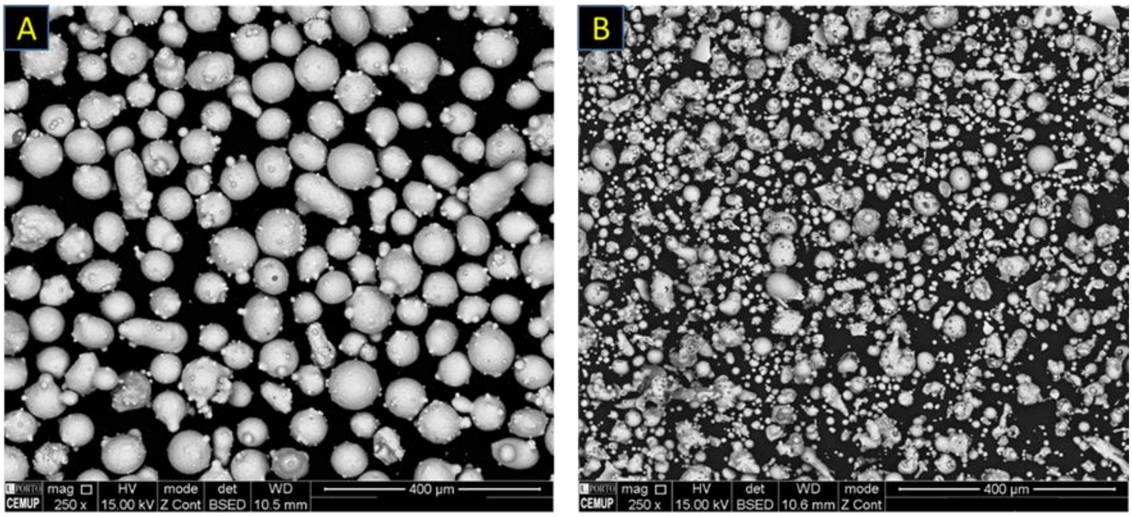

Figure 1. Powder morphology. (A) MetcoClad 625 – M625; (B) NiCrWMo – D4006.

Table 1. Powders chemical composition.

Powders	C	Cr	Fe	Mo	Nb	B	Cu	W	Ni
M625	-	21.3	4.1	9.2	4.6	-	-	-	Balance
D4006	0.75	20.5	0.9	9.0	-	0.75	4.0	10.0	Balance

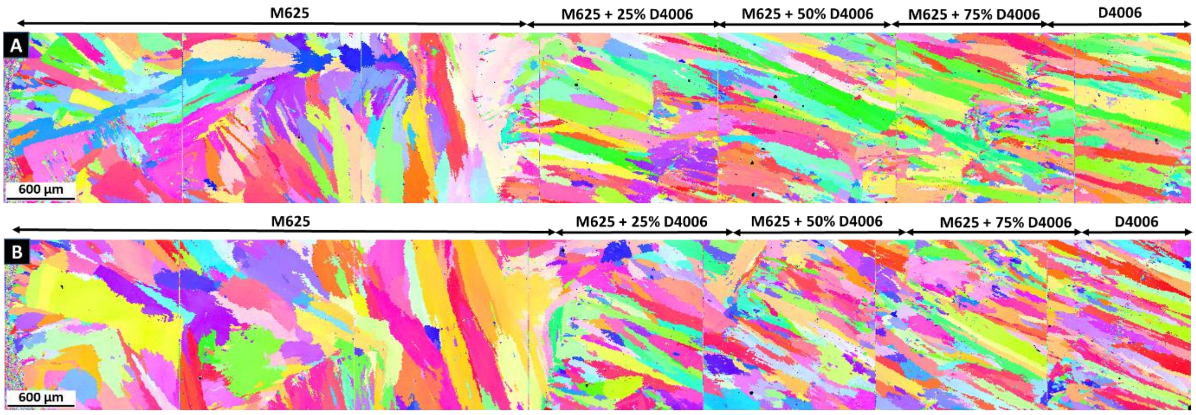

Figure 2. EBSD maps of the as-built Functionally Graded Materials (FGM): (A) without PHT and (B) With PHT.

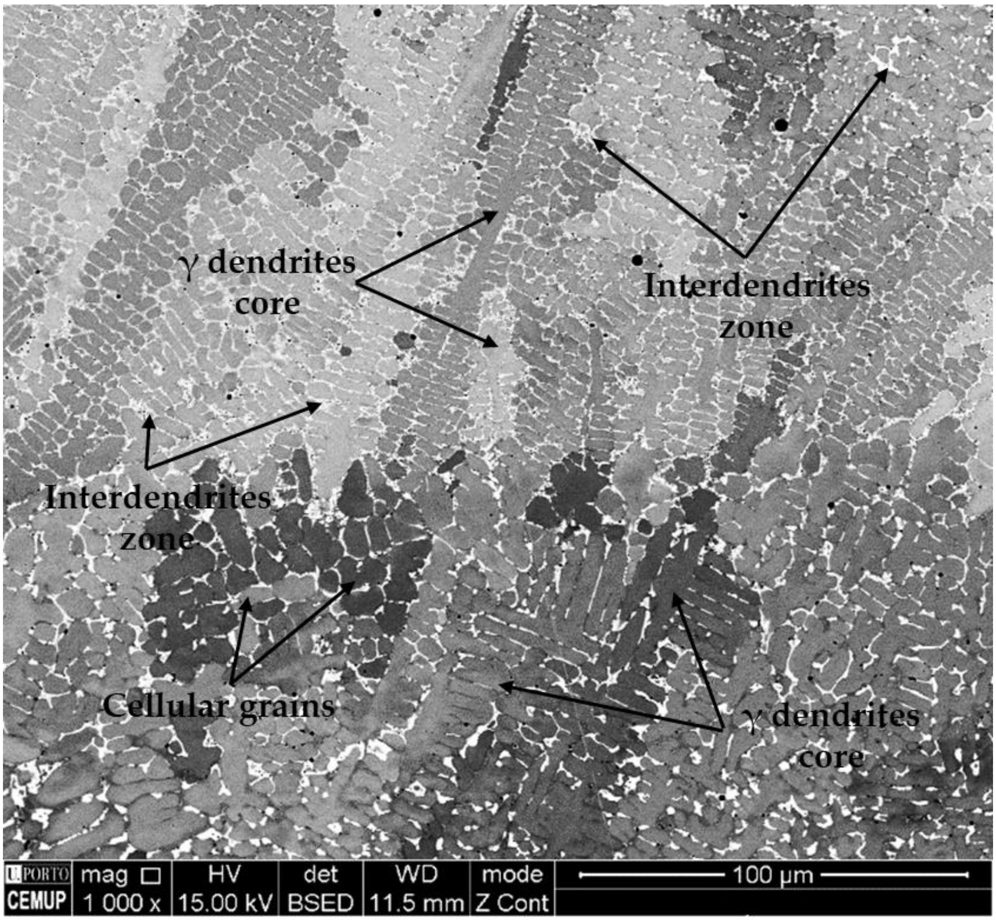

Figure 3. Microscopic morphology obtained by scanning microscopy (SEM) of the FGM produced by direct laser deposition (DLD). Image taken in the transition from M625-25% D4006 to M625-50% D4006.

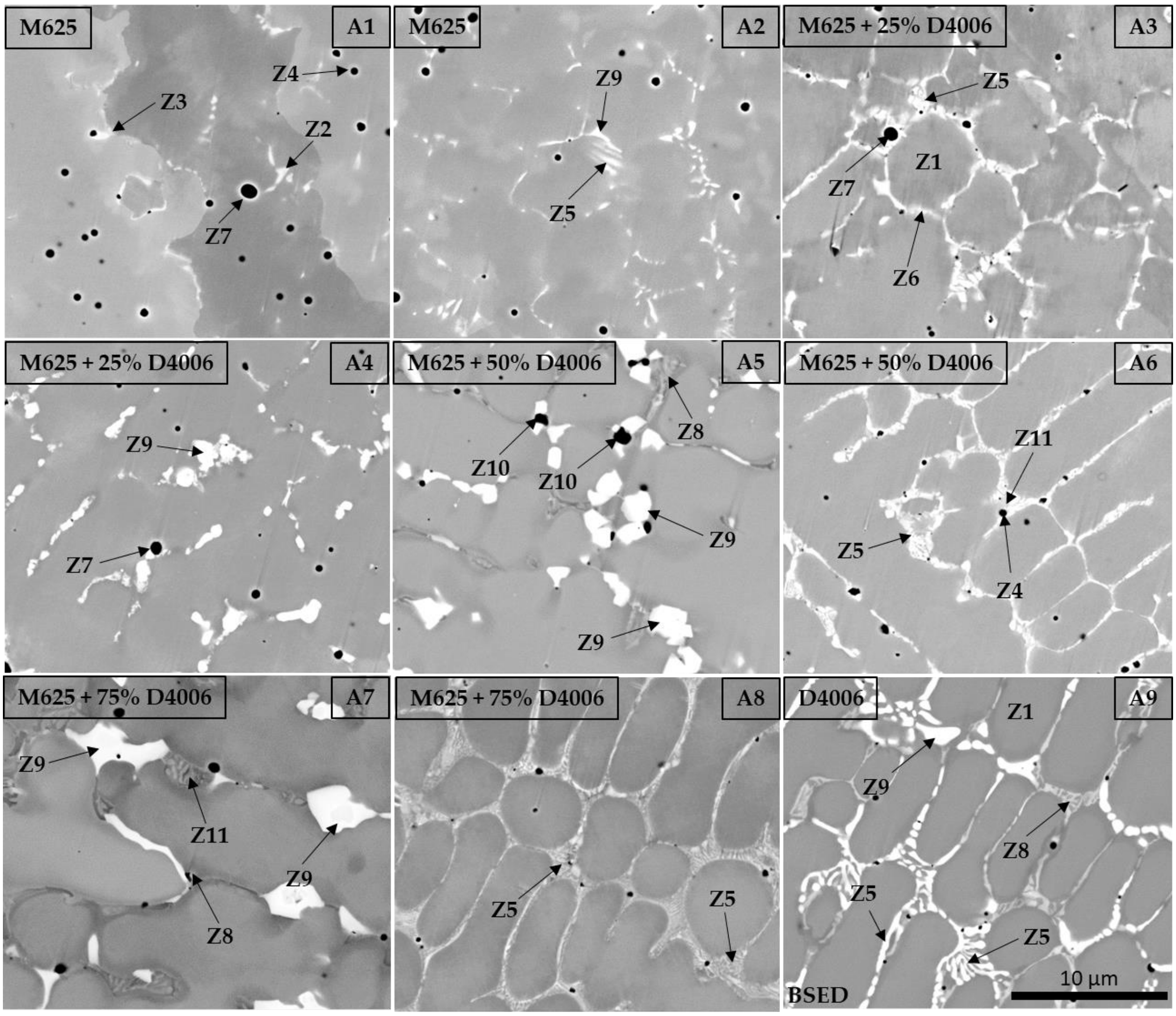

Figure 4. Microstructural constituents in the matrix and interdendritic zones of FGM.

Table 2. EDX chemical composition (in at%) and possible phases, based on phase diagrams [58]–[61], EDX and EBSD analysis of the different zones presented in the SEM images in Figure 8.

Zone	Chemical Composition in (At %)												
	B	C	O	Al	Si	W	Nb	Mo	Mn	Cr	Fe	Ni	Cu
Z1	-	4.0	-	-	-	1.2	1.3	5.2	-	22.3	3.4	61.0	1.7
Z2	-	44.6	-	-	-	-	55.4	-	-	-	-	-	-
Z3	-	26.9	-	-	12.4	-	19.6	41.1	-	-	-	-	-
Z4	-	2.9	60.4	3.3	18.0	-	2.5	1.5	11.4	-	-	-	-
Z5	-	13.0	-	-	-	-	22.9		-	18.4	9.3	36.5	-
Z6	-	5.6	-	-	-	2.1	5.1	17.6	-	30.9	2.1	36.6	-
Z7	-	3.4	30.3	0.7	7.3	-	3.0	6.6	-	22.9	-	25.8	-
Z8	-	4.1	-	-	-	1.3	1.6	8.8	-	37.6	0.7	45.9	-
Z9	-	10.9	-	-	-	5.7	4.9	17.6	-	22.3	0.8	37.7	-
Z10	6.8	3.2	43.4	-	-	0.7	1.1	6.1	-	33.5	-	5.3	-
Z11	-	5.6	-	-	-	3.9	1.8	16.0	-	36.6	-	36.0	-

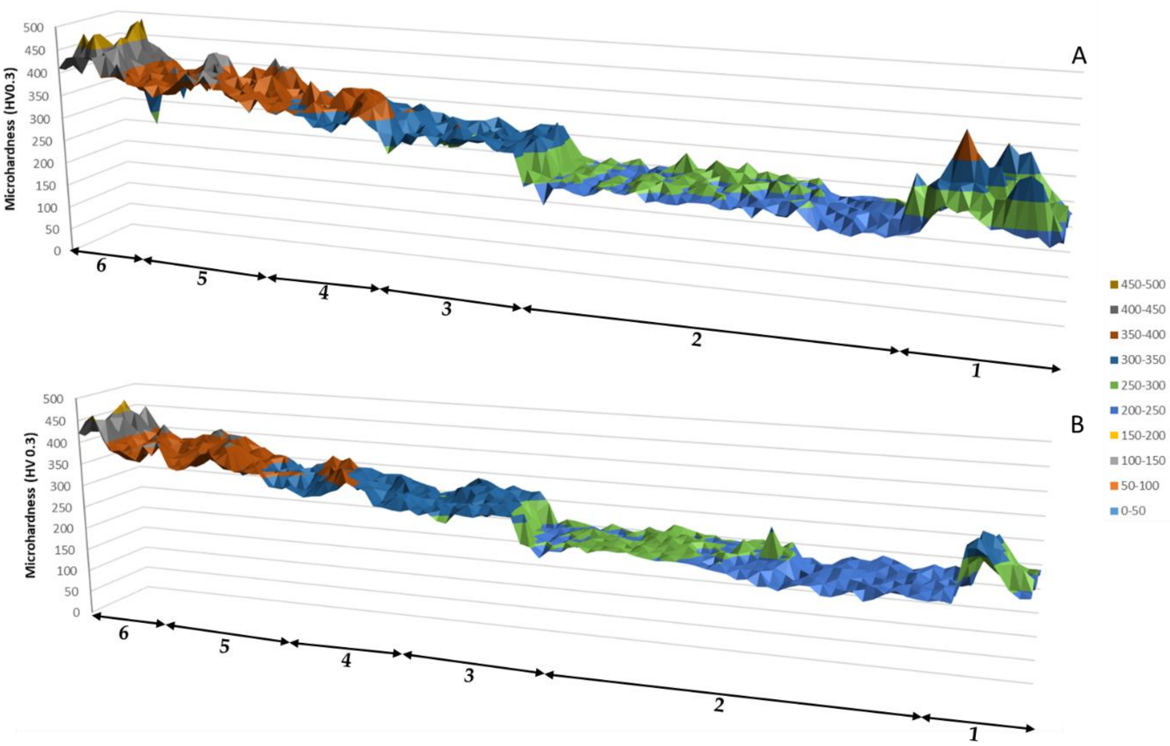

Figure 5. FGM microhardness mapping - (A) without PHT and (B) with PHT. Microhardness regions: 1 – HAZ; 2 – 100% M625; 3 – M625 + 25% D4006; 4 – M625 + 50% D4006; 5 – M625 + 75% D4006; 6 – 100% D4006.

For future work, bulks were produced that will allow the evaluation of the mechanical and microstructural properties of each layer. Tests are underway to determine the fatigue resistance of bulks produced with M625 + M42C and M625 + NiCrMoW selected compositions. For the latter combination (M625 + NiCrMoW), mixing the powders is essential because 100% NiCrMoW exhibits low metallurgical bonding to the steel substrate, with deposited material detachment, even with changes in processing parameters.

Chapter 7

GENERAL CONCLUSIONS

General Conclusions

This PhD thesis was established to demonstrate the industrial applicability in producing innovative materials for the repair/reconstruction process of industrial components such as gears. Throughout this investigation, emphasis was given to evaluating the mechanical, microstructural and fractographic characterization of single lines, FGM's and bulks. Synergies of different properties of these innovative materials were also explored to obtain a repair/reconstruction with the required characteristics. The main conclusions obtained in this investigation are presented below.

- ✓ The analysis of the deposition of AISI 431 steel powder (Metco 42C) clads on a 42CrMo4 steel substrate revealed a martensitic structure with delta ferrite. This structure is susceptible to the appearance of cracks in the cladding area, this cracking being more common when the substrates were pre-heated to 300 °C. Increasing laser power and scan speed increases the possibility of cracking. The use of complex experimental parameters made it possible to define the conditions that prevent cracking and guarantee a sound clad with a good deposition yield. The use of a genetic optimization algorithm indicated that the best processing conditions were obtained with speeds of 10 mm/s, feed rate of 15 g/min, and laser powers of 1.5 and 1.7 kW for samples with and without pre-heating, respectively.
- ✓ The deposition of Inconel 625 claddings onto a 42CrMo4 steel substrate was performed under varying processing conditions: laser power, scanning speed, feed rate, and pre-heating. A DLD process window map considering processing variables shows that several combinations can be used. However, the cladding produced with 2 kW of laser power, a scanning speed of 6 mm/s, and a 20 g/min feed rate presented adequate dilution and wettability. The

deposited layers were produced without significant structural defects such as cracks, pores, or other types of discontinuities. Substrate pre-heating to 300 °C influences the microstructure of the cladding/substrate interface, reducing the formation of the deleterious Laves phase. PHT also alters the hardness profile, mainly in the heat-affected zone, due to modification of the martensite microstructure and increased residual austenite.

- ✓ The bulk produced with M625 powder by DLD did not present relevant defects, such as cracks or porosities, which could compromise its structural integrity. Columnar dendrites are the main microstructural feature seen throughout the entire bulk. Laves phase, carbides and complex oxides resulting from microsegregation were detected. The metallurgical bonding of the bulk to the substrate is continuous and without stress concentrations. Tensile samples with an M625/steel interface in the central region suffer rupture by the M625 (less resistant material) away from the interface. Tensile samples with their length parallel to the substrate surface are slightly more strong and less ductile than those with length perpendicular to that surface, indicating a texture effect, which can be correlated to the epitaxial growth of columnar grains. The wear behaviour showed a linear development, representing a constant wear rate throughout the tests, and the worn surfaces showed abrasive wear.
- ✓ Functional Gradient Materials (FGM) combine materials with different compositions, leveraging the best properties of each and exploring reactions that can give rise to unexpected properties. FGMs respond to the growing demand from various industrial sectors for materials with better performance, allowing them to produce components with unique characteristics and a gradient of properties along a specific direction. The production FGM by the DLD technique was evaluated. The deposition started with layers of nickel-based superalloy (M625 powders) and ended with layers of martensitic stainless steel (M42C powders). Three mixtures of powders were used in intermediate deposits, sequentially increasing by 25 wt.% the amounts of M42C

powder. Cracking-free production of the Inconel 625/AISI 431 steel FGM, applying DLD, is only verified up to a certain composition. The addition of stainless steel cannot exceed 50 wt.%. The grain microstructure in Inconel 625/AISI 431 FGM is essentially columnar, regardless of pre-heating. Pre-heating influenced the microstructural evolution and microhardness in the substrate and the first deposited layers; the region of planar grains observed in the vicinity of the substrate only formed without pre-heating. A marked increase in grain size and a reduction in martensite were observed in the pre-heated substrate HAZ, decreasing the hardness of this region.

- ✓ A bulk material composed of 50% Inconel 625 mixed with AISI 431 alloy was successfully produced by laser direct deposition process. Moreover, individual blocks of Inconel 625 and AISI 431 alloys were similarly produced and to be used as references. The 42CrMo4 steel was selected as substrate pre-heated to 300 °C. Uniaxial tensile test was conducted, and a digital image correlation methodology was implemented to evaluate plastic deformation behaviours. Abrasive wear resistance was performed using ball cratering analysis. Microstructure observations were performed for microstructure analysis, such as fracture surface, wear measurements, and phase formations. The mechanical behaviour of the bulk deposited material is not very far from the Inconel 625; the worst results were obtained for the M42C alloy. The UTS and elongation of the bulk material are higher in the direction in parallel with building construction than in the horizontal direction. Fracture analysis supports the plastic deformation behaviour of the M625 and the bulk materials when exposed to uniaxial stress, respectively, in parallel with the building direction and perpendicular direction, i.e. the presence of dimples seemed more dominant than cleavages face in these materials. The bulk material has good bonding with the substrate alloy since the fracture happed to the deposited material. The bulk material illustrates a similar behaviour in the abrasive wear test as the M625 alloy.

- ✓ A crack-free, high-density, quality FGM structure was produced according to the transition route: 42CrMo4 → M625 → M625 + 25% D4006 → M625 + 50% D4006 → M625 + 75% D4006→ D4006. The elemental concentration gradient was detected by performing linear chemical analysis along the FGM, for both processing (with and without PHT), by EDX technique. It is clearly observed that Ni compositional decreases with the increase in the composition of the elements Nb, Mo, W and Cr. The elemental distribution maps show the elemental segregation and the heterogeneity of the alloy formed, allowing us to observe the interdendritic zones and the core dendrites. The phase-detection made it possible to observe the compositional diversity and the influence on the gradient hardness. The microhardness mapping showed that with the compositional increase of D4006, there was a significant increase in hardness, mainly due to the alloying elements W, Mo and Cu, driving the formation of carbides, TCP phases, oxides and solid-solution strengtheners. With the substrate pre-heating, there was a decrease in hardness in the HAZ, promoted by the formation of self-tempering martensite. PHT also allowed the Fe diffusion to M625 and Ni, Mo to the substrate, increasing the percentage of austenite in the HAZ.

APPENDIX

SCIENTIFIC DISSEMINATION

Appendix A – Oral Presentation in 2nd International Conference on Advanced Joining Processes

Functionally Graded Materials Fabricated by Direct Laser Deposition for Gear Repair

A. A. Ferreira[1,2], A. R. Reis[1,2], J. P. Sousa[2], P.C. Romio[1], J. Cruz, J.H. Seabra[1,2], M.F. Vieira[1,2]

[1]Faculty of Engineering of the University of Porto, 4200-465 Porto, Portugal.

[2]LAETA/INEGI—Institute of Science and Innovation in Mechanical and Industrial Engineering, 4200-465 Porto, Portugal.

[3]SERMEC-Group, 4425-348 Folgosa-Maia, Portugal.

Functionally Graded Materials (FGM) production is an option for various industrial sectors and many engineering applications. FGMs are materials that gradually change composition and structure. In this study, FGMs were produced by Direct Laser Deposition (DLD) to repair gears. These gears are subject to various chemical and mechanical solicitations during their life cycle. These phenomena can lead to surface defects or cracks, compromising the structural integrity of the component and the entire structure to which it is attached. Repairing these components is a common practice and necessary to make them viable again. In addition, DLD component repair offers great potential for saving time and cost compared to conventional manufacturing technologies such as casting, plastic forming, and cutting or joining processes. Two different types of functionally graded FGMs were produced by mixing nickel superalloy powders, type Inconel 625, with martensitic stainless-steel powders, type AISI 431, or with NiCrWMo powders. Metallurgical, chemical, and mechanical characterizations of the FGMs and repaired components were performed, and their correlation with process parameters was determined and discussed. Microstructural characterization and phase identification were performed by scanning electron microscopy, chemical analysis by energy-dispersive X-ray spectroscopy, and electron backscatter diffraction. The microhardness mapping and tensile tests supported the mechanical characterization. The compositions of the FGMs and the processing conditions that guarantee an effective repair of the gear were selected.

Appendix B – Oral Presentation in 14th World Congress in Computational Mechanics (WCCM)

14th World Congress in Computational Mechanics (WCCM)
ECCOMAS Congress 2020
19 – 24 July 2020, Paris, France

NUMERICAL PREDICTION OF MELT POOL SHAPE AND DILUTION IN ADDITIVE MANUFACTURING OF METALLIC POWDERS

Roya Darabi[1,2*], André Ferreira[2], Manuel Jimenez[2], Margarida Machado[1], Marco Parente[1,2] and Jose Cesar de Sa[1,2]

[1] INEGI - Institute of Science and Innovation in Mechanical and Industrial Engineering, Rua Dr. Roberto Frias 400, 4200-465, Porto (PORTUGAL), E-mail: rdarabi@inegi.up.pt (corresponding author), URL: http://www.inegi.pt/

[2] FEUP - Faculty of Engineering of University of Porto, Rua Dr. Roberto Frias, 4200-465, Porto (PORTUGAL), URL: https://sigarra.up.pt/up/en/

Keywords: Additive manufacturing, Laser metal deposition, Computational model, Melt pool.

A transient finite-element approach is proposed for numerical simulation of additive manufacturing technology of laser metal deposition (LMD) towards predicting temperature distribution, melt pool shape and dilution [1]. This computational model was implemented in ABAQUS suite (FE software) and validated throughout 1D line experiments of LMD. At each time increment, heat source [2] and progressive element activation feature were implemented via user subroutines, as well as the correspondent variation of the heat loss coefficient [3]. Experimental work was carried out using nickel-based superalloy powders (MetcoClad 625®) as adding material and a tempering steel (42CrMo4) as substrate. The power and scan speed have been changed for different deposit lines to investigate their effect on the amount of the dilution from the substrate and on the melt pool morphology of the solid-liquid interface.

REFERENCES

[1] Fallah, Vahid, et al. "Temporal development of melt-pool morphology and clad geometry in laser powder deposition." Computational materials science 50.7 (2011): 2124-2134.

[2] John Goldak, Aditya Chakravarti, Malcolm Bibby, A new finite element model for welding heat sources, Metallurgical Transactions B, June 1984, Volume 15, Issue 2, pp 299–305

[3] Fanous, Ihab FZ, Maher YA Younan, and Abdalla S. Wifi. "3-D finite element modeling of the welding process using element birth and element movement techniques." J. Pressure Vessel Technol. 125.2 (2003): 144-150.

Acknowledgement:

Authors gratefully acknowledge the funding of Project Acknowledgement: Authors gratefully acknowledge the funding of Project ADDing (POCI-01-0145-FEDER-030490), financed by FEDER funds through the Operational Program Competitiveness and Internationalization - COMPETE 2020 and by National Funds (PIDDAC) through the FCT/MCTES, Portugal.